



SAPIENZA  
UNIVERSITÀ DI ROMA

Ph.D. in Earth Sciences

Cycle XXXV

STRUCTURAL BREAKDOWN AND THERMAL BEHAVIOR OF SELECTED  
BOROSILICATE MINERALS

PhD candidate:  
Beatrice Celata

Supervisor:  
Prof. Giovanni B. Andreozzi



# Index

<b>Thesis objectives</b>	<b>5</b>
<b>1 Introduction</b>	<b>5</b>
1.1 Borosilicate minerals	5
1.2 Tourmaline	5
1.3 Axinite	12
1.4 Geological implications: water and boron recycling in subduction systems	14
<b>2 Experimental work</b>	<b>20</b>
2.1 Crystal chemistry of starting materials	22
2.1.1 Schorl ( <i>published paper</i> ):	22
Crystal-chemical behavior of Fe <sup>2+</sup> in tourmaline dictated by structural stability: insights from a schorl with formula Na <sup>Y</sup> (Fe <sup>2+</sup> <sub>2</sub> Al) <sup>Z</sup> (Al <sub>3</sub> Fe <sup>2+</sup> )(Si <sub>6</sub> O <sub>18</sub> )(BO <sub>3</sub> ) <sub>3</sub> (OH) <sub>3</sub> (OH,F) from Seagull batholith (Yukon Territory, Canada)	
2.1.2. Mn-bearing fluor-elbaite ( <i>published paper</i> ):	32
Mn-bearing purplish-red tourmaline from the Anjanabonoina pegmatite, Madagascar	
2.1.3. Oxy-dravite–maruyamaite series ( <i>manuscript about to be submitted</i> ):	45
Crystal chemistry of the oxy-dravite–maruyamaite series from the Kokchetav Massif (Kazakistan)	
2.1.4 Schorl 1-A ( <i>published paper</i> ):	64
Schorl 1-A from Langesundsfjord (Norway)	
2.2. High-Temperature experiments	76
2.2.1. Fe-rich fluor-elbaite ( <i>published paper</i> ):	76
In situ high-temperature behaviour of fluor-elbaite: breakdown conditions and products	
2.2.2. Mn-bearing fluor-elbaite ( <i>published paper</i> ):	85
HT breakdown of Mn-bearing elbaite from the Anjanabonoina pegmatite, Madagascar	
2.2.3 Uvite ( <i>published paper</i> ):	97
<i>In-situ</i> high-temperature behaviour and breakdown conditions of uvite at room pressure	

2.2.4 Schorl ( <i>published paper</i> ):	108
Thermal behavior of schorl up to breakdown temperature at room pressure	
2.2.5. Axinite ( <i>manuscript about to be submitted</i> ):	119
In situ thermal behavior of axinite at room pressure and breakdown products	
2.3. High-Pressure High-Temperature experiments	129
2.3.1. Schorl ( <i>published paper</i> )	129
Schorl breakdown at upper mantle conditions: insights from an experimental study at 3.5 GPa	
<b>3. Discussion and conclusions</b>	<b>141</b>



## **Thesis objectives**

The specific objective of this thesis was the definition of thermal behavior, breakdown mechanisms and breakdown products of selected borosilicates, specifically tourmalines and axinites, which are the most and the less investigated borosilicate phases, respectively, occurring in geological settings. The general objective was to assess the role of borosilicates in the dehydration embrittlement process along the downgoing slab, leading to the definition of their stability fields and to the quantitative evaluation of B-enriched fluids released during possible oxidation-deprotonation processes and structural breakdown of such mineral phases.

## **1. Introduction**

### 1.1 Borosilicate minerals

Borosilicates are minerals where the essential constituent is represented by boron, accommodated in their structure in planar triangular or tetrahedral coordination with hydrogen or hydroxyl groups (Hawthorne, 1996; Grew, 1996). They are very widespread accessory minerals commonly found in metamorphic rocks and constitute the main boron carriers in the crust, while the Mantle is rather depleted in boron. For this reason, the occurrence of boron in subducted slab is of crucial importance as it may provide information about the extent of crustal recycling. Important borosilicates include tourmaline, axinite, werdingite, boralsilite, dumortierite, holtite, howlite, and grandidierite. In this research project, only tourmaline (the most important) and axinite (one of the less investigated) are considered.

### 1.2 Tourmaline

Tourmalines are fascinating minerals ranging from the rare colorless species (achroites) to the most vibrant-colored and multi-colored ones. Known from centuries because of their eye-catching beauty, tourmalines were commercialized and appreciated by traders and buyers by ancient communities of the far East (Pezzotta and Laurs 2011). Confined to the gemologic imagery for ages, over the last few decades tourmalines scientific relevance has become more and more substantial because of their physico-chemical properties, particularly appealing for geological research. Tourmalines' widespread occurrence as nonopaque accessory minerals in sediments of all types and ages is due to their crystal structure that leads to an impressive thermal and mechanical stability. Such an ubiquity in almost all

the geological settings misled on tourmaline's value as a powerful diagnostic tool to infer precise information on its geological environment, leading to a limited interest in this mineral group. Tourmaline neglect ceased only after years of systematic research on this complex group of minerals, and a specific classification combined to the information derived from the chemical composition defined "a new mineralogical era" dominated by tourmaline. Tourmalines commonly occur as euhedral crystals showing a predominantly prismatic habit and a variety of morphological forms (Goldschmidt, 1922), reported in Figure 1.

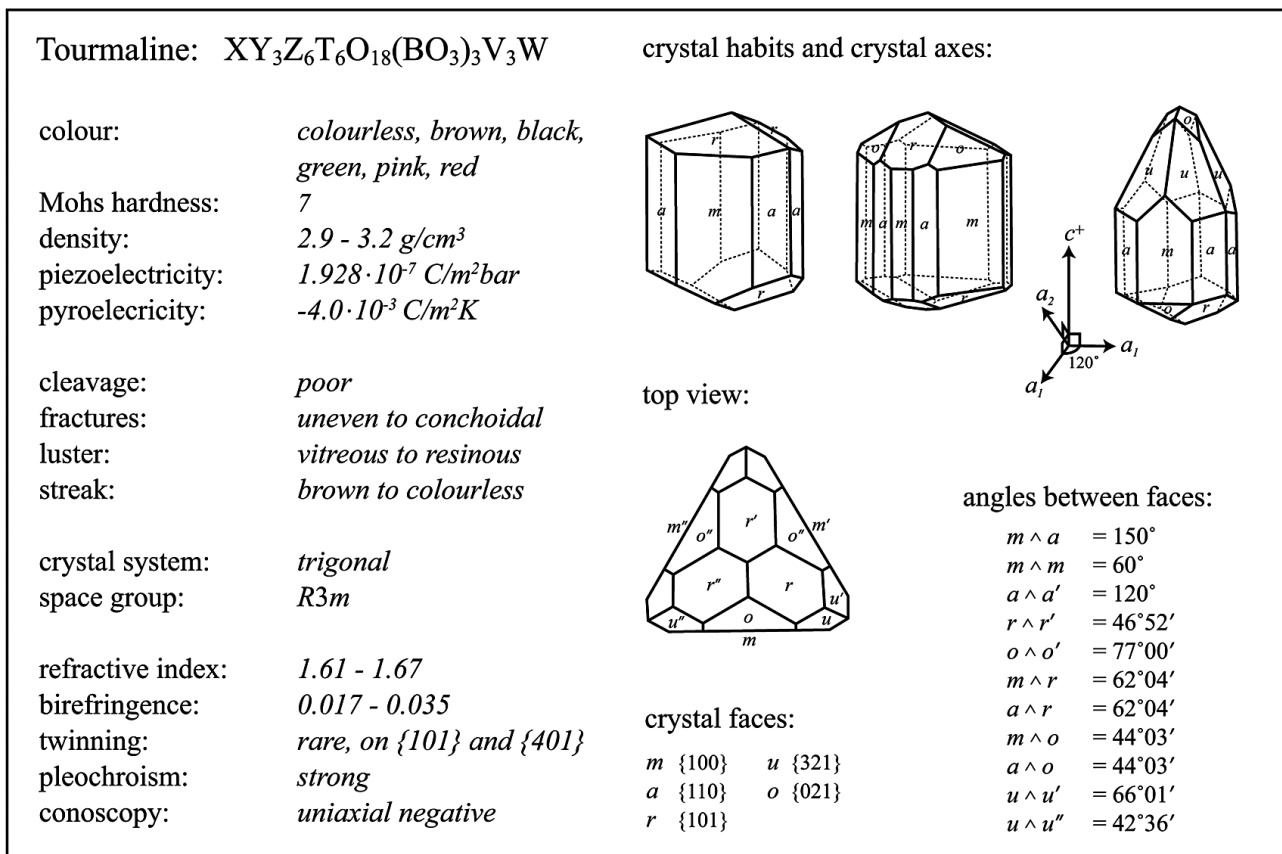


**Figure 1** Tourmaline's morphology, crystallographic information and main physical properties. From van Hinsberg et al. (2011).

One of the most obvious characteristics of tourmaline's morphology is the *hemimorphism*, id est the occurrence of different forms at the termination of the crystal, along the crystallographic axis *c* (Fig. 2). This feature leads to distinctive physical properties of tourmaline, as *pyroelectricity* and different growth rates at the two poles, respectively defined antilogous (+*c*) and analogous (-*c*). Vertical striations on the prism faces are common and lead to an easier identification of hand samples.

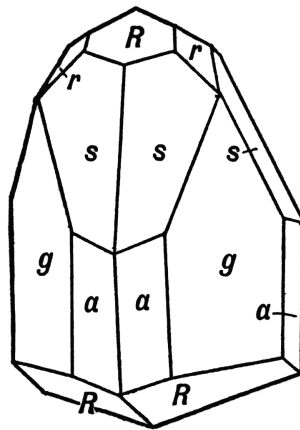


**Figure 2** Tourmaline exhibits hemimorphism in the direction of the vertical axis. Its forms are the prisms, (*g*), which as a result of hemimorphism appears as a trigonal prism, and (*a*); the scalenohedron, (*s*), and the two rhombohedrons, (*R*) and (*r*), at the antilogue pole, while only (*R*) occurs at the analogue pole. From George Huntington Williams (1892) *Elements of Crystallography for Students of Chemistry, Physics, and Mineralogy* (New York, NY: Henry Holt and Company)

### Crystal chemistry of tourmaline

Tourmaline is classified among the subclass of cyclosilicates, because of its distinctive structural feature of the six-membered tetrahedral rings stacking along the crystallographic axis *c* (Figure 3). All the [TO<sub>4</sub>] tetrahedra point towards the -*c* direction of the *c* axis, making tourmaline *non-centrosymmetric*.

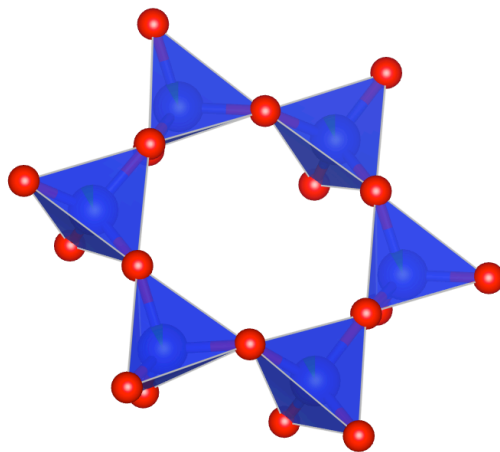


**Figure 3** The six-membered tetrahedral ring of tourmaline.

Tourmaline is a *borosilicate* mineral, since it is inextricably built over the  $\text{BO}_3$  triangular planar polyhedron which only contains boron (a full description of tourmaline structure is reported in Bosi 2018 and Hawthorne and Dirlam 2011). This polyhedron is linked to the trigonal antiprism  $\text{XO}_9$  (with which it shares an edge) that lies on the corners of a rhombohedral unit cell thus defining its space group symmetry  $R3m$ . Every  $\text{XO}_9$  antiprism is bordered by a six-membered tetrahedral ring  $[\text{T}_6\text{O}_{18}]$  and linked to two sets of octahedra: a triplet of  $\text{YO}_6$  octahedra which caps the antiprism towards the +c axis and another triplet of  $\text{YO}_6$  octahedra which caps the six-membered tetrahedral ring towards the -c axis. Such a defined unit of polyhedra ( $\text{T}_6\text{O}_{18} + \text{XO}_9 + \text{YO}_6$ ) forms a structural “island” stacking along the c axis (Figure 4a). Every structural island is framed by a “spiral” of  $\text{ZO}_6$  octahedra that define the tridimensional structure of tourmaline (Figure 4b). In particular, such a tridimensional structure is the key to understand the high tourmaline mechanical resistance and hardness (7-7 $\frac{1}{2}$  on Mohs scale).

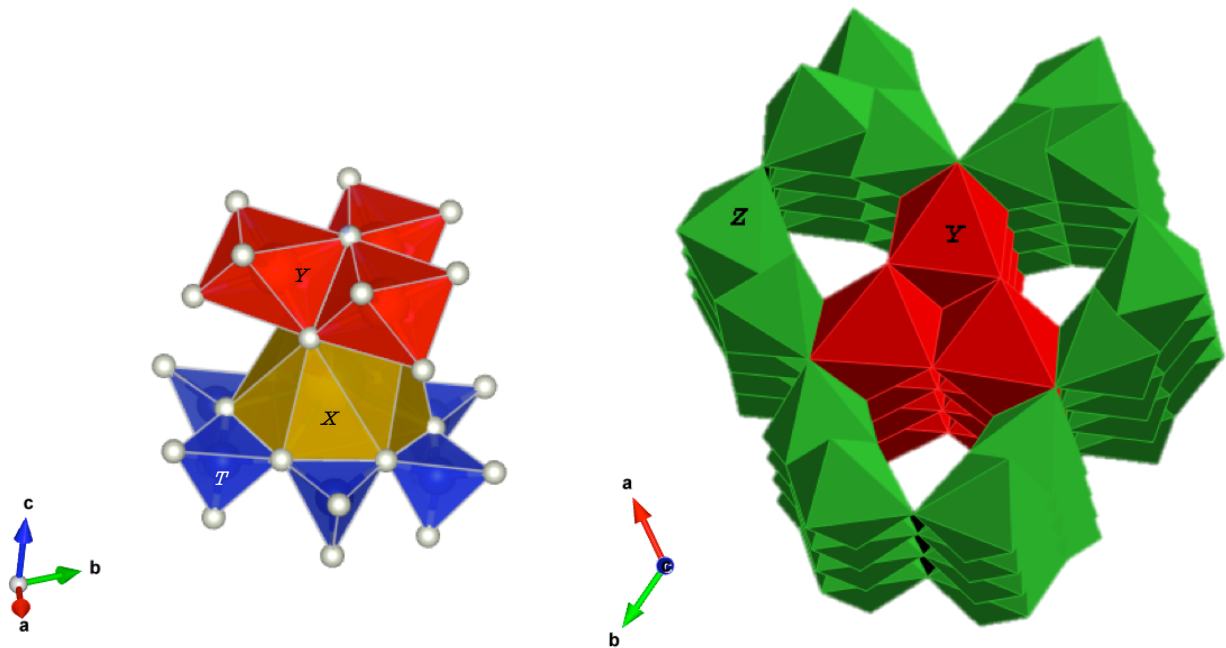


**Figure 4** Tourmaline structure: a) the "island" made of  $\text{T}_6\text{O}_{18}$  (in blue) +  $\text{XO}_9$  (in yellow) +  $\text{YO}_6$  (in red) polyhedral; b) the “spiral” of  $\text{ZO}_6$  octahedra (in green).

The crystal-chemical formula for tourmaline supergroup minerals is defined as follows:  $XY_3Z_6T_6O_{18}(BO_3)_3V_3W$ , where  $X$  represents the nine-fold coordinated polyhedra, crystallographically referred as  $^{[9]}X$  site,  $Y$  is the  $YO_6$  polyhedra referred as  $^{[6]}Y$  site, and  $Z$  stands for the spiral of octahedral  $^{[6]}Z$  sites framing the tourmaline structure.  $T_6O_{18}$  is the six-membered tetrahedral ring referred as  $^{[4]}T$  site,  $BO_3$  is the triangular planar site reserved to boron ( $^{[3]}B$  site).  $V$  and  $W$  are intended as group of anions occupying  $^{[3]}O3$  and  $^{[3]}O1$  sites, respectively.

Evidence of tetrahedral boron in substitution of Si were reported by Ertl et al. (1997), for olenite (4.225 apfu of B), Ertl et al. (2008; 2010) and of B/Al in substitution of Si by Hawthorne (1996) and in several experimental works on synthetic tourmalines (Wodara and Schreyer 1997; 1998; Berryman et al., 2016).

Tourmaline structure is very "flexible" as it can accommodate a wide range of chemical constituents and this feature is the key for its survival at very different pressure and temperature conditions. The  $X$  site population is represented by  $Na^+$ ,  $K^+$ ,  $Ca^{2+}$  cations; when the site is vacant, it is conventionally symbolized as " $\square$ ". The dominance of one cation over the others or over vacancies at the  $X$  site leads to a preliminary classification of tourmalines (Henry et al., 2011) into three groups: alkali, calcic or vacant (Figure 5).

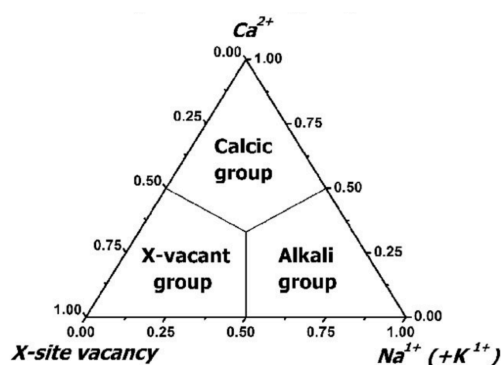


**Figure 5** Ternary system for the primary tourmaline groups based on the dominant occupancy of the  $X$  site. From Henry et al., (2011).

The  $X$  site population is not only important for classification purposes, but it also affects the structural parameters of tourmaline. In fact, going from Ca dominant ( $Ca^{2+}=1.18 \text{ \AA}$ ) to K dominant ( $K^+=1.55 \text{ \AA}$ ) tourmalines implies a significant increase in size of the  $X$ -site coordination polyhedron and corresponding shortening of the neighboring O1-H1 bonds. Moreover, the unit cell volume increases

from  $1560 \pm 3 \text{ \AA}^3$  of tourmaline with vacant  $X$  site to  $1590 \pm 2 \text{ \AA}^3$  of calcic tourmaline and such an increase is mainly borne by the  $c$  axis (Berryman et al., 2016).

The  $Y$  site is a quite regular octahedron which can be occupied by mono or multi-valent cations, e.g.:  $\text{Li}^{1+}$ ,  $\text{Mg}^{2+}$ ,  $\text{Fe}^{2+}$ ,  $\text{Mn}^{2+}$ ,  $\text{Cu}^{2+}$ ,  $\text{Al}^{3+}$ ,  $\text{Cr}^{3+}$ ,  $\text{V}^{3+}$ ,  $\text{Fe}^{3+}$ ,  $\text{Mn}^{3+}$  and  $\text{Ti}^{4+}$ . The expansion of the  $Y$  site due to the accommodation of larger cations affects the tetrahedral ring configuration, leading to a smaller puckering of it, and the smaller the  $Y$  site the more the  $Z$  octahedron is smaller and more compressed (Foit, 1989). The  $Z$  site is commonly occupied by  $\text{Mg}$ ,  $\text{Fe}^{2+}$ ,  $\text{Al}$ ,  $\text{Fe}^{3+}$ ,  $\text{Cr}^{3+}$ ,  $\text{V}^{3+}$  with a certain disorder extent given by the following formula  ${}^Y\text{Al} + {}^Z\text{R} \rightarrow {}^Y\text{R} + {}^Z\text{Al}$  where "R" is a generic cation.

Tourmaline's intra-crystalline volume diffusion rates are so low that any composition acquired during a given growth stage of its formation history is largely preserved. Therefore, tourmaline is a very powerful tool to investigate its host rock history, acting not unlike a "geological DVD" (Dutrow and Henry, 2011; van Hinsberg et al., 2011). The ability of tourmaline to adjust its chemical composition as a function of the available chemical constituents is the key for its extensive stability field covering a wide range of geological settings, from diagenetic environments to Ultra High Pressure (UHP) conditions (Lussier et al., 2016). A preliminary stability field diagram of tourmaline, depending on its composition, is given by van Hinsberg et al., (2011) and reported in Figure 6.

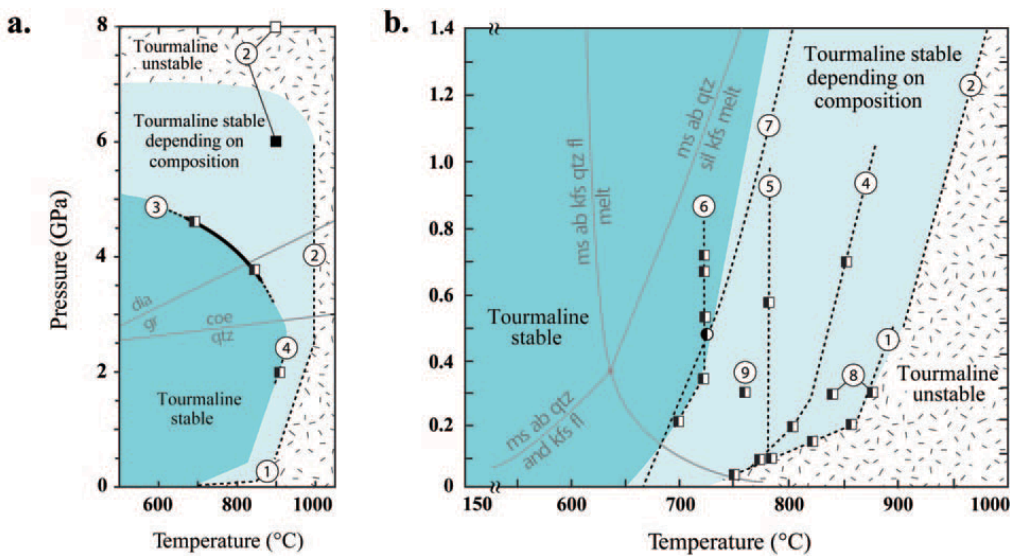


**Figure 6** Upper P–T stability estimates for tourmaline of various compositions based on constraints from natural samples (circle) and experimental data (squares), with extrapolations (dashed lines); from van Hinsberg et al. (2011). Selected reaction boundaries (gray lines) are shown for reference. (A) High-pressure and high-temperature stability. (B) Lower-pressure and high-temperature stability. Dravite: (1) Robbins and Yoder (1962); (2) Krosse (1995); (3) Ota et al. (2008).

Magnesio-foitite: (4) Werding and Schreyer (1996). Na-free Mg system (5) and Na-bearing Mg system: (6) von Goerne et al. (1999). Natural tourmaline: (7) Kawakami (2001); (8) Spicer et al. (2004). Schorl: (9) Holtz and Johannes (1991). Mineral abbreviations: dia = diamond, gr = graphite, coe = coesite, qtz = quartz, ms = muscovite, ab = albite, and = andalusite, kfs = K feldspar, fl = fluid, sil = sillimanite.

### 1.3 Axinite

Minerals of the axinite groups are borosilicates occurring as accessory phases, commonly found in metamorphic environments, characterized by an axe morphology given by their acute edges. Seldom used as gemstones, axinites are colorful minerals ranging from blue to pinkish orange.

Axinite minerals crystallize in  $P\bar{1}$  space group in the triclinic crystal system. Their crystal-chemical formula is expressed as follows:  $[X1 X2 Y Z1 Z2]_2[T1 T2 T3 T4 T5]_2O_{30}(O_wOH_{1-w})_2$ . The sites X1, X2, Y, Z1 and Z2 are octahedrally coordinated and sites T1, T2, T3, T4 and T5 are tetrahedrally-coordinated. The highly distorted octahedrally-coordinated X1 site accommodates Ca (and very minor Na) and the smaller octahedrally-coordinated site X2 is occupied by Ca and minor Mn (for tinzenite, X2 = Mn). Four end-member terms were defined depending on the Y site population (Andreozzi et al., 2004): axinite-(Mn) if Y = Mn (also true for tinzenite), axinite-(Fe) if Y =  $Fe^{2+}$  or axinite-(Mg) if Y = Mg, with minor Al and  $Fe^{3+}$  (Figure 7). Z1 = Al and  $Fe^{3+}$ ; Z2 = Al; T1, T2, and T3 = Si; T4 = Si (and presumably very minor B); T5 = B and minor Si.

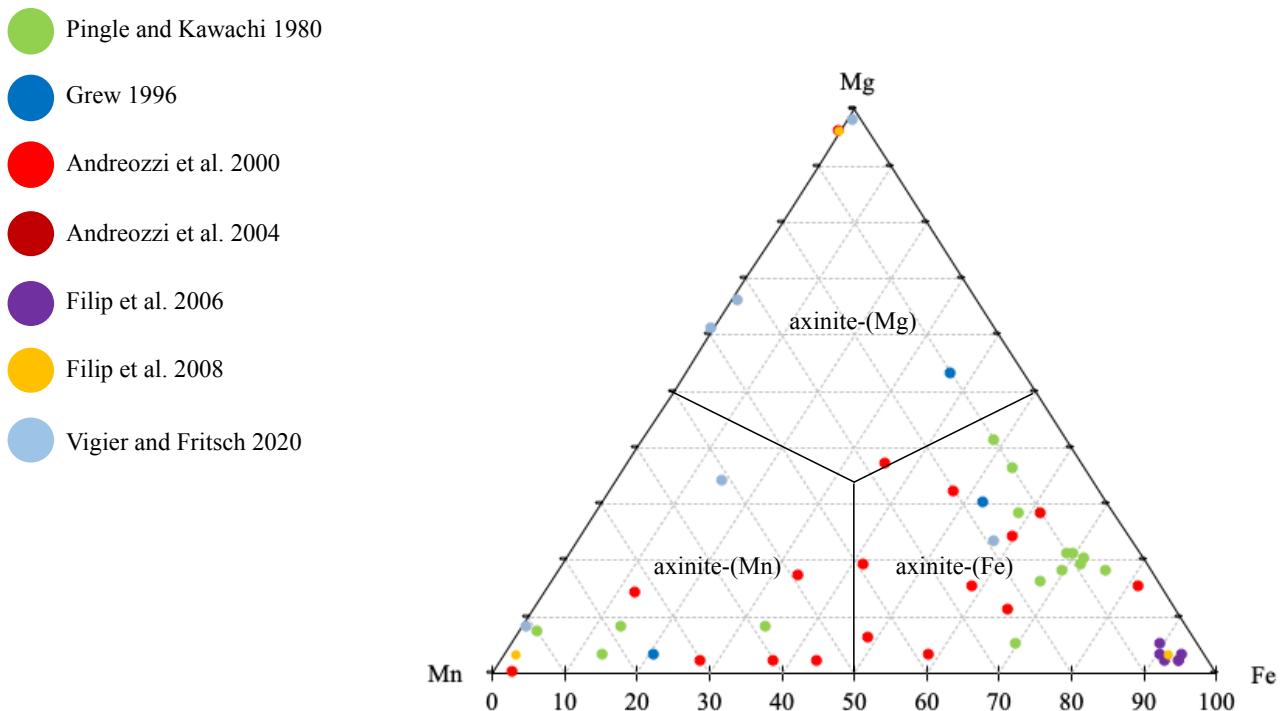


**Figure 7** Ternary plot for the axinites classification based on the dominant occupancy of the Y site. Colored dots are compositions of axinites reported in literature from Pringle and Kawachi (1980), Grew (1996), Andreozzi et al. (2000), Filip et al. (2006; 2008), Vigier and Fritsch (2020).



Most of the axinites described in literature range from axinite-(Fe) to (minor) axinite-(Mn) with very few samples falling in the axinite-(Mg) portion, as reported in Fig. 7. Axinites composition is observed to vary depending on the metamorphic grade: more ferroan at low metamorphic grade and more manganous with increasing metamorphic grade (Pringle and Kawachi, 1980).

The reason why we have a lack of a complete Mn-Mg solid solution is allegedly to infer to the unusual enrichment in both Mn and Mg of formation fluids rather than a structural constraint.

Axinites are sorosilicates, therefore their fundamental unit is made of  $\text{Si}_2\text{O}_7$  tetrahedral groups. Two  $\text{Si}_2\text{O}_7$  groups are bonded by  $\text{BO}_4$  tetrahedra in order to make a six-membered ring (Figure 8).

For this reason, axinites can be also ascribed to the cyclosilicates class. Each ring is then stacked over a layer of X1-X2-Y-Z1-Z2 octahedra (Figure 9).

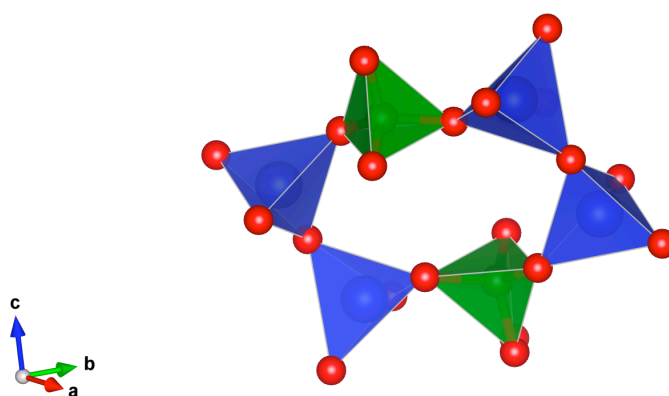


**Figure 8** Six-membered ring of axinite: the  $\text{Si}_2\text{O}_7$  tetrahedral groups are represented in blue, the  $\text{BO}_4$  tetrahedra are represented in green.

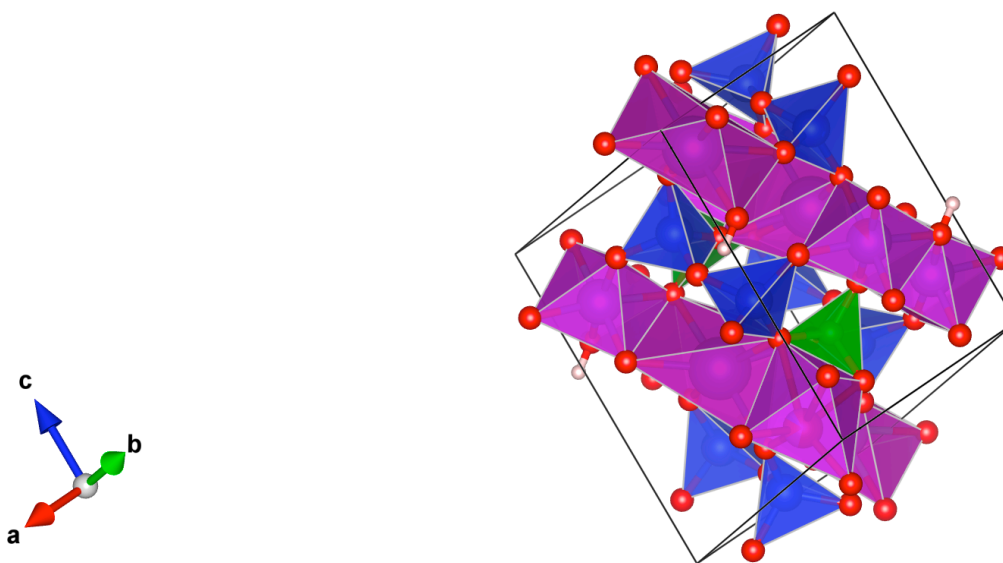


**Figure 9** Axinite crystal structure: the  $\text{Si}_2\text{O}_7$  tetrahedral groups are represented in blue, the  $\text{BO}_4$  tetrahedra are represented in green. The layer of X1-X2-Y-Z1-Z2 octahedra is represented in magenta.

#### 1.4 Geological implications: water and boron recycling in subduction systems

Understanding the rheology of geological systems is crucial to explain the complex phenomena occurring at inaccessible parts of the Earth such as subduction zones, where crustal material experiences a recycling process and new phases are formed at different temperatures and pressures along the slab. Water is a key factor in affecting the rheology of any geological system, and hydrogen ions are naturally stored in the crystal structure of hydrous minerals; when they approach their breakdown conditions, some dehydrogenation occurs (i.e., the loss of  $\text{H}^+$  from the crystal structure), and water is progressively released into the system. Once the breakdown conditions of a specific mineral are reached, its crystal structure collapses and the hosted chemical elements, together with the remaining water, are thus ready to reorganize themselves in new structures which are stable at the new temperatures and pressures. In a dynamical view, the newly formed mineral phases become carriers of both the recycled elements and water at higher depths down the slab, until their breakdown conditions are reached, and their chemical elements are released once again until water reaches the regions where it gets stored in Nominally Anhydrous Minerals (NAMs) as H point defect in the crystal structure. Notably, some of the released elements are strongly partitioned into the fluid phase (as holds true especially for B) and are therefore able to migrate and act as metasomatic fluids that can contaminate the surrounding rocks and promote their partial melting. Specifically, B is well-known to lower both the solidus temperature of the rocks and the viscosity of the melts (Pichavant 1981; Dingwell et al. 1992) as water does (Ni et al., 2016; Kohn and Grant 2006; Hirschmann et al., 2009).

Mapping out the water path through this sort of “relay race” along the slab down the mantle is therefore important to get a more detailed picture of the rheological behavior of subduction systems. As a common feature of many subduction systems, clusters of intermediate-depth earthquakes [ $\sim 70$ -300 km in depth, (Gutenberg and Richter, 1954)], occurring along two parallel layers separated by an aseismic portion of circa 40 km in thickness, have been observed, defining the so-called *double seismic zones* [e.g., Tonga (Kawakatsu, 1985); Alaska (Ratchkovsky et al., 1997), northeast Taiwan (Kao and Rau, 1999), Cape Mendocino (Smith et al., 1993), northern Chile (Comte et al., 1999), eastern Aleutians (Hudnut and Taber, 1987)].

However, intra-slab earthquakes are not supposed to occur at those locations, because temperature and pressure are too high to allow a brittle failure of the rock. So, the most accepted interpretation of those intermediate-depth earthquakes is addressed as "dehydration embrittlement", that is the transition from ductile to brittle behavior of a rock due to dehydration reactions within the slab that release a certain amount of water, thus increasing the pore fluid pressure and overcoming the confining pressure of the rock (Seno and Yamasaki, 2003). Specifically, earthquakes occur within the slab's portions where a certain degree of hydration is expected, whereas they are not observed where the slab is predicted to be anhydrous (Hacker et al., 2003). The sudden stress drop of the rock due to mineral dehydration was experimentally observed for serpentine which is the most abundant phase among the subducting material, at least at the top of the slab as a result of ocean-ridge hydrothermal alteration (Raileigh and Paterson, 1965).

Approaching 300 °C and 1 GPa along the subducting slab, water is mainly stored in zeolite, prehnite and pumpellyite, and the bulk water content of the upper crust is 6–9 wt% (Schmidt and Poli, 1998; Peacock, 1993). Upon further P-T increase to around 600 °C and 2.5 GPa (high-pressure blueschist to eclogite facies at the forearc depths, <80 km) the slab continues to dehydrate appreciably and the major hydrous minerals include chlorite, amphibole, micas, and epidote, with lawsonite only stable for a cold subduction path (Zheng, 2019). Across the amphibole-out boundary, the bulk water content decreases from ~2 wt% to ~1 wt%, corresponding to a volume fraction increase of NAMs from ~50% to >70%. Along a cold subduction path, the already highly-dehydrated oceanic crust enters a P-T regime (500–800 °C and 2.5–10 GPa) with dehydration rates notably lower than at previous stages. Furthermore, both the variety and abundance of hydrous minerals are significantly reduced, with the major phases including lawsonite, zoisite, chloritoid, talc and phengite. Increasing fraction of water is distributed in NAMs, and the bulk water content further drops to only a few 1000 ppm at the subarc (80–160 km) and postarc (>200 km) depths. If subduction proceeds along a hot path, the oceanic crust will plunge into the melting regime (650–950 °C and <5 GPa). Zoisite, amphibole and micas are the major water hosts, and the bulk water content remains >1 wt% before melting at P < 2.5 GPa. At higher pressures, amphibole is no longer stable, resulting in a bulk water content of <1 wt% in the crust before melting (Ni et al., 2017).

It was experimentally determined that accessory minerals containing boron (illite, muscovite, tourmaline) in the subducting slab play a crucial role in water and light elements transport and release, at least down to 300 km depth (e.g., Schmidt and Poli, 1998; Ono, 1998). When illite and muscovite are no longer stable along the subducting slab (i.e., in the granulite to amphibolite facies conditions), tourmaline becomes the dominant sink for boron (Sperlich et al., 1996; Henry and Dutrow, 1996) and therefore, boron fate deep down the slab is strictly related to tourmaline's stability.

## References

- Andreozzi GB, Ottolini L, Lucchesi S, Graziani G, Russo U (2000) Crystal chemistry of the axinite-group minerals: A multi-analytical approach. *American Mineralogist* 85:698–706.
- Andreozzi GB, Lucchesi S, Graziani G, Russo U (2004) Site distribution of Fe<sup>2+</sup> and Fe<sup>3+</sup> in the axinite mineral group: New crystal-chemical formula. *American Mineralogist* 89(11–12):1763–1771.
- Berryman EJ, Wunder B, Rhede D, Schettler G, Herinrich W (2016) P–T–X controls on Ca and Na distribution between Mg–Al tourmaline and fluid. *Contributions to Mineralogy and Petrology* 171, 31.
- Bosi F (2018) Tourmaline crystal chemistry. *American Mineralogist* 103(2):298–306.
- Comte D, Dorbath L, Pardo M, Monfret T, Haessler H, Rivera L, Frogneux M, Glass B, Meneses C (1999) A double-layered seismic zone in Arica, northern Chile. *Geophysical Research Letters* 26(13):1965–1968.
- Dingwell DB, Knoche R, Webb SL, Pichavant M (1992) The effect of B<sub>2</sub>O<sub>3</sub> on the viscosity of haplogranitic liquids. *American Mineralogist* 77(5–6):457–461.
- Dutrow BL, Henry DJ (2011) Tourmaline: a geologic DVD. *Elements* 7(5):301–306.
- Ertl A, Hughes JM, Prowatke S, Ludwig T, Brandstätter F, Körner W, Dyar MD (1997) Tetrahedrally coordinated boron in li-bearing olenite from “mushroom” tourmaline from momeik, myanmar. *The Canadian Mineralogist* 45(4):891–899.
- Ertl A, Tillmanns E, Ntaflos T, Francis C, Giester G, Körner W, Hughes JM, Lengauer C, Prem M (2008) Tetrahedrally coordinated boron in Al-rich tourmaline and its relationship to the pressure–temperature conditions of formation. *European Journal of Mineralogy* 20(5):881–888.
- Ertl A, Marschall HR, Giester G, Henry DJ, Schertl HP, Ntaflos T, Luvizzotto GL, Nasdala L, Tillmanns E (2010) Metamorphic ultrahigh-pressure tourmaline: Structure, chemistry, and correlations to *P-T* conditions. *American Mineralogist* 95(1):1–10.
- Filip J, Kolitsch U, Novak M, Schneeweiss O (2006) The crystal structure of near-end-member ferroaxinite from an iron-contaminated pegmatite at Malešov, Czech Republic. *The Canadian Mineralogist* 44:1159–1170.
- Filip J, Dachs E, Tuček J, Novák M, Bezdička P (2008) Low-temperature calorimetric and magnetic data for natural end-members of the axinite group. *American Mineralogist* 93:548–557.
- Foit FF Jr (1989) Crystal chemistry of alkali-deficient schorl and tourmaline structural relationships. *American Mineralogist*, 74:422–431.

- Goldschmidt VM (1922) Atlas der Kristallformen. Carl Winters Universitäts Buchhandlung, Heidelberg, Germany IX, 193 pp.
- Grew ES (1996) Borosilicates (exclusive of tourmaline) and boron in rock-forming minerals in metamorphic environments. In L.M. Anovitz and E.S. Grew, Eds., Boron: Mineralogy, Petrology, and Geochemistry, 33:387–502. Reviews in Mineralogy, Mineralogical Society of America, Washington, D.C.
- Gutenberg B, Richter CF (1954) Seismicity of the Earth and Associated Phenomena, 2nd ed., Princeton Univ. Press. Princeton, New Jersey, 310 pp.
- Hacker BR, Peacock SM, Abers GA, Holloway SD (2003) Subduction factory 2. Are intermediate-depth earthquakes in subducting slabs linked to metamorphic dehydration reactions? Journal of Geophysical Research 108(B1):2030.
- Hawthorne FC (1996) Structural mechanisms for light-element variations in tourmaline. The Canadian Mineralogist 34(1):123–132.
- Hawthorne FC, Dirlam DM (2011) Tourmaline the Indicator Mineral: From Atomic Arrangement to Viking Navigation. Elements 7(5):307–312.
- Henry DJ, Dutrow BL (1996) Metamorphic tourmaline and its petrologic applications. In: Grew ES, Anovitz LM (eds) Boron: Mineralogy, Petrology and Geochemistry. Reviews in Mineralogy 33:503–557.
- Henry DJ, Novák M, Hawthorne FC, Ertl A, Dutrow BL, Uher P, Pezzotta F (2011) Nomenclature of the tourmaline-supergroup minerals. American Mineralogist 96(5–6):895–913.
- Hirschmann MM, Tenner T, Aubaud C, Withers AC (2009) Dehydration melting of nominally anhydrous mantle: The primacy of partitioning. Physics of the Earth and Planetary Interiors 176(1–2):54–68.
- Holtz F, Johannes W (1991) Effect of tourmaline on melt fraction and composition of first melts in quartzofeldspathic gneiss. European Journal of Mineralogy 3:527–536.
- Hudnut KW, Taber JJ (1987) Transition from double to single Wadati-Benioff seismic zone in the Shumagin Islands, Alaska. Geophysical Research Letters 14:143–146.
- Huntington Williams G (1892) Elements of Crystallography for Students of Chemistry, Physics, and Mineralogy (New York, NY: Henry Holt and Company), 300 pp.
- Kao H, Rau RJ (1999) Detailed structures of the subducted Philippine Sea Plate beneath northeast Taiwan: A new type of double seismic zone. Journal of Geophysical Research 104(B1):1015–1033.

- Kawakami T (2001) Boron depletion controlled by the breakdown of tourmaline in the migmatite zone of the Aoyama area, Ryoke metamorphic belt, southwestern Japan. *The Canadian Mineralogist* 39:1529–1546.
- Kawakatsu H (1985) Double seismic zone in Tonga. *Nature* 316:53–55.
- Kohn SC, Grant KJ (2006) The Partitioning of Water Between Nominally Anhydrous Minerals and Silicate Melts. *Reviews in Mineralogy and Geochemistry* 62(1):231–241.
- Krosse S (1995) Hochdrucksynthese, Stabilität und Eigenschaften der Borsilikate Dravit und Kornerupin, sowie Darstellung und Stabilitätsverhalten eines neuen Mg–Al-borates. Thesis, Ruhr-Universität Bochum, Germany.
- Lussier A, Ball NA, Hawthorne FC, Henry DJ, Shimizu R, Ogasawara Y, Ota T (2016) Maruyamaite,  $K(MgAl_2)(Al_5Mg)Si_6O_{18}(BO_3)_3(OH)_3O$ , a potassium-dominant tourmaline from the ultrahigh-pressure Kokchetav massif, northern Kazakhstan: Description and crystal structure. *American Mineralogist* 101(2):355–361.
- Ni HW, Zhang L, Guo X (2016) Water and partial melting of Earth's mantle. *Science China Earth Sciences* 59:720–730.
- Ni H, Zheng YF, Mao Z, Wang Q, Chen RX, Zhang L (2017) Distribution, cycling and impact of water in the Earth's interior. *National Science Review* 4(6):879–891.
- Ono T (1998) Stability limits of hydrous minerals in sediment and mid-ocean ridge basalt compositions: Implications for water transport in subduction zones. *Journal of Geophysical Research* 103(B8):18,253–18,267.
- Ota T, Kobayashi K, Katsura T, Nakamura E (2008) Tourmaline breakdown in a pelitic system: implications for boron cycling through subduction zones. *Contribution to Mineralogy and Petrology* 155: 19–32.
- Peacock SM (1993) Large-scale hydration of the lithosphere above subducting slabs. *Chemical Geology* 108(1–4):49–59.
- Pezzotta F, Laurs BM (2011) Tourmaline: the kaleidoscopic gemstone. *Elements* 7(5):333–338.
- Pichavant M (1981) An experimental study of the effect of boron on a water saturated haplogranite at 1 Kbar vapour pressure. *Contributions to Mineralogy and Petrology* 76:430–439.
- Pringle IJ, Kawachi Y (1980) Axinite mineral group in low-grade regionally metamorphosed rocks in southern New Zealand. *American Mineralogist*, 65:1119–1129.
- Raileigh CB, Paterson MS (1965) Experimental deformation of serpentine and its tectonic implications. *Journal of Geophysical Research* 70(16):3965–3985.

- Ratchkovsky NA, Pujol J, Biswas NH (1997) Relocation of earthquakes in the Cook Inlet area, south central Alaska, using the joint hypocenter determination method. *Bulletin of the Seismological Society of America* 87(3):620–636.
- Robbins CR, Yoder HS Jr (1962) Stability relations of dravite, a tourmaline. *Carnegie Institute Washington Yearbook* 61:106–108.
- Schmidt MW, Poli S (1998) *Earth and Planetary Science Letters* 163(1–4):361–379.
- Smith S. W. Knapp J. S. McPherson R. C. (1993) Seismicity of the Gorda plate, structure of the continental margin, and an eastward jump of the Mendocino triple junction *Journal of Geophysical Research* 98(B5):8153–8171.
- Sperlich R, Giere R, Frey M (1996) Evolution of compositional polarity and zoning in tourmaline during prograde metamorphism of sedimentary rocks in the Swiss Central Alps. *American Mineralogist* 81(9–10):1222–1236.
- Spicer EM, Stevens G, Buick IS (2004) The low-pressure partial-melting behaviour of natural boron-bearing metapelites from the Mt. Stafford area, central Australia. *Contributions to Mineralogy and Petrology* 148:160–179.
- van Hinsberg VJ, Henry DJ, Marschall HR (2011) Tourmaline: an ideal indicator of its host environment. *The Canadian Mineralogist* 49(1):1–16.
- Vigier M, Fritsch E (2020) Pink axinite from Merelani, Tanzania: a natural luminescent mineral irradiated in the Neoproterozoic Mozambique Metamorphic Belt. *The Journal of Gemmology* 37(2):192-205
- von Goerne G, Franz G (1999) Upper thermal stability of tourmaline + quartz in the system MgO–Al<sub>2</sub>O<sub>3</sub>–SiO<sub>2</sub>–B<sub>2</sub>O<sub>3</sub>–H<sub>2</sub>O and Na<sub>2</sub>O–MgO–Al<sub>2</sub>O<sub>3</sub>–SiO<sub>2</sub>–B<sub>2</sub>O<sub>3</sub>–H<sub>2</sub>O–HCl in hydrothermal solutions and siliceous melts. *The Canadian Mineralogist* 37:1025–1039.
- Werding G, Schreyer W (1996) Experimental studies on borosilicates and selected borates. *Boron: Mineralogy, Petrology, and Geochemistry*, edited by Lawrence M. Anovitz and Edward S. Grew, Berlin, Boston: De Gruyter, 117-164.
- Wodara U, Schreyer W (1997) Turmaline mit Borüberschuß im System Na<sub>2</sub>O–Al<sub>2</sub>O<sub>3</sub>–B<sub>2</sub>O<sub>3</sub>–SiO<sub>2</sub>–H<sub>2</sub>O (NABSH). *Berichte der Deutschen Mineralogischen Gesellschaft, Beih. z. European Journal of Mineralogy* 9(1):394.
- Wodara U, Schreyer W (1998) Tetrahedral boron in tourmalines of the system Na<sub>2</sub>O–Al<sub>2</sub>O<sub>3</sub>–B<sub>2</sub>O<sub>3</sub>–SiO<sub>2</sub>–H<sub>2</sub>O. *Terra Abstracts, Abstract supplement No.1 to Terra nova* 10:68.
- Yamasaki T, Seno T (2003) Double seismic zone and dehydration embrittlement of the subducting slab. *Journal of Geophysical Research* 108(B4):2212.
- Zheng YF (2019) Subduction zone geochemistry. *Geoscience Frontiers* 10(4):1223–1254.

## 2. Experimental work

In this research project, the breakdown conditions of a wide compositional suite of borosilicate minerals were investigated. Natural tourmaline (the most important boron carrier in the crust) and axinite (one of the less investigated) of various composition were used as starting materials. Notably, different compositions of such mineral phases were chosen with the call to investigate a possible correlation between chemistry and stability.

All the samples were fully characterized in this experimental work or previously by the work of other authors (see Table 1) always through a multi-analytical approach, including Scanning Electron Microscopy (SEM), Electron MicroProbe Analysis (EMPA), Single Crystal X-Ray Diffraction (SC-XRD) and Infrared (IR) Spectroscopy. The starting material that was characterized but not yet used in the experiments, as the anortho-schorl, will be investigated in future research projects.

Two different sets of experiments were carried out: HT experiments at Room Pressure (*RP-HT*), High-Pressure High-Temperature experiments (*HP-HT*), see Table 2.

**Table 1** List of the samples used in the experimental work.

Sample	Characterized in this work	Characterized by other Authors
Schorl	X	
Fe-rich fluor-elbaite		X
Mn-bearing fluor-elbaite	X	
Uvite		X
Axinite		X
Anortho-schorl	X	
Oxy-dravite	X	
Maruyamaite	X	



**Table 2** List of the samples used in the experimental work along with their composition.

Sample	RP-HT	HP-HT	Formula
Schorl	X	X	$X(\text{Na}_{0.74}\square_{0.24}\text{K}_{0.01}\text{Ca}_{0.01})_{\Sigma 1.00} Y(\text{Fe}^{2+}_{2.05}\text{Al}_{0.92}\text{Ti}_{0.02}\text{Mn}_{0.01}\text{Zn}_{0.01})_{\Sigma 3.00} Z(\text{Al}_{5.41}\text{Fe}^{2+}_{0.53}\text{Mg}_{0.06})_{\Sigma 6.00} (\text{Si}_6\text{O}_{18})(\text{BO}_3)_3$ $V(\text{OH})_3 W[(\text{OH})_{0.46}\text{F}_{0.41}\text{O}_{0.13}]$
Fe-rich fluor-elbaite	X		$X(\text{Na}_{0.79}\square_{0.18}\text{Ca}_{0.02}\text{K}_{0.01})_{\Sigma 1.00} Y(\text{Al}_{0.95}\text{Fe}^{2+}_{0.94}\text{Li}_{0.86}\text{Mn}^{2+}_{0.18}\text{Zn}_{0.11}\text{Ti}_{0.01})_{\Sigma 3.05} Z\text{Al}_6 T(\text{Si}_{5.99}\text{Al}_{0.01})_{\Sigma 6.00} \text{B}_{2.98}\text{O}_{27} V(\text{OH})_3$ $W[(\text{OH})_{0.43}\text{F}_{0.58}]_{\Sigma 1.01}$
Mn-bearing fluor-elbaite	X		$X(\text{Na}_{0.41}\square_{0.35}\text{Ca}_{0.24})_{\Sigma 1.00} Y(\text{Al}_{1.81}\text{Li}_{1.00}\text{Fe}^{3+}_{0.04}\text{Mn}^{3+}_{0.02}\text{Mn}^{2+}_{0.12}\text{Ti}_{0.004})_{\Sigma 3.00}$ $Z\text{Al}_6 [T(\text{Si}_{5.60}\text{B}_{0.40})_{\Sigma 6.00}\text{O}_{18}](\text{BO}_3)_3(\text{OH})_3 W[(\text{OH})_{0.50}\text{F}_{0.13}\text{O}_{0.37}]_{\Sigma 1.00}$
Uvite	X		$X(\text{Ca}_{0.61}\text{Na}_{0.35}\square_{0.04})_{\Sigma 1.00} Y(\text{Mg}_{1.51}\text{Fe}^{2+}_{0.47}\text{Al}_{0.70}\text{Fe}^{3+}_{0.14}\text{Ti}_{0.18})_{\Sigma 3.00} Z(\text{Al}_{4.54}\text{Fe}^{3+}_{0.18}\text{V}^{3+}_{0.02}\text{Mg}_{1.27})_{\Sigma 6.01} T(\text{Si}_{5.90}\text{Al}_{0.10})_{\Sigma 6.00}$ $(\text{BO}_3)_3 V(\text{OH})_3 W[(\text{OH})_{0.55}\text{F}_{0.05}\text{O}_{0.40}]_{\Sigma 1.00}$
axinite	X		$VI[\text{Ca}_{2.00}(\text{Ca}_{1.95}\text{Mn}_{0.05})(\text{Mn}_{0.48}\text{Fe}^{2+}_{0.67}\text{Mg}_{0.80}\text{Fe}^{3+}_{0.01}\text{Al}_{0.04})(\text{Al}_{1.92}\text{Fe}^{3+}_{0.04})\text{Al}_2]$ $IV[(\text{B}_{1.95}\text{Si}_{0.04})\text{Si}_{8.00}]\text{O}_{29.99}(\text{OH})_{2.01}$

## 2.1. Crystal chemistry of starting materials

### 2.1.1 Schorl



# Crystal-chemical behavior of Fe<sup>2+</sup> in tourmaline dictated by structural stability: insights from a schorl with formula Na<sup>Y</sup>(Fe<sup>2+</sup><sub>2</sub>Al)<sup>Z</sup>(Al<sub>5</sub>Fe<sup>2+</sup>)(Si<sub>6</sub>O<sub>18</sub>)(BO<sub>3</sub>)<sub>3</sub>(OH)<sub>3</sub>(OH,F) from Seagull batholith (Yukon Territory, Canada)

Giovanni B. Andreozzi<sup>1</sup> · Ferdinando Bosi<sup>1</sup> · Beatrice Celata<sup>1</sup> · Luca S. Capizzi<sup>1</sup> · Vincenzo Stagno<sup>1</sup> · Christopher E. Beckett-Brown<sup>2</sup>

Received: 21 February 2020 / Accepted: 23 April 2020 / Published online: 7 May 2020  
© Springer-Verlag GmbH Germany, part of Springer Nature 2020

## Abstract

A black tourmaline sample from Seagull batholith (Yukon Territory, Canada) was established to be a schorl with concentrations of Fe<sup>2+</sup> among the highest currently found in nature (FeO<sub>tot</sub> ~ 18 wt.% and Fe<sup>2+</sup> ~ 100% of Fe<sub>tot</sub>) on the basis of a multi-analytical characterization through Mössbauer spectroscopy, electron microprobe, Laser-Ablation Inductively-Coupled-Plasma Mass-Spectrometry and single-crystal X-ray diffraction. From the crystal-chemical analysis, the following empirical formula is proposed: X(Na<sub>0.74</sub>□<sub>0.24</sub>K<sub>0.01</sub>Ca<sub>0.01</sub>)<sub>Σ1.00</sub>Y(Fe<sup>2+</sup><sub>2.05</sub>Al<sub>0.92</sub>Ti<sub>0.02</sub>Mn<sub>0.01</sub>Zn<sub>0.01</sub>)<sub>Σ3.00</sub>Z(Al<sub>5.41</sub>Fe<sup>2+</sup><sub>0.53</sub>Mg<sub>0.06</sub>)<sub>Σ6.00</sub>(Si<sub>6</sub>O<sub>18</sub>)(BO<sub>3</sub>)<sub>3</sub>V(OH)<sub>3</sub>W[(OH)<sub>0.46</sub>F<sub>0.41</sub>O<sub>0.13</sub>]<sub>Σ1.00</sub>, which can be approximated as Na<sup>Y</sup>(Fe<sup>2+</sup><sub>2</sub>Al)<sup>Z</sup>(Al<sub>5</sub>Fe<sup>2+</sup>)(Si<sub>6</sub>O<sub>18</sub>)(BO<sub>3</sub>)<sub>3</sub>(OH)<sub>3</sub>(OH,F). Compared to the formula of the ideal *ordered* schorl, Na<sup>Y</sup>(Fe<sup>2+</sup><sub>3</sub>)<sup>Z</sup>(Al<sub>6</sub>)(Si<sub>6</sub>O<sub>18</sub>)(BO<sub>3</sub>)<sub>3</sub>(OH)<sub>3</sub>(OH), the studied sample has a partial disorder of Fe<sup>2+</sup> across the Y and the Z sites that can be expressed by the intracrystalline order–disorder reaction <sup>Y</sup>Al + <sup>Z</sup>Fe<sup>2+</sup> → <sup>Y</sup>Fe<sup>2+</sup> + <sup>Z</sup>Al. Such a partial cation disorder must be invoked to explain tourmaline structural stability because an ideal ordered schorl results in a large misfit between the < <sup>Y</sup>Fe<sup>2+</sup>–O > and < <sup>Z</sup>Al<sup>3+</sup>–O > mean bond lengths (that is, between the YO<sub>6</sub> and ZO<sub>6</sub> polyhedra). This misfit is reduced by introducing Al at Y (i.e., through the < Y–O > shortening) and Fe<sup>2+</sup> at Z (i.e., through the < Z–O > lengthening). The result is that in tourmaline the site distribution of high Fe<sup>2+</sup> concentrations is dictated by long-range structural constraints.

**Keywords** Tourmaline · Schorl · Mössbauer spectroscopy · Electron microprobe · Laser-ablation inductively-coupled-plasma mass-spectrometry · Single-crystal X-ray diffraction

## Introduction

Tourmaline is the most common and earliest boron mineral formed on Earth, recently gaining an interest from the geoscience community (Grew et al. 2016; Dutrow and Henry

2018; Henry and Dutrow 2018). The importance of tourmaline as a powerful geological tool for probing *P–T–X* conditions at all crustal levels in the Earth, resides in its very large *P–T* stability field, common occurrence, and negligible intravolume element diffusion rates (e.g., Henry and Dutrow 1996; van Hinsberg and Schumacher 2007). Moreover, due to its complex crystal chemistry, which allows a large number of chemical substitutions (e.g., Henry and Dutrow 1996, 2018; Bosi 2018), tourmaline is extremely sensitive to its chemical environment and it is, therefore, valuable as both a petrogenetic and provenance indicator (e.g., Henry and Dutrow 1992, 1996; Dutrow and Henry 2011; van Hinsberg et al. 2011a; Bosi et al. 2018a, 2019a; Ertl et al. 2008, 2012, 2018; Ahmadi et al. 2019; Sipahi 2019).

The tourmaline general chemical formula can be written as XY<sub>3</sub>Z<sub>6</sub>T<sub>6</sub>O<sub>18</sub>(BO<sub>3</sub>)<sub>3</sub>V<sub>3</sub>W, where X = Na<sup>+</sup>, K<sup>+</sup>, Ca<sup>2+</sup>, □

**Electronic supplementary material** The online version of this article (<https://doi.org/10.1007/s00269-020-01094-7>) contains supplementary material, which is available to authorized users.

✉ Giovanni B. Andreozzi  
gianni.andreozzi@uniroma1.it

<sup>1</sup> Dipartimento di Scienze della Terra, Sapienza Università di Roma, Piazzale Aldo Moro 5, 00185 Rome, Italy

<sup>2</sup> Harquail School of Earth Sciences, Laurentian University, Sudbury, ON, Canada

(= vacancy); Y = Al<sup>3+</sup>, Fe<sup>3+</sup>, Cr<sup>3+</sup>, V<sup>3+</sup>, Mg<sup>2+</sup>, Fe<sup>2+</sup>, Mn<sup>2+</sup>, Zn<sup>2+</sup>, Li<sup>+</sup>, Ti<sup>4+</sup>, □; Z = Al<sup>3+</sup>, Fe<sup>3+</sup>, Cr<sup>3+</sup>, V<sup>3+</sup>, Mg<sup>2+</sup>, Fe<sup>2+</sup>; T = Si<sup>4+</sup>, Al<sup>3+</sup>, B<sup>3+</sup>; B = B<sup>3+</sup>; V = (OH)<sup>-</sup>, O<sup>2-</sup>; W = (OH)<sup>-</sup>, F<sup>-</sup>, O<sup>2-</sup>. The letters X, Y, Z, T and B represent groups of cations accommodated at the <sup>[9]</sup>X, <sup>[6]</sup>Y, <sup>[6]</sup>Z, <sup>[4]</sup>T and <sup>[3]</sup>B crystallographic sites (identified with *italicized* letters); the letters V and W represent groups of anions accommodated at the <sup>[3]</sup>O(3) and <sup>[3]</sup>O(1) crystallographic sites, respectively. The H atoms occupy the H(3) and H(1) sites, which are related to O(3) and O(1), respectively. It is worth mentioning that, unlike amphibole or spinel, the structural and the chemical formula of tourmaline coincide: each crystallographic site in the structural formula matches a (non-italicized) letter in the chemical formula (Bosi et al. 2019b).

Tourmaline-supergrain minerals are currently classified into three groups based on the X-site occupancy: vacant, alkali and calcic (Henry et al. 2011). The X-site occupancy is usually related to both paragenesis and crystallization conditions of the rock in which tourmaline crystallized, and these relations may be used to reconstruct the host-rock thermal history (Henry and Dutrow 1996; van Hinsberg et al. 2011a, b, 2017; Dutrow and Henry 2018; Bosi et al. 2018a, 2019a). A further level of classification into subgroups is based on charge arrangements at the Y and Z sites, where small cations such as Al and Mg and relatively larger cations such as Fe<sup>2+</sup> can be accommodated.

Using a large set of structural data, Bosi and Lucchesi (2007) presented a structural-stability field for tourmaline as a function of  $\langle Y-O \rangle$  and  $\langle Z-O \rangle$  mean bond lengths. The endpoints of this field indicate that the tourmaline structure can tolerate only a limited mismatch in dimensions between  $\langle Y-O \rangle$  and  $\langle Z-O \rangle$  (i.e., their difference,  $\Delta_{(Y-Z)} = \langle Y-O \rangle - \langle Z-O \rangle$ , should be smaller than 0.15 Å). The empirical

validation of the occurrence of a long-range structural constraint and its effect on the occupancy of Y and Z sites are of particular interest. In fact, cation ordering in tourmaline structure may be exploited for geothermometric purposes (e.g., Henry and Dutrow 1992; Ertl et al. 2008; Filip et al. 2012; Bosi et al. 2016a, b; Ertl et al. 2018), while its variation can affect tourmaline physical properties, such as intrinsic dipole moment (Kim et al. 2018) and bulk moduli (Berryman et al. 2019). The possibility of Fe<sup>2+</sup> to partially disorder across the Y and the Z sites, in particular, has been deeply investigated and largely discussed in several papers (see for example Andreozzi et al. 2008; Bosi and Andreozzi 2013, and references therein).

In the present study, a natural schorl with Fe<sup>2+</sup> concentrations very close to that of schorlitic end-members was studied with an inclusive, multi-analytical approach with the aim to confirm that the crystal-chemical behavior of Fe<sup>2+</sup> in tourmaline is controlled by structural stability requirements.

## Material and experimental methods

The sample used for this study is a black tourmaline from a quartz-tourmaline orbicule found in the leucogranites of the Seagull batholith in the Yukon Territory, Canada (Fig. 1). According to Sinclair and Richardson (1992), the orbicules are considered to have developed during the final crystallization stages in which a hydrous melt/fluid (enriched in B, F, Cl and Fe) separated from a peraluminous granite, and tourmalines from the Seagull batholith are schorl with up to ~ 20 wt.% FeO and normalized Fe<sup>2+</sup> cations up to 2.78 atoms per formula unit (apfu). To the best of our knowledge, these Fe<sup>2+</sup> concentrations are the highest found in natural schorl so far.

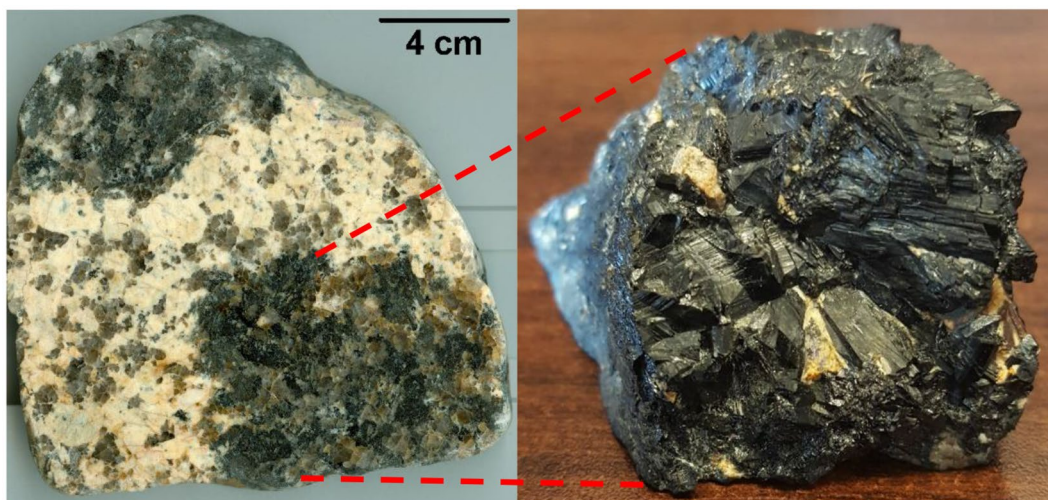


**Fig. 1** Quartz-tourmaline pegmatitic orbicules included in leucogranites from Seagull batholith (Yukon Territory, Canada). Black tourmaline crystals up to 2-cm large are visible in the right inset

In the present study, the Fe oxidation state was obtained by <sup>57</sup>Fe Mössbauer Spectroscopy (MS); the chemical composition was obtained by using Electron MicroProbe (EMP) for major and minor elements and Laser-Ablation Inductively-Coupled-Plasma Mass-Spectrometry (LA-ICP-MS) for trace elements (including Li) and B; crystal-structure details were obtained by Structure REFinement (SREF) of X-ray single-crystal diffraction data.

**MS**

A fragment of the black Seagull tourmaline was ground under ethanol with an agate mortar, and 15 mg of the recovered fine powder was packed to make a disk of 10 mm of diameter. The absorber was then loaded in a Plexiglas® sample holder, and measurements were performed using a conventional spectrometer with a <sup>57</sup>Co source of 0.99 GBq (25 mCi) embedded in a Rh matrix available at the Earth Sciences Department, Sapienza University of Rome (Italy). The spectrum was collected in transmission mode, at room temperature and at velocities between -4 to + mm/s, and recorded in a multichannel analyzer with 512 channels. The velocity was calibrated with a 25-µm thick α-iron foil. The obtained absorption spectrum was fitted to Lorentzian line-shapes using the RECOIL 1.04 fitting program (Lagarec and Rancourt 1998), with results reported in Table 1.

**EMP**

Electron microprobe analysis for the Seagull tourmaline sample was obtained using a wavelength-dispersive spectrometer (WDS mode) with a Cameca SX50 instrument at the “Istituto di Geologia Ambientale e Geoingegneria (Rome, Italy), CNR”, operating at an accelerating potential of 15 kV, with a 15 nA current and a 10 µm beam diameter. Minerals and synthetic compounds were used as standards: wollastonite (Si, Ca), magnetite (Fe), rutile (Ti), corundum (Al), vanadinite (V), fluorphlogopite (F), periclase (Mg), jadeite (Na), orthoclase (K), sphalerite (Zn), rhodonite (Mn), metallic Cr, Ni and Cu. The PAP correction procedure for quantitative electron probe microanalysis was applied

**Table 1** Room temperature <sup>57</sup>Fe Mössbauer parameters for Seagull schorl from Yukon Territory (Canada)

$\chi^2$	$\delta$	$\Delta E_Q$	$\Gamma$	% Area	Assignment
0.75	1.10	2.43	0.31	26	<sup>Y</sup> Fe <sup>2+</sup>
	1.11	2.11	0.31	36	<sup>Y</sup> Fe <sup>2+</sup>
	1.11	1.69	0.30	13	<sup>Y</sup> Fe <sup>2+</sup>
	1.08	1.20	0.46	25	<sup>Z</sup> Fe <sup>2+</sup>

Centroid shift ( $\delta$ ) in mm/s relative to α-Fe foil; errors are estimated no less than ± 0.02 mm/s for  $\delta$ , quadrupole splitting ( $\Delta E_Q$ ), and peak width ( $\Gamma$ ), and no less than ± 3% for doublets areas

(Pouchou and Pichoir 1991). Results are reported in Table 2 and represent the mean values of 10 spot analyses across the crystal used for SREF study. Vanadium, Cr, Ni and Cu were below their respective detection limits (0.03 wt%) in the studied sample.

**LA-ICP-MS**

In-situ trace-element and boron analyses were collected using Laser-Ablation Inductively-Coupled-Plasma mass-spectrometry at Laurentian University (Canada). Samples were ablated using Resonetic Resolution M-50 coupled to a Thermo Electron XSeries II quadrupole ICP-MS. A 193 nm argon fluoride excimer laser was operated at a rate of 8 Hz. Line scans were completed using a 40 µm beam width and a scan speed of 20 µm/s with a measured fluence of ~ 3 j/cm<sup>2</sup>. Line scans were utilized to test for chemical zonation, which in turn was not present. Dwell times for rare-earth elements were increased to 15 ms from 10 ms (for other trace elements) to improve detection limits. External reference materials include: (1) NIST 610 (Jochum et al. 2011), (2) NIST 612 (Jochum et al., 2011) and (3) BHVO2G (Raczek et al. 2001). Standards were ablated every 10–15 analyses of the unknowns. Drift correction was applied using the baseline reduction scheme in IOLITE (Paton et al. 2011). Reference standards were utilized to assess the accuracy of the analyses. Results are reported in Table 3,

**Table 2** Chemical composition of Seagull schorl from Yukon Territory (Canada)

Oxides	wt.%	Ions	apfu
SiO <sub>2</sub>	34.79 (35)	Si	5.998
TiO <sub>2</sub>	0.13 (3)	Ti <sup>4+</sup>	0.016
B <sub>2</sub> O <sub>3</sub> <sup>a</sup>	10.08	B	3.000
Al <sub>2</sub> O <sub>3</sub>	31.18 (31)	Al	6.334
FeO <sup>b</sup>	17.91 (22)	Fe <sup>2+</sup>	2.582
MgO	0.23 (22)	Mg	0.058
MnO	0.04 (3)	Mn <sup>2+</sup>	0.006
ZnO	0.05 (5)	Zn	0.006
CaO	0.04 (6)	Ca	0.008
Na <sub>2</sub> O	2.22 (5)	Na	0.741
K <sub>2</sub> O	0.04 (1)	K	0.010
F	0.75 (12)	F	0.409
H <sub>2</sub> O <sup>c</sup>	3.01	(OH)	3.463
-O≡F	-0.32		
Total	100.15		

Uncertainties for oxides and fluorine (in brackets) are standard deviation of 10 EMP spots across the crystal used for SREF study. Number of ions normalized to 31 (O, OH, F)

<sup>a</sup>Calculated by stoichiometry, in agreement with LA-ICP-MS results for B

<sup>b</sup>According to Mössbauer spectroscopy results

<sup>c</sup>Calculated by stoichiometry (see text)

together with elemental detection limits, and represent the mean values of 9 analyses across the sample.

## SREF

A representative crystal fragment of the Seagull tourmaline was selected for X-ray diffraction measurements on a Bruker KAPPA APEX-II single-crystal diffractometer (Sapienza University of Rome, Earth Sciences Department), equipped with a CCD area detector ( $6.2 \times 6.2$  cm active detection area,  $512 \times 512$  pixels) and a graphite-crystal monochromator, using  $\text{MoK}\alpha$  radiation from a fine-focus sealed X-ray tube. The sample-to-detector distance was 4 cm. A total of 3681 exposures (step =  $0.2^\circ$ , time/step = 20 s) covering a full reciprocal sphere with a redundancy of about 12 was collected. Final unit-cell parameters were refined using the Bruker AXS SAINT program on 9981 reflections with  $I > 10 \sigma(I)$  in the range  $5^\circ < 2\theta < 80^\circ$ . The associated intensities were processed and corrected for Lorentz and background effects plus polarization, using the APEX2 software program of Bruker AXS. The data were corrected for absorption using a multi-scan method (SADABS). The absorption correction led to a significant improvement in  $R_{\text{int}}$ . No violation of  $R3m$  symmetry was detected.

Structure refinement was done using the SHELXL-2014 program (Sheldrick 2015). Starting coordinates were taken from Bosi et al. (2015). Variable parameters were: scale factor, extinction coefficient, atom coordinates, site-scattering values (for  $X$ ,  $Y$  and  $Z$ ) and atomic-displacement factors. Regarding the atomic model refinement, the  $X$  site was modeled using the Na scattering factor. The occupancies of the  $Y$  and  $Z$  sites were obtained considering the presence of Al versus Fe. The  $T$ ,  $B$  and anion sites were modeled, respectively, with Si, B and O scattering factors and with a fixed occupancy of 1, because refinement with unconstrained occupancies showed no significant deviations from this value. A final refinement was then performed by modelling the site occupancy of the O(1) site with O and F fixed to the value obtained from the empirical formula (see below). Similar chemical constraints were applied to refine the H(1) and H(3) sites. There were no correlations greater than 0.7 between the parameters at the end of the refinement. Table 4 lists crystal data, data-collection information and refinement details; Table 5 displays the fractional atom coordinates, site occupancy factors and equivalent isotropic-displacement parameters; Table 6 shows selected bond lengths. A CIF file is included in supplemental material.

## Results and discussion

### Chemical composition and iron speciation

The black tourmaline sample from Seagull batholith (Yukon Territory, Canada) is chemically homogeneous and was

**Table 3** Boron and trace-elements contents of Seagull schorl from Yukon Territory (Canada)

Elements	Detection limit (ppm)	Average value (ppm)
$^7\text{Li}$	50	bdl
$^9\text{Be}$	50	bdl
$^{11}\text{B}$	25	33,725 (1973)
$^{31}\text{P}$	15	bdl
$^{33}\text{S}$	100	bdl
$^{39}\text{K}$	5	483 (39)
$^{45}\text{Sc}$	0.5	84 (14)
$^{47}\text{Ti}$	4	2538 (812)
$^{51}\text{V}$	0.8	3 (2)
$^{52}\text{Cr}$	1.5	bdl
$^{55}\text{Mn}$	1	543 (22)
$^{59}\text{Co}$	0.1	0.93 (0.21)
$^{60}\text{Ni}$	1.5	bdl
$^{65}\text{Cu}$	1.5	16 (9)
$^{66}\text{Zn}$	1	349 (30)
$^{69}\text{Ga}$	0.5	139 (8)
$^{72}\text{Ge}$	0.5	5.8 (0.5)
$^{75}\text{As}$	2	69 (15)
$^{85}\text{Rb}$	0.2	bdl
$^{88}\text{Sr}$	0.02	5 (1)
$^{89}\text{Y}$	0.02	1.2 (0.7)
$^{90}\text{Zr}$	0.04	1.0 (0.4)
$^{93}\text{Nb}$	0.05	8 (4)
$^{95}\text{Mo}$	0.25	bdl
$^{115}\text{In}$	0.01	2.3 (0.6)
$^{118}\text{Sn}$	0.1	40 (15)
$^{121}\text{Sb}$	0.05	1.4 (0.7)
$^{139}\text{La}$	0.01	4 (1)
$^{140}\text{Ce}$	0.01	9 (3)
$^{141}\text{Pr}$	0.02	1.0 (0.3)
$^{146}\text{Nd}$	0.15	3 (1)
$^{147}\text{Sm}$	0.20	0.5 (0.2)
$^{153}\text{Eu}$	0.05	bdl
$^{157}\text{Gd}$	0.10	0.4 (0.2)
$^{159}\text{Tb}$	0.02	0.07 (0.05)
$^{163}\text{Dy}$	0.15	0.4 (0.2)
$^{165}\text{Ho}$	0.03	0.08 (0.04)
$^{166}\text{Er}$	0.08	0.2 (0.1)
$^{169}\text{Tm}$	0.02	0.04 (0.03)
$^{172}\text{Yb}$	0.07	0.3 (0.2)
$^{175}\text{Lu}$	0.03	bdl
$^{178}\text{Hf}$	0.10	bdl
$^{208}\text{Pb}$	0.30	8 (4)
$^{232}\text{Th}$	0.01	0.2 (0.1)
$^{238}\text{U}$	0.05	0.3 (0.2)

Data from LA-ICP-MS, average of 9 analyses across the sample  
bdl below detection limit



**Table 4** Single-crystal X-ray diffraction data details for Seagull schorl from Yukon Territory (Canada)

Crystal sizes (mm)	0.20 × 0.20 × 0.24
<i>a</i> (Å)	15.9957 (3)
<i>c</i> (Å)	7.1863 (2)
<i>V</i> (Å <sup>3</sup> )	1592.36 (7)
Range for data collection, 2θ (°)	6–80
Reciprocal space range <i>hkl</i>	−23 ≤ <i>h</i> ≤ 25 −27 ≤ <i>k</i> ≤ 28 −12 ≤ <i>l</i> ≤ 11
Total number of frames	3681
Set of reflections	13,875
Unique reflections, <i>R</i> <sub>int</sub> (%)	2181, 1.96
Redundancy	12
Absorption correction method	SADABS
Refinement method	Full-matrix least-squares on <i>F</i> <sup>2</sup>
Structural refinement program	SHELXL
Extinction coefficient	0.00037 (12)
Flack parameter	0.04 (1)
<i>wR</i> 2 (%)	3.44
<i>R</i> 1 (%) all data	1.53
<i>R</i> 1 (%) for <i>I</i> > 2σ( <i>I</i> )	1.47
GooF	1.054
Largest diff. peak and hole (± e <sup>−</sup> /Å <sup>3</sup> )	−0.65 and 1.08

*R*<sub>int</sub> = merging residual value; *R*1 = discrepancy index, calculated from *F*-data; *wR*2 = weighted discrepancy index, calculated from *F*<sup>2</sup>-data; GooF = goodness of fit; Diff. Peaks = maximum and minimum residual electron density. Radiation, MoKα = 0.71073 Å. Data collection temperature = 293 K. Space group *R*3*m*; *Z* = 3

established to be a schorl (see below) with concentrations of Fe<sup>2+</sup> among the highest currently found in nature (FeO<sub>tot</sub> ~ 18 wt.%, Table 2). The Mössbauer absorption spectrum of the Seagull tourmaline shows two dominant absorptions between −1 and +3 mm/s (Fig. 2). The spectrum was deconvoluted using Lorentzian doublets in agreement with models already used in the existing literature (Andreozzi et al. 2008; Bosi et al. 2019b). Accordingly, a model with five doublets was initially adopted and their hyperfine parameters were tentatively refined. Four doublets gave center shift (δ) values around 1.10(2) mm/s and were assigned to <sup>61</sup>Fe<sup>2+</sup>. They are distinguished by their quadrupole splitting (Δ*E*<sub>Q</sub>) values: the first three doublets, conventionally labelled *Y*1, *Y*2 and *Y*3, have Δ*E*<sub>Q</sub> = 2.43(9), 2.11(6), 1.69(11) were interpreted as Fe<sup>2+</sup> at the *Y* sites with different nearest and next-nearest neighbor coordination environments. The fourth Fe<sup>2+</sup> doublet, which has Δ*E*<sub>Q</sub> = 1.20(5) mm/s was interpreted as <sup>61</sup>Fe<sup>2+</sup> in a different chemical environment (or crystallographic-site symmetry) from the *Y* sites, that is Fe<sup>2+</sup> at the *Z* site. This interpretation is in agreement with the model described in Andreozzi et al. (2008) and Bosi et al. (2015). A potential fifth doublet, centered around 0.3 mm/s and representing <sup>61</sup>Fe<sup>3+</sup>, was quantified to be ≤ 2% of the Fe<sub>tot</sub>, but its area was smaller than the experimental uncertainty (± 3%) and its hyperfine parameters could not be refined. The contribution of <sup>61</sup>Fe<sup>3+</sup> was therefore considered to be negligible and all the Fe was eventually considered as <sup>61</sup>Fe<sup>2+</sup> (Table 1). Notably, the same conclusions were also obtained by Sinclair and Richardson (1992). Concerning site distribution of Fe<sup>2+</sup>, the absorption doublet assigned to <sup>2</sup>Fe<sup>2+</sup> was quantified at 25(5)% of the Fe<sub>tot</sub>, which corresponds to 0.65(13) apfu and converges to <sup>2</sup>Fe<sup>2+</sup> obtained by SREF data (see below).

**Table 5** Fractional atom coordinates (*x,y,z*), site occupancy factors (s.o.f.) and equivalent-isotropic (*U*<sub>eq</sub>) and isotropic (*U*<sub>iso</sub>) displacement parameters (in Å<sup>2</sup>) for Seagull schorl from Yukon Territory (Canada)

Site	<i>x</i>	<i>y</i>	<i>z</i>	<i>U</i> <sub>eq</sub>	s.o.f
<i>X</i>	0	0	0.2289 (3)	0.0226 (6)	Na <sub>0.781</sub> (9)
<i>Y</i>	0.12556 (2)	0.06278 (2)	0.62788 (6)	0.00894 (8)	Fe <sub>0.697</sub> (4) Al <sub>0.303</sub> (4)
<i>Z</i>	0.29881 (2)	0.26176 (2)	0.61151 (6)	0.00607 (9)	Al <sub>0.912</sub> (2) Fe <sub>0.088</sub> (2)
<i>B</i>	0.11023 (6)	0.22046 (13)	0.4559 (2)	0.0072 (2)	B <sub>1.00</sub>
<i>T</i>	0.19178 (2)	0.18983 (2)	0	0.00519 (7)	Si <sub>1.00</sub>
O(1) (≡W)	0	0	0.7825 (4)	0.0342 (7)	O <sub>0.5912</sub> F <sub>0.4088</sub>
O(2)	0.06155 (5)	0.12311 (9)	0.48594 (19)	0.0139 (2)	O <sub>1.00</sub>
O(3) (≡V)	0.26873 (11)	0.13437 (5)	0.51074 (17)	0.0130 (2)	O <sub>1.00</sub>
O(4)	0.09294 (5)	0.18588 (9)	0.06854 (16)	0.0093 (2)	O <sub>1.00</sub>
O(5)	0.18616 (10)	0.09308 (5)	0.09067 (16)	0.00946 (19)	O <sub>1.00</sub>
O(6)	0.19777 (6)	0.18768 (6)	0.77707 (12)	0.00805 (14)	O <sub>1.00</sub>
O(7)	0.28452 (6)	0.28502 (6)	0.07988 (11)	0.00782 (13)	O <sub>1.00</sub>
O(8)	0.20964 (6)	0.27039 (6)	0.44196 (13)	0.00966 (14)	O <sub>1.00</sub>
H(1)	0	0	0.916 (4)	0.041*	H <sub>0.5912</sub>
H(3)	0.260 (2)	0.1299 (10)	0.383 (3)	0.016*	H <sub>1.00</sub>

\**U*<sub>iso</sub>: H(1) and H(3) hydrogen atoms were constrained to have a *U*<sub>iso</sub> 1.2 times the *U*<sub>eq</sub> value of the O(1) and O(3) oxygen atoms, respectively

**Table 6** Selected bond distances (Å) for Seagull schorl from Yukon Territory (Canada)

Bond distance - Value (Å)	Bond distance - Value (Å)	Bond distance - Value (Å)	Bond distance - Value (Å)
<i>B</i> -O(2)	1.366 (2)	<i>Y</i> -O(2) <sup>B</sup> (× 2)	2.0020 (8)
<i>B</i> -O(8) <sup>A</sup> (× 2)	1.3807 (13)	<i>Y</i> -O(6) <sup>C</sup> (× 2)	2.0414 (9)
< <i>B</i> -O >	1.376	<i>Y</i> -O(1)	2.0640 (15)
<i>T</i> *-O(6)	1.6063 (9)	<i>Y</i> -O(3)	2.1546 (15)
<i>T</i> -O(7)	1.6093 (8)	< <i>Y</i> -O >	2.051
<i>T</i> -O(4)	1.6267 (5)	<i>Z</i> -O(6)	1.8753 (9)
<i>T</i> -O(5)	1.6397 (5)	<i>Z</i> -O(7) <sup>E</sup>	1.8901 (8)
< <i>T</i> -O >	1.621	<i>Z</i> -O(8) <sup>E</sup>	1.8910 (9)
<i>X</i> -O(2) <sup>B,F</sup> (× 3)	2.514 (2)	<i>Z</i> -O(8)	1.9326 (9)
<i>X</i> -O(5) <sup>B,F</sup> (× 3)	2.7635 (15)	<i>Z</i> -O(7) <sup>D</sup>	1.9710 (9)
<i>X</i> -O(4) <sup>B,F</sup> (× 3)	2.8210 (15)	<i>Z</i> -O(3)	1.9819 (6)
< <i>X</i> -O >	2.700	< <i>Z</i> -O >	1.924

Standard uncertainty in parentheses. Superscript letters: A = (*y* - *x*, *y*, *z*); B = (*y* - *x*, -*x*, *z*); C = (*x*, *x* - *y*, *z*); D = (*y* - *x* + 1/3, -*x* + 2/3, *z* + 2/3); E = (-*y* + 2/3, *x* - *y* + 1/3, *z* + 1/3); F = (-*y*, *x* - *y*, *z*). Transformations relate coordinates to those of Table 5

*T*\* = positioned in adjacent unit cell

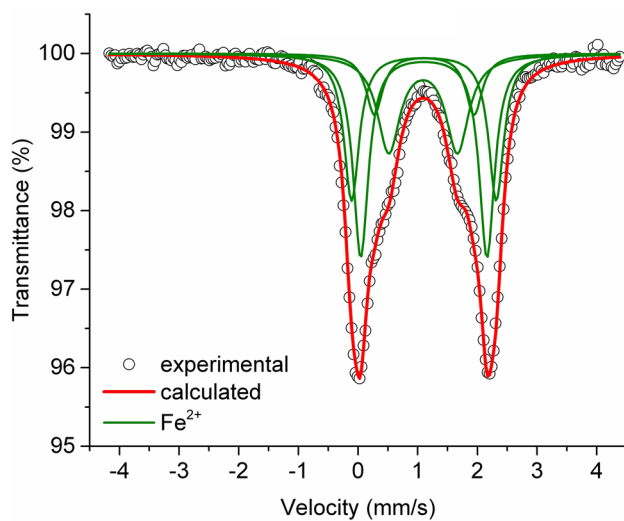


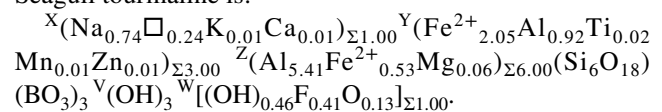
**Fig. 2** Room temperature <sup>57</sup>Fe Mössbauer spectrum for Seagull schorl from Yukon Territory (Canada). Experimental spectrum (exp) is represented by open circles, calculated spectrum (calc) by thick red curve (reduced  $\chi^2 = 0.68$ ). Lorentzian absorption doublets assigned to <sup>66</sup>Fe<sup>2+</sup> are represented by thin green lines

## Site populations

The Li content was considered negligible for crystal-chemical purposes because it is below the detection limit of LA-ICP-MS analysis. The B content was assumed to be stoichiometric (B = 3.00 apfu corresponding to B<sub>2</sub>O<sub>3</sub> = 10.08 wt.%) as corresponding to the LA-ICP-MS results, within

the experimental uncertainty (Table 3). A stoichiometric B content is further supported by the SREF results (Tables 5, 6): the values of the *B*- and *T*-site occupancy factors and the < *B*-O > and < *T*-O > distances are effectively consistent with the *B* and *T* sites fully occupied by B and Si, respectively (e.g., Bosi and Lucchesi 2007). Based on MS results, the oxidation state of all Fe atoms was considered exclusively +2. The (OH) contents and the atomic fractions were then calculated by charge balance under the assumption of (T + Y + Z) = 15.00 apfu and 31 anions. The excellent agreement between the number of electrons per formula unit (epfu) derived from chemistry and from SREF (258.3 epfu versus 258.6 epfu, respectively) supports the above stoichiometric assumptions.

With regard to the site populations at *X*, *B*, *T*, O(3) (≡ V) and O(1) (≡ W), the standard site preference suggested for tourmaline (e.g., Henry et al. 2011) were actually satisfied, while the *Y* and *Z* site populations were optimized according to the procedure of Bosi et al. (2017) and by fixing the minor elements Ti<sup>4+</sup>, Mn<sup>2+</sup> and Zn at *Y*. The robustness of this optimized cation distribution was successively confirmed by the procedure of Wright et al. (2000) in which the default setting was assumed, but the chemical variability was constrained by electroneutrality. The resulting empirical formula for the Seagull tourmaline is:



The refined site-scattering values and those calculated from the optimized site-populations are in excellent



agreement (Table 7). It is worth noting the occurrence at Z site of significant amounts of Fe<sup>2+</sup> (0.53 apfu), which is a cation heavier than Al and it is thus required to justify the refined Z-site scattering value (Z-m.a.n, where m.a.n. is the mean atomic number) of 14.14(3), considerably larger than the expected value for a Z site fully occupied by Al (Z-m.a.n = 13). Such a cation distribution is also corroborated by the refined < Z–O > value (1.924 Å), which is larger than the typical < Z–O > values observed for a Z site fully occupied by Al (1.902–1.913 Å; Bosi and Andreozzi 2013) and reflects the presence of cations larger than Al at the Z site (as, for example, Fe<sup>2+</sup>). Finally, as previously highlighted, the amounts of Fe<sup>2+</sup> at Z retrieved by SREF (0.53 apfu) are consistent with the absorption area of the MS doublet assigned to <sup>Z</sup>Fe<sup>2+</sup> (Table 1), which corresponds to ~ 0.65(13) apfu.

**Influence of the tourmaline structural stability on the Al-Fe<sup>2+</sup> order-disorder**

The empirical formula of the Seagull tourmaline is consistent with a tourmaline belonging to the alkali group (Henry et al. 2011): Na-dominant at the X position of the tourmaline general chemical formula and (OH)-dominant at W (OH > F). The Y and Z positions are dominated by Fe<sup>2+</sup> and Al, respectively. In accord with the IMA-CNMNC rules (Bosi et al. 2019d), the end-member formula is X(Na)<sup>Y</sup>(Fe<sup>2+</sup>)<sub>3</sub><sup>Z</sup>(Al)<sub>6</sub>(Si<sub>6</sub>O<sub>18</sub>)(BO<sub>3</sub>)<sub>3</sub>(OH)<sub>3</sub>(OH), corresponding to schorl (Henry et al. 2011). By our most comprehensive understandings, the Seagull schorl is the Fe<sup>2+</sup>-richest schorl investigated by SREF thus far, even richer than the fluor-schorl from Steinberg, Germany, for which FeO<sub>tot</sub> = 16.5 wt.% and Fe<sup>2+</sup> ≤ 96% of Fe<sub>tot</sub> (Ertl et al. 2016).

The composition of the studied schorl can be approximated as Na<sup>Y</sup>(Fe<sup>2+</sup><sub>2</sub>Al)<sup>Z</sup>(Al<sub>5</sub>Fe<sup>2+</sup>)(Si<sub>6</sub>O<sub>18</sub>)(BO<sub>3</sub>)<sub>3</sub>(OH)<sub>3</sub>(OH,F). With respect to the ideal ordered schorl (Fe<sup>2+</sup> ordered at Y and Al at Z, see above), the observed partial disorder of Fe<sup>2+</sup> over the Y and the Z sites (68% and 9% atoms/site, respectively) can be explained by the intracrystalline order-disorder reaction <sup>Y</sup>Al + <sup>Z</sup>Fe<sup>2+</sup> → <sup>Y</sup>Fe<sup>2+</sup> + <sup>Z</sup>Al, which is needed to satisfy the long-range structural stability of tourmaline (Bosi 2018). In fact, in the ideal ordered schorl the expected difference between the < <sup>Y</sup>Fe<sup>2+</sup>–O >

and < <sup>Z</sup>Al–O > would be Δ<sub>(Y-Z)</sub> = 0.232 Å [< <sup>Y</sup>Fe<sup>2+</sup>–O > = 2.136(1) Å and < <sup>Z</sup>Al–O > = 1.904(3) Å, calculated from the ionic radii of Bosi (2018)], that is too large and inconsistent with the structural stability limits of the tourmaline supergroup minerals: Δ<sub>(Y-Z)</sub> less than 0.15 Å [as proposed by Bosi and Lucchesi (2007) and successively confirmed by Bosi (2018) using 322 SREF data sets]. Consequently, the structure of the ordered schorl would be unstable (Fig. 3). In the studied schorl, the misfit between < Y–O > and < Z–O > is reduced to 0.127 Å by the reaction <sup>Y</sup>Al + <sup>Z</sup>Fe<sup>2+</sup> → <sup>Y</sup>Fe<sup>2+</sup> + <sup>Z</sup>Al, which mitigates the potential misfit by shortening < Y–O > up to 2.051 Å (introducing <sup>Y</sup>Al) and increasing < Z–O > up to 1.924 Å (introducing <sup>Z</sup>Fe<sup>2+</sup>). Therefore, the data are consistent with the partial disordering of significant amounts of Fe<sup>2+</sup> into the Z sites as a mechanism to establish long-range structural stability (Fig. 3).

The site redistribution of Fe–Mg–Al over the Y and Z sites was experimentally investigated at high temperature for schorl, dravite, Fe-bearing oxy-dravite, lucchesiite and Fe-rich fluor-elbaite by Filip et al. (2012), Bosi et al. (2016a,b, 2018b, 2019c). These studies, conducted at both oxidizing and reducing conditions, showed significant Fe–Mg–Al intersite exchanges when Fe-bearing tourmalines were heated up to 700–800 °C, with Fe always involved in the disordering process (up to 0.37 apfu of <sup>Z</sup>Fe for schorl and lucchesiite). Although the possibility of a geothermometric exploitation of tourmaline intersite exchanges is encouraging, the present results (with <sup>Z</sup>Fe<sup>2+</sup> = 0.53 apfu) suggest adopting some precautions, at least for very high Fe contents, due to the important role of the long-range structural constraints on Fe<sup>2+</sup> site distribution.

**Conclusions**

The comprehensive multi-analytical approach of this study of a schorl sample from Seagull batholith (Yukon Territory, Canada) constrains the crystal-chemical behavior of Fe<sup>2+</sup> in tourmaline. The studied sample is the Fe<sup>2+</sup>-richest schorl with SREF data known in the literature.

From a crystal-chemical viewpoint, a partial disorder of Fe<sup>2+</sup> over the Y and Z sites was observed, and this is required for the long-range structural constraints to be

**Table 7** Site-scattering values and optimized site-populations for Seagull schorl from Yukon Territory (Canada)

Site	Refined site-scattering (epfu)	Optimized site-population (apfu)	Calculated site-scattering (epfu)
X	8.59 (8)	0.74 Na + 0.24 □ + 0.01 K + 0.01 Ca	8.49
Y	66.18 (26)	2.05 Fe <sup>2+</sup> + 0.92 Al + 0.02 Ti <sup>4+</sup> + 0.01 Mn <sup>2+</sup> + 0.01 Zn	66.01
Z	84.86 (17)	5.41 Al + 0.53 Fe <sup>2+</sup> + 0.06 Mg	84.82

epfu electrons per formula unit, apfu atoms per formula unit

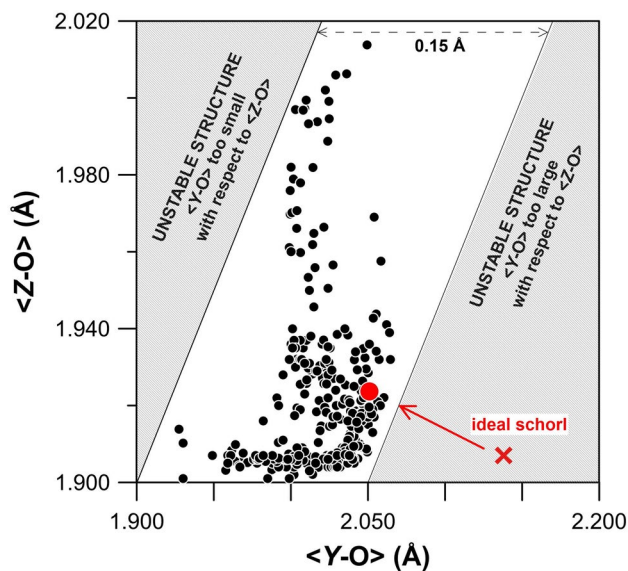


**Fig. 3** Relation between  $\langle Z-O \rangle$  and  $\langle Y-O \rangle$  showing the structural-stability limits for tourmaline minerals. Solid diagonal lines: left = ratio 1:1 between  $\langle Z-O \rangle$  and  $\langle Y-O \rangle$ ; right = ratio 1:1 shifted by 0.15 Å. The full red circle represents the partially disordered Seagull schorl from Yukon Territory (Canada); the red cross is the ideal ordered schorl; black dots represents 322 data sets with SREF. Modified from Bosi (2018)

fulfilled. Similar arguments were applied to explain the observed partial disorder of Mg over Y and Z for dravite and fluor-dravite, as well as the failure in synthesizing the tsilaisite end-member composition (Bosi and Lucchesi 2007; Clark et al. 2011; Bosi et al. 2012; Bosi 2018). For tourmaline to be stable, the 3-D framework of  $ZO_6$  octahedra must be able to accommodate the structural islands made of  $(XO_9 + YO_6 + BO_3 + TO_4)$  polyhedra. With Z site fully occupied by Al, very high amounts ( $\gg 2$  apfu) of  $Mg^{2+}$ ,  $Fe^{2+}$  and  $Mn^{2+}$  ordered at the Y site would make tourmaline unstable, because the resulting difference between  $\langle Y-O \rangle$  and  $\langle Z-O \rangle$  would be too large [i.e.,  $\Delta_{(Y-Z)} > 0.15$  Å]. A partial disorder of Al and  $R^{2+}$ -cations over Y and Z is, therefore, necessary to reduce the misfit between  $YO_6$  and  $ZO_6$  and to guarantee tourmaline structure stability.

**Acknowledgements** The Seagull schorl was generously made available by Dave Sinclair (Geological Survey of Canada). Funding by the Deep Energy Community of the Deep Carbon Observatory (UCLA Subaward Number 2090 G UA406 to G.B. Andreozzi) and by Sapienza University of Rome (Prog. Università 2017 to V. Stagno and 2018 to F. Bosi) is gratefully acknowledged. The authors sincerely thank the Editor Milan Rieder for his professional handling, and Darrell J. Henry and an anonymous reviewer for their constructive comments that helped to improve the manuscript.

## References

- Ahmadi S, Tahmasbi Z, Khalaji AA, Zal F (2019) Chemical variations and origin of tourmalines in laleh zar granite of Kerman (Southeast Iran). *Period Mineral* 88:117–129
- Andreozzi GB, Bosi F, Longo M (2008) Linking Mossbauer and structural parameters in elbaite-schorl-dravite tourmalines. *Am Mineral* 93:658–666
- Berryman EJ, Zhang D, Wunder B, Duffy TS (2019) Compressibility of synthetic Mg-Al tourmalines to 60 GPa. *Am Mineral* 104:1005–1015
- Bosi F (2018) Tourmaline crystal chemistry. *Am Mineral* 103:298–306
- Bosi F, Lucchesi S (2007) Crystal chemical relationships in the tourmaline group: structural constraints on chemical variability. *Am Mineral* 92:1054–1063
- Bosi F, Andreozzi GB (2013) A critical comment on Ertl et al. (2012): limitations of  $Fe^{2+}$  and  $Mn^{2+}$  site occupancy in tourmaline: evidence from  $Fe^{2+}$ - and  $Mn^{2+}$ -rich tourmaline. *Am Mineral* 98:2183–2192
- Bosi F, Skogby H, Agrosi G, Scandale E (2012) Tsilaisite,  $NaMn_3Al_6(Si_6O_{18})(BO_3)_3(OH)_3OH$ , a new mineral species of the tourmaline supergroup from Grotta d'Oggi, San Pietro in Campo, island of Elba, Italy. *Am Mineral* 97:989–994
- Bosi F, Andreozzi GB, Hälenius U, Skogby H (2015) Experimental evidence for partial  $Fe^{2+}$  disorder at the Y and Z sites of tourmaline: a combined EMP, SREF, MS, IR and OAS study of schorl. *Min Mag* 79:515–528
- Bosi F, Skogby H, Balić-Žunić T (2016a) Thermal stability of extended clusters in dravite: a combined EMP, SREF and FTIR study. *Phys Chem Mineral* 43:395–407
- Bosi F, Skogby H, Hälenius U (2016b) Thermally induced cation redistribution in Fe-bearing oxy-dravite and potential geothermometric implications. *Contrib Mineral Petrol* 171:47
- Bosi F, Reznitskii L, Hälenius U, Skogby H (2017) Crystal chemistry of Al-V-Cr oxy-tourmalines from Sludyanka complex, Lake Baikal, Russia. *Eur J Mineral* 29:457–472
- Bosi F, Naitza S, Skogby H, Secchi F, Conte AM, Cuccuru S, Hälenius U, De La Rosa N, Kristiansson P, Nilsson EJC, Ros L, Andreozzi GB (2018a) Late magmatic controls on the origin of schorlitic and foititic tourmalines from late-Variscan peraluminous granites of the Arbus pluton (SW Sardinia, Italy) Crystal-chemical study and petrological constraints. *Lithos* 308:395–411
- Bosi F, Skogby H, Hälenius U, Ciriotti M (2018b) Experimental cation redistribution in the tourmaline lucchesiite,  $CaFe^{2+}_3Al_6(Si_6O_{18})(BO_3)_3(OH)_3O$ . *Phys Chem Mineral* 45:621–632
- Bosi F, Naitza S, Secchi F, Conte AM, Cuccuru S, Andreozzi GB, Skogby H, Hälenius U (2019a) Petrogenetic controls on the origin of tourmalinite veins from Mandrolisai igneous massif (Central Sardinia, Italy): Insights from tourmaline crystal chemistry. *Lithos* 342–343:333–344
- Bosi F, Biagioni C, Oberti R (2019b) On the chemical identification and classification of minerals. *Minerals* 9(10):591
- Bosi F, Skogby H, Hälenius U (2019c) Thermally induced cation redistribution in fluor-elbaite and Fe-bearing tourmalines. *Phys Chem Mineral* 46:371–383
- Bosi F, Hatert F, Hälenius U, Pasero M, Miyawaki R, Mills SJ (2019d) On the application of the IMA-CNMNC dominant-valency rule to complex mineral compositions. *Mineral Mag* 83:627–632
- Clark CM, Hawthorne FC, Ottolini L (2011) Fluor-dravite,  $NaMg_3Al_6Si_6O_{18}(BO_3)_3(OH)_3F$ , a new mineral species of the tourmaline group from the Crabtree emerald mine, Mitchell County, North Carolina: description and crystal structure. *Can Mineral* 49:57–62
- Dutrow B, Henry D (2011) Tourmaline: a geologic DVD. *Elements* 7:301–306

- Dutrow B, Henry D (2018) Tourmaline compositions and textures: reflections of the fluid phase. *J Geosci* 63:99–110
- Ertl A, Tillmanns E, Ntafos T, Francis C, Giester G, Körner W, Hughes JM, Lengauer C, Prem M (2008) Tetrahedrally coordinated boron in Al-rich tourmaline and its relationship to the pressure–temperature conditions of formation. *Eur J Mineral* 20:881–888
- Ertl A, Schuster R, Hughes JM, Ludwig T, Meyer H-P, Finger F, Dyar MD, Ruschel K, Rossman GR, Klötzli U, Brandstätter F, Lengauer CL, Tillmanns E (2012) Li-bearing tourmalines in Variscan pegmatites from the Moldanubian nappes, Lower Austria. *Eur J Mineral* 24:695–715
- Ertl A, Kolitsch U, Dyar MD, Meyer HP, Rossman GR, Henry DJ, Prem M, Ludwig T, Nasdala L, Lengauer CL, Tillmanns E, Niedermayr G (2016) Fluor-schorl, a new member of the tourmaline supergroup, and new data on schorl from the cotype localities. *Eur J Mineral* 28:163–177
- Ertl A, Henry DJ, Tillmanns E (2018) Tetrahedral substitutions in tourmaline: a review. *Eur J Mineral* 30:465–470
- Filip J, Bosi F, Novák M, Skogby H, Tuček J, Čuda J, Wildner M (2012) Iron redox reactions in the tourmaline structure: High-temperature treatment of Fe<sup>3+</sup>-rich schorl. *Geochim Cosmochim Acta* 86:239–256
- Grew ES, Krivovichev SV, Hazen RM, Hystad G (2016) Evolution of structural complexity in boron minerals. *Can Mineral* 54:125–143
- Henry DJ, Dutrow BL (1992) Tourmaline in a low grade clastic meta-sedimentary rock: an example of the petrogenetic potential of tourmaline. *Contrib Mineral Petrol* 112:203–218
- Henry DJ, Dutrow BL (1996) Metamorphic tourmaline and its petrologic applications. In: Grew ES, Anovitz LM (eds), *Boron: mineralogy, petrology and geochemistry*. *Rev Mineral Geochem* 33:503–557
- Henry DJ, Dutrow BL (2018) Tourmaline studies through time: contributions to scientific advancements. *J Geosci* 63:77–98
- Henry DJ, Novák M, Hawthorne FC, Ertl A, Dutrow BL, Uher P, Pezzotta F (2011) Nomenclature of the tourmaline supergroup minerals. *Am Mineral* 96:895–913
- Jochum KP, Weis U, Stoll B, Kuzmin D, Yang Q, Raczek I, Jacob DE, Stracke A, Birbaum K, Frick DA, Günther D, Enzweiler J (2011) Determination of reference values for NIST SRM 610–617 glasses following ISO guidelines. *Geostand Geoanal Res* 35:397–429
- Kim Y, Jong K, Li G, Kim C, Jon Y, Jong C (2018) Numerical simulation of intrinsic dipole moment according to ion substitution and order-disorder reactions in tourmaline. *Can Mineral* 56:951–965
- Lagarec K, Rancourt DG (1998) RECOIL, Mössbauer spectral analysis software for windows (version 1.0). Department of Physics, University of Ottawa, Canada
- Paton C, Hellstrom J, Paul B, Woodhead J, Hergt J (2011) Iolite: Free-ware for the visualisation and processing of mass spectrometric data. *J Anal Atom Spectrom* 26:2508–2518
- Pouchou JL, Pichoir F (1991) Quantitative analysis of homogeneous or stratified microvolumes applying the model “PAP”. In: Heinrich KFJ, Newbury DE (eds) *Electron probe quantitation*. Plenum, New York, pp 31–75
- Raczek I, Stoll B, Hofmann AW, Jochum KP (2001) High-precision trace element data for the USGS reference materials BCR-1, BCR-2, BHVO-1, BHVO-2, AGV-1, AGV-2, DTS-1, DTS-2, GSP-1 and GSP-2 by ID-TIMS and MIC-SSMS. *Geostandards Newslett* 25:77–86
- Sheldrick GM (2015) Crystal structure refinement with SHELXL. *Acta Crystallogr C* 71:3–8
- Sipahi F (2019) Nature of tourmaline formation in quartz porphyry in the E Sakarya zone (NE Turkey): Geochemistry and isotopic approach. *Period Mineral* 88:333–351
- Sinclair WD, Richardson JM (1992) Quartz-tourmaline orbicules in the Seagull Batholith, Yukon Territory. *Can Mineral* 30:923–935
- Wright SE, Foley JA, Hughes JM (2000) Optimization of site occupancies in minerals using quadratic programming. *Am Mineral* 85:524–531
- van Hinsberg VJ, Schumacher JC (2007) Intersector element partitioning in tourmaline: a potentially powerful single crystal thermometer. *Contrib Mineral Petrol* 153:289–301
- van Hinsberg VJ, Henry DJ, Marschall HR (2011a) Tourmaline: an ideal indicator of its host environment. *Can Mineral* 49:1–16
- van Hinsberg VJ, Henry DJ, Dutrow BL (2011b) Tourmaline as a petrologic forensic mineral: a unique recorder of its geologic past. *Elements* 7:327–332
- van Hinsberg VJ, Franz G, Wood BJ (2017) Determining subduction-zone fluid composition using a tourmaline mineral probe. *Geochem Persp Lett* 3:160–169


**Publisher's Note** Springer Nature remains neutral with regard to jurisdictional claims in published maps and institutional affiliations.

### 2.1.2. Mn-bearing fluor-elbaite



## Article

# Mn-bearing purplish-red tourmaline from the Anjanabonoina pegmatite, Madagascar

Ferdinando Bosi<sup>1\*</sup> , Beatrice Celata<sup>1</sup>, Henrik Skogby<sup>2</sup>, Ulf Hålenius<sup>2</sup>, Gioacchino Tempesta<sup>3</sup>, Marco E. Ciriotti<sup>4,5</sup>, Erica Bittarello<sup>5,6</sup> and Alessandra Marengo<sup>5,6</sup>

<sup>1</sup>Department of Earth Sciences, Sapienza University of Rome, Piazzale Aldo Moro 5, I-00185 Rome, Italy; <sup>2</sup>Department of Geosciences, Swedish Museum of Natural History, SE-10405 Stockholm, Sweden; <sup>3</sup>Department of Earth and Geoenvironmental Sciences, University of Bari “Aldo Moro”, via Orabona 4, I-70125 Bari, Italy; <sup>4</sup>Associazione Micromineralogica Italiana, via San Pietro 55, I-10073 Devesi-Cirié, Italy; <sup>5</sup>Department of Earth Sciences, University of Turin, via Tommaso Valperga Caluso 35, I-10125 Torino, Italy; and <sup>6</sup>SpectraLab s.r.l. Academic spin-off of the University of Turin, via Tommaso Valperga Caluso 35, I-10125 Torino, Italy

### Abstract

A gem-quality purplish-red tourmaline sample of alleged liddicoatitic composition from the Anjanabonoina pegmatite, Madagascar, has been fully characterised using a multi-analytical approach to define its crystal-chemical identity. Single-crystal X-ray diffraction, chemical and spectroscopic analysis resulted in the formula:  $X(\text{Na}_{0.41}\square_{0.35}\text{Ca}_{0.24})_{\Sigma 1.00} Y(\text{Al}_{1.81}\text{Li}_{1.00}\text{Fe}_{0.04}^{3+}\text{Mn}_{0.02}^{3+}\text{Mn}_{0.12}^{2+}\text{Ti}_{0.004})_{\Sigma 3.00} Z\text{Al}_6[\text{T}(\text{Si}_{5.60}\text{B}_{0.40})_{\Sigma 6.00}\text{O}_{18}](\text{BO}_3)_3(\text{OH})_3 W[(\text{OH})_{0.50}\text{F}_{0.13}\text{O}_{0.37}]_{\Sigma 1.00}$  which corresponds to the tourmaline species elbaite having the typical space group  $R3m$  and relatively small unit-cell dimensions,  $a = 15.7935(4)$  Å,  $c = 7.0860(2)$  Å and  $V = 7.0860(2)$  Å<sup>3</sup>.

Optical absorption spectroscopy showed that the purplish-red colour is caused by minor amounts of  $\text{Mn}^{3+}$  ( $\text{Mn}_2\text{O}_3 = 0.20$  wt.%). Thermal treatment in air up to 750°C strongly intensified the colour of the sample due to the oxidation of all  $\text{Mn}^{2+}$  to  $\text{Mn}^{3+}$  ( $\text{Mn}_2\text{O}_3$  up to 1.21 wt.%). Based on infrared and Raman data, a crystal-chemical model regarding the electrostatic interaction between the X cation and W anion, and involving the Y cations as well, is proposed to explain the absence or rarity of the mineral species ‘liddicoatite’.

**Keywords:** purplish-red tourmaline, crystal-structure refinement, electron microprobe, laser induced breakdown spectroscopy, Raman spectroscopy, infrared spectroscopy, optical absorption spectroscopy

(Received 16 December 2020; accepted 24 February 2021; Accepted Manuscript published online: 1 March 2021; Associate Editor: Ian T. Graham)

### Introduction

Tourmaline is the most common and the earliest-formed boron mineral on Earth and has recently received increasing interest from the geoscience community (Grew *et al.*, 2016; Dutrow and Henry, 2018; Henry and Dutrow, 2018). Tourmaline minerals are complex borosilicates that have been studied extensively in terms of their crystal structure and crystal chemistry (e.g. Foit, 1989; Grice and Ercit, 1993; Ertl *et al.*, 2002; Novák *et al.*, 2004; Bosi and Lucchesi, 2007; Bosi 2013, 2018; Novák *et al.*, 2011; Henry and Dutrow, 2011; Henry *et al.*, 2011; Cempírek *et al.*, 2013; Ertl *et al.*, 2018; Andreozzi *et al.*, 2020).

The general chemical formula of tourmaline can be written as:  $\text{XY}_3\text{Z}_6\text{T}_6\text{O}_{18}(\text{BO}_3)_3\text{V}_3\text{W}$ , where X = Na, K, Ca and  $\square$  (= vacancy); Y = Al, Cr, V, Fe, Mg, Mn, Zn, Cu, Li and Ti; Z = Al, Cr, V, Fe and Mg; T = Si, Al and  $\text{B}^{3+}$ ; B =  $\text{B}^{3+}$ ; V = (OH) and O; and W = (OH), F and O. Note that the non-italicised letters X, Y, Z and B represent groups of cations hosted at the  $^{[9]}X$ ,  $^{[6]}Y$ ,  $^{[6]}Z$ ,  $^{[4]}T$  and

$^{[3]}B$  crystallographic sites (letters italicised). The letters V and W represent groups of anions accommodated at the  $^{[3]}O3$  and  $^{[3]}O1$  crystallographic sites, respectively. The H atoms occupy the H3 and H1 sites, which are related to O3 and O1, respectively. The dominance of specific ions at one or more sites of the structure gives rise to a range of distinct mineral species.

Tourmaline-supergroup minerals are currently classified into three groups, vacant, alkali and calcic, based on the X-site occupancy (Henry *et al.*, 2011). The X-site occupancy is usually related to both paragenesis and crystallisation conditions of the host rock, and these relations may be used to reconstruct the host-rock thermal and chemical history (e.g. Henry and Dutrow, 1996; van Hinsberg *et al.*, 2011a,b; Dutrow and Henry, 2018; Bosi *et al.*, 2018, 2019c; Ahmadi *et al.*, 2019). A further level of classification into subgroups is based on charge arrangements at the Y and Z sites. Tourmalines are also distinguished by the dominant anion at the W position of the general formula into hydroxy-, fluor- and oxy-species.

Tourmaline is also one of the most important gem materials on the market today, particularly renowned for its spectrum of colours: from colourless, through red, pink, yellow, orange, green, blue and violet, to brown and black (Pezzotta and Laurs, 2011). The transition elements (Ti, V, Cr, Fe, Mn and Cu) are

\*Author for correspondence: Ferdinando Bosi, Email: [ferdinando.bosi@uniroma1.it](mailto:ferdinando.bosi@uniroma1.it)  
Cite this article: Bosi F., Celata B., Skogby H., Hålenius U., Tempesta G., Ciriotti M.E., Bittarello E. and Marengo A. (2021) Mn-bearing purplish-red tourmaline from the Anjanabonoina pegmatite, Madagascar. *Mineralogical Magazine* 85, 242–253. <https://doi.org/10.1180/mgm.2021.20>



often invoked as colour-causing agents. Red tourmalines are commonly given the varietal name 'rubellite', which refers to tourmalines with colours ranging from rose, dark pink to purplish red, but do correspond to several regular mineral species: elbaite, fluor-elbaite, rossmanite, fluor-liddicoatite (Pezzotta and Laurs, 2011) and oxy-dravite (Bosi and Skogby, 2013).

Specifically, fluor-liddicoatite was redetermined and renamed in 2011 by the Subcommittee on Tourmaline Nomenclature of the International Mineralogical Association's Commission on New Minerals, Nomenclature and Classification (IMA-CNMNC) when the nomenclature of tourmaline-super group minerals was reconsidered (Henry *et al.*, 2011) and the 'liddicoatite' from the Antandrokomby type locality (Dunn *et al.*, 1977; Aurisicchio *et al.*, 1999; Webber, 2002; Dirlam *et al.*, 2002; Ertl *et al.*, 2006; Lussier *et al.*, 2011; Lussier and Hawthorne, 2011) regained proper attention. Note that with the renaming of the type material as fluor-liddicoatite, the hydroxy species 'liddicoatite' is no longer properly defined as a species. A new type material definition is necessary to re-establish the name. Two gem-quality samples of purplish-red prismatic crystals of alleged 'liddicoatite' on quartz matrix from the collection of M.E. Ciriotti (MEC) were analysed with a Jeol JSM IT300LV scanning electron microscope (SEM) and energy dispersive X-ray spectroscopy (EDS) (University of Turin, Earth Sciences Department) to verify if they were F-dominant species. Although B and Li were not measured, both samples were determined to be F-dominant and were classified as fluor-liddicoatite. A small portion of a further alleged 'liddicoatite' sample (presented as 'probed' liddicoatite by its seller) in quartz-rhodizite matrix from Antandrokomby localities (the same type of purplish-red crystals are shown in the specimen in Fig. 1) was obtained by MEC, courtesy of the new owner. The sample was analysed through SEM-EDS and surprisingly showed no trace of F; in addition, its composition did not fit 'liddicoatite' in terms of Na and Ca.

In the present study, such a tourmaline sample from the Anjanabonoina pegmatite, central Madagascar, has been fully characterised by X-ray single-crystal diffraction, electron microprobe analysis, laser induced breakdown spectroscopy, micro-Raman, infrared and optical absorption spectroscopy, with the aim of defining its crystal-chemical identity and species.

## Occurrence

The indexed stout prismatic purplish-red crystal was labelled (by the supplier) 'liddicoatite' from Anjanabonoina pegmatites, Ambohimambola, Betafo, Vakinankaratra, Madagascar, ~55 km west-southwest of the city of Antsirabe. In addition to Anjanabonoina, 'liddicoatite' has been identified from several localities in central and south-central Madagascar, including Antaboaka, Jochy, Lacamisinten, Malakialina, Maroandro and the Sahatany Valley, as well as Vohitrakanga (De Vito, 2002a,b; Dirlam *et al.*, 2002), but the present labelled locality is correct (F. Pezzotta, personal communication).

The Anjanabonoina aplite-pegmatite field is situated in the Neoproterozoic Itremo Group, which consists of a lower unit of gneisses and an upper unit of quartzites, schists and marbles (Pezzotta and Franchi, 1997; Fernandez *et al.*, 2001). The pegmatites were emplaced in a complex geological environment, perhaps at the contact between the lower and upper unit. The gem-bearing pegmatites postdate the main tectonic phase and, therefore, are thought to have intruded during a late phase of the magmatic cycle about 490 Ma (Paquette and Nédélec, 1998). The Li-Cs-Ta (with minor Nb-Y-F) aplite-pegmatite field extends for ~2.5 km. The veins are 2 to 12 m thick and large parts are kaolinised feldspars and/or deeply weathered (De Vito, 2002a,b).

More details about the history of the 1500s to 2000s explorations and mining of the Malagasy tourmaline gem deposits can be found in Strunz (1979), Pezzotta (1999) and Dirlam *et al.* (2002).

## Experimental methods and results

### Thermal treatment

In order to study potential dehydration and redox effects, two oriented and polished crystals were heat treated in air at 700°C (20 h) and 750°C (90 h). These thermal conditions have previously been shown to be sufficient to impose changes in Fe redox states and intracrystalline cation distribution (e.g. Filip *et al.*, 2012; Bosi *et al.*, 2016a,b). The 55 and 309 µm thick samples were placed in a gold container and inserted in a preheated



**Fig. 1.** Crystals of Mn-bearing purplish-red tourmaline from Madagascar, up to 1 cm in size (field of view ca. 5 cm). Sample deposited in the collections of the Natural History Museum of Milano, Italy (photo by R. Appiani).

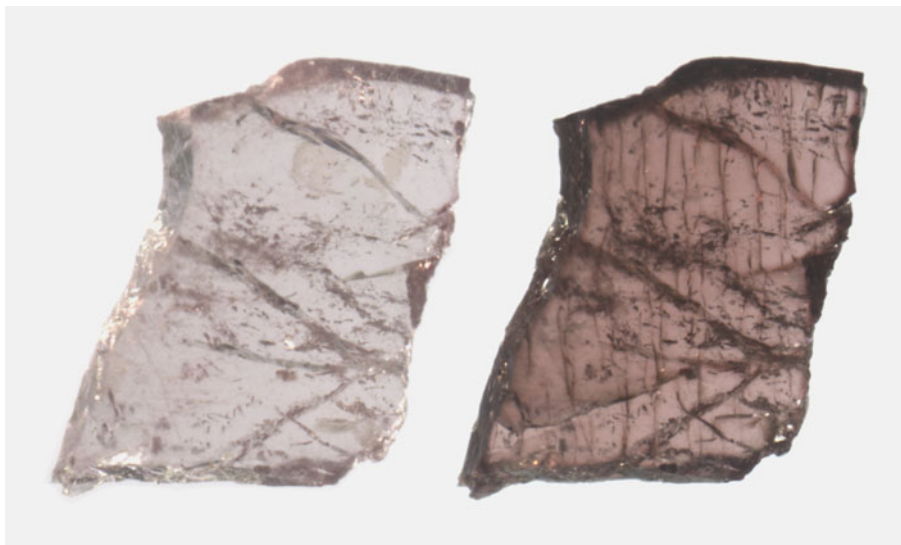


**Fig. 2.** Microphoto of Mn-bearing tourmaline from Madagascar before (on the left) and after (on the right) heat treatment at 750°C. Sample thickness 300  $\mu\text{m}$ , long edge corresponds to 2 mm.

horizontal tube furnace equipped with a quartz-glass tube. The experiments were ended by pushing the sample container out to the cold zone of the quartz tube, which caused the sample to cool to room temperature within one minute. A distinct increase in colour intensity appeared after heat treatment, as shown in Fig. 2. Minor cracks appeared in the thicker sample after treatment at the higher temperature.

### Single-crystal structure refinement (SREF)

A representative crystal fragment of the purplish-red tourmaline from Madagascar was selected for X-ray diffraction measurements on a Bruker KAPPA APEX-II single-crystal diffractometer (Sapienza University of Rome, Earth Sciences Department), equipped with a charge-coupled device (CCD) area detector (6.2 cm  $\times$  6.2 cm active detection area, 512  $\times$  512 pixels) and a graphite-crystal monochromator using MoK $\alpha$  radiation from a fine-focus sealed X-ray tube. The sample-to-detector distance was 4 cm. A total of 3577 exposures (step = 0.2°, time/step = 20 s) covering a full reciprocal sphere with a redundancy of  $\sim$ 12 was collected. Final unit-cell parameters were refined using the Bruker AXS SAINT program on reflections with  $I > 10 \sigma(I)$  in the range  $5^\circ < 2\theta < 78^\circ$ . The intensity data were processed and corrected for Lorentz, polarisation and background effects using the APEX2 software program of Bruker AXS. The data were corrected for absorption using a multi-scan method (SADABS, Bruker AXS). The absorption correction led to an improvement in  $R_{\text{int}}$  (from 0.033 to 0.027). No violation of  $R3m$  symmetry was detected.

Structure refinement was done using the SHELXL-2013 program (Sheldrick, 2015). Starting coordinates were taken from Bosi *et al.* (2013). Variable parameters were scale factor, extinction coefficient, atom coordinates, site-scattering values (for X, Y and Z sites) and atomic-displacement factors. Attempts to refine the extinction coefficient yielded values within its standard uncertainty, thus it was not refined. Neutral scattering factors were used for the cations and oxygen atoms. As for the atomic model refinement and in accordance with the chemical analysis results (see below), the X site was modelled by setting the vacancy content to 0.32 atoms per formula unit (apfu) and allowing the remainder of the site to refine as Ca = (0.65 – Na). Similarly, the Y site was refined by setting the (Mn+Fe) occupancy to 0.19 apfu and allowing the remainder of the site to refine as

Al = (2.81 – Li) apfu. The T site was modelled by Si versus B. The Z, B and anion sites were modelled with Al, B and O scattering factors, respectively, and with a fixed occupancy of 1 as refinement with unconstrained occupancies showed no significant deviations from this value. A final refinement was then performed by modelling the site occupancy of the O1 site with O and F fixed to the value obtained from the empirical formula (see below). Similar chemical constraints were applied to refine the H1 and H3 sites. There were no correlations greater than 0.7 between the parameters at the end of the refinement.

Table 1 lists crystal data, data-collection information and refinement details; Table 2 gives the fractional atom coordinates

**Table 1.** Single-crystal X-ray diffraction data details for the purplish-red tourmaline from Madagascar.

<b>Crystal data</b>	
Crystal sizes (mm)	0.10 $\times$ 0.16 $\times$ 0.18
Space group; Z	$R3m$ , 3
$a$ ( $\text{\AA}$ )	15.7935(4)
$c$ ( $\text{\AA}$ )	7.0860(2)
$V$ ( $\text{\AA}^3$ )	1530.69(9)
<b>Data collection</b>	
Data collection temperature (K)	293
Range for data collection, $2\theta$ ( $^\circ$ )	5–78
Radiation, wavelength ( $\text{\AA}$ )	MoK $\alpha$ , 0.71073
Reciprocal space range, $hkl$	$-26 \leq h \leq 25$ $-22 \leq k \leq 24$ $-12 \leq l \leq 12$
Total number of frames	3577
Measured reflections	12,849
Unique reflections, $R_{\text{int}}$ (%)	2026, 3.03
Redundancy	12
Absorption correction method	SADABS
<b>Refinement</b>	
Refinement method	Full-matrix least-squares on $F^2$
Structural refinement program	SHELXL-2013
Extinction coefficient	0.0017(3)
Flack parameter	0.05(7)
$wR_2$ (%)	3.98
$R_1$ (%) all data	1.89
$R_1$ (%) for $I > 2\sigma(I)$	1.80
Goof	1.020
Largest diff. peak and hole ( $\pm e^-/\text{\AA}^3$ )	–0.45 and 0.35

Notes:  $R_{\text{int}}$  = merging residual value;  $R_1$  = discrepancy index, calculated from  $F$ -data;  $wR_2$  = weighted discrepancy index, calculated from  $F^2$  data; Goof = goodness of fit; Diff. Peaks = maximum and minimum residual electron density.

**Table 2.** Fractional atom coordinates, equivalent isotropic and isotropic displacement parameters ( $\text{\AA}^2$ ) and site occupancies for the purplish-red tourmaline from Madagascar.

Site	$x/a$	$y/b$	$z/c$	$U_{\text{eq}}$	Site occupancy
X	0	0	0.2208(2)	0.0206(6)	Na <sub>0.396(10)</sub> Ca <sub>0.259(10)</sub>
Y	0.12118(5)	0.06059(2)	0.63828(10)	0.00809(17)	Li <sub>0.260(4)</sub> Al <sub>0.680(4)</sub> Mn <sub>0.0604</sub>
Z	0.29680(3)	0.26032(3)	0.60773(7)	0.00650(8)	Al <sub>1.00</sub>
B	0.10901(7)	0.21802(14)	0.4521(2)	0.0063(3)	B <sub>1.00</sub>
T	0.19143(2)	0.18954(2)	0	0.00515(9)	Si <sub>0.916(4)</sub> B <sub>0.084(4)</sub>
O1(≡W)	0	0	0.7750(3)	0.0200(5)	O <sub>0.872</sub> F <sub>0.128</sub>
O2	0.06014(5)	0.12028(10)	0.4891(2)	0.0139(3)	O <sub>1.00</sub>
O3(≡V)	0.26161(11)	0.13080(6)	0.50677(17)	0.0119(2)	O <sub>1.00</sub>
O4	0.09391(5)	0.18781(11)	0.07377(18)	0.0107(2)	O <sub>1.00</sub>
O5	0.18629(11)	0.09314(5)	0.09516(17)	0.0109(2)	O <sub>1.00</sub>
O6	0.19435(6)	0.18391(6)	0.77405(13)	0.00771(15)	O <sub>1.00</sub>
O7	0.28640(6)	0.28591(6)	0.07611(11)	0.00743(15)	O <sub>1.00</sub>
O8	0.20947(7)	0.27000(7)	0.43694(13)	0.00766(15)	O <sub>1.00</sub>
H1	0	0	0.909(4)	0.024 <sup>a</sup>	H <sub>0.5011</sub>
H3	0.2543(19)	0.1271(9)	0.379(3)	0.014 <sup>a</sup>	H <sub>1.00</sub>

<sup>a</sup>Isotropic displacement parameters ( $U_{\text{iso}}$ ) for H1 and H3 constrained to have a  $U_{\text{iso}}$  1.2 times the  $U_{\text{eq}}$  value of the O1 and O3 oxygen atoms.

**Table 3.** Selected bond lengths ( $\text{\AA}$ ) for the purplish-red tourmaline from Madagascar.

X–O2 ×3	2.5145(18)	Z–O6	1.8737(9)	B–O2	1.362(2)
X–O5 ×3	2.6989(15)	Z–O7	1.8816(9)	B–O8 ×2	1.3785(13)
X–O4 ×3	2.7720(16)	Z–O8	1.8820(9)	<B–O>	1.373
<X–O>	2.662	Z–O8'	1.8977(9)	T–O7	1.6045(9)
		Z–O7'	1.9365(9)	T–O6	1.6054(9)
Y–O1	1.9199(14)	Z–O3	1.9666(7)	T–O4	1.6138(5)
Y–O6 ×2	1.9503(10)	<Z–O>	1.906	T–O5	1.6295(6)
Y–O2 ×2	1.9605(10)			<T–O>	1.613
Y–O3	2.1349(16)				
<Y–O>	1.979				

and equivalent isotropic displacement parameters; Table 3 shows selected bond lengths. A Supplementary Table with anisotropic displacement parameters and a crystallographic information file have been deposited with the Principal Editor of *Mineralogical Magazine* and are available as Supplementary material (see below).

### Electron microprobe analysis (EMPA)

Electron microprobe analysis, carried out on the same crystal that was used for the SREF, was performed using a wavelength dispersive spectrometer (WDS mode) with a Cameca SX50 instrument at the Istituto di Geologia Ambientale e Geoingegneria, CNR, Rome, Italy. The following analytical conditions were used: accelerating voltage 15 kV, beam current 15 nA and spot diameter 10  $\mu\text{m}$ . Minerals and synthetic compounds were used as standards: wollastonite (Si, Ca), magnetite (Fe), rutile (Ti), corundum (Al), vanadinite (V), fluorophlogopite (F), periclase (Mg), jadeite (Na), orthoclase (K), sphalerite (Zn), rhodonite (Mn), metallic Cr and Cu. The PAP routine was applied (Pouchou and Pichoir, 1991). The results (Table 4) represent mean values of 8 spot analyses. Vanadium, Cr, Cu, Zn and K were below detection limits (<0.03 wt.%). Chemical analysis is given in Table 4; no other elements heavier than F were detected.

### Micro-laser induced breakdown spectroscopy ( $\mu\text{-LIBS}$ )

Lithium analysis, carried out on a representative sample fragment, was performed using a double pulse Q-Switched (Nd-YAG,  $\lambda =$

**Table 4.** Chemical composition for the purplish-red tourmaline from Madagascar.

	Average of 8 spots		Atoms normalised to 31 anions	
SiO <sub>2</sub> wt.%	35.59(35)		Si (apfu)	5.600
TiO <sub>2</sub>	0.04(2)		Ti <sup>4+</sup>	0.004
B <sub>2</sub> O <sub>3</sub>	12.51 <sup>a</sup>		B	3.400
Al <sub>2</sub> O <sub>3</sub>	42.11(50)		Al	7.810
Fe <sub>2</sub> O <sub>3</sub>	0.31(3)		Fe <sup>3+</sup>	0.036
MnO <sub>tot</sub>	1.09(2)		Mn <sup>3+</sup>	0.024
CaO	1.43(5)		Mn <sup>2+</sup>	0.121
Na <sub>2</sub> O	1.36(4)		Ca	0.241
Li <sub>2</sub> O	1.59(11) <sup>b</sup>		Na	0.414
F	0.26(8)		Li	1.004
H <sub>2</sub> O	3.34 <sup>a</sup>		F	0.128
–O = F	–0.11		OH	3.501
MnO	0.91 <sup>c</sup>			
Mn <sub>2</sub> O <sub>3</sub>	0.20 <sup>c</sup>			
Total	99.52			

<sup>a</sup>Calculated by stoichiometry, (Y+Z+T+B) = 18.000 apfu.

<sup>b</sup>Determined by  $\mu\text{-LIBS}$ .

<sup>c</sup>Determined by OAS.

Errors for oxides and fluorine are standard deviations (in brackets); apfu = atoms per formula unit.

1064 nm) laser with a 1  $\mu\text{s}$  delay between the two pulses with an energy of 110 mJ per pulse. The small spot size (7–10  $\mu\text{m}$ ) was obtained using a petrographic optical microscope (objective lens 10X NA 0.25 WD 14.75 mm). The LIBS spectra were acquired by an AvaSpec Fiber Optic Spectrometer (390–900 nm with 0.3 nm resolution) with a delay of 2  $\mu\text{s}$  after the second pulse and an integration time of 1 ms.

The main problem regarding Li quantification by LIBS concerns the self-absorption of the emission line used to extract quantitative data. In the present tourmaline, the quantitative data were obtained from linear regression using the main Li emission line intensity ( $I_{\text{Li}} = 670.706 \text{ nm}$ , corresponding to the resonance transition  $1s^2 2s > 1s^2 2p$ ) in the range from 0.009 to 2.04 wt.% of Li<sub>2</sub>O. In this regard, we verified that the self-absorption effect of this specific line was negligible in the studied concentration range, hence, not affecting the measurements. This is consistent with previous studies on beryl (McMillan *et al.*, 2006; Tempesta and Agrosi, 2016; Tempesta *et al.*, 2020). Moreover, the



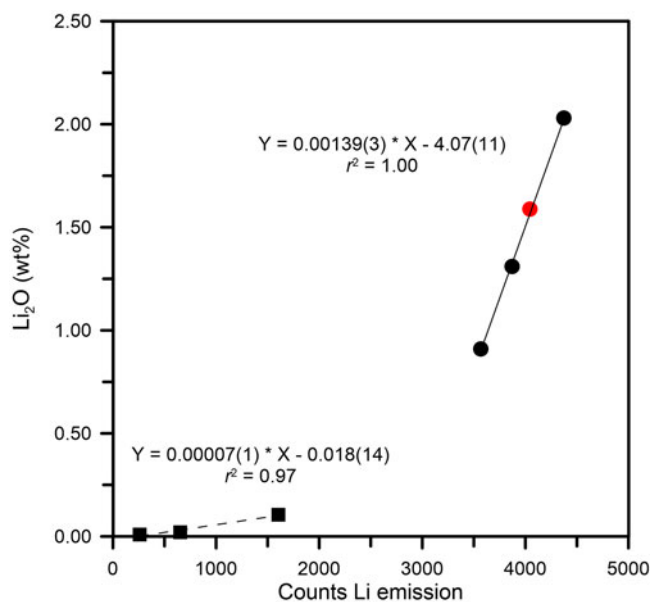


**Fig. 3.** Calibration of the Li emission line at 670.7 nm. The calibration resulted in two branches (one below and the other above 0.1 Li<sub>2</sub>O wt.%) described by two regression lines. Black squares represent samples from NIST standard glasses (SRM 610 and 612) and Filip *et al.* (2012), black circles are from Bosi *et al.* (2005, 2019d) and Grew *et al.* (2018); and a red filled circle represents the present sample.

low variability of counts, verified by measurements on uniform matrix materials such as that of NIST glass samples, allowed us to perform measurements on tourmaline samples which normally have chemical zoning. The calibration, obtained using spectra recorded on two NIST standard glasses (SRM 610 and 612) and four Li-bearing tourmalines from Bosi *et al.* (2005), Filip *et al.* (2012), Grew *et al.* (2018) and Bosi *et al.* (2019d), resulted in two calibration curves: one below and the other above 0.1 Li<sub>2</sub>O wt.% (Fig. 3). The latter was used for the present sample to obtain the Li quantification from the linear fit equation:  $\text{Li}_2\text{O} = 0.00139(3) \cdot I_{\text{Li}} - 4.07(11)$ . The result corresponds to 1.59(11) wt.% of Li<sub>2</sub>O (Table 4).

It can be noted that  $\mu$ -LIBS represents a very proficient localised analytical method, in particular if LIBS is mounted to a microscope to achieve a micrometric scale resolution. The intense emissivity of Li in optical emission spectroscopy makes the LIBS technique advantageous for Li quantification. Moreover, the potential of LIBS for Li analysis of geological materials at the micrometric scale has been validated in previous studies (Fabre *et al.*, 2002; Sweetapple and Tassios, 2015; McMillan *et al.*, 2018).

### Micro-Raman spectroscopy

Raman spectra of the Mn<sup>3+</sup>-bearing red tourmaline were obtained using a micro/macro Jobin Yvon Mod. LabRam HRVIS (University of Turin, Interdepartmental Centre “G. Scansetti”), equipped with a motorised x-y stage and an Olympus microscope. The back-scattered Raman signal was collected with a 50× objective and the Raman spectrum was obtained for a 90° (perpendicular to *c*) oriented crystal. The 632.8 nm line of an He–Ne laser was used as excitation; laser power (20 mW) was controlled by means of a series of density filters. The minimum lateral and depth resolution was set to a few  $\mu\text{m}$ . The system was calibrated using the 520.6 cm<sup>-1</sup> Raman band of silicon before each experimental session. The spectra were collected with a multiple and repeated

acquisition (5) with single counting times of 50 seconds to improve the signal-to-noise ratio. The incident excitation light was scrambled to eliminate orientation and polarisation effects. The spectrum was recorded from 100 to 4000 cm<sup>-1</sup> using the *LabSpec 5* software package (Horiba Jobin Yvon GmbH, 2004, 2005). Band-component analysis was undertaken using a Lorentzian function (*Fityk* software package; Wojdyr, 2010). The intensity of the vibrational modes was proven to be very dependent on the polarisability tensor. The Raman spectrum of the present sample in the spectral region of the framework and (OH)-stretching vibrations is shown in Fig. 4.

### Fourier-transform infrared (FTIR) spectroscopy

Polarised Fourier-transform infrared spectra were measured on two doubly polished single-crystal sections oriented by means of optical microscopy, and with thicknesses of 55 and 309  $\mu\text{m}$ . The spectrometer system consisted of a Bruker Vertex 70 spectrometer equipped with a halogen-lamp source and a CaF<sub>2</sub> beam-splitter coupled to a Hyperion 2000 microscope with a ZnSe wire-grid polariser and an InSb detector. Spectra were measured before and after heat-treatment experiments over the wavenumber range 2000–15,000 cm<sup>-1</sup> with a resolution of 2 or 8 cm<sup>-1</sup>. The measuring areas were masked by a 50–100  $\mu\text{m}$  rectangular aperture to avoid cracks and inclusions. The FTIR spectra of the untreated and treated samples (e.g. Fig. 5) show typical, strongly pleochroic absorption bands in the (OH)-stretching region (3300–3800 cm<sup>-1</sup>), including bands above  $\sim 3600$  cm<sup>-1</sup> that demonstrate the presence of <sup>W</sup>(OH) (see below).

### Optical absorption spectroscopy (OAS)

Polarised, room temperature optical absorption spectra in the range 30,000–12,500 cm<sup>-1</sup> (333–800 nm) were recorded at a spectral resolution of 1 nm on the same 309  $\mu\text{m}$  thick section studied by FTIR spectroscopy, using an AVASPEC-ULS2048 × 16 spectrometer attached via a 400  $\mu\text{m}$  ultraviolet (UV) optical fibre cable to a Zeiss Axiotron UV-microscope. A 75 W Xenon arc lamp was used as a light source, and Zeiss Ultrafluar 10× lenses served as objective and condenser. The diameter of the circular aperture was 50  $\mu\text{m}$  for the untreated sample and 30  $\mu\text{m}$  for the treated sample. A UV-quality Glan–Thompson prism with a working range from 40,000 to 3704 cm<sup>-1</sup> (250 to 2700 nm) was used as a polariser. The wavelength scale of the spectrometer was calibrated against Ho<sub>2</sub>O<sub>3</sub>-doped and Pr<sub>2</sub>O<sub>3</sub>/Nd<sub>2</sub>O<sub>3</sub>-doped standards (Hellma glass filters 666F1 and 666F7). Spectral data in the range 12,150–2000 cm<sup>-1</sup> (800–5000 nm) was taken from the FTIR measurements.

The optical absorption spectra of the untreated sample (Fig. 6) at energies below the UV-absorption edge show a set of broad absorption bands at 21,950, 19,800,  $\sim 18,000$ , 13,500 and  $\sim 9500$  cm<sup>-1</sup> (corresponding to 456, 505, 556, 741 and 1053 nm). In addition, a very weak and sharp absorption band occurs at 24,330 cm<sup>-1</sup> (418 nm), and a set of very sharp, overlapping bands are recorded in the NIR spectral range between 6700–7200 cm<sup>-1</sup> (1492–1389 nm). The absorption bands recorded in spectra of the untreated sample at 24,330, 21,950 and  $\sim 18,000$  cm<sup>-1</sup> are more intense for light polarised perpendicular to the crystallographic *c*-axis. Conversely, the absorption band 19800 cm<sup>-1</sup> is only observed as a broad shoulder in the E||*c*-spectrum. The set of sharp bands between 6700–7200 cm<sup>-1</sup> is also completely E||*c*-polarised.

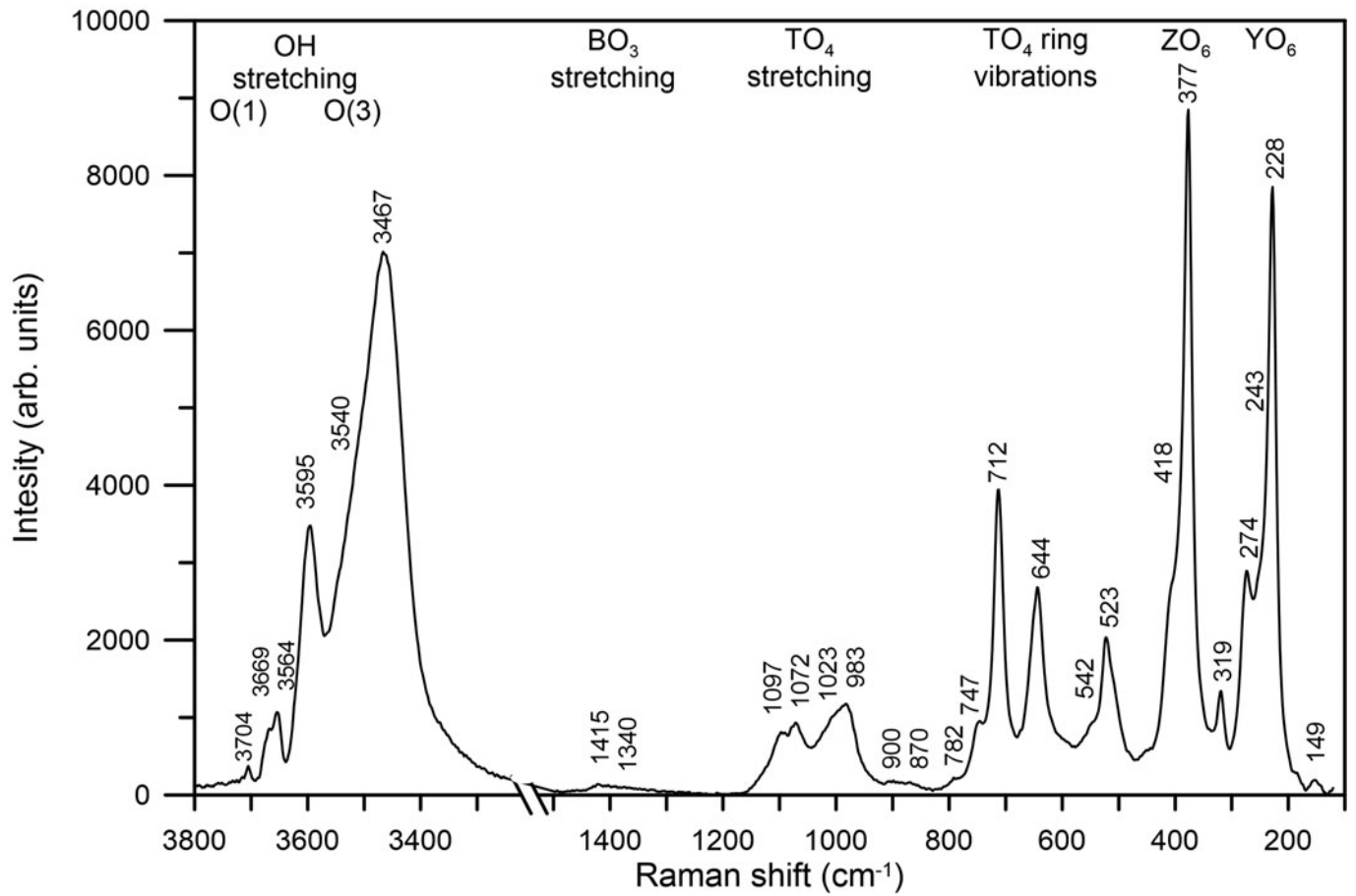


Fig. 4. Raman spectrum of the untreated Mn-bearing purplish-red tourmaline from Madagascar.

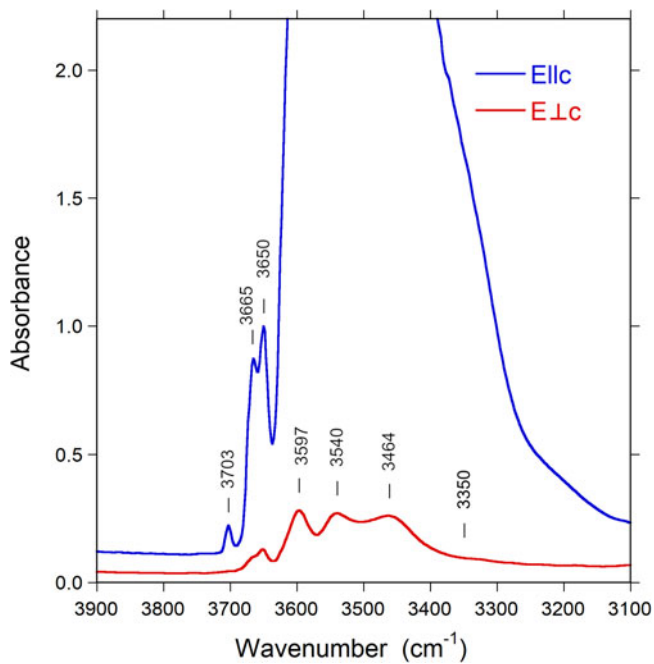


Fig. 5. Polarised FTIR spectra (E||c and E⊥c) of untreated Mn-bearing purplish-red tourmaline from Madagascar. Sample thickness 55 μm. Spectra are vertically off-set for clarity. Peak positions are indicated.

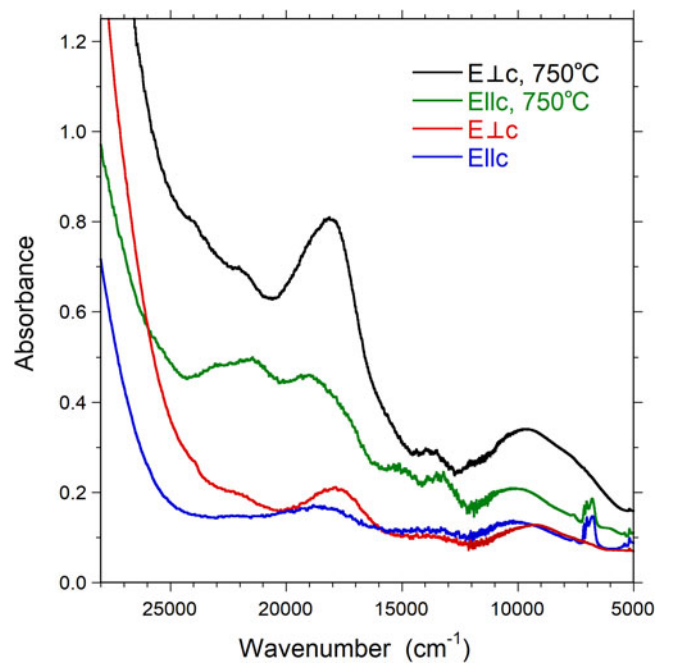


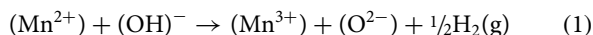
Fig. 6. Polarised OAS spectra (E||c and E⊥c) of untreated and treated Mn-bearing purplish-red tourmaline from Madagascar. Sample thickness 309 μm. Spectra are vertically off-set for clarity.

The absorption spectra recorded on the heat-treated sample (Fig. 6) display comparable features to those observed in the spectra of the natural sample. However, all absorption bands at 21,950, 19,800, ~18,000, 13,500 and ~9500 cm<sup>-1</sup> show pronounced intensity gains, and the set of sharp absorption bands between 6700–7200 cm<sup>-1</sup> distinctly decreases in intensity.

#### Determination of atomic fractions

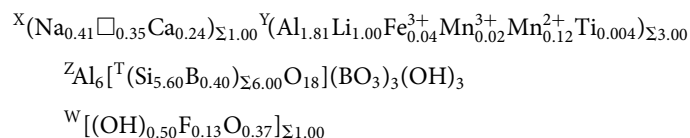
For the untreated sample, manganese oxidation state was determined by OAS (see below and Table 4). All Fe was considered to be Fe<sup>3+</sup> based on the OAS results and Mn and Fe redox potential arguments. Lithium was determined by  $\mu$ -LIBS. Regarding the B<sup>3+</sup>, the SREF data indicate that it fully occupies the B site, but relatively small amounts of B<sup>3+</sup> also occur at the T site:  $T$ -m.a.n. = 13.24(7) and  $\langle T-O \rangle = 1.613$  Å are in fact significantly smaller than the expected value for a T site fully occupied by Si ( ${}^T$ Si-m.a.n. = 14 and  $\langle {}^T$ Si-O  $\rangle = 1.619 \pm 0.001$  Å; Bosi and Lucchesi, 2007), reflecting the presence of cations lighter and smaller than Si, such as B<sup>3+</sup> (Ertl *et al.*, 2018). As a result, the B<sub>2</sub>O<sub>3</sub> and (OH) content were calculated by charge balance with the assumption (T + Y + Z + B) = 18.00 apfu and 31 anions.

For the heat-treated sample, all Mn was considered as Mn<sup>3+</sup> (i.e. Mn<sub>2</sub>O<sub>3</sub> = 1.21 wt.%), in conformity with the heat treatment conditions and the redox reaction:



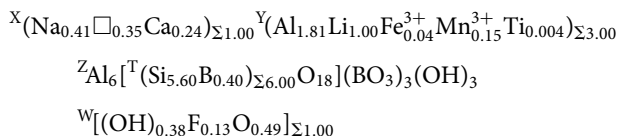
#### Determination of site population and mineral formula

The anion site populations in the samples studied follow the general preference suggested for tourmaline (e.g. Henry *et al.*, 2011): the O3 site (V position in the general formula) is occupied by (OH)<sup>-</sup>, while the O1 site (W position in the general formula) can be occupied by O<sup>2-</sup>, (OH)<sup>-</sup> and F<sup>-</sup>. The refined Z-site scattering and  $\langle Z-O \rangle$  values (13 and 1.906 Å, respectively) are the typical values observed for a Z site fully occupied by Al (Bosi and Andreozzi, 2013). The resulting empirical formula for the untreated sample is as follows:



The bond-valence analysis is consistent with the proposed site populations (Table 5). Moreover, the amount of 0.40 <sup>T</sup>B<sup>3+</sup> apfu is consistent with the relation of Hughes *et al.* (2004):  ${}^{[4]}B = [53.404 - 0.0346 \cdot V_{\text{cell}}] = 0.44$  apfu.

As for the treated sample, the following ordered formula is proposed:



## Discussion

### Tourmaline classification

The empirical formula of the untreated sample is consistent with a tourmaline belonging to the alkali-group, subgroup 2 (Henry *et al.*, 2011): it is Na-dominant (Na >  $\square$  > Ca) at the X position

**Table 5.** Weighted bond valences (valence units) for the purplish-red tourmaline from Madagascar.

Site	X	Y	Z	T	B	SUM
O1		0.42 <sup>x3</sup> →				1.25
O2	0.12 <sup>x3</sup> ↓	0.39 <sup>x2</sup> ↓→			1.02	1.91
O3		0.24	0.43 <sup>x2</sup> →			1.09
O4	0.06 <sup>x3</sup> ↓			0.99 <sup>x2</sup> →		2.04
O5	0.07 <sup>x3</sup> ↓			0.95 <sup>x2</sup> →		1.97
O6		0.40 <sup>x2</sup> ↓	0.55	1.01		1.96
O7			0.54	1.01		2.01
			0.46			
O8			0.51		0.98 <sup>x2</sup> ↓	2.03
			0.54			
SUM	0.73	2.24	3.02	3.96	2.98	
MAV <sup>a</sup>	0.90	2.29	3.00	3.93	3.00	

Note: Weighted bond valence according to Bosi (2014). Bond valence parameters from Brown and Altermatt (1985).

<sup>a</sup>Expected mean atomic valence (or formal charge) from the empirical formula.

of the general formula of tourmaline XY<sub>3</sub>Z<sub>6</sub>T<sub>6</sub>O<sub>18</sub>(BO<sub>3</sub>)<sub>3</sub>V<sub>3</sub>W and hydroxy-dominant at W with (OH+F) > O and (OH) >> F. Because Al and Si are the dominant cations at the Z and T sites (respectively), the end-member formula can be approximated as <sup>X</sup>(Na)(Y<sub>3</sub>)<sup>Σ6+</sup> <sup>Z</sup>(Al<sub>6</sub>)<sup>T</sup>(Si<sub>6</sub>O<sub>18</sub>)(BO<sub>3</sub>)<sub>3</sub><sup>V</sup>(OH)<sub>3</sub><sup>W</sup>(OH). For formula electroneutrality reasons, the valency-imposed double site-occupancy for the Y site is required with an atomic arrangement (Li<sub>1.5</sub>Al<sub>1.5</sub>)<sup>Σ6+</sup>. In accordance with the tourmaline nomenclature and the IMA-CNMNC rules (Henry *et al.*, 2011; Bosi *et al.*, 2019a,b), the present sample can be classified as Mn-bearing elbaite, Na(Li<sub>1.5</sub>Al<sub>1.5</sub>)Al<sub>6</sub>Si<sub>6</sub>O<sub>18</sub>(BO<sub>3</sub>)<sub>3</sub>(OH)<sub>3</sub>OH.

Note that, although the empirical site-total-charge at Y (= +6.986) is very close to +7, suggesting the arrangement <sup>Y</sup>(Al<sub>2</sub>Li)<sup>Σ7+</sup>, the latter must be ruled out because it would lead to a charge imbalanced end-member formula: [Na(Al<sub>2</sub>Li)Al<sub>6</sub>(Si<sub>6</sub>O<sub>18</sub>)(BO<sub>3</sub>)<sub>3</sub>(OH)<sub>3</sub>OH]<sup>Σ1+</sup>. Thus, only atomic arrangements consistent with (Y<sub>3</sub>)<sup>Σ6+</sup>, such as (Al<sub>1.5</sub>Li<sub>1.5</sub>)<sup>Σ6+</sup>, can occur (Bosi *et al.*, 2019a,b).

### Micro-Raman spectroscopy in the framework vibration region

In accordance with the studies of Mihailova *et al.* (1996), Reddy *et al.* (2007), McKeown (2008) and Watenphul *et al.* (2016b), five main ranges of framework vibrations can be identified in the Raman spectrum of the untreated sample (Fig. 4) and attributed to the following vibrating groups. (1) The range ~200–300 cm<sup>-1</sup> is dominated by YO<sub>6</sub> vibrations; in particular, the band at ~274 cm<sup>-1</sup> corresponds to the Mn–O bond, previously observed in a pink-tourmaline by Reddy *et al.* (2007). (2) The range ~300–400 cm<sup>-1</sup> (the strongest Raman peak) is generated by ZO<sub>6</sub> vibrations, in particular the sharp peak at 377 cm<sup>-1</sup> may be given by the <sup>Z</sup>Al–O bond. (3) The range ~500–750 cm<sup>-1</sup> is dominated by breathing modes of bridging oxygen atoms of TO<sub>4</sub> rings. (4) The range ~950–1100 cm<sup>-1</sup> is generated mainly from TO<sub>4</sub> stretching vibrations. (5) The range ~1300–1400 cm<sup>-1</sup> arises from B–O stretching vibrations.

With regard to the region of the (OH)-stretching vibrations (3300–3800 cm<sup>-1</sup>), the Raman scattering peaks of the untreated sample show wavenumbers similar to those of the infrared absorption bands (cf. Fig. 4 with Fig. 5); thus, the (OH)-stretching modes are discussed below.

### FTIR spectra in the (OH)-stretching region and band assignment

Infrared spectra of the untreated and treated samples recorded in polarised mode parallel to the *c*-axis direction display a very intense absorption feature in the 3400–3600  $\text{cm}^{-1}$  region, which is truncated due to excessive absorption (Fig. 5). This problem is commonly encountered in polarised transmission spectra of tourmaline single crystals, and it is normally not possible to thin samples sufficiently to get this main band ‘on scale’. Bands of lower intensity occur on both the low-energy (ca. 3340  $\text{cm}^{-1}$ ) and high-energy (3650, 3665 and 3703  $\text{cm}^{-1}$ ) sides of the major absorption band. Spectra polarised perpendicular to the *c*-axis direction ( $E_{\perp c}$ ) show a set of bands with substantially lower intensities (Fig. 5). The spectral range that is obscured by excessive absorption in the  $E_{\parallel c}$  direction displays here the presence of three bands at wavenumbers 3464, 3540 and 3597  $\text{cm}^{-1}$ , indicating (OH)-dipoles aligned close to, but with a small inclination to the *c*-axis (Gatta *et al.*, 2014).

After thermal treatment, a number of changes can be observed in the FTIR spectra: the sharp band at 3665  $\text{cm}^{-1}$  progressively decreases in intensity and almost disappears in the  $E_{\parallel c}$  direction (Fig. 7), whereas a new band appears at 3395  $\text{cm}^{-1}$ , visible in the  $E_{\perp c}$  direction (Fig. 8). The (OH) bands in the overtone region (Fig. 9) show a distinct decrease in absorption intensity, amounting to  $17 \pm 3\%$  as estimated from spectral fitting. However, a general decrease in absorption band intensity is not observed in the principal (OH)-region in spectra of the heat-treated samples polarised in the  $E_{\perp c}$  direction. Instead, we observe a weak increase in intensity, probably related to a decrease in polarisation efficiency due to microcracks and other crystal imperfections formed during heat treatment, leading to minor contributions from the extremely intense absorbance in the  $E_{\parallel c}$  direction.

In the tourmaline structure, the O1 site ( $\equiv W$ ) is surrounded by three Y cations, whereas the O3 site ( $\equiv V$ ) is surrounded by

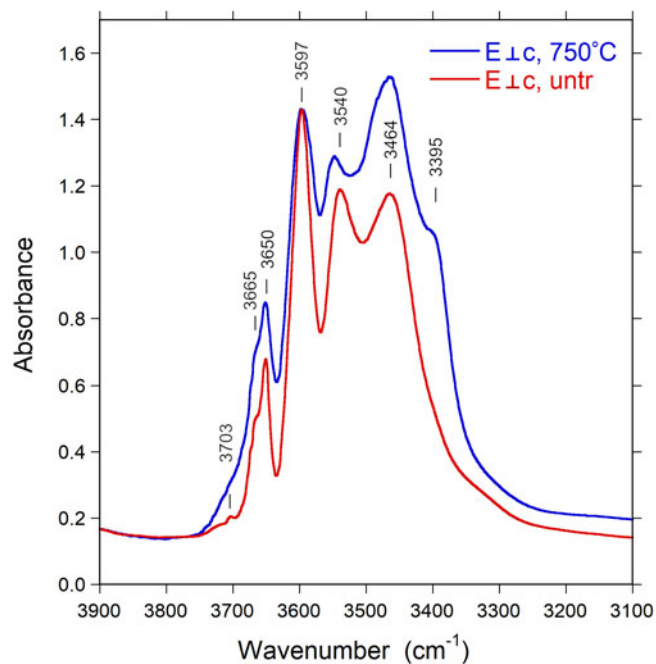


Fig. 8. Polarised FTIR spectra ( $E_{\perp c}$ ) of untreated Mn-bearing tourmaline. Sample thickness 309  $\mu\text{m}$ . Spectra are vertically off-set for clarity. Peak positions are indicated. Note new band appearing at 3395  $\text{cm}^{-1}$  after treatment.

one Y and two Z cations. In accord with Gatta *et al.* (2014), we assume that: the  $O^1(\text{OH})$  group forms a very weak hydrogen bond (bond strength  $< 0.05$  valence units, vu) with O4 and O5, whereas the  $O^3(\text{OH})$  group forms a weak hydrogen bond (bond strength  $\sim 0.11$  vu) with the closest O5 atom ( $\text{O}3\text{--H}3\cdots\text{O}5$ ); the strength of the hydrogen bond will cause a frequency shift of

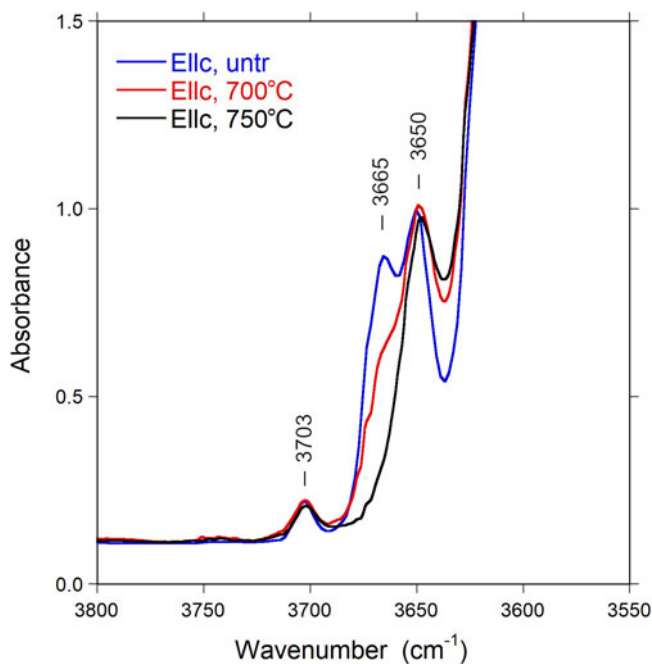


Fig. 7. Polarised FTIR spectra ( $E_{\parallel c}$ ) of untreated and heat-treated Mn-bearing tourmaline. Sample thickness 55  $\mu\text{m}$ . Spectra are vertically off-set for clarity. Peak positions are indicated.

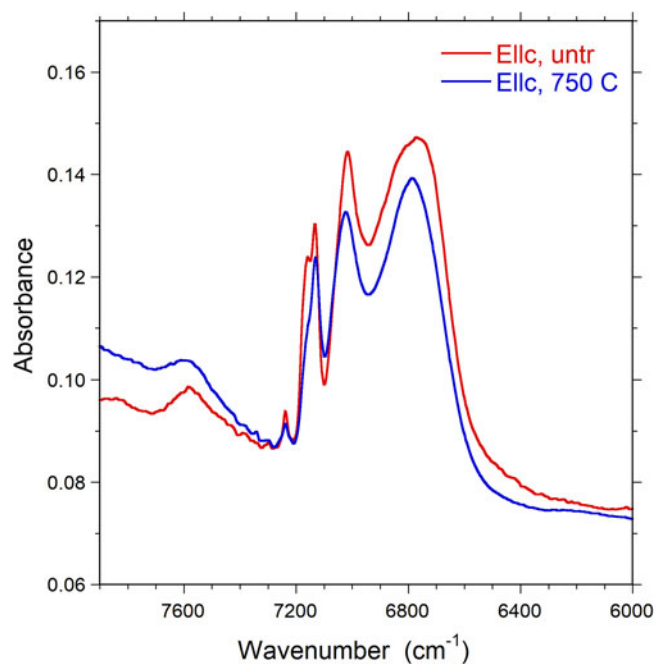


Fig. 9. Polarised FTIR/NIR spectra ( $E_{\parallel c}$ ) of untreated and heat-treated Mn-bearing tourmaline in the OH-overtone region. Sample thickness 309  $\mu\text{m}$ . Spectra are vertically adjusted for clarity.



the principal (OH)-stretching vibration (e.g. Libowitzky, 1999). Therefore, the relative weak vibrational bands above  $\sim 3600\text{ cm}^{-1}$  may be assigned to the O1 site, whereas the strong bands below  $\sim 3600\text{ cm}^{-1}$  may be assigned to the O3 site (e.g. Gonzalez-Carreño *et al.*, 1988; Bosi *et al.*, 2015). Based on the studies of Skogby *et al.* (2012), Bosi *et al.* (2012, 2016b), Watenphul *et al.* (2016a) and Kutzschbach *et al.* (2016) as well as on the observed site populations, the FTIR bands of the present purplish-red tourmaline may be related to the following atomic arrangements:

$\sim 3350\text{ cm}^{-1}$  is assigned to hydrogen bond  $\text{O}^3\text{O}-\text{H}3\cdots\text{O}5$ , which may reflect both the presence of  ${}^{\text{T}}\text{B}^{3+}$  and the X-site occupancy;  $\sim 3395\text{ cm}^{-1}$  is assigned to  $3[\text{Y}(\text{Mn}^{3+},\text{Al})^{\text{Z}}\text{Al}^{\text{Z}}\text{Al}]^{-\text{O}3}(\text{OH})_3$ ;  $\sim 3464, 3540$  and  $3597\text{ cm}^{-1}$  to  $3[\text{Y}(\text{Li},\text{Mn}^{2+},\text{Al})^{\text{Z}}\text{Al}^{\text{Z}}\text{Al}]^{-\text{O}3}(\text{OH})_3$ ;  $\sim 3650\text{ cm}^{-1}$  is assigned to  $\text{Y}(\text{LiAlAl})^{-\text{O}1}(\text{OH})^{-\text{X}}(\square)$ ;  $\sim 3665\text{ cm}^{-1}$  is assigned to  $\text{Y}(\text{LiMn}^{2+}\text{Al})^{-\text{O}1}(\text{OH})^{-\text{X}}(\square)$ ; and  $\sim 3703\text{ cm}^{-1}$  is assigned to  $\text{Y}(\text{LiAlAl})^{-\text{O}1}(\text{OH})^{-\text{X}}(\text{Na})$ .

The main difference between the FTIR spectra of the untreated and treated sample occurs in gradual decrease in the intensity of the band at  $3665\text{ cm}^{-1}$  and the appearance of the band at  $3395\text{ cm}^{-1}$  with the increase in temperature up to  $750^\circ\text{C}$ . As a result, these bands, in particular that at  $3665\text{ cm}^{-1}$ , may be correlated directly with the decreased  $\text{Mn}^{2+}$  and increased  $\text{Mn}^{3+}$  content, according to the redox reaction (1), reported in the section ‘Determination of atomic fractions’. However, it appears that (OH) is also lost by mechanisms other than the redox reaction. Only a partial loss of 0.12 (OH) apfu can be coupled to the oxidation of  $\text{Mn}^{2+}$ , whereas the total (OH) loss as estimated from the decrease of (OH) overtone intensities ( $17 \pm 3\%$ ) corresponds to ca. 0.6 (OH) apfu. The reason for this additional dehydration is unknown, but may be related to initial breakdown processes of the crystal structure.

Of particular interest is also the association of the  $\text{O}^1(\text{OH})$  stretching modes with the X-site constituents: the bands between

$\sim 3600\text{--}3700\text{ cm}^{-1}$  are considered associated with  $\text{X}_{\square}$ , whereas those above  $3700\text{ cm}^{-1}$  are considered associated with  $\text{XNa}^+$ . This distinction is related to the repulsive electrostatic interaction between the  $\text{X}^{n+}$  cation and  $\text{H}^+$  of the  $\text{O}^1(\text{OH})$  group, which reinforces the strength of the  $\text{O}^1\text{O}-\text{H}$  bond, shifting the (OH)-stretching mode towards higher wavenumbers (e.g. Gonzalez-Carreño *et al.*, 1988; Berryman *et al.*, 2016; Watenphul *et al.*, 2016a). Consequently, the presence of  $\text{XNa}^+$  determines an electrostatic repulsion with  ${}^{\text{H}1}\text{H}^+$  along the crystallographic c-axis, whereas the substitution  $\text{X}_{\square} \rightarrow \text{XNa}^+$  removes such a repulsion (Fig. 10). From the energetic-stability viewpoint, the rossmanite type arrangements  $(\text{YYY})^{-\text{O}1}(\text{OH})^{-\text{X}}(\square)$  should hence be more likely to occur than the elbaite type arrangement  $(\text{YYY})^{-\text{O}1}(\text{OH})^{-\text{X}}(\text{Na})$ . The  $\text{X}^{n+}-\text{H}^+$  repulsion effect will be stronger with the substitution  $\text{XCa}^{2+} \rightarrow \text{XNa}^+$ . On the other hand, this cation-cation repulsion can be removed by the chemical substitution  $\text{O}^1\text{F}^- \rightarrow \text{O}^1(\text{OH})^-$  or the deprotonation process  $\text{O}^1(\text{OH})^- + \frac{1}{4}\text{O}_2(\text{g}) \rightarrow \text{O}^1\text{O}^{2-} + \frac{1}{2}\text{H}_2\text{O}(\text{g})$ , both of which would favour the occurrence of fluor-liddicoatite and darrellhenryite type arrangements  $(\text{YYY})^{-\text{O}1}(\text{O},\text{F})^{-\text{X}}(\text{Na},\text{Ca})$ .

### Optical spectra

With the exception of the broad absorption band at  $\sim 9500\text{ cm}^{-1}$ , the characteristics (band energy, band width and polarisation) of all observed bands in the spectra of the present sample are in very good agreement with those recorded for  $\text{Mn}^{3+}$ -bearing tourmaline specimens (Reinitz and Rossman, 1988; Ertl *et al.*, 2005; Novák *et al.*, 2013; Bosi *et al.*, 2017a). In agreement with these previously published studies we assign bands at 21,950, 19,800,  $\sim 18,000$ ,  $13,500\text{ cm}^{-1}$  to electronic transitions in octahedrally coordinated  $\text{Mn}^{3+}$  and the very weak and sharp band at  $24,330\text{ cm}^{-1}$  to an electronic transition in octahedrally coordinated  $\text{Mn}^{2+}$ . The set of strongly E||c-polarised, sharp bands in the

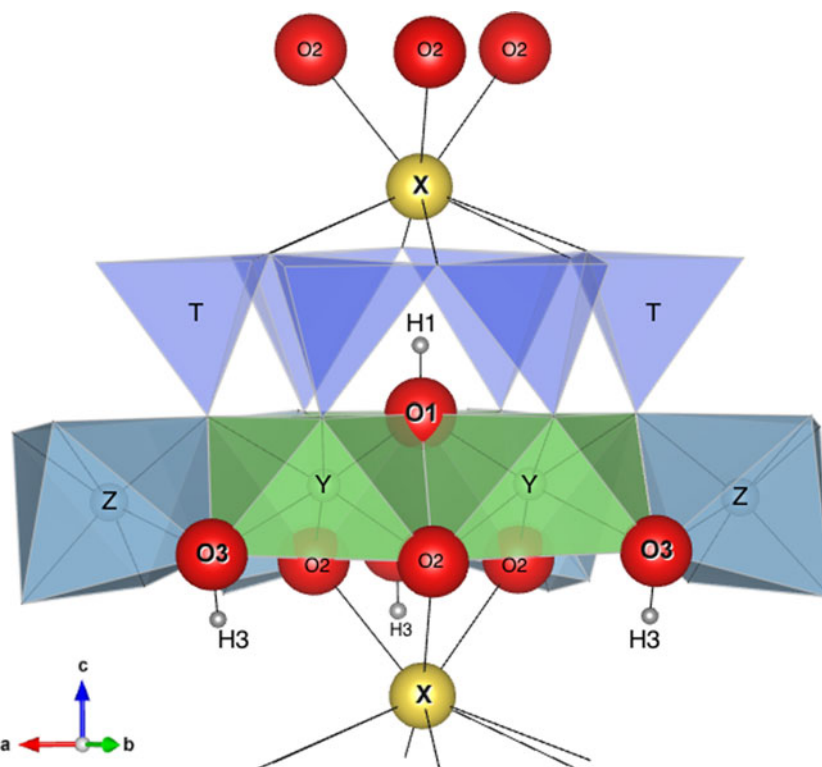


**Fig. 10.** Simplified structure of tourmaline showing the relative positions of H1, H3, O1, O3 and X with respect to Y, Z and the ring of tetrahedra  $\text{TO}_4$ . Of particular interest is the strong interaction between X and H1 (distance  $\approx 2.21\text{ \AA}$ ) and the very weak interaction between X and H3 (distance  $\approx 3.65\text{ \AA}$ ).

NIR region between 6700–7200  $\text{cm}^{-1}$  are due to overtones of the fundamental (OH)-stretching modes.

Based on the intensity of the  $\text{Mn}^{3+}$  band at  $\sim 18,000 \text{ cm}^{-1}$  in the spectrum perpendicular to the *c*-axes (Fig. 6) in combination with the published molar absorption coefficient for that absorption band (Reinitz and Rossman, 1988), we calculate an  $\text{Mn}_2\text{O}_3$  content of  $\sim 1 \text{ wt.}\%$ . However, the strong intensity increase by a factor of  $\sim 4\times$  for this band in spectra of our heat-treated sample, in combination with the analysed  $\text{MnO}_{\text{tot}}$  content, strongly suggests that the absorption coefficient for the band is somewhat higher than that indicated by Reinitz and Rossman (1988). Assuming that all  $\text{Mn}^{2+}$  was oxidised to  $\text{Mn}^{3+}$  during the heat treatment of our sample we determine an absorption coefficient of  $\sim 30 \text{ l mole}^{-1} \text{ cm}^{-1}$ , compared to the value of  $\sim 7.5$  suggested by Reinitz and Rossman (1988). Based on this revised absorption coefficient we calculate a  $\text{Mn}_2\text{O}_3$  content of  $\sim 0.2 \text{ wt.}\%$  for the untreated sample.

In view of the limited set of transition metals (Mn, Fe and Ti) in the present tourmaline, the number of potential origins for the broad absorption band recorded at  $\sim 9500 \text{ cm}^{-1}$  is very limited as well. The broadness of this band and its relatively high intensity exclude that it is caused by electron transitions in  $\text{Mn}^{2+}$  or  $\text{Fe}^{3+}$ , which all give rise to much weaker and also sharper spin-forbidden absorption bands. Furthermore, redox potential arguments exclude the presence of  $\text{Fe}^{2+}$  in a  $\text{Mn}^{3+}$ -bearing substance. Finally,  $\text{Ti}^{4+}$  is not a chromophore and  $\text{Ti}^{3+}$  is also excluded on the basis of redox potential considerations. Consequently, there remain only transitions in  $\text{Mn}^{3+}$  as a cause for the  $\sim 9500 \text{ cm}^{-1}$  band. This assignment is in agreement with observations of a broad  $\text{Mn}^{3+}$ -related absorption band at  $\sim 1040 \text{ nm}$  (corresponding to  $\sim 9615 \text{ cm}^{-1}$ ) in optical spectra of oxidised  $\text{Mn}^{2+}$ -rich elbaite (Ertl *et al.*, 2012). It is also in agreement with the observed increase in band intensity on heat treatment (oxidation) of the present sample. The relatively low energy of this band offers two main alternative assignment schemes. Firstly, low-energy bands caused by transitions in  $\text{Mn}^{3+}$  are frequently observed in spectra of substances, in which the cation is at the centre of octahedra that are characterised by one or two metal–ligand bonds deviating strongly from the remaining ones, either by being considerably shorter or longer (Burns, 1993). Secondly, transitions in tetrahedrally coordinated  $^{41}\text{Mn}^{3+}$  may also give rise to spectral bands of relatively low energy, as shown by a broad absorption band at  $10,800 \text{ cm}^{-1}$  in spectra of  $^{41}\text{Mn}^{3+}$ -doped spinel (Bosi *et al.*, 2007). The observed intensity increase for the  $\sim 9500 \text{ cm}^{-1}$  band in response to heat treatment, i.e. oxidation, represents a strong argument against this second suggestion, as this would require  $\text{Mn}^{2+}$  to be located initially at the tetrahedrally coordinated sites of tourmaline, which is highly unlikely (Bačík and Fridrichová, 2020). Furthermore, the SREF results provides no indications for  $^{41}\text{Mn}^{3+}$  and consequently we prefer the suggestion that the band is caused by a transition in  $\text{Mn}^{3+}$  cations at octahedrally coordinated sites, where the local electronic field around the cation is strongly distorted from the  $O_h$  symmetry.

## Conclusions

The comprehensive multi-analytical approach of the present study shows that the gem-quality purplish-red colour of the hand specimen of elbaite from the Anjanabonoina pegmatite (Madagascar) is caused by  $\text{Mn}^{3+}$ , which occurs as a minor element ( $\text{Mn}_2\text{O}_3 = 0.20 \text{ wt.}\%$ , corresponding to 0.02 apfu). The colour

intensity strongly increases with increasing  $\text{Mn}^{3+}$  concentrations ( $\text{Mn}_2\text{O}_3$  up to 1.21 wt.%, corresponding to 0.15 apfu).

Although the bulk chemical composition of the present sample corresponds to elbaite, based on the electrostatic  $\text{H}^+ - \text{Na}^+$  repulsion, the more intense FTIR bands related to O1 could be ascribed to the rossmanite-type arrangements  $(\text{YYY}) - \text{O}^1(\text{OH}) - \text{X}(\square)$  rather than elbaite-type ones  $(\text{YYY}) - \text{O}^1(\text{OH}) - \text{X}(\text{Na})$ .

Following this model of the electrostatic interaction between the X cation and W anions, the substitution  $\text{F}^- \rightarrow (\text{OH})^-$  as well as the removal of H from the  $^{\text{W}}(\text{OH})$  group would favour the occurrence of fluor-liddicoatite- and darrellhenryite-type clusters. On the other hand, the presence of H in the  $^{\text{W}}(\text{OH})$  group could explain the absence or rarity of tourmalines such as ‘liddicoatite’, ideally  $\text{Ca}(\text{Li}_2\text{Al})\text{Al}_6\text{Si}_6\text{O}_{18}(\text{BO}_3)_3(\text{OH})_3\text{OH}$ . The latter is still, in fact, a missing mineral species. Similar arguments might be applied to uvite,  $\text{CaMg}_3\text{Al}_6\text{Si}_6\text{O}_{18}(\text{BO}_3)_3(\text{OH})_3\text{OH}$  (Bosi *et al.*, 2020), but in this case we have to consider the increased total charge at the Y site of uvite (+6) compared to ‘liddicoatite’ (+5), which may accommodate composition with a strong  $\text{H}^+ - \text{Ca}^{2+}$  repulsive effect. In this regard, Ertl and Bačík (2020) described the correlations between the F content and the X-site charge, whereas Henry and Dutrow (2011) showed: (1) that interaction among the X, Y and O1 sites can accommodate unfavourable compositions; (2) the latter may also be influenced by the petrological environment, which may yield deviation from the limitations imposed by the tourmaline crystal chemistry. Bosi *et al.* (2017b) showed that direct correlation between F and Cr observed in Cr tourmalines from the Sludyanka complex, Lake Baikal, Russia, requires the occurrence of the local arrangements  $^{\text{Y}}(\text{CrCrCr}) - \text{O}^1(\text{F})$ , which should be unstable from a short-range bond-valence perspective (e.g. Bosi, 2013, 2018).

**Supplementary material.** To view supplementary material for this article, please visit <https://doi.org/10.1180/mgm.2021.20>

**Acknowledgements.** Chemical analyses were completed with the kind assistance of M. Serracino, to whom the authors express their gratitude. Funding by Sapienza University of Rome (Prog. Università 2018 to F. Bosi) is gratefully acknowledged. We thank F. Pezzotta for providing the photo of the sample analysed in this study. Comments and suggestions by the Associate Editor Ian T. Graham, A. Ertl and two anonymous reviewers were much appreciated.

## References

- Ahmadi S., Tahmasbi Z., Khalaji A.A. and Zal F. (2019) Chemical variations and origin of tourmalines in laleh zar granite of Kerman (Southeast Iran). *Periodico di Mineralogia*, **88**, 117–129.
- Andreozzi G.B., Bosi F., Celata B., Capizzi L.S., Stagno V. and Beckett-Brown C. (2020) Crystal-chemical behavior of  $\text{Fe}^{2+}$  in tourmaline dictated by structural stability: insights from a schorl with formula  $\text{Na}^{\text{Y}}(\text{Fe}_2^+\text{Al})^{\text{Z}}(\text{Al}_3\text{Fe}^{2+})(\text{Si}_6\text{O}_{18})(\text{BO}_3)_3(\text{OH})_3(\text{OH},\text{F})$  from Seagull batholith (Yukon Territory, Canada). *Physics and Chemistry of Minerals*, **47**, 25.
- Aurisicchio C., Demartin F., Ottolini L. and Pezzotta F. (1999) Homogeneous liddicoatite from Madagascar: a possible reference material? First EMPA, SIMS and SREF data. *European Journal of Mineralogy*, **11**, 237–242.
- Bačík P. and Fridrichová G. (2020) Cation partitioning among crystallographic sites based on bond-length constraints in tourmaline-supergroup minerals. *American Mineralogist*, <https://doi.org/10.2138/am-2021-7804>
- Berryman E.J., Wunder B., Ertl A., Koch-Müller M., Rhede D., Scheidl K., Giester G. and Heinrich W. (2016) Influence of the X-site composition on tourmaline’s crystal structure: Investigation of synthetic K-dravite, dravite, oxy-uvite, and magnesio-foitite using SREF and Raman spectroscopy. *Physics and Chemistry of Minerals*, **43**, 83–102.

- Bosi F. (2013) Bond-valence constraints around the O1 site of tourmaline. *Mineralogical Magazine*, **77**, 343–351.
- Bosi F. (2014) Bond valence at mixed occupancy sites. I. Regular polyhedra. *Acta Crystallographica*, **B70**, 864–870.
- Bosi F. (2018) Tourmaline crystal chemistry. *American Mineralogist*, **103**, 298–306.
- Bosi F. and Andreozzi G.B. (2013) A critical comment on Ertl et al. (2012): “Limitations of Fe<sup>2+</sup> and Mn<sup>2+</sup> site occupancy in tourmaline: Evidence from Fe<sup>2+</sup>- and Mn<sup>2+</sup>-rich tourmaline”. *American Mineralogist*, **98**, 2183–2192.
- Bosi F. and Lucchesi S. (2007) Crystal chemical relationships in the tourmaline group: structural constraints on chemical variability. *American Mineralogist*, **92**, 1054–1063.
- Bosi F. and Skogby H. (2013) Oxy-dravite, Na(Al<sub>2</sub>Mg)(Al<sub>5</sub>Mg)(Si<sub>6</sub>O<sub>18</sub>)(BO<sub>3</sub>)<sub>3</sub>(OH)<sub>3</sub>O, a new mineral species of the tourmaline supergroup. *American Mineralogist*, **98**, 1442–1448.
- Bosi F., Agrosi G., Lucchesi S., Melchiorre G. and Scandale E. (2005) Mn-tourmaline from island of Elba (Italy). Crystal chemistry. *American Mineralogist*, **90**, 1661–1668.
- Bosi F., Hälenius U., Andreozzi G.B., Skogby H. and Lucchesi S. (2007) Structural refinement and crystal chemistry of Mn-doped spinel: a case for tetrahedrally coordinated Mn<sup>3+</sup> in an oxygen-based structure. *American Mineralogist*, **92**, 27–33.
- Bosi F., Skogby H., Agrosi G. and Scandale E. (2012) Tsilaisite, NaMn<sub>3</sub>Al<sub>6</sub>(Si<sub>6</sub>O<sub>18</sub>)(BO<sub>3</sub>)<sub>3</sub>(OH)<sub>3</sub>OH, a new mineral species of the tourmaline supergroup from Grotta d’Oggi, San Pietro in Campo, island of Elba, Italy. *American Mineralogist*, **97**, 989–994.
- Bosi F., Andreozzi G.B., Skogby H., Lussier A.J., Abdu Y. and Hawthorne F.C. (2013) Fluor-elbaite, Na(Li<sub>1.5</sub>Al<sub>1.5</sub>)Al<sub>6</sub>(Si<sub>6</sub>O<sub>18</sub>)(BO<sub>3</sub>)<sub>3</sub>(OH)<sub>3</sub>F, a new mineral species of the tourmaline supergroup. *American Mineralogist*, **98**, 297–303.
- Bosi F., Skogby H., Lazor P. and Reznitskii L. (2015) Atomic arrangements around the O3 site in Al- and Cr-rich oxy-tourmalines: a combined EMP, SREF, FTIR and Raman study. *Physics and Chemistry of Minerals*, **42**, 441–453.
- Bosi F., Skogby H. and Hälenius U. (2016a) Thermally induced cation redistribution in Fe-bearing oxy-dravite and potential geothermometric implications. *Contributions to Mineralogy and Petrology*, **171**, 47.
- Bosi F., Skogby H. and Balić-Zunić T. (2016b) Thermal stability of extended clusters in dravite: a combined EMP, SREF and FTIR study. *Physics and Chemistry of Minerals*, **43**, 395–407.
- Bosi F., Cámara F., Ciriotti M.E., Hälenius U., Reznitskii L. and Stagno V. (2017a) Crystal-chemical relations and classification problems of tourmalines belonging to the oxy-schorl–oxy-dravite–bosiite–povondraite series. *European Journal of Mineralogy*, **29**, 445–455.
- Bosi F., Reznitskii L., Hälenius U. and Skogby H. (2017b) Crystal chemistry of Al–V–Cr oxy-tourmalines from Sludyanka complex, Lake Baikal, Russia. *European Journal of Mineralogy*, **29**, 457–472.
- Bosi F., Naitza S., Skogby H., Secchi F., Conte A.M., Cuccuru S., Hälenius U., De La Rosa N., Kristiansson P., Charlotta Nilsson E.J., Ros L. and Andreozzi G.B. (2018) Late magmatic controls on the origin of schorlitic and foititic tourmalines from late-Variscan peraluminous granites of the Arbus pluton (SW Sardinia, Italy): Crystal-chemical study and petrological constraints. *Lithos*, **308–309**, 395–411.
- Bosi F., Biagioni C. and Oberti R. (2019a) On the chemical identification and classification of minerals. *Minerals*, **9**, 591.
- Bosi F., Hatert F., Hälenius U., Pasero M., Miyawaki R. and Mills S.J. (2019b) On the application of the IMA–CNMNC dominant-valency rule to complex mineral compositions. *Mineralogical Magazine*, **83**, 627–632.
- Bosi F., Naitza S., Secchi F., Conte A.M., Cuccuru S., Andreozzi G.B., Skogby H. and Hälenius U. (2019c) Petrogenetic controls on the origin of tourmalinite veins from Mandrolisai igneous massif (Central Sardinia, Italy): Insights from tourmaline crystal chemistry. *Lithos*, **342–343**, 333–344.
- Bosi F., Skogby H. and Hälenius U. (2019d) Thermally induced cation redistribution in fluor-elbaite and Fe-bearing tourmalines. *Physics and Chemistry of Minerals*, **46**, 371–383.
- Bosi F., Biagioni C., Pezzotta F., Skogby H., Hälenius U., Cempírek J., Hawthorne F.C., Lussier A.J., Abdu Y.A., Day M.C., Fayek M., Clark C.M., Grice J.D. and Henry D.J. (2020) Uvite, IMA 2019-113. CNMNC Newsletter No. 54, April 2020, page 362. *Mineralogical Magazine*, **84**, 359–365.
- Brown I.D. and Altermatt D. (1985) Bond-valence parameters obtained from a systematic analysis of the Inorganic Crystal Structure Database. *Acta Crystallographica*, **B41**, 244–247.
- Burns R.G. (1993) *Mineralogical Applications of Crystal Field Theory*. 2nd ed., 576 p. Cambridge University Press, Cambridge, U.K.
- Cempírek J., Houzar S., Novák M., Groat L.A., Selway J.B. and Šrein V. (2013) Crystal structure and compositional evolution of vanadium-rich oxy-dravite from graphite quartzite at Bitoványky, Czech Republic. *Journal of Geosciences*, **58**, 149–162.
- De Vito C., Aurisicchio C., Ferrini V. and Pezzotta F. (2002a) Nb-Ta oxides from Anjanabonoina pegmatite. *International Mineralogical Association 18<sup>th</sup> General Meeting (Edinburgh)*, Program Abstract, 275.
- De Vito C., Aurisicchio C., Ferrini V. and Pezzotta F. (2002b) Chemical composition and B, O and H isotopes of tourmaline from Anjanabonoina pegmatite. *International Mineralogical Association, 18<sup>th</sup> General Meeting (Edinburgh)*, Program Abstract, 208.
- Dirlam D.M., Laurus B.M., Pezzotta F. and Simmons W.B. (2002) Liddicoatite tourmaline from Anjanabonoina, Madagascar. *Gems & Gemology*, **38**, 28–53.
- Dunn P.J., Appleman D.E. and Nelen J.E. (1977) Liddicoatite, a new calcium end-member of the tourmaline group. *American Mineralogist*, **62**, 1121–1124.
- Dutrow B.L. and Henry D.J. (2018) Tourmaline compositions and textures: reflections of the fluid phase. *Journal of Geosciences*, **63**, 99–110.
- Ertl A. and Bacik P. (2020) Considerations about Bi and Pb in the crystal structure of Cu-bearing tourmaline. *Minerals*, **10**, 706.
- Ertl A., Hughes J.M., Pertlik F., Foit F.F. Jr., Wright S.E., Brandstatter F. and Marler B. (2002) Polyhedron distortions in tourmaline. *The Canadian Mineralogist*, **40**, 153–162.
- Ertl A., Rossman G.R., Hughes J.M., Prowatke S. and Ludwig T. (2005) Mn-bearing “oxy-rossmanite” with tetrahedrally coordinated Al and B from Austria: Structure, chemistry and infrared and optical spectroscopic study. *American Mineralogist*, **90**, 481–487.
- Ertl A., Hughes J.M., Prowatke S., Ludwig T., Prasad P.S.R., Brandstatter F., Körner W., Schuster R., Pertlik F. and Marschall H. (2006) Tetrahedrally coordinated boron in tourmalines from the liddicoatite-elbaite series from Madagascar: Structure, chemistry, and infrared spectroscopic studies. *American Mineralogist*, **91**, 1847–1856.
- Ertl A., Kolitsch U., Dyar D., Hughes J.M., Rossman G.R., Pieczka A., Henry D.J., Pezzotta F., Prowatke S., Lengauer C.L., Körner W., Brandstatter F., Francis C. A., Prem M. and Tillmanns E. (2012) Limitations of Fe<sup>2+</sup> and Mn<sup>2+</sup> site occupancy in tourmaline: Evidence from Fe<sup>2+</sup> and Mn<sup>2+</sup>-rich tourmaline. *American Mineralogist*, **97**, 1402–1416.
- Ertl A., Henry D.J. and Tillmanns E. (2018) Tetrahedral substitutions in tourmaline: a review. *European Journal of Mineralogy*, **30**, 465–470.
- Fabre C., Boiron M.C., Dubessy J., Chabiron A., Charoy B. and Crespo T.M. (2002) Advances in lithium analysis in solids by means of laser-induced breakdown spectroscopy: An exploratory study. *Geochimica et Cosmochimica Acta*, **66**, 1401–1407.
- Fernandez A., Huber S., Schreurs G., Villa I. and Rakotondrazafy M. (2001) Tectonic evolution of the Itremo region (central Madagascar) and implications for Gondwana assembly. *Gondwana Research*, **4**, 165–168.
- Filip J., Bosi F., Novák M., Skogby H., Tuček J., Čuda J. and Wildner M. (2012) Redox processes of iron in the tourmaline structure: example of the high-temperature treatment of Fe<sup>3+</sup>-rich schorl. *Geochimica et Cosmochimica Acta*, **86**, 239–256.
- Foit F.F. Jr. (1989) Crystal chemistry of alkali-deficient schorl and tourmaline structural relationships. *American Mineralogist*, **74**, 422–431.
- Gatta G.D., Bosi F., McIntyre G.J. and Skogby H. (2014) First accurate location of two proton sites in tourmaline: A single-crystal neutron diffraction study of oxy-dravite. *Mineralogical Magazine*, **78**, 681–692.
- Gonzalez-Carreño T., Fernandez M. and Sanz J. (1988) Infrared and electron microprobe analysis in tourmalines. *Physics and Chemistry of Minerals*, **15**, 452–460.
- Grew E.S., Krivovichev S.V., Hazen R.M. and Hystad G. (2016) Evolution of structural complexity in boron minerals. *The Canadian Mineralogist*, **54**, 125–143.

- Grew E.S., Bosi F., Gunter M., Hälenius U., Trumbull R.B. and Yates M.G. (2018) Fluor-elbaite, lepidolite and Ta-Nb oxides from a pegmatite of the 3000 MA Sinceni pluton, Swaziland: Evidence for lithium-cesium-tantalum (LCT) pegmatites in the Mesoarchean. *European Journal of Mineralogy*, **30**, 205–218.
- Grice J.D. and Ercit T.S. (1993) Ordering of Fe and Mg in the tourmaline crystal structure: the correct formula. *Neues Jahrbuch für Mineralogie, Abhandlungen*, **165**, 245–266.
- Henry D.J. and Dutrow B.L. (1996) Metamorphic tourmaline and its petrologic applications. Pp. 503–557 in: *Boron: Mineralogy, Petrology and Geochemistry* (E.S. Grew and L.M. Anvitz, editors). Reviews in Mineralogy and Geochemistry, vol. 33. Mineralogical Society of America, Chantilly, Virginia, USA.
- Henry D.J. and Dutrow B.L. (2011) The incorporation of fluorine in tourmaline: Internal crystallographic controls or external environmental influences? *The Canadian Mineralogist*, **49**, 41–56.
- Henry D.J. and Dutrow B.L. (2018) Tourmaline studies through time: contributions to scientific advancements. *Journal of Geosciences*, **63**, 77–98.
- Henry D.J., Novák M., Hawthorne F.C., Ertl A., Dutrow B., Uher P. and Pezzotta F. (2011) Nomenclature of the tourmaline-supergroup minerals. *American Mineralogist*, **96**, 895–913.
- Horiba Jobin Yvon GmbH (2004, 2005) *LabSpec software for Raman spectroscopic data analysis, acquisition and manipulation*. Version 5.64.15. HORIBA Jobin Yvon SAS, Villeneuve d'Ascq, France.
- Hughes J.M., Ertl A., Dyar M.D., Grew E.S., Wiedenbeck M. and Brandstätter F. (2004) Structural and chemical response to varying  $^{14}\text{B}$  content in zoned Fe-bearing olenite from Koralpe, Austria. *American Mineralogist*, **89**, 447–454.
- Kutzschbach M., Wunder B., Rhede D., Koch-Müller M., Ertl A., Giester G., Heinrich W. and Franz G. (2016) Tetrahedral boron in natural and synthetic HP/UHP tourmaline: evidence from Raman spectroscopy, EMPA, and single-crystal XRD. *American Mineralogist*, **101**, 93–104.
- Libowitzky E. (1999) Correlation of O-H stretching frequencies and O-H...O hydrogen bond lengths in minerals. *Monatshefte für Chemie*, **130**, 1047–1059.
- Lussier A.J. and Hawthorne F. (2011) Oscillatory zoned liddicoatite from Anjanabonoina, central Madagascar. II. Compositional variation and mechanism of substitution. *The Canadian Mineralogist*, **49**, 89–103.
- Lussier A.J., Abdu Y., Hawthorne F.C., Michaelis V.K., Aguiar P.M. and Kroeker S. (2011) Oscillatory zoned liddicoatite from Anjanabonoina, central Madagascar. I. Crystal chemistry and structure by SREF and  $^{11}\text{B}$  and  $^{27}\text{Al}$  MAS NMR spectroscopy. *The Canadian Mineralogist*, **49**, 63–88.
- McKeown D.A. (2008) Raman spectroscopy, vibrational analysis, and heating of buergerite tourmaline. *Physics and Chemistry of Minerals*, **35**, 259–270.
- McMillan N.J., McManus C.E., Harmon R.S., De Lucia Jr., F.C. and Miziolek A.W. (2006) Laser induced breakdown spectroscopy analysis of complex silicate minerals – beryl. *Analytical and Bioanalytical Chemistry*, **385**, 263–27.
- McMillan N.J., Curry J., Dutrow B.L. and Henry D.J. (2018) Identification of the host lithology of tourmaline using laser-induced breakdown spectroscopy for application in sediment provenance and mineral exploration. *The Canadian Mineralogist*, **56**, 393–410.
- Mihailova B., Gasharova B. and Konstantinov L. (1996) Influence on non-tetrahedral cations in Si–O vibrations in complex silicates. *Journal of Raman Spectroscopy*, **27**, 829–833.
- Novák M., Povondra P. and Selway J.B. (2004) Schorl-oxy-schorl to dravite-oxydravite tourmaline from granitic pegmatites; examples from the Moldanubicum, Czech Republic. *European Journal of Mineralogy*, **16**, 323–333.
- Novák M., Škoda P., Filip J., Macek I. and Vaculovič T. (2011) Compositional trends in tourmaline from intragranitic NYF pegmatites of the Třebíč Pluton, Czech Republic; electron microprobe, Mössbauer and LA-ICP-MS study. *The Canadian Mineralogist*, **49**, 359–380.
- Novák M., Ertl A., Povondra P., Vašinová Galiová M., Rossman G.R., Pristacz H., Prem M., Giester G., Gadas P. and Škoda R. (2013) Darrellhenryite, Na(LiAl<sub>2</sub>)Al<sub>6</sub>(BO<sub>3</sub>)<sub>3</sub>Si<sub>6</sub>O<sub>18</sub>(OH)<sub>3</sub>O, a new mineral from the tourmaline supergroup. *American Mineralogist*, **98**, 1886–1892.
- Paquette J.L. and Nédélec A. (1998) A new insight into Pan-African tectonics in the East–West Gondwana collision zone by U–Pb zircon dating of granites from central Madagascar. *Earth and Planetary Science Letters*, **155**, 45–56.
- Pezzotta F. (1999) Madagascar – Das Paradies der Mineralien und Edelsteine. *Extra Lapis*, **17**, 56–59 [in German].
- Pezzotta F. and Franchi M. (1997) Miarolitic shallow depth pegmatites of the Betafo and Antsirabe areas, central Madagascar; genetic inferences. P. 71 in: *Proceedings of the UNESCO-IUGS-IGCP-348/368 International Field Workshop on Proterozoic Geology of Madagascar, Antananarivo, August 16–30* (R. Cox and L.D. Ashwal, editors). Gondwana Research Group Miscellaneous Publication No. 5.
- Pezzotta F. and Laurs B.M. (2011) Tourmaline: The kaleidoscopic gemstone. *Elements*, **7**, 331–336.
- Pouchou J.L. and Pichoir F. (1991) Quantitative analysis of homogeneous or stratified microvolumes applying the model “PAP”. Pp. 31–75 in: *Electron Probe Quantitation* (K.F.J. Heinrich and D.E. Newbury, editors). Plenum, New York.
- Reddy B.J., Frost R.L., Martens W.N., Wain D.L. and Klopogge J.T. (2007) Spectroscopic characterization of Mn-rich tourmalines. *Vibrational Spectroscopy*, **44**, 42–49.
- Reinitz I. and Rossman G.R. (1988) Role of natural radiation in tourmaline coloration. *American Mineralogist*, **73**, 822–825.
- Sheldrick G.M. (2015) Crystal structure refinement with SHELXL. *Acta Crystallographica*, **C71**, 3–8.
- Skogby H., Bosi F. and Lazor P. (2012) Short-range order in tourmaline: a vibrational spectroscopic approach to elbaite. *Physics and Chemistry of Minerals*, **39**, 811–816.
- Strunz H. (1979) Anjanabonoina, Fundort schönster Tourmaline. *Lapis*, **1**, 24–27, 47–48 [in German].
- Sweetapple M.T. and Tassios S. (2015) Laser-induced breakdown spectroscopy (LIBS) as a tool for in situ mapping and textural interpretation of lithium in pegmatite minerals. *American Mineralogist*, **100**, 2141–2151.
- Tempesta G. and Agrosi G. (2016) Standardless, minimally destructive chemical analysis of red beryls by means of laser induced breakdown spectroscopy. *European Journal of Mineralogy*, **28**, 571–580.
- Tempesta G., Bosi F. and Agrosi G. (2020) Crystal chemical characterisation of red beryl by ‘standardless’ laser-induced breakdown spectroscopy and single-crystal refinement by X-ray diffraction: an example of validation of an innovative method for the chemical analysis of minerals. *Geostandards and Geoanalytical Research*, **44**, 685–693.
- van Hinsberg V.J., Henry D.J. and Dutrow B.L. (2011a) Tourmaline as a petrologic forensic mineral: a unique recorder of its geologic past. *Elements*, **7**, 327–332.
- van Hinsberg V.J., Henry D.J. and Marschall H.R. (2011b) Tourmaline: an ideal indicator of its host environment. *The Canadian Mineralogist*, **49**, 1–16.
- Webber K.L., Simmons W.B. and Falster A.U. (2002) Tourmaline from the Antandromby and Fianarantsoa Pegmatites, Madagascar. *Mineralogical Record*, **33**, 82.
- Watenphul A., Burgdorf M., Schlüter J., Horn I., Malcherek T. and Mihailova B. (2016a) Exploring the potential of Raman spectroscopy for crystallochemical analyses of complex hydrous silicates: II. Tourmalines. *American Mineralogist*, **101**, 970–985.
- Watenphul A., Schlüter J., Bosi F., Skogby H., Malcherek T. and Mihailova B. (2016b) Influence of the octahedral cationic-site occupancies on the framework vibrations of Li-free tourmalines, with implications for estimating temperature and oxygen fugacity in host rocks, *American Mineralogist*, **101**, 2554–2563.
- Wojdyr M. (2010) Fityk: a general-purpose peak fitting program. *Journal of Applied Crystallography*, **43**, 1126–1128.



### 2.1.3 Oxy-dravite–maruyamaite series

#### **Crystal chemistry of the oxy–dravite-maruyamaite series from the Kokchetav Massif (Kazakistan)**

Beatrice Celata<sup>1</sup>, Ferdinando Bosi<sup>1</sup>, Kira A. Musyachenko<sup>2</sup>, Andrey Korsakov<sup>2</sup> and Giovanni B. Andreozzi<sup>1</sup>

<sup>1</sup>Department of Earth Sciences, Sapienza University of Rome, Piazzale Aldo Moro 5, I-00185 Rome, Italy;

<sup>2</sup>Sobolev Institute of Geology and Mineralogy, Siberian Branch of the RAS, Novosibirsk, Russian Federation

#### **Abstract**

Nine crystals of natural K-bearing oxy-dravite to maruyamaite extracted from a quartzofeldspathic gneiss from the ultra-high pressure (UHP) region of Kokchetav Massif (Kazakistan) were fully characterized with a multi-analytical approach. The whole oxy-dravite-maruyamaite series was investigated through Scanning Electron Microscope (SEM), Electron MicroProbe Analysis (EMPA) and single crystal X-Rays diffraction (SC-XRD), to better understand the impact of K content on tourmaline structure.

In the studied samples, the Na-K substitution at the X site is part of a more general substitution, expressed as:  $^x\text{K}+^y\text{Al}+^w\text{O} = ^x\text{Na}+^y\text{Mg}+^w(\text{OH},\text{F})$ , which leads from maruyamaite to oxy-dravite. From the discrepancy ( $\delta$ , in valence units *vu*) between bond valence sum (BVS) and formal mean charge at the X site, it is shown that with a K content increase, X sees a compression of its bonds (overbonded cation) where low contents of K lead to a stretching of the bonds (underbonded cation) of X polyhedron.

**Keywords:** k-rich tourmaline, ultra-high-pressure minerals, maruyamaite, crystal-structure refinement, electron microprobe, single-crystal X-Rays Diffraction

#### **Introduction**

The element potassium (K) is an incompatible element that strongly partitions into melts and fluids released during partial melting and devolatilization of mantle peridotites and subducted crustal material (e.g. Schmidt, 1996; Thomsen and Schmidt, 2008).

Along subduction zones, among the potential water-B-K getters and carriers [e.g. sanidine, phlogopite, K-bearing amphiboles (see Harlow and Davies, 2004)], tourmaline has always been underestimated thus only being nominally confined to shallower geological settings. In contrast to what is commonly believed, tourmaline's stability field is way larger than expected, as tourmaline actually crystallizes in a variety of geological settings, representing the most important boron rock-forming mineral from the surface of the crust to the upper Mantle (e.g., Marschall et al. 2009; Lussier et al. 2016).

From a crystal-chemical viewpoint, tourmalines are a supergroup of complex cyclosilicates-borates, listed among the earliest minerals that made their first appearance on Earth (Grew et al. 2016). In the last few decades, tourmaline structure and chemistry has been extensively investigated, as it was very clearly exposed and overviewed by Bosi (2018). Its flexible structure is one of the most accommodating in terms of different elements that can be hosted, leading to an unmatched wide stability over very different pressure and temperature conditions (Dutrow and Henry, 2011; van Hinsberg et al. 2011). This peculiar feature is revealed by its general formula:  $XYZ_3T_6O_{18}(BO_3)_3V_3W_3$ , where, commonly,  $X = Na^+, K^+, Ca^{2+}, \square$  (= vacancy);  $Y = Al^{3+}, Cr^{3+}, V^{3+}, Fe^{2+/3+}, Mg^{2+}, Mn^{2+}, Li^+, Ti^{4+}$ ;  $Z = Al^{3+}, Cr^{3+}, V^{3+}, Fe^{2+/3+}, Mg^{2+}$ ;  $T = Si^{4+}, Al^{3+}, B^{3+}$ ;  $B = B^{3+}$ ;  $V = (OH)^-, O^{2-}$ ;  $W = (OH)^-, F^-, O^{2-}$ . When not italicized, letters represent groups of cations at the  $^{[9]}X$ ,  $^{[6]}Y$ ,  $^{[6]}Z$ ,  $^{[4]}T$ , and  $^{[3]}B$  crystallographic sites (letters italicized). When groups of anions are located at the

$^{[3]}O3$  and  $^{[3]}O1$  sites, letters V and W are respectively used. Hydrogen atoms occupy the H3 and H1 sites, which are related to O3 and O1, respectively. On the basis of X site dominant occupancy, tourmalines can be primarily classified as vacant, alkali and calcic (Henry et al. 2011). Among alkali tourmalines, K-dominant tourmalines are so far originated only from one unique location on Earth: Kokchetav Massif, Northern Kazakhstan, and are officially named as *maruyamaite*  $[K(MgAl_2)(Al_5Mg)Si_6O_{18}(BO_3)_3(OH)_3O]$ . About maruyamaite, in addition to its compositional peculiarity that reveals a true singularity in the chemistry of the formation environment, the *P-T* conditions that occurred at the moment of its crystallization were also estimated. Those conditions were framed into an UHP environment because micro-diamond inclusions were found into maruyamaite and K-oxy-dravite crystals from quartzo-feldspathic gneisses of the Kundy-Kol area of the Kokchetav Massif (Lussier et al. 2016). Thus, high pressure was apparently claimed to be the reason for K accommodation at the X site (Shimizu and Ogasawara, 2005; 2013; Ota et al., 2008). Anyway, the genesis of maruyamaite in UHP environment is still under debate, since, as reported in

Berryman et al. (2014) and formerly postulated by Marschall et al. (2009), the absence of Na as a competitor for  $X$  site occupancy during tourmaline formation could have led to the otherwise disfavoured K incorporation. Moreover, a new occurrence of maruyamaite in the Barchi-Kol site (Musiyachenko et al., 2021) allowed to claim for a high K activity in the forming environment over UHP conditions, based on petrological observations and thermodynamic calculations, showing a similarity with experimental studies on K-bearing clinopyroxene, where it was observed that K oversaturation over pressure runs the game (Safonov et al., 2011). In addition, tourmaline developed in other UHP terrains typically do not exhibit comparable K contents, and generally contains  $<0.05$  apfu K (cf. Ertl et al. 2010).

Apart from K-dominant tourmalines formation, their breakdown conditions - and thus, water, B, and K release - could be indeed influenced by K occupancy at the  $X$  site, since experimental work by Likhacheva et al. (2019) performed on maruyamaite (K-dominant tourmaline), showed a stabilizing function of K at  $P > 15$  GPa and an overall structural resistance up to 20 GPa, even if the role of temperature has not been investigated so far. So, K-bearing tourmalines could transport K down to upper Mantle conditions, where also nominally anhydrous phases can host it to deeper parts of the Mantle, as documented by findings of high  $K_2O$  contents in clinopyroxene in diamondiferous ecogites and inclusion in diamonds from South African and Yakutian kimberlites (Erlank and Kushiro, 1970; Sobolev, 1977; Prinz et al., 1975; Bishop et al., 1978). For nominally anhydrous phases an important role of pressure for K to be accommodated into the crystal structure was observed, specifically  $P > 20$  GPa for garnet (e.g. Wang and Takahashi, 1999). Therefore, maruyamaite's structural characterization and stability at different  $P$  and  $T$  is crucial to understand how tourmaline allows K to accommodate and how the structure adapts to that unusual composition. In this study, 9 samples of natural K-bearing oxy-dravite to maruyamaite from the UHP region of Kokchetav Massif (Kazakhstan) were characterized through SEM, EMPA and single crystal X-Rays diffraction, analyzing the whole oxy-dravite-maruyamaite series to better understand the impact of K content on tourmaline structure.

## **Methods**

### **Starting material**

Tourmaline crystals were mechanically extracted from the host rock (a quartzofeldspathic gneiss from the Kundy-Kol area, collected by Andrey Korsakov's research team) by a stainless steel clamp and selected under the microscope. More than 400 fragments of oxy-dravite were isolated and embedded

in epoxy to obtain 4 samples containing roughly 100 fragments disposed in rows (Figure 1), each one characterized by a size of 100 to 500 microns. Through Scanning Electron Microscopy (SEM) the presence of a possible zonation was checked with EDS spectra and a preliminary location of the portions with homogeneous K content was therefore defined for each fragment. With the Electron MicroProbe (EMP) the portions with a homogeneous K content were mapped out through single spot quantitative analysis performed in WDS mode. Some of the homogeneous portions with an increasing content of K were mechanically extracted with a gold sewing needle from each fragment of interest and mounted on glass fibers in order to perform Single Crystal X-Rays Diffraction (SCXRD) and compare the obtained structural data to the EMPA.

## **SEM**

The scanning electron microscopy was performed on each sample with a Carl Zeiss SEM EVO® 50 available at the Department of Earth Sciences (Sapienza University of Rome), equipped with a W filament target and SE Everhart-Thornley detector plus a QBS detector, coupled with an EDS for qualitative elemental analysis. The resolution at 30 kV was 3.0 nm and the acceleration voltage range was 0.2 to 30 kV with a magnification power going from 5 to 1000000x.

## **EMP**

Electron microprobe analysis for the tourmaline sample was obtained using a wavelength-dispersive spectrometer (WDS mode) with a Cameca SX50 instrument at the “Istituto di Geologia Ambientale e Geoingegneria (Rome, Italy), CNR”, operating at an accelerating potential of 15 kV, with a 15 nA current and a 10 µm beam diameter. Minerals and synthetic compounds were used as standards: wollastonite (Si, Ca), magnetite (Fe), rutile (Ti), corundum (Al), vanadinite (V), fluorophlogopite (F), periclase (Mg), jadeite (Na), orthoclase (K), sphalerite (Zn), rhodonite (Mn), metallic Cr, Ni and Cu. The PAP correction procedure for quantitative electron probe microanalysis was applied (Pouchou and Pichoir 1991). Results are reported in Table 2. Vanadium, Cr, Ni and Cu were below their respective detection limits (0.03 wt%) in the studied sample.

## **SC-XRD**

Nine crystal fragments with composition ranging from K-bearing oxy-dravite to maruyamaite from Kokchetav Massif (Kazakistan) were selected for X-ray diffraction measurements on a Bruker

KAPPA APEX-II single-crystal diffractometer (Sapienza University of Rome, Earth Sciences Department), equipped with a charge-coupled device (CCD) area detector (6.2 cm  $\times$  6.2 cm active detection area, 512  $\times$  512 pixels) and a graphite-crystal monochromator using MoK $\alpha$  radiation from a fine-focus sealed X-ray tube. The sample-to-detector distance was 4 cm. A total of 3577 exposures (step = 0.2°, time/step = 20 s) covering a full reciprocal sphere with a redundancy of  $\sim$ 12 was collected. Final unit-cell parameters were refined using the Bruker AXS SAINT program on reflections with  $I > 10 \sigma(I)$  in the range  $6^\circ < 2\theta < 75^\circ$ . The intensity data were processed and corrected for Lorentz, polarisation and background effects using the APEX2 software program of Bruker AXS. The data were corrected for absorption using a multi-scan method (SADABS, Bruker AXS). The absorption correction led to an improvement in Rint. No violation of R3m symmetry was detected. Structure refinement was done using the SHELXL-2013 program (Sheldrick, 2015). Starting coordinates were taken from Lussier et al. (2016). Variable parameters were scale factor, extinction coefficient, atom coordinates, site-scattering values (for X, Y and Z sites) and atomic-displacement factors. Attempts to refine the extinction coefficient yielded values within its standard uncertainty, thus it was not refined. Neutral scattering factors were used for the cations and oxygen atoms. As for the atomic model refinement and in accordance with the chemical analysis results (see below), the X site was modelled by setting the vacancy content to a variable content of atoms per formula unit (apfu), and allowing the remainder of the site to refine as  $\text{Ca} = (0.65 - \text{Na})$ . The Y site was refined by fixing the (Mn+Fe) occupancy to 1 apfu. The T site was constrained by an occupancy of Si equals to 1 apfu. The Z, B and anion sites were modelled with Al, B and O scattering factors, respectively, and with a fixed occupancy of 1 as refinement with unconstrained occupancies showed no significant deviations from this value. A final refinement was then performed by modelling the site occupancy of the O1 site with O and F fixed to the value obtained from the empirical formula (see below). Similar chemical constraints were applied to refine the H1 and H3 sites. There were no correlations greater than 0.7 between the parameters at the end of the refinement. Table 1 lists crystal data, data-collection information and refinement details.

Site populations were determined by a minimization procedure which simultaneously takes into account both structural and chemical data (Bosi and Lucchesi 2004). Iron oxidation ratio was assigned after MS data reported in Lussier et al. (2016).

Any deficiency of B at B site was excluded because the mean bond distance  $\langle B-O \rangle$  of all samples corresponds to the typically observed bond distance for B in planar triangular coordination in inorganic structures (Hawthorne et al., 1996).

## Results and Discussion

Chemical composition obtained by EMPA is reported in Table 2. All the studied crystals belong to the maruyamaite-oxy-dravite series as displayed in Figure 2. Specifically, they can be classified as Fe<sup>2+</sup>-rich maruyamaite (samples 24c2a and 2c2b), and Fe<sup>2+</sup>- and F-rich oxy-dravite (the remaining samples), as reported in Table 3. Calculated and observed mean atomic numbers for the nine tourmaline samples at the different structural sites are listed in Table 4.

In all samples the *T* site can be considered as practically fully occupied by Si as shown by the limited variation of the mean bond distances <T–O> ranging from 1.618 to 1.620 Å, which correspond to the ideal distance <Si–O> = 1.619(1) Å (e.g., Bosi and Lucchesi, 2007). The *Z* site shows a quite constant site population, where the Al:Mg ratio is about 5:1, as shown by the very limited variation of <Z–O> (see Table 5), ranging from 1.929 to 1.933 Å. The largest chemical variation is observed at the *Y* site, which is dominated by Mg ranging from 1.28 to 1.51 apfu, Al ranging from 1.10 to 1.27 apfu, Fe<sup>2+</sup> ranging from 0.29 apfu to 0.33 apfu, and with Ti up to 0.25 apfu. Consistently, the <Y–O> is negatively correlated to Al (Fig. 3a). Notably, the linear fit equals to 1.906 Å when <sup>Y</sup>Al is 3 apfu, in line with the ionic radii of Bosi and Lucchesi (2007).

The *X* site is dominated by the homovalent substitution of K (ranging from 0.03 to 0.47 apfu) for Na (0.33 to 0.56 apfu). The incorporation of K at the *X* site enlarges the <X–O> from 2.665 to 2.687 Å, through a linear fit (Fig. 3b). The datum from Berryman et al (2014) falls out this trend, maybe because their sample presents vacancies at *X* site (0.3 apfu) that may enlarge the site itself. Moreover, their sample has been synthesized at 4 GPa.

The increase in K content linearly increases the *c*-parameter from 7.197 to 7.223 Å, as reported in Figure 3c; no correlation between K content and the *a*-parameter was found.

The unit cell volume increases from 1.582 to 1.586 Å<sup>3</sup> with the K content (Figure 3d).

In the studied samples, the Na-K substitution at the *X* site is part of a more general substitution, expressed as: <sup>X</sup>K + <sup>Y</sup>Al + <sup>W</sup>O = <sup>X</sup>Na + <sup>Y</sup>Mg + <sup>W</sup>(OH,F), which leads from maruyamaite to oxy-dravite (Figure 4). Our samples are also rich in Ca, which is positively correlated to Na (*R*<sup>2</sup> = 0.62) and inversely correlated to K (*R*<sup>2</sup> = 0.93), representing the minor uvite component of the samples. Fluorine is incorporated in the studied samples with an inverse correlation with <sup>W</sup>O<sup>2-</sup> (*R*<sup>2</sup> = 0.80), through the overall substitution 2<sup>X</sup>K + 2<sup>Y</sup>Al + <sup>W</sup>O = <sup>X</sup>(Na+Ca) + 2<sup>Y</sup>Mg + <sup>W</sup>(OH,F).

In accordance with Shimizu and Ogasawara (2013), our samples show a clear zonation from a K-rich core to a Na (and Ca) rich rim, coherently with the retrograde metamorphism experienced by their host rock. Consequently, K was accommodated in tourmaline's structure at high pressure conditions, becoming less stable at lower pressure and getting replaced by Na (and Ca). However, it is worth noting that K-dominant tourmaline with povondraite composition also occurs in sedimentary rocks (sample 35899 of Grice et al., 1993). The possibility for K to be accommodated in povondraite's

(sample 35899 of Grice et al., 1993). The possibility for K to be accommodated in povondraite's structure at low pressure is favoured by the larger 3D-framework made of  ${}^Z\text{Fe}^{3+}\text{O}_6$  polyhedra (Hovis et al., 2022) with respect to the other members of tourmaline supergroup which are usually built over a network of  ${}^Z\text{AlO}_6$  polyhedra (exception made for chromdravite).

The X site shows distortion indices ranging from  $9.8 \cdot 10^4$  (for the sample with 0.47 apfu of K) to  $2.14 \cdot 10^3$  (for the sample with 0.03 apfu of K), which were calculated with the following formula  $\Delta_X = \frac{1}{9} \sum_1^9 [(d_i - d_m/d_m)^2]$  edited from the bond-length distortion indices formulae of Ertl et al. (2002) and listed in Table 7. From the discrepancy ( $\delta$ , in valence units *vu*) between bond valence sum (BVS) and formal mean charge at the X site, listed in Table 7, it is shown that with a K content increase, X is in compression (overbonding) where low contents of K lead to an extension (underbonding) of X (Figure 5).

## References

- Berryman E, Wunder B, Rhede D (2014) Synthesis of K-dominant tourmaline. *American Mineralogist* 99(2–3):539–542.
- Bishop FC, Smith JV, Dawson JB (1978) Na, K, P and Ti in garnet, pyroxene and olivine from peridotite and eclogite xenoliths from African kimberlites. *Lithos* 11(2):155–173.
- Bosi F, Lucchesi S (2004) Crystal chemistry of the schorl-dravite series. *European Journal of Mineralogy* 16(2): 335–344.
- Bosi F, Lucchesi S (2007) Crystal chemical relationships in the tourmaline group: Structural constraints on chemical variability. *American Mineralogist* 92(7):1054–1063.
- Bosi F (2018) Tourmaline crystal chemistry. *American Mineralogist* 103(2):298–306
- Dutrow BL, Henry DJ (2011) Tourmaline; a geologic DVD. *Elements* 7(5):301–306.
- Erlank AJ, Kushiro I (1970) Potassium contents of synthetic pyroxenes at high temperatures and pressures. *Carnegie Inst. Wash yearbook* 68:439–442.
- Ertl A, Hughes JM, Pertlik F, Foit FF Jr, Wright SE, Brandstätter F, Marler B (2002) Polyhedron distortions in tourmaline. *The Canadian Mineralogist* 40: 153–163.
- Ertl A, Marschall HR, Giester G, Henry DJ, Schertl HP, Ntaflos T, Luvizzotto GL, Nasdala L, Tillmanns E (2010) Metamorphic ultrahigh-pressure tourmaline: Structure, chemistry, and correlations to *P-T* conditions. *American Mineralogist* 95(1):1–10.
- Grew ES, Krivovichev SV, Hazen RM, Hystad G (2016) Evolution of structural complexity in boron minerals. *The Canadian Mineralogist* 54(1):125–143.

- Grice JD, Ercit TS, Hawthorne FC (1993) Povondraite, a redefinition of the tourmaline ferridravite. *American Mineralogist* 78(3–4):433–436.
- Harlow GE, Davies R (2004) Status report on stability of K-rich phases at mantle conditions. *Lithos* 77(1–4):647–653.
- Hawthorne FC (1996) Structural mechanisms for light-element variations in tourmaline. *The Canadian Mineralogist* 34(1):123–132.
- Henry DJ, Novák M, Hawthorne FC, Ertl A, Dutrow BL, Uher P, Pezzotta F (2011) Nomenclature of the tourmaline-supergroup minerals. *American Mineralogist* 96(5–6):895–913.
- Hovis GL, Tribaudino M, Altomare C, Bosi F (2022) Thermal expansion of minerals in the tourmaline supergroup. *American Mineralogist* (in press).
- Likhacheva AY, Rashchenko SV, Musiyachenko KA, Korsakov AV, Collings IE, Hanfland M (2019) Compressibility and structure behaviour of maruyamaite (K-tourmaline) from the Kokchetav massif at high pressure up to 20 GPa. *Mineralogy and Petrology* 113:613–623.
- Lussier A, Ball NA, Hawthorne FC, Henry DJ, Shimizu R, Ogasawara Y, Ota T (2016) Maruyamaite,  $K(MgAl_2)(Al_5Mg)Si_6O_{18}(BO_3)_3(OH)_3O$ , a potassium-dominant tourmaline from the ultrahigh-pressure Kokchetav massif, northern Kazakhstan: Description and crystal structure. *American Mineralogist* 101(2):355–361.
- Marschall HR, Korsakov AV, Luvizotto GL, Nasdala L, Ludwig T (2009) On the occurrence and boron isotopic composition of tourmaline in (ultra)high-pressure metamorphic rocks. *Journal of the Geological Society* 166:811–823.
- Musiyachenko KA, Korsakov AV, Letnikov FA (2021) A New Occurrence of Maruyamaite. *Doklady Earth Sciences* 498:403–408.
- Ota T, Kobayashi K, Katsura T, Nakamura E (2008) Boron cycling by subducted lithosphere; insights from diamondiferous tourmaline from the Kokchetav ultrahigh-pressure metamorphic belt. *Geochimica et Cosmochimica Acta* 72(14): 3531–3541.
- Prinz M, Mansoni DV, Hlava PF, Keil K (1975) Inclusions in diamonds: garnet lherzolite and eclogite assemblages. *Physics and Chemistry of the Earth*, 797:815.
- Pouchou JL, Pichoir F (1991) Quantitative analysis of homogeneous or stratified microvolumes applying the model "PAP". In: Heinrich KFJ, Newbury DE (eds) *Electron probe quantitation*. Plenum, New York, 31–75.
- Safonov OG, Bindi L, Vinograd VL (2011) Potassium-bearing clinopyroxene: a review of experimental, crystal chemical and thermodynamic data with petrological applications. *Mineralogical Magazine* 75(4):2467–2484.



- Shimizu R, Ogasawara Y (2005) Discovery of "K-tourmaline" in Diamond-Bearing Tourmaline-K-Feldspar-Quartz Rock From the Kokchetav Massif, Kazakhstan. American Geophysical Union, Fall Meeting 2005, abstract id. V43A-1561.
- Shimizu R, Ogasawara Y (2013) Diversity of potassium-bearing tourmalines in diamondiferous Kokchetav UHP metamorphic rocks: A geochemical recorder from peak to retrograde metamorphic stages. *Journal of Asian Earth Sciences* 63:39–55.
- Schmidt MW (1996) Experimental Constraints on Recycling of Potassium from Subducted Oceanic Crust. *Science* 272(5270):1927–1930.
- Sheldrick GM (2015) Crystal structure refinement with SHELXL. *Acta Crystallographica Section C* 71(1):3–8.
- Sobolev, NV (1977) Deep-seated inclusions in kimberlites and the problem of the composition of the upper mantle. Washington, D.C., American Geophysical Union, 279 p.
- Thomsen TB, Schmidt MW (2008) Melting of carbonated pelites at 2.5–5.0 GPa, silicate–carbonatite liquid immiscibility, and potassium–carbon metasomatism of the mantle. *Earth and Planetary Science Letters* 267(1–2):17–31.
- van Hinsberg VJ, Henry DJ, Marschall HR (2011) Tourmaline: an ideal indicator of its host environment. *The Canadian Mineralogist* 49(1):1–16.
- Wang W, Takahashi E (1999) Subsolidus and melting experiments of a K-rich basaltic composition to 27 GPa: Implication for the behavior of potassium in the mantle. *American Mineralogist* 84:357–361.

**Table 1** Single-crystal X-ray diffraction data collected at room temperature.

Sample	MRY24C2a	MRY2C2b	MRY14b	MRY25b	MRY32a	MRY111a	MRY92a	MRY92b	MRY92c
crystal size (mm)	0.16 x 0.20 x 0.20	0.24 x 0.21 x 0.07	0.12 x 0.10 x 0.02	0.28 x 0.28 x 0.20	0.16 x 0.12 x 0.09	0.20 x 0.14 x 0.12	0.16 x 0.14 x 0.08	0.24 x 0.21 x 0.16	0.16 x 0.12 x 0.04
<i>a</i> (Å)	15.92628(19)	15.9246(2)	15.9284(2)	15.92900(14)	15.93109(19)	15.92922(18)	15.9211(3)	15.9273(3)	15.9218(2)
<i>c</i> (Å)	7.22263(10)	7.21910(10)	7.20010(10)	7.20700(10)	7.19726(9)	7.19972(10)	7.2149(2)	7.20670(10)	7.21340(10)
<i>V</i> (Å <sup>3</sup> )	1586.55(4)	1585.44(5)	1582.02(5)	1583.66(4)	1581.93(4)	1582.10(4)	1583.82(7)	1583.26(6)	1583.63(5)
Data collection range, <i>2θ</i> (°)	6-75	6-75	6-73	6-73	6-73	6-73	6-73	6-73	5-73
Reciprocal space range <i>hkl</i>	-27 ≤ <i>h</i> ≤ 26 -24 ≤ <i>k</i> ≤ 27 -12 ≤ <i>l</i> ≤ 11	-26 ≤ <i>h</i> ≤ 26 -26 ≤ <i>k</i> ≤ 27 -12 ≤ <i>l</i> ≤ 11	-25 ≤ <i>h</i> ≤ 26 -26 ≤ <i>k</i> ≤ 26 -8 ≤ <i>l</i> ≤ 11	-26 ≤ <i>h</i> ≤ 26 -26 ≤ <i>k</i> ≤ 26 -10 ≤ <i>l</i> ≤ 11	-26 ≤ <i>h</i> ≤ 26 -26 ≤ <i>k</i> ≤ 26 -12 ≤ <i>l</i> ≤ 12	-26 ≤ <i>h</i> ≤ 26 -26 ≤ <i>k</i> ≤ 26 -11 ≤ <i>l</i> ≤ 10	-26 ≤ <i>h</i> ≤ 26 -26 ≤ <i>k</i> ≤ 26 -10 ≤ <i>l</i> ≤ 8	-26 ≤ <i>h</i> ≤ 26 -26 ≤ <i>k</i> ≤ 22 -11 ≤ <i>l</i> ≤ 11	-26 ≤ <i>h</i> ≤ 26 -26 ≤ <i>k</i> ≤ 22 -10 ≤ <i>l</i> ≤ 10
Number reflections	11867	11927	11781	11682	11710	11731	11795	11676	11846
Unique reflections, <i>R<sub>int</sub></i> (%)	1770, 1.19	1902, 1.81	1698, 2.91	1679, 1.37	1850, 1.86	1813, 1.83	1636, 1.96	1804, 3.42	1718, 2.57
Redundancy	12	12	12	12	12	12	12	12	12
Extinction coefficient	0.00070(17)	0.00114(17)	0.00047(17)	0.00055(17)	0.00049(16)	0.00056(17)	0.00056(17)	0.0009(2)	0.00038(18)
Flack parameter	0.09(3)	0.10(4)	0.07(5)	0.08(4)	0.10(4)	0.10(4)	0.08(4)	0.07(4)	0.08(4)
<i>wR</i> <sup>2</sup> (%)	3.21	3.26	3.79	3.27	3.35	3.33	3.33	3.62	3.60
<i>R</i> <sub>1</sub> (%) all data	1.27	1.35	1.83	1.25	1.39	1.31	1.35	1.43	1.71
<i>R</i> <sub>1</sub> (%) for <i>I</i> > 2σ( <i>I</i> )	1.26	1.30	1.68	1.24	1.36	1.29	1.32	1.43	1.59
GooF	1.090	1.099	1.051	1.088	1.083	1.109	1.080	1.074	1.050

**Table 2** Chemical composition of the 9 crystal fragments studied.

Sample	MRY24C2a	MRY2C2b	MRY14b	MRY25b	MRY32a	MRY111a	MRY92a	MRY92b	MRY92c
	avg of 5 spots	avg of 3 spots	avg of 3 spots	avg of 10 spots	avg of 3 spots	avg of 6 spots	avg of 11 spots	avg of 9 spots	avg of 5 spots
SiO <sub>2</sub> (wt.%)	36.12(0.29)	36.22(0.15)	36.49(0.38)	35.99(0.26)	36.97(0.21)	36.43(0.27)	35.91(0.24)	35.77(0.41)	36.16(0.49)
TiO <sub>2</sub>	1.03(0.04)	1.05(0.05)	0.67(0.14)	0.66(0.10)	0.63(0.06)	0.61(0.05)	0.70(0.06)	0.70(0.07)	0.66(0.08)
B <sub>2</sub> O <sub>3</sub>	10.46 <sup>c</sup>	10.49 <sup>c</sup>	10.57 <sup>c</sup>	10.51 <sup>c</sup>	10.71 <sup>c</sup>	10.55 <sup>c</sup>	10.45 <sup>c</sup>	10.46 <sup>c</sup>	10.52 <sup>c</sup>
Al <sub>2</sub> O <sub>3</sub>	31.96(0.25)	32.10(0.25)	32.13(0.59)	32.14(0.24)	32.05(0.10)	31.44(0.19)	31.96(0.33)	32.24(0.35)	32.02(0.44)
Cr <sub>2</sub> O <sub>3</sub>	0.03(0.03)	0.04(0.04)	0.04(0.03)	0.00	0.07(0.01)	0.07(0.02)	0.00	0.04(0.02)	0.00
V <sub>2</sub> O <sub>3</sub>	0.08(0.02)	0.06(0.01)	0.05(0.03)	0.04(0.02)	0.05(0.01)	0.04(0.02)	0.05(0.02)	0.04(0.02)	0.04(0.02)
FeO <sub>tot</sub>	2.82(0.18)	2.98(0.12)	2.84(0.46)	2.80(0.31)	2.45(0.13)	2.65(0.31)	2.92(0.13)	2.89(0.14)	2.80(0.29)
MgO	8.92(0.14)	8.80(0.09)	9.33(0.47)	9.32(0.46)	10.11(0.07)	9.95(0.27)	9.15(0.27)	9.07(0.09)	9.37(0.44)
CaO	1.12(0.05)	1.08(0.03)	1.64(0.23)	1.62(0.23)	1.99(0.08)	2.00(0.13)	1.48(0.20)	1.42(0.05)	1.61(0.29)
Na <sub>2</sub> O	1.02(0.06)	1.07(0.04)	1.74(0.07)	1.53(0.22)	1.66(0.15)	1.43(0.68)	1.31(0.20)	1.16(0.05)	1.40(0.22)
K <sub>2</sub> O	2.21(0.10)	2.12(0.05)	0.52(0.29)	0.88(0.53)	0.14(0.05)	0.30(0.07)	1.31(0.45)	1.65(0.07)	1.04(0.58)
F	0.16(0.07)	0.11(0.06)	0.33(0.18)	0.33(0.13)	0.57(0.07)	0.43(0.10)	0.40(0.13)	0.35(0.05)	0.34(0.05)
H <sub>2</sub> O	2.84	2.88	2.87	2.89	2.90	2.95	2.83	2.86	2.89
-O = F	-0.07	-0.05	-0.14	-0.14	-0.24	-0.18	-0.17	-0.15	-0.15
FeO	2.54	2.68	2.56	2.52	2.21	2.39	2.63	2.60	2.52
Fe <sub>2</sub> O <sub>3</sub>	0.31	0.33	0.32	0.31	0.27	0.29	0.32	0.32	0.31
Total	98.75	99.00	99.11	98.65	100.08	98.71	98.34	98.52	98.78
Atoms per formula unit									
(apfu) normalised to 31 anions									
Si(apfu)	6.000	6.000	6.000	5.955	6.000	6.000	5.970	5.942	5.977
Ti	0.128	0.131	0.083	0.082	0.076	0.076	0.088	0.087	0.082
B	3.000	3.000	3.000	3.000	3.000	3.000	3.000	3.000	3.000
Al	6.257	6.267	6.227	6.266	6.129	6.103	6.261	6.313	6.237
Cr	0.004	0.006	0.005	0.000	0.008	0.009	0.000	0.005	0.000
V	0.011	0.008	0.006	0.006	0.006	0.005	0.007	0.005	0.005

Fe3+	0.039	0.041	0.039	0.039	0.033	0.037	0.041	0.040	0.039
Fe2+	0.353	0.372	0.351	0.349	0.299	0.329	0.366	0.361	0.348
Mg	2.209	2.174	2.288	2.298	2.447	2.443	2.268	2.246	2.308
Ca	0.200	0.191	0.289	0.287	0.346	0.353	0.263	0.252	0.285
Na	0.330	0.344	0.556	0.491	0.521	0.458	0.422	0.375	0.449
K	0.469	0.449	0.108	0.186	0.029	0.063	0.278	0.350	0.220
F	0.084	0.060	0.170	0.170	0.290	0.224	0.210	0.182	0.180
OH	3.152	3.179	3.144	3.194	3.138	3.245	3.139	3.166	3.182

<sup>a</sup>Standard deviation is reported in brackets.

<sup>b</sup>avg = average

<sup>c</sup>Calculated by stoichiometry, (Y+Z+T+B) = 18.000 apfu.

<sup>d</sup>FeO/Fe<sub>2</sub>O<sub>3</sub> ratio is referred to the value measured in Lussier et al. (2016).

**Table 3** Crystal-chemical formula per each tourmaline crystal fragment and its classification.

Sample	Crystal-chemical formula
24c2a (maruyamaite)	$^X(\text{K}_{0.47}\text{Na}_{0.33}\text{Ca}_{0.20})_{\Sigma 1.00} \text{ } ^Y(\text{Mg}_{1.28}\text{Al}_{1.27}\text{Fe}^{2+}_{0.31}\text{Ti}_{0.13}\text{V}_{0.01})_{\Sigma 3.00} \text{ } ^Z(\text{Al}_{4.99}\text{Mg}_{0.93}\text{Fe}^{2+}_{0.04}\text{Fe}^{3+}_{0.04})_{\Sigma 6.00} \text{ } ^T\text{Si}_6\text{O}_{18}(\text{BO}_3)_3 \text{ } ^{\text{O}3}(\text{OH})_3 \text{ } ^{\text{O}1}[(\text{OH})_{0.15}\text{F}_{0.08}\text{O}_{0.77}]_{\Sigma 1.00}$
2c2b (maruyamaite)	$^X(\text{K}_{0.45}\text{Na}_{0.34}\text{Ca}_{0.19}\square_{0.02})_{\Sigma 1.00} \text{ } ^Y(\text{Mg}_{1.31}\text{Al}_{1.25}\text{Fe}^{2+}_{0.29}\text{Ti}_{0.25}\text{V}_{0.01}\text{Cr}_{0.01})_{\Sigma 3.00} \text{ } ^Z(\text{Al}_{5.01}\text{Mg}_{0.87}\text{Fe}^{2+}_{0.08}\text{Fe}^{3+}_{0.04})_{\Sigma 6.00} \text{ } ^T\text{Si}_6\text{O}_{18}(\text{BO}_3)_3 \text{ } ^{\text{O}3}(\text{OH})_3 \text{ } ^{\text{O}1}[(\text{OH})_{0.18}\text{F}_{0.06}\text{O}_{0.76}]_{\Sigma 1.00}$
14b (oxy-dravite)	$^X(\text{K}_{0.11}\text{Na}_{0.56}\text{Ca}_{0.29}\square_{0.05})_{\Sigma 1.00} \text{ } ^Y(\text{Mg}_{1.44}\text{Al}_{1.15}\text{Fe}^{2+}_{0.31}\text{Ti}_{0.08}\text{V}_{0.01}\text{Cr}_{0.01})_{\Sigma 3.00} \text{ } ^Z(\text{Al}_{5.07}\text{Mg}_{0.84}\text{Fe}^{2+}_{0.04}\text{Fe}^{3+}_{0.04})_{\Sigma 6.00} \text{ } ^T\text{Si}_6\text{O}_{18}(\text{BO}_3)_3 \text{ } ^{\text{O}3}(\text{OH})_3 \text{ } ^{\text{O}1}[(\text{OH})_{0.14}\text{F}_{0.17}\text{O}_{0.69}]_{\Sigma 1.00}$
25b (oxy-dravite)	$^X(\text{K}_{0.19}\text{Na}_{0.49}\text{Ca}_{0.29}\square_{0.04})_{\Sigma 1.00} \text{ } ^Y(\text{Mg}_{1.43}\text{Al}_{1.15}\text{Fe}^{2+}_{0.32}\text{Ti}_{0.08}\text{V}_{0.01})_{\Sigma 3.00} \text{ } ^Z(\text{Al}_{5.07}\text{Mg}_{0.86}\text{Fe}^{2+}_{0.03}\text{Fe}^{3+}_{0.04})_{\Sigma 6.00} \text{ } [^T(\text{Si}_{5.95}\text{Al}_{0.05})_{\Sigma 6.00} \text{ } \text{O}_{18}](\text{BO}_3)_3 \text{ } ^{\text{O}3}(\text{OH})_3 \text{ } ^{\text{O}1}[(\text{OH})_{0.19}\text{F}_{0.17}\text{O}_{0.64}]_{\Sigma 1.00}$
32a (oxy-dravite)	$^X(\text{K}_{0.03}\text{Na}_{0.52}\text{Ca}_{0.35}\square_{0.10})_{\Sigma 1.00} \text{ } ^Y(\text{Mg}_{1.51}\text{Al}_{1.10}\text{Fe}^{2+}_{0.29}\text{Ti}_{0.08}\text{V}_{0.01}\text{Cr}_{0.01})_{\Sigma 3.00} \text{ } ^Z(\text{Al}_{5.02}\text{Mg}_{0.93}\text{Fe}^{2+}_{0.01}\text{Fe}^{3+}_{0.03})_{\Sigma 6.00} \text{ } ^T\text{Si}_6\text{O}_{18}(\text{BO}_3)_3 \text{ } ^{\text{O}3}(\text{OH})_3 \text{ } ^{\text{O}1}[(\text{OH})_{0.14}\text{F}_{0.29}\text{O}_{0.57}]_{\Sigma 1.00}$
111 (oxy-dravite)	$^X(\text{K}_{0.06}\text{Na}_{0.46}\text{Ca}_{0.35}\square_{0.13})_{\Sigma 1.00} \text{ } ^Y(\text{Mg}_{1.51}\text{Al}_{1.10}\text{Fe}^{2+}_{0.30}\text{Ti}_{0.08}\text{V}_{0.01}\text{Cr}_{0.01})_{\Sigma 3.00} \text{ } ^Z(\text{Al}_{5.00}\text{Mg}_{0.93}\text{Fe}^{2+}_{0.03}\text{Fe}^{3+}_{0.04})_{\Sigma 6.00} \text{ } ^T\text{Si}_6\text{O}_{18}(\text{BO}_3)_3 \text{ } ^{\text{O}3}(\text{OH})_3 \text{ } ^{\text{O}1}[(\text{OH})_{0.25}\text{F}_{0.22}\text{O}_{0.53}]_{\Sigma 1.00}$
92a (oxy-dravite)	$^X(\text{K}_{0.28}\text{Na}_{0.42}\text{Ca}_{0.26}\square_{0.04})_{\Sigma 1.00} \text{ } ^Y(\text{Mg}_{1.32}\text{Al}_{1.27}\text{Fe}^{2+}_{0.32}\text{Ti}_{0.09}\text{V}_{0.01})_{\Sigma 3.00} \text{ } ^Z(\text{Al}_{4.96}\text{Mg}_{0.95}\text{Fe}^{2+}_{0.05}\text{Fe}^{3+}_{0.04})_{\Sigma 6.00} \text{ } [^T(\text{Si}_{5.97}\text{Al}_{0.03})_{\Sigma 6.00} \text{ } \text{O}_{18}](\text{BO}_3)_3 \text{ } ^{\text{O}3}(\text{OH})_3 \text{ } ^{\text{O}1}[(\text{OH})_{0.14}\text{F}_{0.21}\text{O}_{0.65}]_{\Sigma 1.00}$
92b (oxy-dravite)	$^X(\text{K}_{0.35}\text{Na}_{0.38}\text{Ca}_{0.25}\square_{0.02})_{\Sigma 1.00} \text{ } ^Y(\text{Mg}_{1.38}\text{Al}_{1.20}\text{Fe}^{2+}_{0.33}\text{Ti}_{0.09}\text{V}_{0.01}\text{Cr}_{0.01})_{\Sigma 3.00} \text{ } ^Z(\text{Al}_{5.06}\text{Mg}_{0.87}\text{Fe}^{2+}_{0.04}\text{Fe}^{3+}_{0.04})_{\Sigma 6.00} \text{ } [^T(\text{Si}_{5.94}\text{Al}_{0.06})_{\Sigma 6.00} \text{ } \text{O}_{18}](\text{BO}_3)_3 \text{ } ^{\text{O}3}(\text{OH})_3 \text{ } ^{\text{O}1}[(\text{OH})_{0.17}\text{F}_{0.18}\text{O}_{0.65}]_{\Sigma 1.00}$
92c (oxy-dravite)	$^X(\text{K}_{0.22}\text{Na}_{0.45}\text{Ca}_{0.29}\square_{0.05})_{\Sigma 1.00} \text{ } ^Y(\text{Mg}_{1.31}\text{Al}_{1.25}\text{Fe}^{2+}_{0.35}\text{Ti}_{0.08}\text{V}_{0.01})_{\Sigma 3.00} \text{ } ^Z(\text{Al}_{4.97}\text{Mg}_{1.00}\text{Fe}^{3+}_{0.03})_{\Sigma 6.00} \text{ } [^T(\text{Si}_{5.98}\text{Al}_{0.02})_{\Sigma 6.00} \text{ } \text{O}_{18}](\text{BO}_3)_3 \text{ } ^{\text{O}3}(\text{OH})_3 \text{ } ^{\text{O}1}[(\text{OH})_{0.18}\text{F}_{0.18}\text{O}_{0.64}]_{\Sigma 1.00}$

**Table 4** Observed and calculated site-scattering values (epfu<sup>a</sup>) for K-oxy-dravite samples studied

Sample/Site	<i>X</i>		<i>Y</i>		<i>Z</i>		<i>T</i>	
	obs	calc	obs	Calc	obs <sup>b</sup>	Calc	obs <sup>b</sup>	calc
24c2a	15.74(6)	16.53	43.01(13)	43.06	78.00	78.14	84.00	84.00
2c2b	15.40(6)	16.14	42.64(13)	42.84	78.00	78.68	84.00	84.00
14b	13.73(7)	13.95	42.34(13)	42.42	78.00	78.24	84.00	84.00
25b	14.26(6)	14.69	42.59(13)	42.60	78.00	78.03	84.00	83.95
32a	13.71(5)	13.20	42.26(13)	42.14	78.00	77.59	84.00	84.00
111	13.99(6)	13.30	42.26(13)	42.23	78.00	77.90	84.00	84.00
92a	15.15(6)	15.19	42.64(13)	42.69	78.00	78.18	84.00	83.97
92b	14.19(7)	15.82	42.68(17)	42.74	78.00	78.12	84.00	83.94
92c	14.87(6)	14.82	43.35(13)	43.17	78.00	77.42	84.00	83.98

Note: Calculated site-scattering values from crystal-chemical formula (Table 4)

<sup>a</sup> epfu = electrons per formula unit

<sup>b</sup> Fixed in the final stages of refinement

**Table 5** Structural parameters and mean bond lengths of the studied crystal fragments, the Calculated Distortion Indices (DI) and the discrepancy ( $\delta$ , in valence units *vu*) between bond valence sum (BVS) and formal mean charge at the *X* site.

sample	<i>a</i> (Å)	<i>c</i> (Å)	<i>V</i> (Å <sup>3</sup> )	< <i>X</i> -O> (Å)	< <i>Y</i> -O> (Å)	< <i>Z</i> -O> (Å)	DI ( $\Delta_X 10^3$ )	$\delta$ ( <i>vu</i> )
24C2	15.9263(19)	7.2260(10)	1586.5534(4)	2.687	2.009	2.009	0.981	0.225
2C2b	15.9246(2)	7.2191(10)	1585.4434(5)	2.684	2.009	2.009	1.118	0.225
14b	15.9284(2)	7.2001(10)	1582.0254(5)	2.666	2.017	2.017	2.102	-0.084
25b	15.9290(14)	7.2070(10)	1583.6608(4)	2.674	2.017	2.017	1.624	-0.036
32a	15.9311(19)	7.1973(9)	1581.9357(4)	2.665	2.017	2.017	2.135	-0.186
111a	15.9292(18)	7.1997(10)	1582.1049(4)	2.668	2.017	2.017	1.870	-0.165

92a	15.9211(3)	7.2149(2)	1583.8246(7)	2.681	2.009	2.009	1.184	0.036
92b	15.9273(3)	7.2067(10)	1583.2570(6)	2.673	2.014	2.014	1.567	0.150
92c	15.9218(2)	7.2134(10)	1583.6345(5)	2.677	2.011	2.011	1.326	-0.016

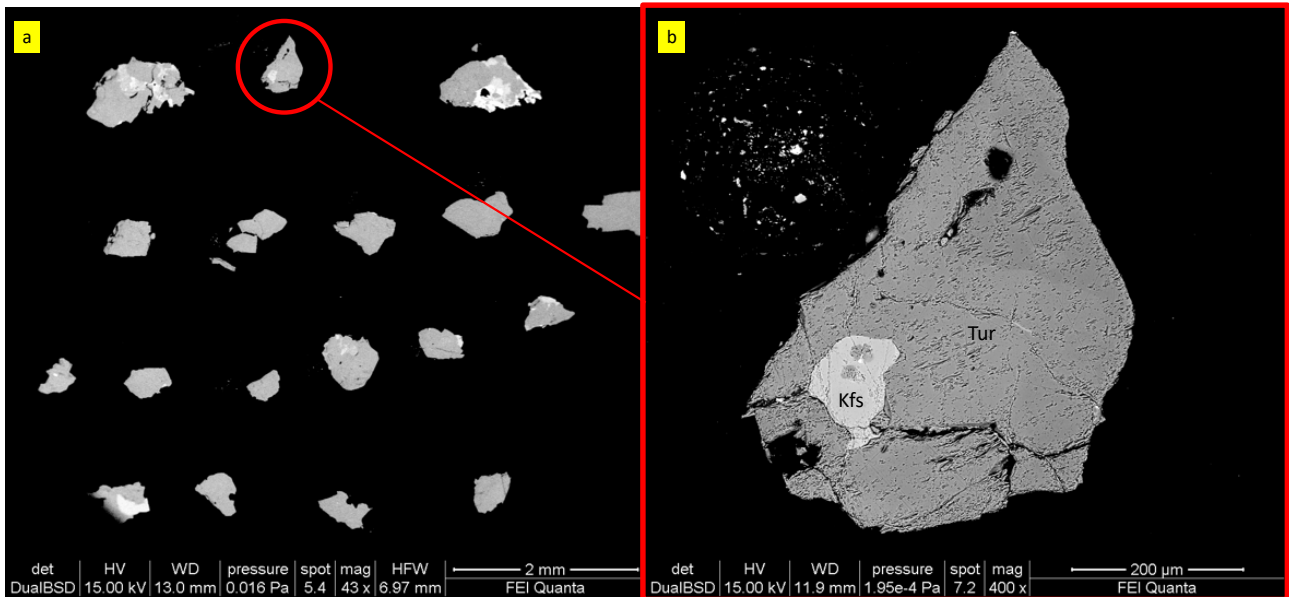


**Figure 1** Back-scattered electrons image of a polished section displaying some of the studied crystal fragments embedded in epoxy (a) and detail of a single fragment (2C2b) selected to extract the tourmaline portion (b); Tur = tourmaline, Kfs = K-feldspar.

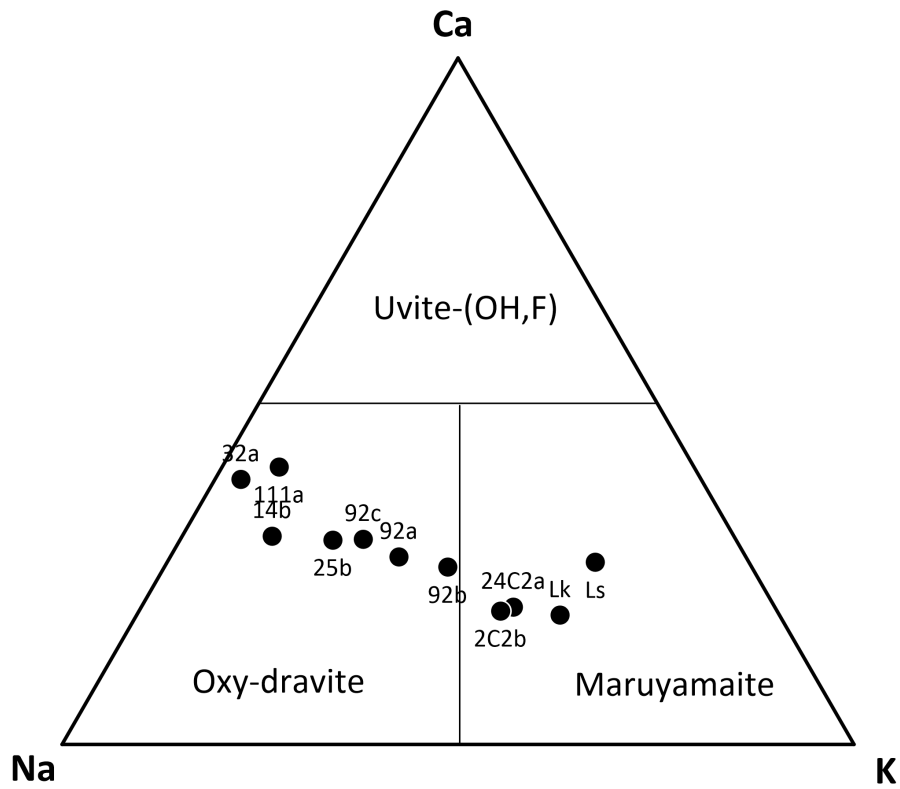


**Figure 2** Ternary plot displaying the studied samples on the basis of their *X* site population. Odrv = oxy-dravite; Mry = maruyamaite; (F)uvt = Fluor-uvite.





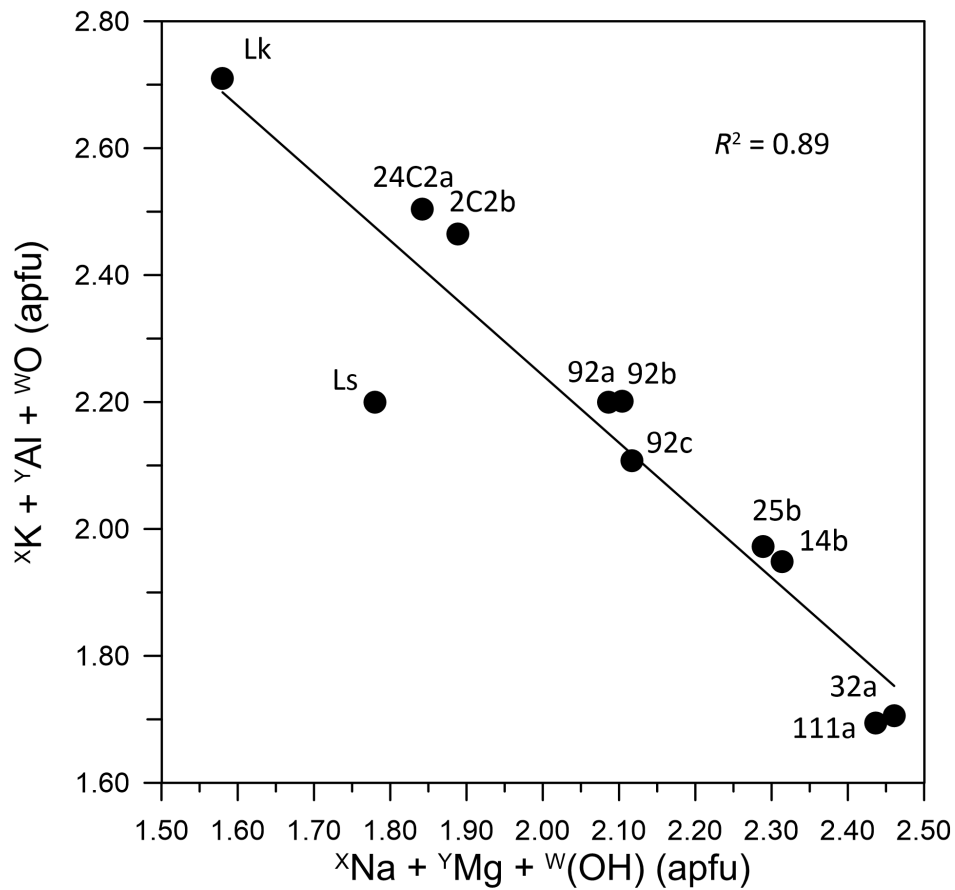


**Figure 4** Substitution  $xK+yAl+wO$  (apfu) =  $xNa+yMg+w(OH)$  that leads from maruyamaite (left) to oxy-dravite (right). Data from Lussier et al. (2016) and Likhacheva et al. (2019) are reported for comparison, respectively as "Ls" and "Lk". Data from Berryman et al. (2014) are not shown because their maruyamaite is synthetic.

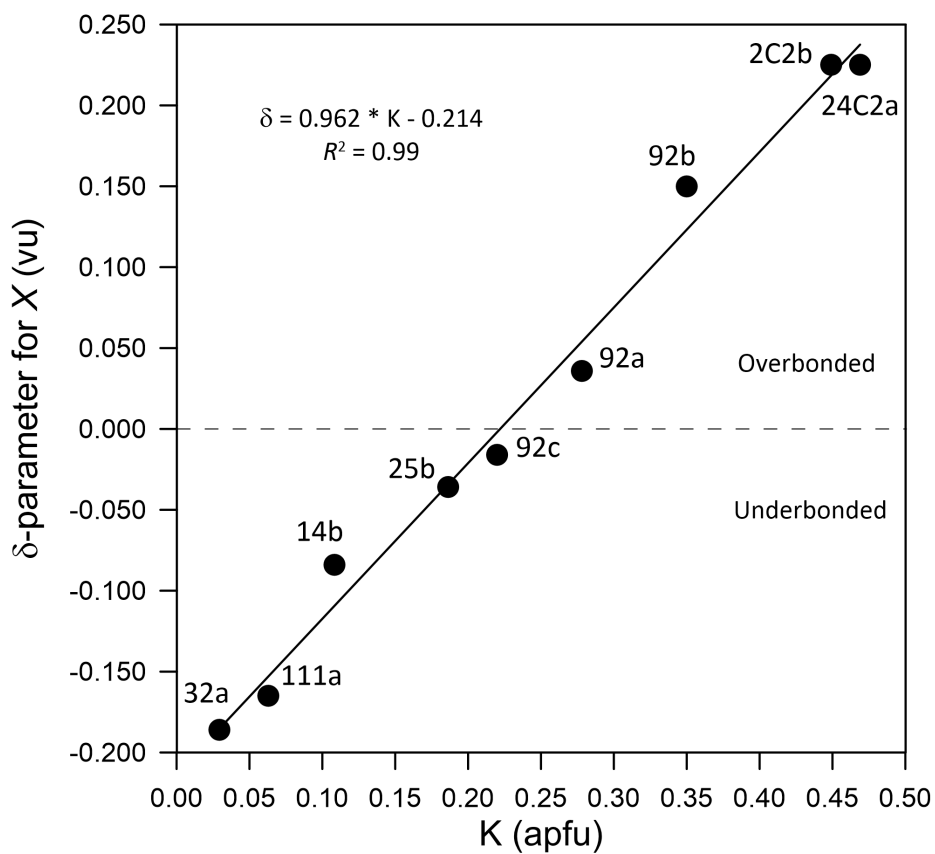


**Figure 5** K content vs the difference between the bond valence sum (BVS) and the formal mean charge for the X site of the nine investigated crystals.

## 2.1.4 Schorl 1-A

Original paper

# Schorl-1A from Langesundsfjord (Norway)

Fernando CÁMARA<sup>1\*</sup>, Ferdinando BOSI<sup>2</sup>, Henrik SKOGBY<sup>3</sup>, Ulf HÅLENIUS<sup>3</sup>, Beatrice CELATA<sup>2</sup>, Marco E. CIRIOTTI<sup>4,5</sup><sup>1</sup> University of Milan, via Mangiagalli 34, I-20133 Milan, Italy; fernando.camara@unimi.it<sup>2</sup> Sapienza University of Rome, Piazzale Aldo Moro 5, I-00185, Rome, Italy<sup>3</sup> Department of Geosciences, Swedish Museum of Natural History, Box 50 007, SE-104 05 Stockholm, Sweden<sup>4</sup> Associazione Micromineralogica Italiana, via San Pietro 55, I-10073 Devesi-Cirié, Italy<sup>5</sup> Dipartimento di Scienze della Terra, Università di Torino, via Tommaso Valperga Caluso 35, I-10025 Torino, Italy

\* Corresponding author



A crystal fragment of schorl from Langesundsfjord (Norway), showing a zonation with a biaxial optic behavior in the rim, was studied by electron microprobe analysis, single-crystal X-ray diffraction, Mössbauer, infrared and optical absorption spectroscopy and optical measurements. Measured  $2V_x$  is  $15.6^\circ$ . We concluded that biaxial character of the sample is not due to internal stress because it cannot be removed by heating and cooling. Diffraction data were refined with a standard  $R3m$  space group model, with  $a = 16.0013(2)$  Å,  $c = 7.2263(1)$  Å, and with a non-conventional triclinic  $R1$  space-group model keeping the same hexagonal triple cell ( $a = 16.0093(5)$  Å,  $b = 16.0042(5)$  Å,  $c = 7.2328(2)$  Å,  $\alpha = 90.008(3)^\circ$ ,  $\beta = 89.856(3)^\circ$ ,  $\gamma = 119.90(9)^\circ$ ), yielded  $R_{\text{all}} = 1.75\%$  (3136 unique reflections) vs.  $R_{\text{all}} = 2.53\%$  (17342 unique reflections), respectively. The crystal-chemical analysis resulted in the chemical formula  $^{x}(\text{Na}_{0.98}\text{K}_{0.01}\square_{0.01})_{\Sigma 1.00}^{y}(\text{Fe}^{2+}_{1.53}\text{Al}_{0.68}\text{Mg}_{0.35}\text{Ti}_{0.20}\text{Fe}^{3+}_{0.20}\text{Mn}_{0.02}\text{V}_{0.01}\text{Zn}_{0.01}\text{Σ}_{3.00})^z(\text{Al}_{5.10}\text{Fe}^{2+}_{0.50}\text{Mg}_{0.40}\text{Σ}_{6.00})(\text{Si}_6\text{O}_{18})(\text{BO}_3)_3(\text{OH})_3[(\text{OH})_{0.39}\text{F}_{0.22}\text{O}_{0.39}\text{Σ}_{1.00}]$ , which agrees well in terms of calculated site-scattering ( $X$  10.9 *epfu*,  $Y$  63.7 *epfu*,  $Z$  83.7 *epfu*) and refined site-scattering ( $X$  11.4 *epfu*,  $Y$  63.4 *epfu*,  $Z$  83.6 *epfu*). About 0.19 *apfu*  $\text{Fe}^{2+}$  is at the  $Z$  sites in the  $R1$  model that showed that one out of six independent  $Z$  sites ( $Zd$ ) has higher refined site scattering [15.5 *eps* vs. mean 13.7(2) *eps* for the other five sites] and larger mean bond length [1.969 Å vs. 1.927(6) Å for the other five sites] and larger octahedral angle variance [ $53^\circ$  vs.  $42(3)^\circ$ ]. All these features support local order of  $\text{Fe}^{2+}$  at the  $Zd$  site. Optical absorption spectra also show evidence of  $\text{Fe}^{2+}$  at the  $Z$  sites. The elongation of the  $Zd$ -octahedron is along a direction that forms an angle of ca.  $73^\circ$  with a unit-cell edge and is coincident with the direction of the  $\gamma$ -refraction index. All these data support the triclinic character of the structure of the optically biaxial part of the tourmaline sample from Langesundsfjord and provide evidence that even in the presence of excellent statistical agreement factors from excellent X-ray diffraction data, the lowering of symmetry due to cation ordering may have been overlooked in many other tourmaline samples in the absence of a check of the optical behaviour. According to the nomenclature rules, the studied triclinic schorl, should be named schorl-1A.

**Keywords:** Tourmaline, crystal structure, electron microprobe, Mössbauer spectroscopy, infrared spectroscopy, optical absorption spectroscopy

Received: 14 December 2021; accepted: 17 February 2022; handling editor: J. Cempirek

The online version of this article (doi: 10.3190/jgeosci.344) contains supplementary electronic material.

## 1. Introduction

It is not uncommon to find references in the literature to anomalous optical behavior in minerals, e.g., birefringence in nominally optically isotropic minerals or the symmetry of optical indicatrix lower than expected for the crystal system of the mineral. For polychrome tourmalines, it has been well known since the 19<sup>th</sup> century (Madelung 1883; Brauns 1891). Change of refractive index caused by strain (Wertheim 1851, 1854) may be related to structural deformation. Several causes have been suggested for such behavior:

- internal stress arising from defects and compositional heterogeneities (“tourmaline”, beryl, “apatite”, “garnet”, quartz; Foord and Mills 1978); topaz (Isogami

and Sunagawa 1975), or by internal stress arising from inclusions (as in diamonds; Howell 2012 and references within) or other minerals (Campomenosi et al. 2020).

- desymmetrization due to order; for example, garnet showing topochemical orthorhombic space group  $Fddd$  (Takeuchi and Haga 1976) or tetragonal and sector zoning (Hofmeister et al. 1988; Grifen et al. 1992; Andrut et al. 2002; Antao 2013; Cesare et al. 2019). It can also be observed by post-growth order-related phase transitions as for rutile (Foord and Mills 1978) or analcime (Akizuki 1981).
- crystal growth; due to differential incorporation of cations and anions among structurally different sites on the surface that in the bulk crystal are structurally

identical. For example, in elbaite (Hughes et al. 2011) or in elbaite–liddicoatite (Shtukenberg et al. 2007), and in garnet (Akizuki 1984; Allen and Buseck 1988). Internal stress can be released through annealing of the crystal as observed by Foord and Cunningham (1978) in tourmaline from San Diego mine, California, and the process was permanent if the crystal was heated until  $2V=0^\circ$ . Similar results were obtained by Hariya and Kimura (1978) in garnet.

As mentioned above, tourmaline samples can show anomalous biaxial behaviour. In 2009, *luinaite-(OH)* was approved (IMA No. 2009-046) with the formula  $(\text{Na}, \square)(\text{Fe}^{2+}, \text{Mg})_3\text{Al}_6(\text{BO}_3)_3\text{Si}_6\text{O}_{18}(\text{OH})_4$ , monoclinic symmetry and *Cm* space group from several different localities. Kolitsch et al. (2011; 2013) reported occurrences of *luinaite-(OH)* and *luinaite-(F)* from the Langesundsfjord area, along with schorl, fluor-schorl, dravite, fluor-elbaite, fluor-liddicoatite and rossmanite, and described it as having *Cm* (monoclinic) that is caused by order of  $\text{Fe}^{3+}$  and  $\text{Al}^{3+}$  as a result of the conditions of crystallization.

Kolitsch and co-workers reported high-resolution data ( $2\theta = 75^\circ \text{ MoK}_\alpha$ ) and  $a = 10.433(2)$ ,  $b = 16.045(3)$ ,  $c = 7.241(1) \text{ \AA}$ ,  $\beta = 117.61(3)^\circ$  and a refined bulk chemical formula (occupancies of individual split *Y* and *Z* sites were not given):  $\sim(\text{Na}_{0.94}\square_{0.06})_{\Sigma 1.00}(\text{Fe}_{2.22}\text{Al}_{0.78})_{\Sigma 3.00}(\text{Al}_{5.10}\text{Fe}_{0.90})_{\Sigma 6.00}(\text{Si}_6\text{O}_{18})(\text{BO}_3)_3(\text{OH})_3(\text{OH}_{0.80}\text{F}_{0.20})_{\Sigma 1.00}$ .

Recently, however, *luinaite-(OH)* has been formally discredited (IMA proposal n. 21-L; Bosi et al. 2022), and any deviation from the reference space group *R3m* symmetry should be accommodated in the nomenclature by adding a suffix to the root name that indicates any atypical symmetry (Henry et al. 2011).

## 2. Sample description

A sample of schorl composition showing a different optical behavior, uniaxial in the dark brownish core

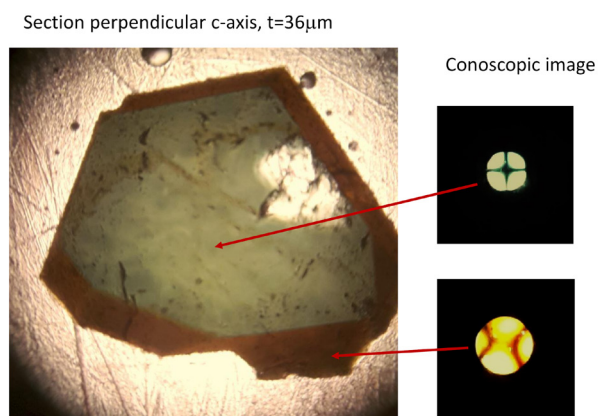


**Fig. 1a** – Image of the crystal cut perpendicular to *c*-axis and the interference images obtained at the core and the rim of the section.

and biaxial in the darker brownish rim, coming from Langesundsfjord (Norway), has been studied (GEO-NRM#19252409, Swedish Museum of Natural History). Schorl has been reported by Brøgger (1890) from the wider Langesundsfjord area in the Larvik Plutonic Complex (LPC). Brøgger (1890) noted two main suites of alkaline pegmatites: the Langesundsfjord and Fredriksvårn suites, which contain different HFSE-minerals. Today these are considered as agpaitic and miaskitic mineral assemblages, respectively. The Langesundsfjord suite shows primary complex Na, Zr silicates (Andersen et al. 2010). A  $36 \mu\text{m}$  section was cut perpendicular to *c*-axis. Conoscopic images (Fig. 1) showing uniaxial behavior in the lighter core of the section and biaxial behavior with the negative optic sign were obtained in the darker rims. The biaxial character of the sample is not due to internal stress because it could not be removed by heating and cooling, as observed in tourmaline samples from the San Diego mine (California) by Foord and Cunningham (1978).

## 3. Experimental methods

### 3.1. Optical measurements

Optical measurements were done with a Supper Co. spindle stage in a Leitz Dialux microscope equipped with a CMOS camera using the Excelibr spreadsheet (Steven and Gunter 2018). A portion corresponding to the dark biaxial rim was first measured, giving  $2V_x = 15.6^\circ$  (in white light). The orientation of the optical indicatrix was obtained using the same crystal mounted on a Rigaku XtaLAB Synergy-S diffractometer ( $\text{MoK}_\alpha$ ):  $\mathbf{c} \wedge X = 2^\circ$ ,  $\mathbf{b} \wedge Z = 164.3^\circ$  and  $\mathbf{a} \wedge Z = 75.8^\circ$ .

### 3.2. Electron MicroProbe Analysis (EMPA)

Electron microprobe analysis on the rim and core of the tourmaline crystal, was done using a wavelength-dispersive spectrometer (WDS mode) with a Cameca SX50 instrument at the Istituto di Geologia Ambientale e Geoingegneria, CNR, Rome, Italy. The following analytical conditions were used: accelerating voltage 15 kV, beam current 15 nA and beam diameter of  $10 \mu\text{m}$ . Minerals and synthetic compounds were used as standards: wollastonite (Si, Ca), magnetite (Fe), rutile (Ti), corundum (Al), vanadinite (V), fluorophlogopite (F), periclase (Mg), jadeite (Na), orthoclase (K), sphalerite (Zn), rhodonite (Mn), metallic Cr and Cu. The PAP routine was applied (Pouchou and Pichoir 1991). Results are reported in Tab. 1. Calcium, Cr and Cu were below detection limits ( $< 0.03 \text{ wt. \%}$ ).

### 3.3. Mössbauer spectroscopy

Mössbauer spectroscopy was used to determine the  $\text{Fe}^{3+}/\Sigma\text{Fe}$  ratio of the sample, using a conventional spectrometer system operated in constant-acceleration mode. An absorber was prepared from 12 mg sample material obtained from the core region of a crystal that was mixed with an acrylic resin and pressed to a 12-mm diameter disc under mild heating ( $< 150^\circ\text{C}$ ). Spectra were collected over 1024 channels in the velocity range  $-4.2$  to  $+4.2$  mm/s using a  $^{57}\text{Co}$  rhodium matrix standard source of 50 mCi nominal activity. The raw spectrum was folded and calibrated against an  $\alpha\text{-Fe}$  foil. The spectrum (Fig. 2) was fitted using the software MossA (Prescher et al. 2012) with four doublets assigned to  $\text{Fe}^{2+}$  and one doublet assigned to  $\text{Fe}^{3+}$ , resulting in an  $\text{Fe}^{3+}/\Sigma\text{Fe}$  ratio of 0.13 (Tab. 2).

### 3.4. Infrared and Optical Absorption Spectroscopy

Fourier-transform infrared spectroscopy (FTIR) was used to characterize the fundamental (OH) vibrational

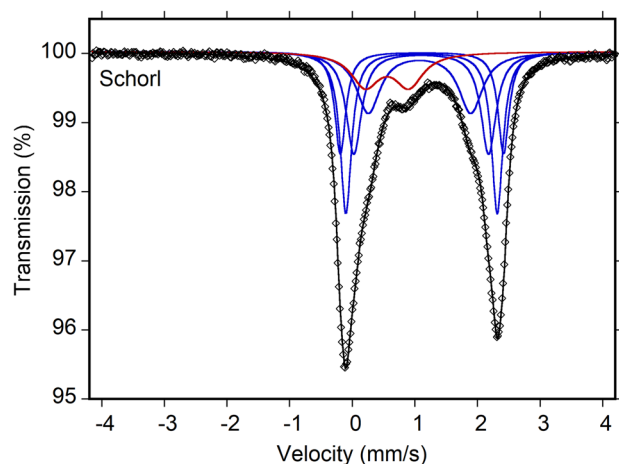


**Fig. 2**  $^{57}\text{Fe}$  Mössbauer spectrum (core region) obtained at room temperature. Fitted absorption doublets assigned to  $\text{Fe}^{2+}$  and  $\text{Fe}^{3+}$  are indicated in blue and red, respectively. Diamonds denote measured spectrum, and the black curve represents summed fitted doublets.

**Tab. 1** Average chemical compositions of the rim and core of the tourmaline crystal from Langesundsfjord, Norway.

	rim ( $n = 10$ )	core ( $n = 20$ )		rim	core
$\text{SiO}_2^{\text{a}}$ (wt. %)	34.55(9)	34.67(22)	Si ( <i>apfu</i> )	6.000	6.000
$\text{TiO}_2$	1.59(8)	0.39(10)	$\text{Ti}^{4+}$	0.207	0.051
$\text{B}_2\text{O}_3^{\text{b}}$	10.01	10.05	B	3.000	3.000
$\text{Al}_2\text{O}_3$	28.22(35)	30.04(43)	Al	5.777	6.128
$\text{V}_2\text{O}_3$	0.08(2)	0.04(2)	$\text{V}^{3+}$	0.011	0.006
$\text{FeO}_{\text{tot}}$	15.29(31)	14.67(19)			
MnO	0.16(4)	0.14(2)	$\text{Mn}^{2+}$	0.023	0.021
MgO	2.92(7)	2.58(6)	Mg	0.755	0.664
ZnO	0.05(5)	0.05(4)	Zn	0.007	0.007
$\text{Na}_2\text{O}$	2.90(5)	2.88(5)	Na	0.975	0.967
$\text{K}_2\text{O}$	0.04(2)	–	K	0.009	–
F	0.41(4)	0.16(9)	F	0.224	0.089
$\text{H}_2\text{O}^{\text{b}}$	2.93	2.96	(OH)	3.393	3.420
O = F	–0.17	–0.07			
FeO	13.93 <sup>c</sup>	12.67 <sup>d</sup>	$\text{Fe}^{2+}$	2.023	1.834
$\text{Fe}_2\text{O}_3$	1.512 <sup>c</sup>	2.22 <sup>d</sup>	$\text{Fe}^{3+}$	0.198	0.289
Total	99.112	98.79			

Notes: Errors for oxides and fluorine are standard deviations (in parentheses) of  $n$  spot WDS analyses; *apfu* = atoms per formula unit, normalized to 31 anions (see text).

<sup>a</sup>  $\text{SiO}_2$  assumed to equal 6.000 *apfu*. The  $\text{SiO}_2$  average value measured in the rim and core of tourmaline crystal are 34.81 wt. % and 35.09 wt. %, respectively.

<sup>b</sup> By stoichiometry

<sup>c</sup> By Optical absorption spectroscopy

<sup>d</sup> By Mössbauer spectroscopy

absorption bands in the range  $3000\text{--}4000\text{ cm}^{-1}$  (Fig. 3). The spectrometer system consisted of a Bruker Vertex 70 spectrometer equipped with a halogen-lamp source and  $\text{CaF}_2$  beam-splitter, coupled to a Hyperion II IR microscope equipped with a ZnSe wire-grid polarizer and an InSb detector. Polarized absorption spectra were acquired on two differently oriented crystal sections; one cut parallel to the **c**-axis with a thickness of  $45\ \mu\text{m}$  (Fig. 1), and one cut perpendicular to the **c**-axis with a thickness of  $36\ \mu\text{m}$  (Fig. 4 and 5). The spectra were measured over the wavenumber range  $2000\text{--}12000\text{ cm}^{-1}$  with a resolution of  $4\text{ cm}^{-1}$ , with the measuring area masked by a rectangular  $75 \times 100\ \mu\text{m}$  aperture.

Polarized room-temperature optical absorption spectra in the range  $30000\text{--}5000\text{ cm}^{-1}$  ( $333\text{--}1000\text{ nm}$ ) were recorded at a spectral resolution of  $1\text{ nm}$  on the same  $45\ \mu\text{m}$

**Tab. 2** Mössbauer parameters obtained at room temperature.

$d$ (mm/s)	$\Delta E_Q$ (mm/s)	$FWHM$ (mm/s)	Area (%)	Assignment
1.11	2.61	0.21	16.4	$\text{VI}\text{Fe}^{2+}$
1.10	2.42	0.22	26.3	$\text{VI}\text{Fe}^{2+}$
1.10	2.15	0.30	22.7	$\text{VI}\text{Fe}^{2+}$
1.07	1.64	0.46	21.0	$\text{VI}\text{Fe}^{2+}$
0.55	0.70	0.54	13.6	$\text{VI}\text{Fe}^{3+}$

$d$  = centroid shift,  $\Delta E_Q$  = quadrupole splitting,  $FWHM$  = full width at half-maximum.

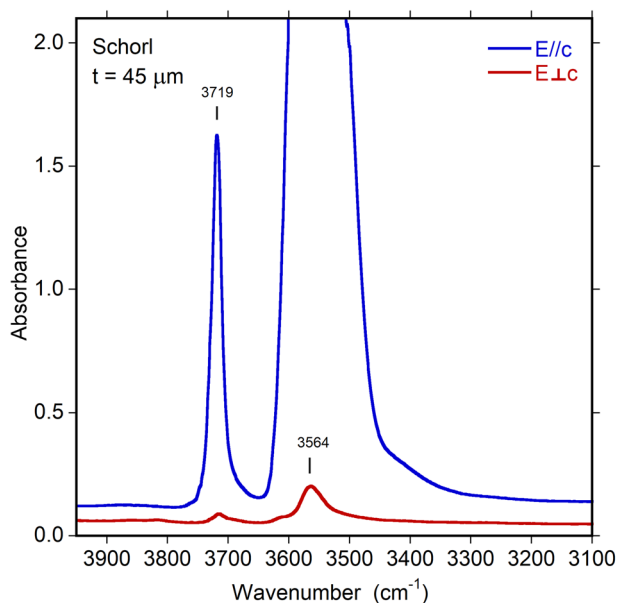


**Fig. 3** Polarized FTIR spectra (core region), vertically off-set for clarity. The main band is truncated around 2 absorbance units in the  $E \parallel c$  direction due to excessive absorption. Sample thickness 45  $\mu\text{m}$ .

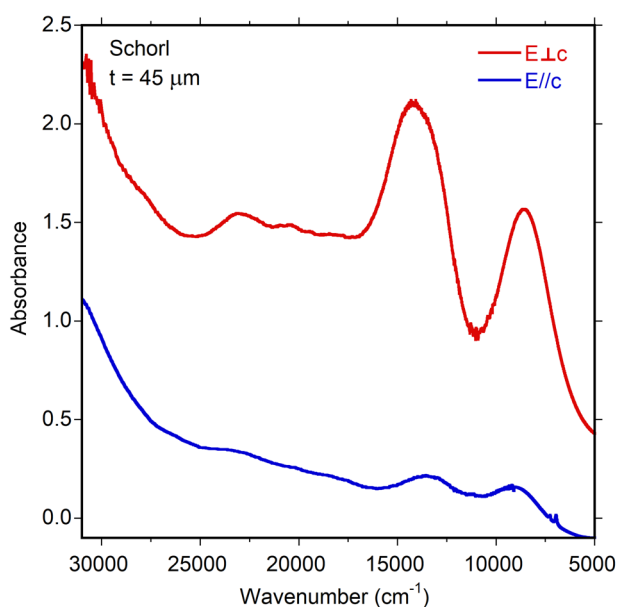


**Fig. 4** Polarized optical absorption spectra of the core of a 45  $\mu\text{m}$  thick single crystal cut parallel to the  $c$ -axis.

thick single crystal section, cut along the  $c$ -axis, that was studied by FTIR spectroscopy. Spectra of the differently coloured core and rim regions (Fig. 5) were measured on a 36  $\mu\text{m}$  thick crystal section cut perpendicular to the  $c$ -axis. All spectra were recorded using an AVASPEC-ULS2048 $\times$ 16 spectrometer (Swedish Museum of Natural History, Stockholm, Sweden) attached via a 400  $\mu\text{m}$  UV fiber cable to a Zeiss Axiotron UV-microscope. A 75 W Xe arc lamp was used as a light source, and Zeiss Ultrafluor 10 $\times$  lenses served as objective and condenser. The

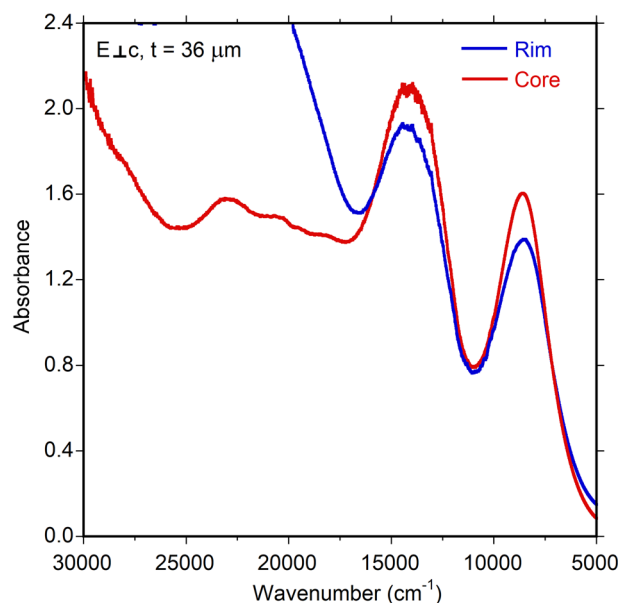


**Fig. 5** Polarized optical absorption spectra of the core and rim of a 36  $\mu\text{m}$  thick single crystal cut perpendicular to the  $c$ -axis. Spectra were recorded at core and rim positions indicated by arrows in Fig. 1.

diameter of the circular measure apertures was in the range 50–75  $\mu\text{m}$ . A UV-quality Glan–Thompson prism with a working range from 40000 to 3704  $\text{cm}^{-1}$  (250 to 2700 nm) was used as a polarizer. The wavelength scale of the spectrometer was calibrated against  $\text{Ho}_2\text{O}_3$ -doped and  $\text{Pr}_2\text{O}_3/\text{Nd}_2\text{O}_3$ -doped standards (Hellma glass filters 666F1 and 666F7). Spectral data in the range 10000–5000  $\text{cm}^{-1}$  (1000–2000 nm) was taken from the FTIR measurements.

### 3.5. Single-crystal X-ray diffraction

A Single-crystal X-ray Structure REFinement (SREF) study was done on a crystal fragment (0.020  $\times$  0.123  $\times$  0.303 mm) from the optically biaxial rim and extracted from a thin section of a tourmaline crystal perpendicular to the prism length. The thin fragment was glued to a glass fibre and mounted on a Rigaku XtaLAB Synergy diffractometer equipped with a Hybrid Pixel Array Detector, using graphite-monochromatized  $\text{MoK}_\alpha$  radiation ( $\lambda = 0.71073 \text{ \AA}$ ); experimental conditions were 50 kV and 1 mA and the detector-to-sample distance was 6.2 cm. A combination of 44  $\omega$  scans at different values of  $\omega$  and  $\phi$ ,  $\chi$  angles as well as different detector positions at several  $\theta$  values, with step scan  $1^\circ$ , was used to collect 5039 images to achieve a complete scan of the reciprocal space up to a resolution of 0.50  $\text{\AA}$ . Exposure time was 10 s per frame at the low  $\theta$  setting and 22 s at the high  $\theta$  setting of the detector. The strategy was meant to obtain a complete dataset of high-resolution data allowing for refinement in the point group 1.



The crystal structure was refined starting from a tourmaline  $R3m$  structure model by Hughes et al. (2011). Neutral-atoms scattering curves from The International Tables (Wilson 1992) were used for all the atom positions keeping full fixed occupancy for  $T$ ,  $B$  and anion sites [but for the O1 ( $\equiv$  W) and O3 ( $\equiv$  V) sites] and occupancies were refined at the  $X$ ,  $Y$  and  $Z$  cation sites refining relative occupancy of Fe and Al for each type of site, and for the O1 sites refining relative occupancies of O versus F. Hydrogen atoms bonded to O3 site were observed in Fourier-difference maps and were added to the model refining atom coordinates and constraining the isotropic displacement to be 20 % higher than the equivalent isotropic value at the O3 site. Refinement was done with SHELXTL (Sheldrick 2015) with anisotropic-displacement parameters for all non-hydrogen

atoms, and the structure was refined on  $F^2$ . At convergence, the discrepancy factor was  $R_1 = 0.017$  for 3079 unique reflections with  $F_o > 4 \sigma(F)$  and  $R_1 = 0.018$  for all 3136 reflections. For the triclinic model, starting coordinates were taken from the tourmaline  $R1$  structure model of Hughes et al. (2011), using the same approach as described above. At convergence, hydrogen atoms bonded to the oxygen at the O3 sites were observed in Fourier-difference maps and were added to the model. The model refined to discrepancy factors of  $R_1 = 0.023$  for 16304 unique reflections with  $F_o > 4 \sigma(F)$  and  $R_1 = 0.025$  for all 17342 reflections.

Experimental details, unit-cell parameters and statistical indices for both  $R1$  and  $R3m$  models are given in Tab. 3. Fractional atom coordinates, site occupancies, isotropic-displacement parameters and weighted bond-valence sums (using the parameters of Gagnè and Hawthorne 2015) are reported in Tab. 4. Bond distances are given in Tab. 5. A crystallographic information file (CIF) containing observed structure factors has been deposited as Supplementary material.

## 4. Results

### 4.1. Infrared and Optical Absorption Spectroscopy

Infrared spectra in the 3100–4000  $\text{cm}^{-1}$  region (Fig. 3) show two prominent bands related to O–H stretching

**Tab. 3** Crystal data and experimental conditions for single-crystal XRD study.

Crystal system	Triclinic	Trigonal
Space group	$R1$	$R3m$
Unit cell dimensions	$a = 16.0093(5) \text{ \AA}$ $b = 16.0042(5) \text{ \AA}$ $c = 7.2328(2) \text{ \AA}$ $\alpha = 90.008(3)^\circ$ $\beta = 89.856(3)^\circ$ $\gamma = 119.90(9)^\circ$	$16.0013(2) \text{ \AA}$   $7.22630(10) \text{ \AA}$
Unit cell volume ( $\text{\AA}^3$ )	1606.6(13)	1602.35(5)
$Z$	3	3
Absorption coefficient	$2.36 \text{ mm}^{-1}$	$2.36 \text{ mm}^{-1}$
$F(000)$	1526	1526
Theta range for data collection	$2.54$ to $44.93^\circ$	$2.54$ to $44.93^\circ$
Index ranges	$-31 \leq h \leq 31, -31 \leq k \leq 31,$ $-14 \leq l \leq 14$	$-31 \leq h \leq 31, -31 \leq k \leq 31,$ $-14 \leq l \leq 14$
Reflections collected	86725	86725
Independent reflections	17342 [ $R_{\text{int}} = 0.0408$ ]	3136 [ $R_{\text{int}} = 0.0662$ ]
Refinement method	Full-matrix least-squares on $F^2$	Full-matrix least-squares on $F^2$
Extinction coefficient	0.00029(7)	0.00055(13)
Flack parameter	0.003(4)	0.029(5)
Data / restraints / parameters	17342 / 3 / 474	3136 / 1 / 95
Goodness-of-fit on $F^2$	0.974	1.069
Final $R$ indices [ $I > 2\sigma(I)$ ]	$R_1 = 0.023, wR_2 = 0.047$	$R_1 = 0.017, wR_2 = 0.040$
$R$ indices (all data)	$R_1 = 0.025, wR_2 = 0.047$	$R_1 = 0.018, wR_2 = 0.040$
Largest diff. peak and hole ( $\text{e\AA}^{-3}$ )	0.937 and $-0.827$	0.837 and $-0.832$

modes at 3564 and 3719  $\text{cm}^{-1}$ , and a weak shoulder feature around 3420  $\text{cm}^{-1}$ . As typically observed for infrared spectra of tourmalines, the (OH) bands are strongly polarized parallel to the  $c$ -axis, with the main band off-scale due to excessive absorption. The relatively strong band at 3719  $\text{cm}^{-1}$ , which occurs in the region where bands due to (OH) at the O1 site ( $\equiv$  W) are expected, indicates a significant amount of  $^w(\text{OH})$ . This band is likely caused by the occurrence of the atomic arrangements  $^y[\text{Fe}^{2+}\text{Fe}^{2+}(\text{Fe}^{2+}, \text{Al})]^{-\text{O}1}(\text{OH})^{-\text{X}}(\text{Na})$ , based on the studies of Watenphul et al. (2016) and Bosi et al. (2016). Conversely, the band at 3564  $\text{cm}^{-1}$  and the shoulder at 3420  $\text{cm}^{-1}$  are related to the presence of (OH) groups at the O3 site ( $\equiv$  V) (e.g., Gonzalez-Carreño et al. 1988; Bosi et al. 2015a).

The optical absorption spectra (Fig. 4 and Fig. 5) show strong and broad absorption bands at 22700,  $\sim 14000$  and  $\sim 9000 \text{ cm}^{-1}$ , which are strongly polarized in  $\mathbf{E} \perp \mathbf{c}$  (Fig. 4). In addition, weak and relatively narrow absorption bands occur at 20600 and 18000  $\text{cm}^{-1}$ . The relatively broad absorption bands at  $\sim 14000$  and 9000  $\text{cm}^{-1}$  are assigned to  $\text{Fe}^{3+}$ -enhanced spin-allowed  $d-d$  transitions in six-coordinated  $\text{Fe}^{2+}$  in accord with previous optical studies of tourmaline (e.g., Mattson and Rossman 1987). Each of these two absorption bands shows a distinct shoulder, which indicates that they are composed of two partly overlapping absorption bands. In detail, the higher energy band shows two-band com-

**Tab. 4** Site occupancy (s.o.), atom coordinates and equivalent isotropic displacement parameters ( $\text{\AA}^2$ ). Equivalent displacement parameter,  $U_{\text{eq}}$ , is defined as one third of the trace of the orthogonalized  $U^{\text{ij}}$  tensor. Bond valence (B.V.S.) in valence units (v.u.).

Site <i>Rl</i>	Atom	s.o.	<i>x/a</i>	<i>y/b</i>	<i>z/c</i>	$U_{\text{eq}}$	B.V.S.
<i>X</i>	Na	1.037(5)	0.00028(7)	0.00024(7)	0.25347(12)	0.0271(3)	0.889
<i>Sia</i>	Si	1	0.85754(3)	0.52376(3)	0.35224(5)	0.00580(6)	4.018
<i>Sib</i>	Si	1	0.66345(3)	0.52318(3)	0.35089(5)	0.00584(6)	4.030
<i>Sic</i>	Si	1	0.47602(3)	0.33507(3)	0.35190(5)	0.00583(6)	4.016
<i>Sid</i>	Si	1	0.85708(3)	0.33515(3)	0.35308(5)	0.00584(6)	4.025
<i>Sie</i>	Si	1	0.66352(3)	0.14148(3)	0.35247(5)	0.00588(6)	4.027
<i>Sif</i>	Si	1	0.47589(3)	0.14180(3)	0.35261(5)	0.00587(6)	4.020
<i>Ya</i>	Al	0.366(3)	0.60366(2)	0.39553(2)	-0.01702(3)	0.00932(7)	2.354
	Fe	0.634(3)	0.60366(2)	0.39553(2)	-0.01702(3)	0.00932(7)	
<i>Yb</i>	Al	0.363(3)	0.79148(2)	0.39597(2)	-0.01564(3)	0.00883(6)	2.558
	Fe	0.637(3)	0.79148(2)	0.39597(2)	-0.01564(3)	0.00883(6)	
<i>Yc</i>	Al	0.399(3)	0.60335(2)	0.20827(2)	-0.01624(3)	0.00912(7)	2.308
	Fe	0.601(3)	0.60335(2)	0.20827(2)	-0.01624(3)	0.00912(7)	
<i>Za</i>	Al	0.953(3)	0.63171(3)	0.70363(3)	0.29762(5)	0.00621(11)	2.892
	Fe	0.047(3)	0.63171(3)	0.70363(3)	0.29762(5)	0.00621(11)	
<i>Zb</i>	Al	0.960(3)	0.96270(3)	0.70130(3)	0.63114(5)	0.00604(11)	2.894
	Fe	0.040(3)	0.96270(3)	0.70130(3)	0.63114(5)	0.00604(11)	
<i>Zc</i>	Al	0.934(3)	1.07095(3)	0.70356(3)	0.29759(5)	0.00629(10)	2.843
	Fe	0.066(3)	1.07095(3)	0.70356(3)	0.29759(5)	0.00629(10)	
<i>Zd</i>	Al	0.811(3)	0.73780(2)	0.70139(2)	0.63033(4)	0.00677(9)	2.659
	Fe	0.189(3)	0.73780(2)	0.70139(2)	0.63033(4)	0.00677(9)	
<i>Ze</i>	Al	0.964(3)	0.96241(3)	0.26211(3)	0.63122(5)	0.00608(11)	2.913
	Fe	0.036(3)	0.96241(3)	0.26211(3)	0.63122(5)	0.00608(11)	
<i>Zf</i>	Al	0.929(3)	0.96511(3)	0.59553(3)	-0.03573(5)	0.00621(10)	2.840
	Fe	0.071(3)	0.96511(3)	0.59553(3)	-0.03573(5)	0.00621(10)	
<i>B1</i>	B	1	0.77933(11)	0.89017(10)	0.4712(2)	0.00774(19)	2.963
<i>B2</i>	B	1	0.77625(10)	0.55377(10)	-0.1905(2)	0.00776(19)	2.966
<i>B3</i>	B	1	0.10989(10)	0.88943(10)	0.4761(2)	0.00776(19)	2.967
<i>O1a</i>	O	0.64(3)	0.66564(12)	0.33260(13)	0.13163(19)	0.0309(4)	1.236
<i>F1a</i>	F	0.36(3)	0.66564(12)	0.33260(13)	0.13163(19)	0.0309(4)	
<i>O2a</i>	O	1	0.54368(8)	0.27197(9)	-0.16428(15)	0.01388(19)	1.982
<i>O2b</i>	O	1	0.72711(9)	0.27113(9)	-0.16167(15)	0.01311(18)	2.011
<i>O2c</i>	O	1	0.72793(9)	0.45593(8)	-0.16350(15)	0.01340(18)	2.044
<i>O3a</i>	O	1	0.53209(8)	0.46779(8)	-0.13486(14)	0.01266(17)	1.119
<i>H3a</i>	H	1	0.5388(19)	0.4640(19)	-0.253(4)	0.015	
<i>O3b</i>	O	1	0.86882(10)	0.73373(10)	0.52987(15)	0.0156(2)	1.118
<i>H3b</i>	H	1	0.8775(19)	0.746(2)	0.409(4)	0.019	
<i>O3c</i>	O	1	0.93420(9)	0.46741(8)	-0.13587(14)	0.01305(18)	1.142
<i>H3c</i>	H	1	0.9310(19)	0.4665(19)	-0.254(4)	0.016	
<i>O4a</i>	O	1	0.75845(7)	0.51964(8)	0.42009(14)	0.01081(16)	2.036
<i>O4b</i>	O	1	0.48010(8)	0.24062(7)	0.42261(14)	0.01061(16)	2.039
<i>O4c</i>	O	1	0.75707(8)	0.24105(7)	0.42044(14)	0.01098(16)	2.049
<i>O5a</i>	O	1	0.57346(7)	0.42544(7)	0.44156(14)	0.01082(16)	1.976
<i>O5b</i>	O	1	0.57262(7)	0.14753(8)	0.44368(14)	0.01087(16)	1.974
<i>O5c</i>	O	1	0.85005(8)	0.42598(7)	0.44215(14)	0.01049(15)	1.984
<i>O6a</i>	O	1	0.86365(8)	0.52161(8)	0.13035(13)	0.00953(15)	2.006
<i>O6b</i>	O	1	0.65550(8)	0.52024(7)	0.12910(13)	0.00924(15)	1.977
<i>O6c</i>	O	1	0.65594(8)	0.13585(7)	0.13063(13)	0.00912(15)	1.965
<i>O6d</i>	O	1	0.86400(8)	0.34366(8)	0.13134(13)	0.00912(15)	2.011
<i>O6e</i>	O	1	0.47859(8)	0.34248(8)	0.13003(13)	0.00951(15)	1.958
<i>O6f</i>	O	1	0.48031(8)	0.13874(8)	0.13137(13)	0.01108(16)	1.937
<i>O7a</i>	O	1	0.66432(8)	0.61744(7)	0.42875(14)	0.01048(15)	1.984
<i>O7b</i>	O	1	0.95017(7)	0.61814(7)	0.43266(13)	0.00907(15)	1.970
<i>O7c</i>	O	1	0.66663(8)	0.04934(7)	0.43268(14)	0.00971(15)	1.970
<i>O7d</i>	O	1	0.38044(7)	0.04865(7)	0.43043(13)	0.00882(14)	1.977
<i>O7e</i>	O	1	0.38104(7)	0.33331(7)	0.43127(13)	0.00923(15)	1.987
<i>O7f</i>	O	1	0.94812(8)	0.33162(8)	0.43604(14)	0.01029(15)	1.976
<i>O8a</i>	O	1	0.87555(7)	0.60366(8)	-0.20605(15)	0.01057(15)	1.945
<i>O8b</i>	O	1	1.06094(7)	0.79018(7)	0.46340(15)	0.01073(16)	1.962
<i>O8c</i>	O	1	1.20888(7)	0.93929(7)	0.46216(14)	0.01028(15)	1.960
<i>O8d</i>	O	1	0.72997(8)	0.79163(7)	0.45430(16)	0.01246(17)	1.965
<i>O8e</i>	O	1	1.06320(8)	0.60691(7)	0.12676(15)	0.01121(16)	1.957
<i>O8f</i>	O	1	0.05962(8)	0.26961(8)	0.46655(15)	0.01178(16)	1.967

ponents at  $\sim 14200$  and  $13100$   $\text{cm}^{-1}$ , and the absorption band at lower energy is composed of components at  $9100$  and  $8300$   $\text{cm}^{-1}$ . This observed splitting of each of the two bands at  $\sim 14000$  and  $\sim 9000$   $\text{cm}^{-1}$  is due to the fact that they are both caused by electronic transitions involving  $\text{Fe}^{2+}$  at *Y*-sites as well as *Z*-sites (e.g., Smith 1978; Mattson and Rossman 1987; Taran et al. 1993; Bosi et al. 2015b). The broad and strong absorption band at  $22700$   $\text{cm}^{-1}$  is caused by  $\text{Fe}^{2+}$ - $\text{Ti}^{4+}$  charge transfer (CT) processes (e.g., Taran et al. 1993). The weak bands at  $20600$  and  $18000$   $\text{cm}^{-1}$  are due to electronic transitions in  $\text{Fe}^{3+}$  pairs at neighboring *Y*-sites (Mattson and Rossman 1984). Additional sharp absorption bands that were observed in the  $\mathbf{E} \parallel \mathbf{c}$ -spectrum in the range  $6700$ – $7000$   $\text{cm}^{-1}$  represent overtones of the fundamental (OH)-stretching modes. Comparison of the  $\mathbf{E} \perp \mathbf{c}$ -spectra of the optically uniaxial core and the optically biaxial rim (Fig. 5) shows a distinct decrease in intensity of the absorption bands at  $\sim 14000$  and  $\sim 9000$   $\text{cm}^{-1}$  for the rim. As the intensities of these two bands are proportional to the  $[\text{Fe}^{2+}]^*[\text{Fe}^{3+}]$  concentration product in the sample, one can conclude that the  $[\text{Fe}^{2+}]^*[\text{Fe}^{3+}]$  value in the crystal rim is only 75% of that of the crystal core. From this observation, in combination with the EMP data for the rim and the  $\text{Fe}^{3+}/\text{Fe}_{\text{tot}}$  ratio for the crystal core as determined by the Mössbauer spectroscopy, it gives 13.92 wt. % FeO and 1.53 wt. %  $\text{Fe}_2\text{O}_3$  for the rim. Consequently, the  $\text{Fe}^{3+}/\text{Fe}_{\text{tot}}$ -ratio in the crystal rim is 0.089 as compared to a ratio of 0.136 in the crystal bulk (from Mössbauer), which is mainly represented by the core composition. The much darker brown color of the crystal rim

(Fig. 1) results from its higher concentration of Fe<sup>2+</sup> and Ti<sup>4+</sup>. The intensified color is explained by a much stronger Fe<sup>2+</sup>-Ti<sup>4+</sup> charge-transfer (CT) band at ca. 22700 cm<sup>-1</sup> in the spectrum of the rim (Fig. 5). According to the EMP data for TiO<sub>2</sub> and FeO in combination with optical absorption spectroscopy (for the rim) and Mössbauer spectroscopy (for the core), the [Fe<sup>2+</sup>]\*[Ti<sup>4+</sup>] concentration product is ~4.5 times higher in the rim as compared to the core. The result for the rim spectrum is an absorbance for the Fe<sup>2+</sup>-Ti<sup>4+</sup> CT band at ca. 22700 cm<sup>-1</sup> that is offscale, although the measured tourmaline crystal is only 36 µm thick.

#### 4.2. Determination of number of atoms per formula unit (apfu)

In agreement with the structure-refinement results, the boron content was assumed to be stoichiometric (B<sup>3+</sup> = 3.000 apfu). Both the site-scattering (see Hawthorne et al. 1995 for the definition of site-scattering and site-populations) and the bond lengths of *B* and *T* are consistent with the *B* site fully occupied by B and no B at the *T* site (e.g., Bosi and Lucchesi 2007). The oxidation state of iron was determined by the MS and OAS in the core and rim, respectively, of the tourmaline crystal. All Mn was considered as Mn<sup>2+</sup>. In accordance with Pesquera et al. (2016), the Li<sub>2</sub>O content was assumed to be insignificant as MgO > 2 wt. % is contained in the sample studied. The (OH) content and the apfu were then calculated based on 31 anions and by charge balance with the assumption (*Y* + *Z*) = 9.000 apfu since the SiO<sub>2</sub> content was assumed to be equal to 6.000 apfu. It is worth noting that the calculated and measured SiO<sub>2</sub> values are practically the same within the standard uncertainty (Tab. 1).

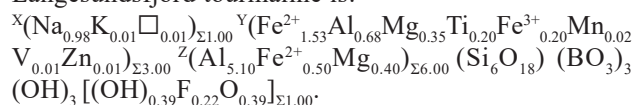
#### 4.3. Single-crystal X-ray diffraction and chemical formula

With regard to the site populations at *X*, *B*, *T*, O3 (≡ *V*) and O1 (≡ *W*), the standard site preference suggested for tourmaline (e.g., Henry et al. 2011) were actually satisfied, while the *Y* and *Z* site populations were optimized according to the procedure of Wright et al. (2000) in which the default setting was assumed, but the chemical variability was constrained by electroneutrality. The resulting empirical chemical formula, with the appropri-

Tab. 4 Continued

Site	Atom	<i>s.o.</i>	<i>x/a</i>	<i>y/b</i>	<i>z/c</i>	<i>U</i> <sub>eq</sub>	<i>B.V.S.</i>
<i>R3m</i>							
<i>X</i>	Na	1.02(1)	0.000000	0.000000	0.2344(3)	0.0263(5)	0.893
<i>Y</i>	Fe	0.626(4)	0.12503(2)	0.06252(2)	0.63132(4)	0.00913(7)	2.441
	Al	0.374(4)	0.12503(2)	0.06252(2)	0.63132(4)	0.00913(7)	
<i>Z</i>	Al	0.928(3)	0.29883(2)	0.26194(2)	0.61186(4)	0.00628(7)	2.854
	Fe	0.072(3)	0.29883(2)	0.26194(2)	0.61186(4)	0.00628(7)	
<i>Si</i>	Si	1	0.19170(2)	0.18984(2)	-0.00023(4)	0.00587(5)	4.037
<i>B</i>	B	1	0.11028(5)	0.22056(11)	0.4553(2)	0.00776(19)	2.972
O1	O	0.496(7)	0.000000	0.000000	0.7790(4)	0.0321(9)	1.164
F1	F	0.496(7)	0.000000	0.000000	0.7790(4)	0.0321(9)	
O2	O	1	0.06137(4)	0.12273(8)	0.48441(17)	0.01353(19)	1.932
O3	O	1	0.26791(11)	0.13396(5)	0.51187(16)	0.01382(19)	1.112
H3	H	1	0.260(3)	0.1298(13)	0.400(5)	0.017	
O4	O	1	0.09258(5)	0.18517(9)	0.06866(16)	0.01088(16)	2.046
O5	O	1	0.18489(9)	0.09245(5)	0.08995(16)	0.01068(16)	1.988
O6	O	1	0.19700(6)	0.18729(6)	0.77805(10)	0.00958(11)	1.974
O7	O	1	0.28428(6)	0.28471(5)	0.07948(11)	0.00963(11)	1.982
O8	O	1	0.20943(6)	0.27010(6)	0.44230(12)	0.01141(12)	1.966

ate grouping of sites, for the optically biaxial rim of the Langesundsfjord tourmaline is:



The calculated site-scattering from EMPA data (*X* 10.97 epfu, *Y* 63.37 epfu, *Z* 84.03 epfu) accords with the refined site-scattering (*X* 11.41 epfu, *Y* 63.34 epfu, *Z* 83.84 epfu). The detailed *Y* and *Z* site populations in the R1 model are reported in Tab. 6. The related weighted bond-valence sums, using Gagné and Hawthorne (2015) parameters, are reported in Tab. 4.

The order of about 0.50 apfu of Fe<sup>2+</sup> at the *Z* sites comes from the structure refinement of the R1 model that showed that one out of 6 independent *Z* sites (labeled as Zd) shows higher refined site scattering (15.5 eps vs. mean 13.7(2) eps for the other 5 sites), as well as longer, mean bond length (1.969 Å vs. 1.927(6) Å for the other 5 sites, Tab. 5) and larger octahedral-angle variance value (OAV, after Robinson et al. 1971; 53.44° vs. 42(3)°, Tab. 5). All these features support the local order of Fe<sup>2+</sup> at the Zd site, and optical absorption spectra support this order. Some Fe<sup>2+</sup> is ordered preferentially at Zf but to a lesser extent than at Zd (almost 1/3 of Zd; Tab. 6).

A less pronounced order of Al at the Yc site was also observed: lower refined scattering, mean bond length, and OAV than the other two *Y* sites is observed at Yc site (Tabs 4 and 5). This site shares one edge with the Zd site and another with Zf, where Fe<sup>2+</sup> is preferentially ordered in *Z* sites. There is prominent order of Fe<sup>3+</sup> and Ti<sup>4+</sup> at the Yb site. Incident bond-valence values are within 1.93 and 2.05 valence units (v.u.) at all anion sites of the R1 model, but for O1 and O3(a,b,c), which shows values of 1.24 v.u. and 1.12–1.14 v.u., respectively, in agreement with the presence of limited O<sup>2-</sup> at O1 and only (OH) groups at O3 sites. In line with short-range bond-valence constraints around the O1 (≡ *W*) site (e.g., Bosi 2011), the

**Tab. 5** Selected interatomic distances (Å) and angle distortion parameters.

				<i>R1</i>				<i>R3m</i>					
<i>Sia</i> –	O6a	1.6090(10)	<i>Sib</i> –	O7a	1.6036(11)	<i>Sic</i> –	O7e	1.6080(10)	<i>Si</i> –	O7	1.6069(8)		
	O7b	1.609(2)		O6b	1.6083(10)		O6e	1.6111(11)		O6	1.6061(8)		
	O4a	1.6291(11)		O4a	1.6298(11)		O4b	1.6277(11)		O4	1.6280(5)		
	O5c	1.6429(11)		O5a	1.644(2)		O5a	1.644(2)		O5	1.6418(5)		
Mean		1.6225	Mean		1.6214	Mean		1.6226	Mean		1.6207		
TAV	(°²)	8.269	TAV	(°²)	8.648	TAV	(°²)	8.984	TAV	(°²)	8.549		
<i>Sid</i> –	O7f	1.6042(11)	<i>Sie</i> –	O7c	1.6085(11)	<i>Sif</i> –	O6f	1.6034(10)					
	O6d	1.6084(10)		O6c	1.6085(10)		O7d	1.612(2)					
	O4c	1.631(2)		O4c	1.627(2)		O4b	1.6296(11)					
	O5c	1.6442(11)		O5b	1.6425(11)		O5b	1.6444(11)					
Mean		1.6221	Mean		1.6217	Mean		1.6224					
TAV	(°²)	8.962	TAV	(°²)	9.209	TAV	(°²)	7.731					
<i>Ya</i> –	O1a	2.0388(19)	<i>Yb</i> –	O1a	2.043(2)	<i>Yc</i> –	O1a	2.031(2)	<i>Y</i> –	O1	2.0349(15)		
	O6b	2.0352(15)		O6a	2.0451(19)		O6f	2.0156(18)		O6	2.0186(8)		
	O6e	2.0386(16)		O6d	2.0383(12)		O6c	2.0391(12)		O6	2.0187(8)		
	O2c	2.0196(18)		O2c	2.0196(14)		O2a	2.0186(14)		O2	2.0340(8)		
	O2a	2.0218(18)		O2b	2.0303(18)		O2b	2.0117(18)		O2	2.0340(8)		
	O3a	2.1686(15)		O3c	2.161(2)		O3b	2.146(2)		O3	2.1600(14)		
Mean		2.0537	Mean		2.0562	Mean		2.0436	Mean		2.0500		
OAV	(°²)	79.728	OAV	(°²)	79.439	OAV	(°²)	70.690	OAV	(°²)	77.053		
<i>Za</i> –	O8d	1.882(2)	<i>Zb</i> –	O8a	1.8957(19)	<i>Zc</i> –	O8b	1.8989(11)	<i>Z</i> –	O8	1.8993(8)		
	O7a	1.9483(12)		O7b	1.8992(11)		O8e	1.9350(11)		O8	1.9370(9)		
	O6d	1.8872(12)		O6c	1.8879(12)		O7c	1.9028(11)		O7	1.9019(8)		
	O7d	1.9000(11)		O8b	1.9313(19)		O6e	1.8931(12)		O6	1.8914(8)		
	O8c	1.9397(19)		O7e	1.9622(12)		O7b	1.979(2)		O7	1.9726(8)		
	O3c	1.9880(13)		O3b	1.9616(14)		O3a	1.987(3)		O3	1.9869(6)		
Mean		1.9241	Mean		1.9230	Mean		1.9326	Mean		1.9315		
OAV	(°²)	38.606	OAV	(°²)	42.178	OAV	(°²)	44.458	OAV	(°²)	43.556		
<i>Zd</i> –	O8f	1.9314(12)	<i>Ze</i> –	O7f	1.8812(11)	<i>Zf</i> –	O6a	1.8857(18)	<i>O3</i> –	H3	0.81(3)		
	O6f	1.9258(18)		O8f	1.9129(11)		O7e	1.9026(15)					
	O7a	1.9358(15)		O6b	1.8853(11)		O8e	1.8986(11)					
	O8d	1.9759(12)		O8c	1.8971(11)		O8a	1.9455(11)					
	O7f	2.0189(14)		O7d	1.962(2)		O7c	1.9780(13)					
	O3b	2.0264(15)		O3a	1.986(2)		O3c	1.9910(14)					
Mean		1.9689	Mean		1.9208	Mean		1.9336					
OAV	(°²)	53.440	OAV	(°²)	39.069	OAV	(°²)	45.639					
<i>B1</i> –	O8d	1.373(2)	<i>B2</i> –	O8f	1.3754(19)	<i>B3</i> –	O8b	1.380(2)	<i>B</i> –	O8×2	1.3772(11)		
	O8e	1.3815(19)		O8a	1.382(2)		O8c	1.377(2)					
	O2a	1.375(2)		O2c	1.371(2)		O2b	1.371(2)		O2	1.3718(19)		
Mean		1.3764	Mean		1.3763	Mean		1.3761	Mean		1.3754		
			<i>Na1</i> –	O2c	2.4803(18)								
				O2a	2.4800(18)								
				O2b	2.4910(15)				<i>Na1</i> –	O2×3	2.4815(19)		
				O5c	2.746(3)								
				O5a	2.7761(19)					O5×3	2.7666(14)		
				O5b	2.8006(18)								
				O4c	2.782(3)					O4×3	2.8316(15)		
O3a–	H3a	0.81(3)		O4b	2.855(3)				Mean		2.6932		
O3b–	H3b	0.89(3)		O4a	2.848(3)								
O3c–	H3c	0.86(3)	Mean		2.6954				<i>O3</i> –	H3	0.81(3)		

Note: TAV and OAV = tetrahedral and octahedral angle variance by Robinson et al. (1972)

amount of calculated O<sup>2-</sup> can be locally related to the presence of Al<sup>3+</sup>–Ti<sup>4+</sup>–Al<sup>3+</sup> or Al<sup>3+</sup>–Fe<sup>3+</sup>–Al<sup>3+</sup> triplets at the Ya–Yb–Yc sites, ca. 38% of probability (with some Al<sup>3+</sup> at Ya being substituted by Fe<sup>3+</sup> or V<sup>3+</sup>). Fluorine is probably related to Fe<sup>2+</sup>–Mg<sup>2+</sup>–Fe<sup>2+</sup> triplets.

## 5. Discussion

Previous studies report optically anomalous tourmaline with biaxial character, which is incompatible with its putative *R3m* symmetry. The optically zoned tourmaline crystal has the chemical composition of schorl in the core and the rim: the former is slightly richer in Al, Fe<sup>3+</sup> and O<sup>2-</sup>, whereas the latter is somewhat richer in Ti, Mg, F and Fe<sup>2+</sup> (Tab. 1).

Regarding the rim zone, the results of structure refinement with an *R1* model show preferential order of Fe<sup>2+</sup> at the Zd and Zf sites, and Fe<sup>3+</sup> and Ti<sup>4+</sup> order at the Yb site, in accord with the spectroscopic results. Interestingly, order at the Z sites occurs in alternating fashion along [110], breaking the symmetry of the 3Y–6Z cluster (Fig. 6). This is related to the observed ellipticity of the optical indicatrix in the Z–Y plane and its relative orientation to the crystallographic axes of the triclinic cell. Order is ascribed to preferential selectivity at the growing surface of the prism. Positions related by symmetry in the bulk of a crystal may be structurally and energetically non-equivalent on a growing surface. These differences lead to an ordered distribution of structural units on the surface that remains metastably included in the structure as the crystal grows if diffusion is too slow. The crystal's symme-





Some schorl samples from the Langesundsfjord area, named as *luinaite-(OH)* and reported as monoclinic (*Cm*) by Kolitsch et al. (2013), should be best termed as schorl-*1M*. Consequently, it can be concluded that trigonal, monoclinic, and triclinic schorl samples may occur in Langesundsfjord area. Our study indicates that even in the presence of excellent statistical residual factors from excellent X-ray diffraction data, the lowering of symmetry due to cation ordering may have been overlooked in many other tourmaline samples in the absence of an opportune check of the optical behavior.

*Acknowledgments.* Chemical analyses were done with the kind assistance of M. Serracino to whom the authors express their gratitude. F.C. acknowledges financial support by the grant Ricerca Locale 2019, Università di Milano and from the Italian Ministry of Education (MIUR) through the project “Dipartimenti di Eccellenza 2018–2022”. Funding by Sapienza University of Rome (Prog. Università 2020 to F.B.) is gratefully acknowledged. Careful reviews by Frank Hawthorne and John Hughes are appreciated.

*Electronic supplementary material.* The crystallographic information files (CIF) are available online on the Journal website (<http://dx.doi.org/10.3190/jgeosci.344>).

## References

- AKIZUKI M (1981) Origin of optical variation in analcime. *Am Mineral* 66: 403–409
- AKIZUKI M (1984) Origin of optical variations in grossular-andradite garnet. *Am Mineral* 66: 403–409
- ALLEN FM, BUSECK PR (1988) XRD, FTIR and TEM studies of optically anisotropic grossular garnets. *Amer Miner* 73: 568–584
- ANDERSEN T, ERAMBERT M, LARSEN AO, SELBEKK RS (2010) Petrology of nepheline syenite pegmatites in the Oslo Rift, Norway: Zirconium silicate mineral assemblages as indicators of alkalinity and volatile fugacity in mildly agpaitic magma. *J Petrol* 51: 2303–2325
- ANDRUT M, WILDNER M, BERAN A (2002) The crystal chemistry of birefringent natural uvarovites. Part IV. OH defect incorporation mechanisms in non-cubic garnets derived from polarized IR spectroscopy. *Eur J Mineral* 14: 1019–1026
- ANTAO SM (2013) The mystery of birefringent garnet: is the symmetry lower than cubic? *Powder Diffr* 28: 265–272
- BOSI F (2011) Stereochemical constraints in tourmaline: from a short-range to a long-range structure. *Canad Mineral* 49: 17–27
- BOSI F, LUCCHESI S (2007) Crystal chemical relationships in the tourmaline group: structural constraints on chemical variability. *Amer Miner* 92: 1054–1063
- BOSI F, SKOGBY H, LAZOR P, REZNITSKII L (2015a) Atomic arrangements around the O3 site in Al- and Cr-rich oxy-tourmalines: a combined EMP, SREF, FTIR and Raman study. *Phys Chem Miner* 42: 441–453
- BOSI F, ANDREOZZI GB, HÅLENIUS U, SKOGBY H (2015b) Experimental evidence for partial Fe<sup>2+</sup> disorder at the Y and Z sites of tourmaline: a combined EMP, SREF, MS, IR and OAS study of schorl. *Mineral Mag* 79: 515–528
- BOSI F, SKOGBY H, BALIĆ-ŽUNIĆ T (2016) Thermal stability of extended clusters in dravite: a combined EMP, SREF and FTIR study. *Phys Chem Miner* 43: 395–407
- BOSI F, SKOGBY H, HÅLENIUS U, CIRIOTTI ME, MILLS SJ (2022) Lowering *R3m* Symmetry in Mg–Fe-tourmalines: the crystal structures of triclinic schorl and oxy-dravite, and the mineral luinaite-(OH) discredited. *Minerals* 12: 430
- BRAUNS R (1891) *Optischen Anomalien der Krystalle*. Bey S. Hirzel, Leipzig (in German)
- BROGGER WC (1890) Die mineralien der syenitpegmatitgänge der Südnorwegischen augit- und nephelinesyenite. *Z Kristallogr Mineral* 16: 1–663 (in German)
- CAMPOMENOSI N, MAZZUCHELLI ML, MIHAILOVA BD, ANGEL RJ, ALVARO M (2020) Using polarized Raman spectroscopy to study the stress gradient in mineral systems with anomalous birefringence. *Contrib Mineral Petrol* 175: 1–16
- CESARE B, NESTOLA F, JOHNSON T, MUGNAIOLI E, DELLA VENTURA G, PERUZZO L, BARTOLI O, VITI C, ERICKSON T (2019) Garnet, the archetypal cubic mineral, grows tetragonal. *Sci Rep* 9: 14672
- CESARE B, CAMPOMENOSI N, SHRIBAK M (2022) Polychromatic polarization: Boosting the capabilities of the good old petrographic microscope. *Geology* 50: 137–141
- FOORD EE, CUNNINGHAM CG (1978) Thermal transformation of anomalously biaxial dimetric crystals. *Amer Miner* 63: 747–749
- FOORD EE, MILLS BA (1978) Biaxiality in ‘isometric’ and ‘dimetric’ crystals. *Amer Miner* 63: 316–325
- GAGNÉ OC, HAWTHORNE FC (2015) Comprehensive derivation of bond-valence parameters for ion pairs involving oxygen. *Acta Crystallogr B* 71: 562–578
- GONZALEZ-CARREÑO T, FERNÁNDEZ M, SANZ J (1988) Infrared and electron microprobe analysis of tourmaline. *Phys Chem Miner* 15: 452–460
- GRIFEN DT, HATCH DM, PHILLIPS WR, KULAKSIZ S (1992) Crystal chemistry and symmetry of a birefringent tetragonal pyralspite<sub>75</sub>–grandite<sub>25</sub> garnet. *Amer Miner* 77: 399–406
- HARIYA Y, KIMURA M (1978) Optical anomaly garnet and its stability field at high pressures and temperatures. *J Fac Sci, Hokkaido Univ, Ser IV*, 18: 611–624
- HAWTHORNE FC, UNGARETTI L, OBERTI R (1995) Site populations in minerals; terminology and presentation of results of crystal-structure refinement. *Canad Mineral* 33(4): 907–911

- HENRY DJ, NOVÁK M, HAWTHORNE FC, ERTL A, DUTROW BL, UHER P, PEZZOTTA F (2011) Nomenclature of the tourmaline-super group minerals. *Amer Miner* 96: 895–913
- HOFMEISTER AM, SCHAAL RB, CAMPBELL KR, BERRY SL, FAGAN TJ (1988) Prevalence and origin of birefringence in 48 garnets from the pyrope–almandine–grossularite–spessartine quaternary. *Amer Miner* 83: 1293–1301
- HOWELL D (2012) Strain-induced birefringence in natural diamond: a review. *Eur J Mineral* 24: 575–585
- HUGHES JM, RAKOVAN J, ERTL A, ROSSMAN GR, BAKSHEEV I, BERNHARDT H-J (2011) Dissymmetrization in tourmaline: the atomic arrangement of sectorally zoned triclinic Ni-bearing dravite. *Canad Mineral* 49: 29–40
- ISOGAMI M, SUNAGAWA I (1975) X-ray topographic study of a topaz crystal. *Amer Miner* 60: 889–897
- KOLITSCH U, HUSDAL TA, BRANDSTÄTTER F, ERTL A (2011) New crystal-chemical data for members of the tourmaline group from Norway: occurrences of fluor-schorl and luinaite-(OH). *Norsk Bergverksmuseum Skrift* 46: 17–24
- KOLITSCH U, ANDRESEN P, HUSDAL TA, ERTL A, HAUGEN A, ELLINGSEN HV, LARSEN AO (2013) Tourmaline-group minerals from Norway, part II: occurrences of luinaite-(OH) in Tvedalen, Larvik and Porsgrunn, and fluor-liddicoatite, fluor-elbaite and fluor-schorl at Ågskardet, Nordland. *Norsk Bergverksmuseum Skrift* 50: 23–41
- MADELUNG A (1883) Beobachtungen mit Brethaupt's Polarisationmikroskop. *Z Kristallogr* 7: 73–76
- MATTSON SM, ROSSMAN GR (1984) Ferric iron in tourmaline. *Phys Chem Miner* 11: 225–234
- MATTSON SM, ROSSMAN GR (1987) Fe<sup>2+</sup>–Fe<sup>3+</sup> interactions in tourmaline. *Phys Chem Miner* 14: 163–171
- MOMMA K, IZUMI F (2011) VESTA 3 for three-dimensional visualization of crystal, volumetric, and morphology data. *J Appl Cryst* 44: 1272–1276
- NICKEL EH, GRICE JD (1998) The IMA Commission on New Minerals and Mineral Names; procedures and guidelines on mineral nomenclature, 1998. *Canad Mineral* 36: 913–926
- PESQUERA A, GIL-CRESPO PP, TORRES-RUIZ F, TORRES-RUIZ J, RODA-ROBLES E (2016) A multiple regression method for estimating Li in tourmaline from electron microprobe analyses. *Mineral Mag* 80: 1129–1133
- POUCHOU JL, PICOIR F (1991) Quantitative analysis of homogeneous or stratified microvolumes applying the model “PAP”. In: HEINRICH KFJ, NEWBURY DE (Eds) *Electron Probe Quantitation*, Pp. 31–75, Plenum, New York
- PRESCHER C, MCCAMMON C, DUBROWINSKY L (2012) MossA: a program for analyzing energy-domain Mössbauer spectra from conventional and synchrotron sources. *J Appl Crystallogr* 45: 329–331
- ROBINSON K, GIBBS GV, RIBBE PH (1971) Quadratic elongation: a quantitative measure of distortion in coordination polyhedra. *Science* 172: 567–570
- SHELDRIK GM (2015) Crystal Structure refinement with SHELX. *Acta Crystallogr C* 71: 3–8
- SHRIBAK M (2015) Polychromatic polarization microscope: Bringing colors to a colorless world. *Sci Rep* 5: 17340
- SHRIBAK M (2017) Polychromatic polarization state generator and its application for real-time birefringence imaging: US Patent 9625369, International Class G01N 21/2
- SHTUKENBERG A, ROZHDESTVENSKAYA I, FRANK-KAMENETSKAYA O, BRONZOVA J, EULER H, KIRFEL A, BANNOVA I, ZOLOTAREV A (2007) Symmetry and crystal structure of biaxial elbaite-liddicoatite tourmaline from the Transbaikalia region, Russia. *Amer Miner* 92: 675–686
- SMITH G (1978) A reassessment of the role of iron in the 5,000–30,000 cm<sup>-1</sup> region of the electronic absorption spectra of tourmaline. *Phys Chem Miner* 3: 343–373
- STEVEN CJ, GUNTER ME (2018) EXCELIBR: An Excel spreadsheet for solving the optical orientation of uniaxial and biaxial crystals. *The Microscope* 65: 147–152
- TAKEUCHI Y, HAGA N (1976) Optical anomaly and structure of silicate garnets. *Proc Jap Acad* 52: 228–231
- TARAN MN, LEBEDEV AS, PLATONOV AN (1993) Optical absorption spectroscopy of synthetic tourmalines. *Phys Chem Miner* 20: 209–220
- WATENPHUL A, BURGDORF M, SCHLÜTER J, HORN I, MALCHEREC T, MIHAILOVA B (2016) Exploring the potential of Raman spectroscopy for crystallochemical analyses of complex hydrous silicates: II. Tourmalines. *Amer Miner* 101: 970–985
- WERTHEIM G (1851) Note sur la double réfraction artificiellement produite dans les cristaux du système régulier. *Compt Rend Acad Sci Paris* 33: 576 (in French)
- WERTHEIM G (1854) Sur la double réfraction temporairement produite dans les corps isotropes, et sur la relation entre l'élasticité mécanique et entre l'élasticité optique. *Ann Chim Phys ser III* 40: 156 (in French)
- WILSON AJC (1992) *International Tables for Crystallography*, Volume C: Mathematical, physical and chemical tables. Kluwer Academic Publishers, Dordrecht, NL, pp 1–883
- WRIGHT SE, FOLEY JA, HUGHES JM (2000) Optimization of site occupancies in minerals using quadratic programming. *Amer Miner* 85, 524–531

## **2.2. High-Temperature experiments**

### 2.2.1. Fe-rich fluor-elbaite





# In situ high-temperature behaviour of fluor-elbaite: breakdown conditions and products

Beatrice Celata<sup>1</sup> · Paolo Ballirano<sup>1</sup> · Giovanni B. Andreozzi<sup>1</sup> · Ferdinando Bosi<sup>1</sup>

Received: 31 March 2021 / Accepted: 19 May 2021 / Published online: 8 June 2021  
© The Author(s) 2021

## Abstract

The thermal behaviour of a fluor-elbaite from Minas Gerais (Brazil) was investigated at room pressure through in situ high-temperature X-ray powder diffraction (HT-XRPD), until the breakdown conditions were reached. The variations of fluor-elbaite structural parameters (unit-cell parameters and mean bond distances) were monitored together with site occupancies, and two main internal reactions were identified: the thermally-induced Fe oxidation process counterbalanced by (OH)<sup>-</sup> deprotonation, which starts at 500 °C (773 K), followed by a partial intracrystalline Fe–Al exchange between the octahedrally-coordinated Y and Z sites. The fluor-elbaite breakdown reaction occurs between 850 °C (1123 K) and 900 °C (1173 K). The breakdown products were identified at room temperature by XRPD and the breakdown reaction can be described by the following reaction: tourmaline → B-bearing mullite + hematite + spinel + B-poor (Na, Li, H<sub>2</sub>O)-bearing glass. Boromullite itself was not observed in the final heating products, and the B-bearing mullite from the breakdown reaction exhibited unit-cell parameters  $a = 7.5382(2)$  Å,  $b = 7.6749(2)$  Å,  $c = 2.8385(1)$  Å,  $V = 164.22(1)$  Å<sup>3</sup> (space group *Pbam*) consistent with an approximate Al<sub>8.5</sub>B<sub>1.5</sub>Si<sub>2</sub>O<sub>19</sub> composition.

**Keywords** Fluor-elbaite · HT-XRPD · Thermal expansion · Iron oxidation · Deprotonation · Intracrystalline cations exchange · Structural breakdown

## Introduction

Tourmaline is one of the most fascinating and colourful accessory mineral occurring in a variety of geological environments, from diagenetic stages to granulite facies grade (e.g., Henry and Dutrow 1996; Dutrow and Henry 2011; Bosi et al. 2018a, 2019a; Andreozzi et al. 2020).

Tourmaline is a cyclosilicate rich in B with a very complex composition represented by the general chemical formula: XY<sub>3</sub>Z<sub>6</sub>T<sub>6</sub>O<sub>18</sub>(BO<sub>3</sub>)<sub>3</sub>V<sub>3</sub>W, where X = Na<sup>+</sup>, K<sup>+</sup>, Ca<sup>2+</sup>, □ (= vacancy); Y = Al<sup>3+</sup>, Fe<sup>3+</sup>, Cr<sup>3+</sup>, V<sup>3+</sup>, Mg<sup>2+</sup>, Fe<sup>2+</sup>, Mn<sup>2+</sup>, Li<sup>+</sup>; Z = Al<sup>3+</sup>, Fe<sup>3+</sup>, Cr<sup>3+</sup>, V<sup>3+</sup>, Mg<sup>2+</sup>, Fe<sup>2+</sup>; T = Si<sup>4+</sup>, Al<sup>3+</sup>, B<sup>3+</sup>; B = B<sup>3+</sup>; V = (OH)<sup>-</sup>, O<sup>2-</sup>; W = (OH)<sup>-</sup>, F<sup>-</sup>, O<sup>2-</sup>. Note that the non-italicized letters X, Y, Z, T and B represent groups of cations at the <sup>[9]</sup>X, <sup>[6]</sup>Y, <sup>[6]</sup>Z, <sup>[4]</sup>T and <sup>[3]</sup>B

crystallographic sites (*italicized letters*) and the letters V and W represent groups of anions accommodated at the [3]-coordinated O3 and O1 crystallographic sites, respectively. Tourmaline-supergroup minerals are currently classified into three groups, vacant, alkali and calcic, based on the X-site occupancy (Henry et al. 2011). A further level of classification into subgroups is based on the charge arrangements at the Y and Z sites. Tourmalines are also distinguished by the dominant anion at the W position of the general formula into hydroxy-, fluor- and oxy-species.

Tourmaline gained more and more interest along the years surely because of its remarkable power to carry a lot of information about its genetic conditions (e.g., Federico et al. 1998; Dutrow and Henry 2011). However, tourmaline relevance stands even more in its role of boron and water carrier from the crust deep down the mantle and the implications it may have (Henry and Dutrow 1996; Ota et al. 2008a, b; Shimizu and Ogasawara 2013; Lussier et al. 2016). In fact, the boron and water released because of tourmaline breakdown reduce both the solidus temperature of the hosting rock and the viscosity of any associated melt (Pichavant 1981; Dingwell et al. 1992). Remarkably, how

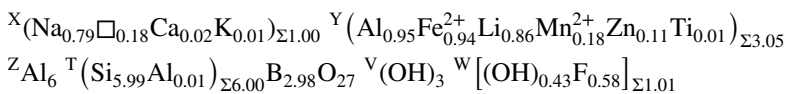
✉ Beatrice Celata  
beatrice.celata@uniroma1.it

✉ Paolo Ballirano  
paolo.ballirano@uniroma1.it

<sup>1</sup> Dipartimento di Scienze della Terra, Sapienza Università di Roma, Piazzale A. Moro 5, 00185 Rome, Italy

the breakdown conditions are reached in terms of structural variations has never been investigated so far, as well as it remains unclear when the deprotonation process exactly starts, i.e., if "water" is actually released throughout the breakdown process or way before the structural collapse as suggested, for example, by the studies of Filip et al. (2012) and Bosi et al. (2018b).

The present work aims at investigating the thermal behaviour of the fluor-elbaite, ideally  $\text{Na}(\text{Li}_{1.5}\text{Al}_{1.5})\text{Al}_6(\text{Si}_6\text{O}_{18})(\text{BO}_3)_3(\text{OH})_3\text{F}$  (Bosi et al. 2013) at room pressure. A Fe-bearing deep green fluor-elbaite sample from the Cruzeiro pegmatite (Minas Gerais, Brazil), previously fully characterized by Bosi et al. (2019b) with the formula:



was studied by in situ high-temperature X-ray powder diffraction (HT-XRPD) up to the structural breakdown.

## Experimental

The fluor-elbaite crystal fragment was gently grinded in ethanol, in an agate mortar; the powder was then loaded in a 0.7 mm diameter  $\text{SiO}_2$ -glass capillary kept open at one side. The capillary was fixed to a hollow corundum tube using a HT cement and mounted and aligned on a goniometer head. The capillary was inserted into the heating chamber for capillaries, developed by MRI and Bruker AXS, that is placed along the beam path of the diffractometer. Characteristics and thermal calibration procedure of the chamber are reported in Ballirano and Melis (2007).

In situ HT-XRPD data were measured on a Bruker AXS D8 Advance that operates in  $\theta/\theta$  geometry in transmission mode. The instrument is fitted with focussing multilayer graded (Göbel) mirrors placed along the incident beam and Soller slits on both the incident ( $2.3^\circ$  opening angle) and diffracted (radial) beams. The data were collected using a position sensitive detector (PSD) VÅntec-1 operating at an opening angle of  $6^\circ 2\theta$ . Details of the data collection are reported in Table 1.

At the end of the heating run, the powder was cooled back at room temperature (RT) within the chamber, removed from the capillary, re-homogenised and charged in a new borosilicate-glass capillary. This procedure was followed to reduce the possible effect of textured recrystallization at the walls of the capillary. As a side effect, re-homogenisation involved also powder lying at the coldest extremity of the capillary where  $T$ , owing to thermal gradients, was significantly smaller than that reached in the analysed part of the sample. A measurement of this sample was performed outside the chamber.

**Table 1** Miscellaneous data of the data collection and Rietveld refinements of the fluor-elbaite studied

$2\theta$ range ( $^\circ$ )	7–145
$2\theta$ step-size ( $^\circ$ )	0.021798
Counting time (s)	3
$T_{\text{max}}$ ( $^\circ\text{C}$ )	850
$T$ steps ( $^\circ\text{C}$ )	50
Rp (%)	1.772–2.275
Rwp (%)	2.392–3.312
$R_{\text{Bragg}}$ (%)	0.907–1.303
DWd	0.801–1.363
$\chi^2$	1.767–2.509

Definition of the statistical indicators, from Young (1993)

Data evaluation was performed by the Rietveld method using Topas 6 (Bruker 2016). The Fundamental Parameters Approach (FPA: Cheary and Coelho 1992) was used to describe the peak shape. The equation of Sabine et al. (1998) for a cylindrical sample was applied for absorption correction using the approach of Ballirano and Maras (2006) for handling the correlation existing between displacement parameters and absorption. In particular, isotropic displacement parameters were constrained as follow:  $B_Y = B_Z = B_B = B_T$ ;  $B_{O2} = B_{O3} = B_{O4} = B_{O5} = B_{O6} = B_{O7} = B_{O8}$ . Preferred orientation effects were corrected using spherical harmonics (8th-order, nine refinable parameters) by selecting the number of appropriate terms following the procedure described by Ballirano (2003). As expected for data collected in transmission-mode on capillaries, the coefficients refined to small values. Starting structural data were those of Bosi et al. (2019b) and each refined structure at a given non-ambient  $T$  was used as input for the subsequent  $T$ . EoSFit7-GUI (Gonzalez-Platas et al. 2016) was used to analyse the dependence of the unit-cell parameters from  $T$  employing the equation of Berman (1988) for fitting the data. This equation has the advantage to permit accommodation of non-linear thermal expansion. It is expressed as  $X_T = X_0 \left[ 1 + a_0(T - T_{\text{ref}}) + \frac{1}{2}a_1(T - T_{\text{ref}})^2 \right]$  with  $X = V, a, c$ . Miscellaneous information regarding the refinements is listed in Table 1 and a representative example of Rietveld plots is shown in Fig. 1. CIF files of the fluor-elbaite structure refined at the various  $T$  are given in Online Resource.

## Results and discussion

### Breakdown products of F-elbaite

The first evidence of fluor-elbaite structural breakdown was observed at 850  $^\circ\text{C}$  owing to the occurrence of very weak

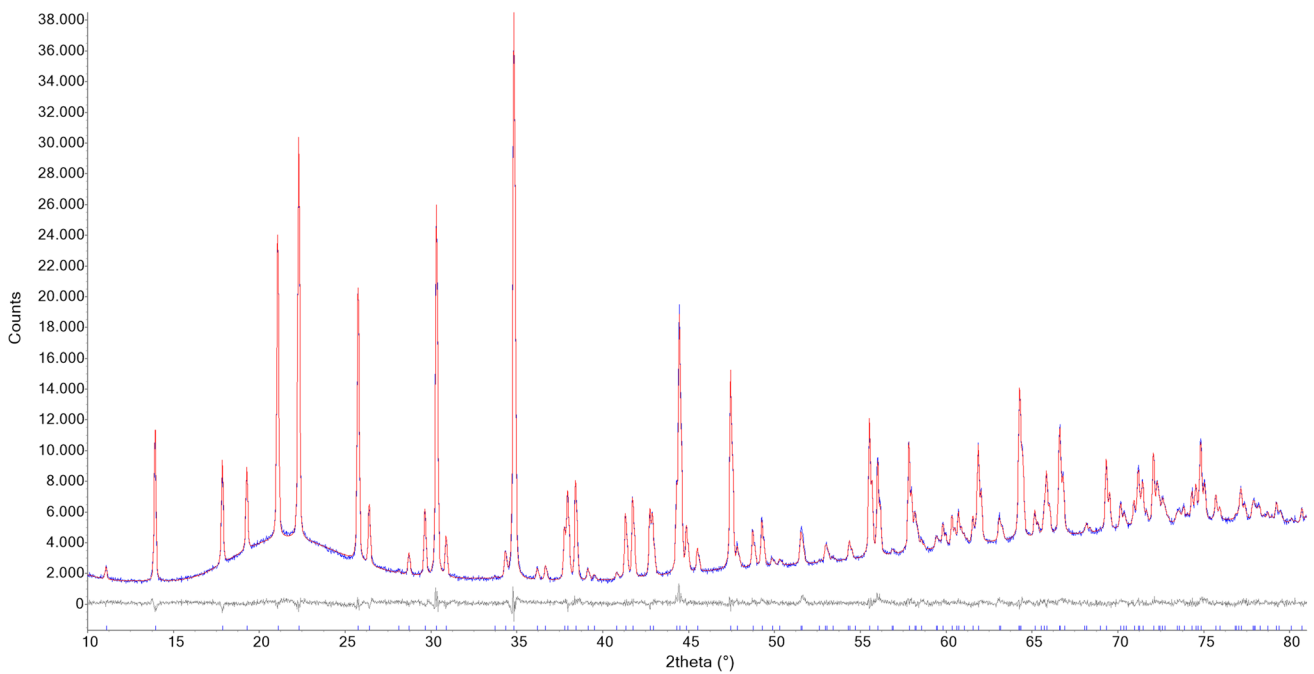


**Fig. 1** Representative example of the Rietveld plots of the diffraction pattern collected at 423 K. Blue: experimental; red: calculated; grey: difference; vertical bars: position of calculated Bragg reflections of the fluor-elbaite studied

diffraction reflections assigned to a mullite-like phase. The breakdown was completed at the  $T$  of 900 °C. The quantitative phase analysis (QPA) of the sample cooled down at RT (Fig. 2) indicates the occurrence of prevailing mullite-like

phase plus minor hematite and traces of spinel as breakdown products. Furthermore, the increased intensity of the broad band centred at ca. 22°  $2\theta$ , in addition to the contribution of the capillary glass, also reveals the occurrence of some

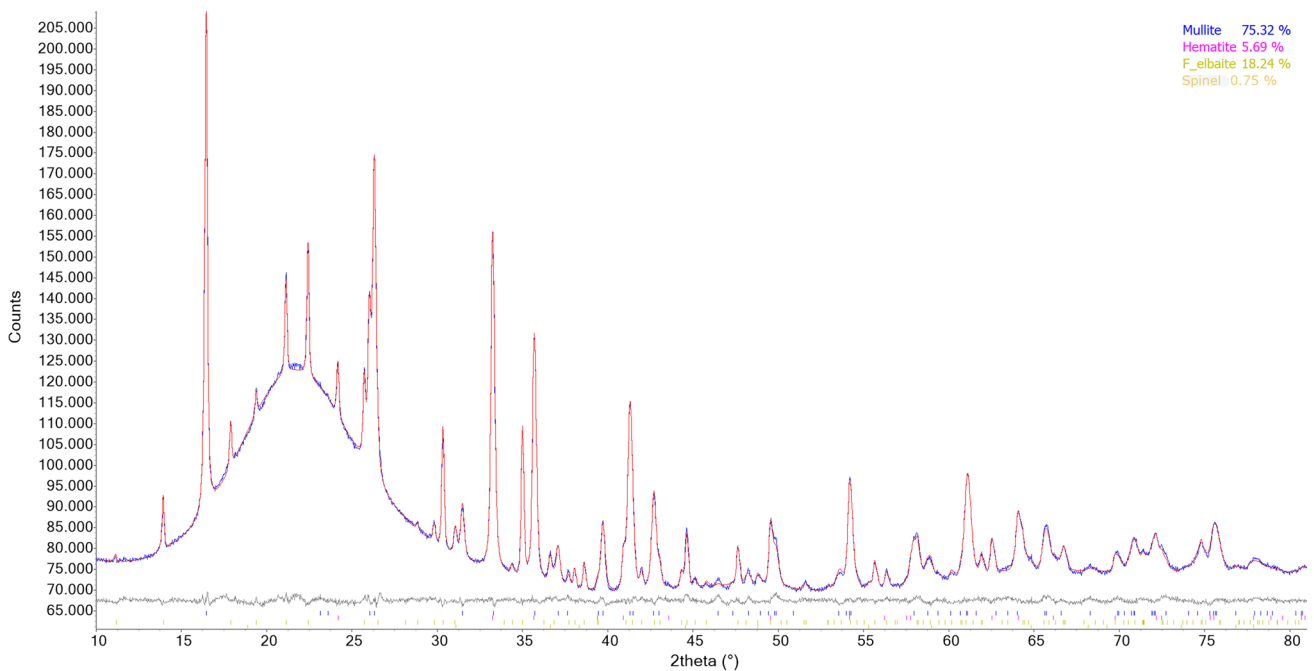


**Fig. 2** Magnified 10–80°  $2\theta$  view of the Rietveld plots of the products of breakdown of the fluor-elbaite studied. Blue: experimental; red: calculated; grey: difference; vertical bars: position of calculated

Bragg reflections of (from above to below) mullite, hematite, fluor-elbaite (unreacted) and spinel

amorphous material, likely being the cooling product of a Si-rich hydrous fluid derived from the tourmaline breakdown. Relicts of unreacted fluor-elbaite were caused by the re-homogenisation of the powder (see “Experimental”).

Refined unit-cell parameters of the mullite-like phase, in the space group *Pbam*, were  $a = 7.5382(2)$  Å,  $b = 7.6749(2)$  Å,  $c = 2.8385(1)$  Å,  $V = 164.22(1)$  Å<sup>3</sup> and are consistent with those of B-mullites (Lührs et al. 2014). An estimation of the B content was carried out using the regression equations proposed by Lührs et al. (2014), based on the *b*- and *c*-parameters ( $b = -0.0030(2) \times B_2O_3$  mol.% + 7.6921(8):  $R^2 = 0.99$ ;  $c = -0.0041(2) \times B_2O_3$  mol.% + 2.8876(19):  $R^2 = 0.96$ ). The results point out to a content of ca. 6–12 mol.% B<sub>2</sub>O<sub>3</sub>, corresponding to the Al<sub>8</sub>B<sub>2</sub>Si<sub>2</sub>O<sub>19</sub>–Al<sub>9</sub>BSi<sub>2</sub>O<sub>19</sub> compositional range. It is worth noting that the mineral boromullite, space group being *Cmc2<sub>1</sub>*,  $a = 5.7168(19)$  Å,  $b = 15.023(5)$  Å,  $c = 7.675(3)$  Å,  $V = 659.2(7)$  Å<sup>3</sup> with composition Al<sub>9</sub>BSi<sub>2</sub>O<sub>19</sub>, has been described by Buick et al. (2008). However, attempts to use this superstructure as starting structure for the present B-mullite (using a 4 × larger supercell  $a' = 2c = 5.6770(1)$  Å,  $b' = 2a = 15.0763(4)$  Å and  $c' = b = 7.6749(2)$  Å, obtained by the transformation matrix 002/200/010) produced relatively strong unobserved reflections, clearly indicating the inability of the model to fit the data. Moreover, Werdning and Schreyer (1992) reported the orthorhombic unit-cell parameters  $a = 5.681(2)$  Å,  $b = 15.014(5)$  Å,  $c = 7.671(4)$  Å,  $V = 654.3(3)$  Å<sup>3</sup> for a sample of Al<sub>8</sub>B<sub>2</sub>Si<sub>2</sub>O<sub>19</sub> composition. It is interesting to notice that  $V'$  of the present sample, calculated from the 4 × larger supercell, is equal to 656.88(3) Å<sup>3</sup>, which is a value located exactly halfway between those of Al<sub>8</sub>B<sub>2</sub>Si<sub>2</sub>O<sub>19</sub> and Al<sub>9</sub>BSi<sub>2</sub>O<sub>19</sub>.

Finally, the recently discovered (Li,Be)-bearing borosilicate mineral vránaite, ideally Al<sub>16</sub>B<sub>4</sub>Si<sub>4</sub>O<sub>38</sub> (Novák et al. 2015; Cempírek et al. 2016), was also considered since it was found as a breakdown product of spodumene in the elbaite-subtype Manjaka granitic pegmatite (Novák et al. 2015), and its space group *I2/m* can be derived from the orthorhombic supergroup *Pbam* (Fischer and Schneider 2008) to which our structural refined data refer to. Vránaite cell parameters are  $a = 10.383(1)$  Å,  $b = 5.668(1)$  Å,  $c = 10.823(1)$  Å,  $\beta = 90.11(1)^\circ$ ,  $V = 637.0(1)$  Å<sup>3</sup>. However, similarly to boromullite, attempts to fit the XRPD data using the structural parameters of vránaite produced significantly worse agreement indices than those obtained for B-mullite. In particular, the markedly different cell parameters resulted in a unit cell volume of ca. 657 Å<sup>3</sup>, significantly larger than that reported for vránaite.

Thus, a mullite-type phase of approximate Al<sub>8.5</sub>B<sub>1.5</sub>Si<sub>2</sub>O<sub>19</sub> composition may represent the breakdown crystalline phase incorporating B.

Because the B/Si ratio observed in pristine fluor-elbaite was 1:2 and that of the present recrystallized B-mullite is

approximately 1.5:2, it is most likely that the Si-rich amorphous component retrieved at the end of the breakdown process is very poor in B.

Moreover, considering that pristine fluor-elbaite is a hydrated phase containing a definite amount of Na and Li and that no hydrated Na- and Li-bearing breakdown products are observed, it is very likely that the silicatic amorphous component may also contain Na and Li and H<sub>2</sub>O, as commonly used in experimental investigation of tourmaline formation (e.g., Orlando et al. 2017).

The observed hematite accommodates the oxidised Fe and spinel probably accommodates the remaining Fe (Mn) and Al of the pristine fluor-elbaite.

## Thermal expansion and HT structure modifications

Variation of unit-cell parameter values for the fluor-elbaite at each *T* is reported in Table 2, and the relative expansion of the same parameters as a function of *T* is shown in Fig. 3.

A non-linear thermal expansion is observed, with the occurrence of several discontinuities. The *a*-parameter deviates from the regularly increasing trend around 500 °C and shows a flattening, suddenly followed by a marked decrease that ends at 700 °C; above this *T*, the *a*-parameter increases again with approximately the same rate observed below 500 °C. The *c*-parameter experiences a different behaviour as the discontinuity occurs at a higher *T* (650 °C) and consists in an increased expansion rate. These opposite behaviours suggest the onset of two different structural

**Table 2** Refined cell parameters at the various temperatures of the fluor-elbaite studied

<i>T</i> (°C)	<i>a</i> (Å)	<i>c</i> (Å)	Volume (Å <sup>3</sup> )
30	15.9187(1)	7.1283(1)	1564.35(2)
50	15.9199(1)	7.1297(1)	1564.87(3)
100	15.9228(1)	7.1328(1)	1566.15(2)
150	15.9262(1)	7.1362(1)	1567.56(3)
200	15.9298(1)	7.1398(1)	1569.04(3)
250	15.9345(1)	7.1441(1)	1570.92(3)
300	15.9387(1)	7.1481(1)	1572.64(3)
350	15.9435(1)	7.1527(1)	1574.59(3)
400	15.9475(1)	7.1572(1)	1576.37(3)
450	15.9504(1)	7.1618(1)	1577.97(3)
500	15.9489(2)	7.1662(1)	1578.63(5)
550	15.9361(3)	7.1701(1)	1576.94(7)
600	15.9193(3)	7.1748(1)	1574.48(6)
650	15.9087(2)	7.1842(1)	1574.63(4)
700	15.9077(1)	7.1965(1)	1577.14(3)
750	15.9097(1)	7.2040(1)	1579.16(3)
800	15.9134(1)	7.2099(1)	1581.20(3)
850	15.9138(2)	7.2181(1)	1583.07(5)

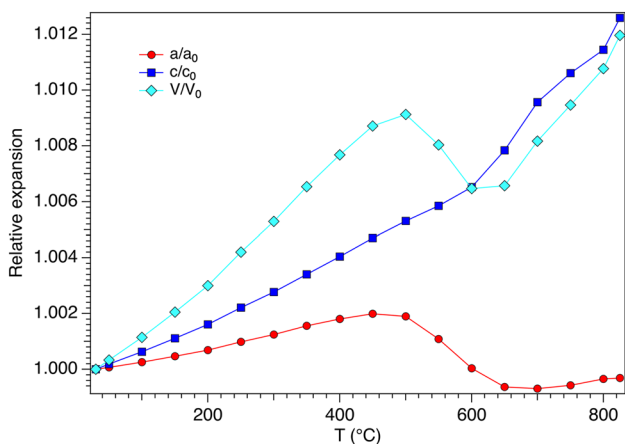


**Fig. 3** Change of normalized unit-cell parameters with  $T$  for the fluor-elbaite studied

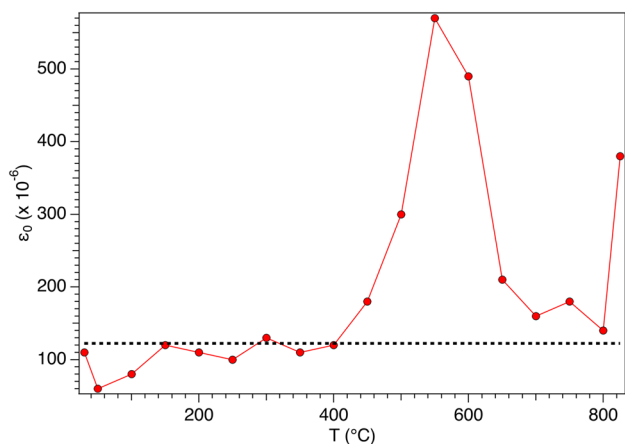


**Fig. 4** Variation of  $\epsilon_0$  microstrain with  $T$  for the fluor-elbaite studied. The dotted horizontal line, corresponding to the  $\epsilon_0$  value at RT, is drawn as a guide for the eye

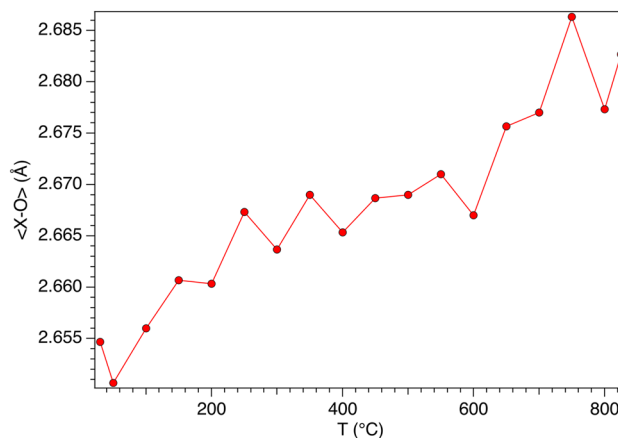
processes and are reflected by the net volume contraction occurring in the 500–600 °C thermal range, followed by the restart of volume increase after 650 °C.

It is worth noting that  $\epsilon_0$  microstrain (lattice strain), defined as  $\beta_i = 4\epsilon_0 \tan \theta$ , where  $\beta_i$  is the integral breadth of the  $j$ th reflection, refined as a part of the profile shape optimization (Ballirano and Sadun 2009), shows a significant increase in the same thermal range (450–700 °C) where the unit-cell parameters deviate from the regular trends (450–700 °C, Fig. 4).

**Table 3** Relevant parameters of the fitting procedure by the Berman equation of the unit-cell parameters vs.  $T$  data of the fluor-elbaite studied

	$V_0$	$a_0, c_0$ (Å <sup>3</sup> , Å, Å)	$a_0$ ( $\times 10^{-5} \text{ K}^{-1}$ )	$a_1$ ( $\times 10^{-9} \text{ K}^{-2}$ )	$X_w^2$
$V$ (Å <sup>3</sup> )	1564.38(6)		1.59(5)	2.6(3)	8.64
$a$ (Å)	15.9188(2)		0.371(17)	0.66(10)	6.26
$c$ (Å)	7.1284(1)		0.849(16)	1.32(9)	3.19

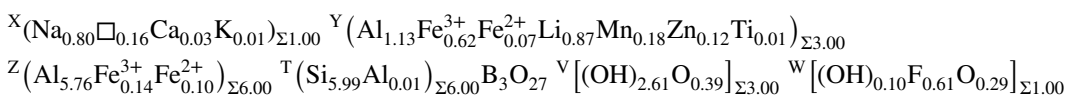
Temperature of reference = 30 °C (303 K)



**Fig. 5** Variation of  $\langle X-O \rangle$  bond distances with  $T$  for the fluor-elbaite studied

The variation of the unit-cell parameters with  $T$  was modelled up to 400 °C, i.e., before the onset of structural modifications, using the Berman equation (Berman 1988). Table 3 reports the relevant parameters of the fitting procedure. The data indicate that the  $c$ -parameter is softer than the  $a$ -parameter against  $T$ .

As far as the structural modifications are referred to, the  $\langle X-O \rangle$  mean bond distance shows an irregular increase with  $T$  (Fig. 5). In spite of a marked enlargement tentatively exhibited at higher temperature, the possibility of Na release and a consequent increase of the  $X$ -site vacant component, which might enlarge  $\langle X-O \rangle$  (Bosi et al. 2005), is not fully supported by experimental data. Moreover, the modifications observed by Bosi et al. (2019b) on a single-crystal fragment of the same fluor-elbaite studied in this work, heated in air at the  $T$  of 800 °C and studied at RT by single crystal X-ray diffraction, confirmed that Na was not released after heating, as reported in their empirical formula,





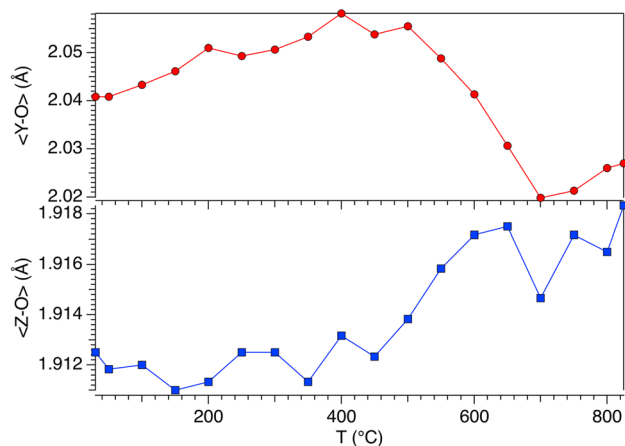


**Fig. 6** Dependence of  $\langle Y-O \rangle$  (upper panel) and  $\langle Z-O \rangle$  (lower panel) bond distances from  $T$  for the fluor-elbaite studied

which has the same Na content of the pristine fluor-elbaite.

The dependence of  $\langle Y-O \rangle$  and  $\langle Z-O \rangle$  bond distances from  $T$  displays a different behaviour (Fig. 6). In particular, the  $\langle Y-O \rangle$  bond distance regularly increases from 2.048 Å to 2.064 Å due to thermal expansion when  $T$  increases from RT to 500 °C, then contracts significantly to 2.027 Å in the range 500–700 °C and slightly increases again up to the breakdown  $T$  of 850 °C. Conversely, the  $\langle Z-O \rangle$  bond distance regularly increases up to the breakdown, although an increment of the expansion is observed at 500 °C.

The  $\langle Y-O \rangle$  and  $\langle Z-O \rangle$  modifications observed in situ correlate nicely with the structural modifications observed by Bosi et al. (2019b) on the same fluor-elbaite as a result of their thermal treatment followed by ex situ study. In fact, these authors observed a marked  $\langle Y-O \rangle$  shrinking together with limited  $\langle Z-O \rangle$  enlargement which was interpreted as the occurrence of  $Fe^{2+}$  oxidation to  $Fe^{3+}$ , counterbalanced by the deprotonation of  $(OH)^-$  groups and described by the reaction  $(Fe^{2+}) + (OH)^- \rightarrow (Fe^{3+}) + (O^{2-}) + 1/2H_2(g)$ . It is worth noting that the whole Fe content of the starting sample of fluor-elbaite was  $Fe^{2+}$ ; therefore, given that the empirical mean ionic radius of  $[6]Fe^{3+}$  is smaller than that of  $[6]Fe^{2+}$  [0.675(15) Å vs. 0.776(1) Å, respectively, Bosi (2018)], we may conclude that in fluor-elbaite the Fe oxidation starts at 500 °C and the heating is definitely the driving force that also rules the associated deprotonation (required to restore the overall charge balance even under reducing conditions, see Bosi et al. 2019b for details).

To explain the observed variation of Fe occupancy at the  $Y$  and  $Z$  sites with  $T$  (Fig. 7), the onset of an intracrystalline exchange process after 650 °C has to be hypothesized. After  $Fe^{2+}$  oxidation to  $Fe^{3+}$ , some amounts of Fe migrate from the larger  $YO_6$  polyhedron to the adjacent smaller  $ZAlO_6$  polyhedron, which in turn moves Al to the  $Y$  site. This process can be described by the intracrystalline order–disorder reaction

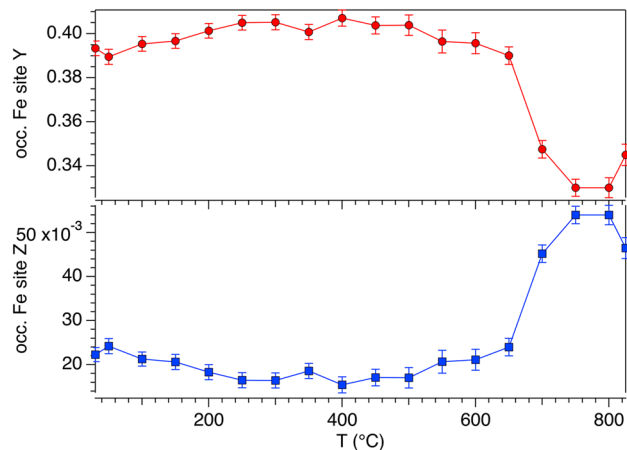


**Fig. 7** Evolution with  $T$  of the Fe (+Mn) occupancy at the  $Y$  and  $Z$  sites for the fluor-elbaite studied

${}^YFe + {}^ZAl \rightarrow {}^ZFe + {}^YAl$ , which was observed on thermally-treated tourmaline single-crystals by Bosi et al. (2019b) for fluor-elbaite, Bosi et al. (2018b) for lucchesiite and Filip et al. (2012) for schorl. In the studied fluor-elbaite, this process probably ends at 750 °C, when the Fe is reasonably supposed to be fully oxidized (Fig. 7).

Both the oxidation reaction of  $Fe^{2+}$  to  $Fe^{3+}$  at the  $Y$  site and the above reported intracrystalline order–disorder reaction contribute to explain the observed dependence of  $\langle Y-O \rangle$  and  $\langle Z-O \rangle$  from  $T$  (Fig. 6). In fact, the abrupt contraction of  $\langle Y-O \rangle$  is consistent with the combination of the two reactions, which leads to the reduction of the aggregate size of the constituent cation  $\langle Y_r \rangle$ . As above mentioned, the empirical mean ionic radius of  $[6]Fe^{3+}$  is smaller than that of  $[6]Fe^{2+}$  [0.675(15) Å vs. 0.776(1) Å, respectively], and the empirical mean ionic radius of  $[6]Al$  is much smaller than that  $[6]Fe^{3+}$  [0.547(3) Å vs. 0.675(15) Å, Bosi (2018)]. The minor expansion of  $\langle Z-O \rangle$  in the same thermal range is consistent with the smaller increase of the aggregate size of the constituent cation  $\langle Z_r \rangle$  than  $\langle Y_r \rangle$  caused by double multiplicity of the  $Z$  site with respect to  $Y$ . A similar behaviour was observed for both Fe-dominant/rich tourmalines (e.g., Filip et al. 2012; Bosi et al. 2018b, 2019b) and Fe-bearing amphiboles (Oberti et al. 2018; Pacella et al. 2020; Ballirano and Pacella 2020).

## Conclusions

The thermal behaviour of fluor-elbaite was investigated up to structural breakdown through in situ HT-XRPD.

Well before the breakdown, heating the fluor-elbaite at 500 °C (773 K) in air was enough to set the Fe oxidation out, counterbalanced by the deprotonation reaction:

( $\text{Fe}^{2+}$ ) + ( $\text{OH}^-$ )  $\rightarrow$  ( $\text{Fe}^{3+}$ ) + ( $\text{O}^{2-}$ ) +  $1/2\text{H}_2(\text{g})$ . Since the capillary acted as a closed system, the early formation of an aqueous fluid may be envisaged at this stage. At a higher temperature, quantified around 650 °C (923 K), Fe starts to migrate from the Y to the Z sites, according to the intracrystalline order–disorder reaction  ${}^Y\text{Fe} + {}^Z\text{Al} \rightarrow {}^Z\text{Fe} + {}^Y\text{Al}$ .

Fluor-elbaite structural breakdown starts at 850 °C (1123 K), owing to the first occurrence of a mullite-like phase in the decomposition products, and the process is complete at 900 °C (1173 K). Tourmaline breakdown products have been identified as B-mullite (for the most part), hematite, spinel and a silicatic B-poor (Na, Li,  $\text{H}_2\text{O}$ )-bearing glass.

**Supplementary Information** The online version contains supplementary material available at <https://doi.org/10.1007/s00269-021-01147-5>.

**Acknowledgements** Sapienza University of Rome grant (Prog. Università 2018 to F. Bosi) is gratefully acknowledged. We sincerely thank Jan Cempírek for his brilliant advices that significantly improved this work and Andreas Ertl for the warm-hearted and careful revision of this manuscript that definitely powered its scientific impact.

**Funding** Open access funding provided by Università degli Studi di Roma La Sapienza within the CRUI-CARE Agreement.

## Declarations

**Conflict of interest** The authors declare no conflict of interest.

**Open Access** This article is licensed under a Creative Commons Attribution 4.0 International License, which permits use, sharing, adaptation, distribution and reproduction in any medium or format, as long as you give appropriate credit to the original author(s) and the source, provide a link to the Creative Commons licence, and indicate if changes were made. The images or other third party material in this article are included in the article's Creative Commons licence, unless indicated otherwise in a credit line to the material. If material is not included in the article's Creative Commons licence and your intended use is not permitted by statutory regulation or exceeds the permitted use, you will need to obtain permission directly from the copyright holder. To view a copy of this licence, visit <http://creativecommons.org/licenses/by/4.0/>.

## References

- Andreozzi GB, Bosi F, Celata B, Capizzi LS, Stagno V, Beckett-Brown CE (2020) Crystal-chemical behavior of  $\text{Fe}^{2+}$  in tourmaline dictated by structural stability: insights from a schorl with formula  $\text{Na}^Y(\text{Fe}^{2+}_2\text{Al})^Z(\text{Al}_5\text{Fe}^{2+})(\text{Si}_6\text{O}_{18})(\text{BO}_3)_3(\text{OH})_3(\text{OH}, \text{F})$  from Seagull batholith (Yukon Territory, Canada). *Phys Chem Miner* 47:1–9
- Ballirano P (2003) Effects of the choice of different ionization level for scattering curves and correction for small preferred orientation in Rietveld refinement: the  $\text{MgAl}_2\text{O}_4$  test case. *J Appl Crystallogr* 36:1056–1061
- Ballirano P, Maras A (2006) In-situ X-ray transmission powder diffraction study of the kinetics of the light induced alteration of realgar ( $\alpha\text{-As}_4\text{S}_4$ ). *Eur J Mineral* 18:589–599
- Ballirano P, Melis E (2007) Thermal behaviour of  $\beta$ -anhydrite  $\text{CaSO}_4$  to 1263 K. *Phys Chem Miner* 34:699–704
- Ballirano P, Sadun C (2009) Thermal behavior of trehalose dihydrate ( $T_h$ ) and  $\beta$ -anhydrous trehalose ( $T_\beta$ ) by in-situ laboratory parallel-beam X-ray powder diffraction. *Struct Chem* 20:815–823
- Ballirano P, Pacella A (2020) Towards a detailed comprehension of the inertisation processes of amphibole asbestos: in situ high-temperature behaviour of fibrous tremolite. *Mineral Mag* 84:888–899
- Berman RG (1988) Internally-consistent thermodynamic data for minerals in the system  $\text{Na}_2\text{O}-\text{K}_2\text{O}-\text{CaO}-\text{MgO}-\text{FeO}-\text{Fe}_2\text{O}_3-\text{Al}_2\text{O}_3-\text{SiO}_2-\text{TiO}_2-\text{H}_2\text{O}-\text{CO}_2$ . *J Petrol* 29:445–522
- Bosi F (2018) Tourmaline crystal chemistry. *Am Mineral* 103:298–306
- Bosi F, Andreozzi GB, Federico M, Graziani G, Lucchesi S (2005) Crystal chemistry of the elbaite-schorl series. *Am Mineral* 90:1784–1792
- Bosi F, Andreozzi GB, Skogby H, Lussier AJ, Abdu Y, Hawthorne FC (2013) Fluor-elbaite,  $\text{Na}(\text{Li}_{1.5}\text{Al}_{1.5})\text{Al}_6(\text{Si}_6\text{O}_{18})(\text{BO}_3)_3(\text{OH})_3\text{F}$ , a new mineral species of the tourmaline supergroup. *Am Mineral* 98:297–303
- Bosi F, Naitza S, Skogby H, Secchi F, Conte AM, Cuccuru S, Hålenius U, De La Rosa N, Kristiansson P, Nilsson EJC, Ros L, Andreozzi GB (2018a) Late magmatic controls on the origin of schorlitic and foititic tourmalines from late-Variscan peraluminous granites of the Arbus pluton (SW Sardinia, Italy) crystal-chemical study and petrological constraints. *Lithos* 308:395–411
- Bosi F, Skogby H, Hålenius U, Ciriotti M (2018b) Experimental cation redistribution in the tourmaline lucchesiite,  $\text{CaFe}^{2+}_3\text{Al}_6(\text{Si}_6\text{O}_{18})(\text{BO}_3)_3(\text{OH})_3\text{O}$ . *Phys Chem Miner* 45:621–632
- Bosi F, Naitza S, Secchi F, Conte AM, Cuccuru S, Andreozzi GB, Skogby H, Hålenius U (2019a) Petrogenetic controls on the origin of tourmalinite veins from Mandrolisai igneous massif (Central Sardinia, Italy): Insights from tourmaline crystal chemistry. *Lithos* 342–343:333–344
- Bosi F, Skogby H, Hålenius U (2019b) Thermally induced cation redistribution in fluor-elbaite and Fe-bearing tourmalines. *Phys Chem Miner* 46:371–383
- Buick I, Grew ES, Armbruster T, Medenbach O, Yates MG, Bebout GE, Clarke GL (2008) Boromullite,  $\text{Al}_9\text{BSi}_2\text{O}_{19}$ , a new mineral from granulite-facies metapelites, Mount Stafford, central Australia and a natural analogue of a synthetic “boron-mullite.” *Eur J Mineral* 20:935–950
- Bruker AXS (2016) Topas V6: general profile and structure analysis software for powder diffraction data. Bruker AXS, Karlsruhe
- Cempírek J, Grew ES, Kampf AR, Ma C, Novák M, Gadas P, Škoda R, Vašíňová-Galiová M, Pezzotta F, Groat LA, Krivovíčov SV (2016) Vránaite, ideally  $\text{Al}_{16}\text{B}_4\text{Si}_4\text{O}_{38}$ , a new mineral related to boralsilite,  $\text{Al}_{16}\text{B}_6\text{Si}_2\text{O}_{37}$ , from the Manjaka pegmatite, Sahatany Valley, Madagascar. *Am Mineral* 101:2108–2117
- Cheary RW, Coelho AA (1992) A fundamental parameters approach of X-ray line-profile fitting. *J Appl Crystallogr* 25:109–121
- Dutrow B, Henry D (2011) Tourmaline: a geologic DVD. *Elements* 7:301–306
- Federico M, Andreozzi GB, Lucchesi S, Graziani G, César-Mendes J (1998) Crystal chemistry of tourmalines. I. Chemistry, compositional variations and coupled substitutions in the pegmatite dikes of the Cruzeiro mine, Minas Gerais, Brazil. *Can Mineral* 36:415–431
- Filip J, Bosi F, Novák M, Skogby H, Tuček J, Čuda WM (2012) Iron redox reactions in the tourmaline structure: high-temperature treatment of  $\text{Fe}^{3+}$ -rich schorl. *Geochim Cosmochim Acta* 86:239–256
- Fischer RX, Schneider H (2008) Crystal chemistry of borates and borosilicates with mullite-type structures: a review. *Eur J Mineral* 20:917–933

- Gonzalez-Platas J, Alvaro M, Nestola F, Angel R (2016) EosFit7-GUI: a new graphical user interface for equation of state calculations, analyses and teaching. *J Appl Crystallogr* 49:1377–1382
- Henry DJ, Dutrow BL (1996) Metamorphic tourmaline and its petrologic applications. In: Grew ES, Anovitz LM (eds), *Boron: mineralogy, petrology and geochemistry*. *Rev Miner Geochem* 33:503–557
- Henry DJ, Novák M, Hawthorne FC, Ertl A, Dutrow BL, Uher P, Pezzotta F (2011) Nomenclature of the tourmaline supergroup minerals. *Am Mineral* 96:895–913
- Lühns H, Soellradl S, King SP, Hanna JV, Konzett J, Fischer RX (2014) Ambient and high-pressure synthesis, composition, and crystal structure of B-mullites. *Cryst Res Tech* 49:21–31
- Lussier A, Ball NA, Hawthorne FC, Henry DJ, Shimizu R, Ogasawara Y, Ota T (2016) Maruyamaite,  $K(MgAl_2)(Al_5Mg)Si_6O_{18}(BO_3)_3(OH)_3O$ , a potassium-dominant tourmaline from the ultrahigh-pressure Kokchetav massif, northern Kazakhstan: description and crystal structure. *Am Mineral* 101:355–361
- Novák M, Cempírek J, Gadas P, Škoda R, Vašíňová-Galiová M, Pezzotta F, Groat LA (2015) Boralsilite and Li, Be-bearing “boron mullite”  $Al_8B_2Si_2O_{19}$ , breakdown products of spodumene from the Manjaka pegmatite, Sahatany Valley, Madagascar. *Can Mineral* 53:357–374
- Oberti R, Boiocchi M, Zema M, Hawthorne FC, Redhammer GJ, Susta U, Della Ventura G (2018) The high-temperature behaviour of riebeckite: expansivity, deprotonation, selective Fe oxidation and a novel cation disordering scheme for amphiboles. *Eur J Mineral* 30:437–449
- Orlando A, Ruggieri G, Chiarantini L, Montegrossi G, Rimondi V (2017) Experimental investigation of biotite-rich schist reacting with B-bearing fluids at upper crustal conditions and correlated tourmaline formation. *Minerals* 7:155–177
- Ota T, Kobayashi K, Katsura T, Nakamura E (2008a) Tourmaline breakdown in a pelitic system: implications for boron cycling through subduction zones. *Contrib Mineral Petrol* 155:19–32
- Ota T, Kobayashi K, Kunihiro T, Nakamura E (2008b) Boron cycling by subducted lithosphere; insights from diamondiferous tourmaline from Kokchetav ultrahigh-pressure metamorphic belt. *Geochim Cosmochim Acta* 72:3531–3541
- Pacella A, Tomatis M, Viti C, Bloise A, Arizza L, Ballirano P, Turci F (2020) Thermal inertization of amphiboles asbestos modulates Fe topochemistry and surface reactivity. *J Hazard Mater* 398:123119
- Sabine TM, Hunter BA, Sabine WR, Ball CJ (1998) Analytical expressions for the transmission factor and peak shift in absorbing cylindrical specimens. *J Appl Crystallogr* 31:47–51
- Shimizu R, Ogasawara Y (2013) Diversity of potassium-bearing tourmalines in diamondiferous Kokchetav UHP metamorphic rocks: a geochemical recorder from peak to retrograde metamorphic stages. *J Asian Earth Sci* 63:39–55
- Werding G, Schreyer W (1992) Synthesis and stability of werdingite, a new phase in the system  $MgO-Al_2O_3-B_2O_3-SiO_2$  (MABS), and another new phase in the ABS-system. *Eur J Mineral* 4:193–207
- Young RA (1993) Introduction to the Rietveld method. In: Young RA (ed) *the Rietveld method*. Oxford University Press, Oxford, pp 1–38

**Publisher's Note** Springer Nature remains neutral with regard to jurisdictional claims in published maps and institutional affiliations.



## 2.2.2 Mn-bearing fluor-elbaite

Original paper

# HT breakdown of Mn-bearing elbaite from the Anjanabonoina pegmatite, Madagascar

Paolo BALLIRANO<sup>1</sup>, Beatrice CELATA<sup>1\*</sup>, Henrik SKOGBY<sup>2</sup>, Giovanni B. ANDREOZZI<sup>1</sup>, Ferdinando BOSI<sup>1</sup>

<sup>1</sup> Department of Earth Sciences, Sapienza University of Rome, Piazzale Aldo Moro 5, I-00185 Rome, Italy; [beatrice.celata@uniroma1.it](mailto:beatrice.celata@uniroma1.it)

<sup>2</sup> Department of Geosciences, Swedish Museum of Natural History, SE-10405 Stockholm, Sweden

\* Corresponding author



The thermal behavior of a gem-quality purplish-red Mn-bearing elbaite from the Anjanabonoina pegmatite, Madagascar, with composition  $X(\text{Na}_{0.41}\square_{0.35}\text{Ca}_{0.24})_{\Sigma 1.00}Y(\text{Al}_{1.81}\text{Li}_{1.00}\text{Fe}^{3+}_{0.04}\text{Mn}^{3+}_{0.02}\text{Mn}^{2+}_{0.12}\text{Ti}_{0.004})_{\Sigma 3.00}Z\text{Al}_6[\text{T}(\text{Si}_{5.60}\text{B}_{0.40})_{\Sigma 6.00}\text{O}_{18}](\text{BO}_3)_3(\text{OH})_3W[(\text{OH})_{0.50}\text{F}_{0.13}\text{O}_{0.37}]_{\Sigma 1.00}$  was investigated using both *in situ* High-Temperature X-Ray powder diffraction (HT-pXRD) and *ex situ* X-Ray single-crystal diffraction (SC-XRD) on two single crystals previously heated in the air up to 750 and 850 °C. The first occurrence of mullite diffraction peaks allowed us to constrain the breakdown temperature of Mn-bearing elbaite at ambient pressure, at 825 °C. The breakdown products from the HT-pXRD experiments were cooled down to ambient temperature and identified via pXRD, represented by B-mullite and  $\gamma$ -LiAlSi<sub>2</sub>O<sub>6</sub>. A thermally induced oxidation of Mn<sup>2+</sup> to Mn<sup>3+</sup> was observed with both *in-situ* and *ex-situ* techniques; it started at 470 °C and is assumed to be counterbalanced by deprotonation, according to the equation:  $\text{Mn}^{2+} + (\text{OH})^- \rightarrow \text{Mn}^{3+} + \text{O}^{2-} + 1/2\text{H}_2$ . At temperatures higher than 752 °C, a partial disorder between the Y and Z sites is observed from unit-cell parameters and mean bond distances, possibly caused by the inter-site exchange mechanism  ${}^Y\text{Li} + {}^Z\text{Al} \rightarrow {}^Z\text{Li} + {}^Y\text{Al}$ .

**Keywords:** lithium tourmaline; high-temperature breakdown; powder X-Ray diffraction; crystal-structure refinement; single-crystal X-Ray diffraction

Received: 30 December 2021; accepted: 10 June 2022; handling editor: J. Cempirek

The online version of this article (doi: 10.3190/jgeosci.347) contains supplementary electronic material.

## 1. Introduction

Among borosilicates, minerals of the tourmaline supergroup show an extensive occurrence in various geological settings, from diagenetic stages to UHP environments, because of their flexible composition and structural stability (e.g., Dutrow and Henry 2011). In the tourmaline structure, cations are accommodated in a relatively large number of constituent-coordination environments (Bosi 2018), as it follows from the general chemical formula (Henry et al. 2011):  $XY_3Z_6(T_6O_{18})(\text{BO}_3)_3V_3W$ , where where  $X = \text{Na}^+, \text{K}^+, \text{Ca}^{2+}, \square$  (= vacancy);  $Y = \text{Al}^{3+}, \text{Fe}^{3+}, \text{Cr}^{3+}, \text{V}^{3+}, \text{Mg}^{2+}, \text{Fe}^{2+}, \text{Mn}^{2+}, \text{Li}^+$ ;  $Z = \text{Al}^{3+}, \text{Fe}^{3+}, \text{Cr}^{3+}, \text{V}^{3+}, \text{Mg}^{2+}, \text{Fe}^{2+}$ ;  $T = \text{Si}^{4+}, \text{Al}^{3+}, \text{B}^{3+}$ ;  $B = \text{B}^{3+}$ ;  $V = (\text{OH})^-, \text{O}^{2-}$ ;  $W = (\text{OH})^-, \text{F}^-, \text{O}^{2-}$ . Note that the letters X, Y, T, Z and B represent groups of cations at the <sup>[9]</sup>X, <sup>[6]</sup>Y, <sup>[6]</sup>Z, <sup>[4]</sup>T and <sup>[3]</sup>B crystallographic sites (designated by *italicized letters*). The letters V and W in the formula represent groups of anions accommodated at the [3]-coordinated O(3) and O(1) crystallographic sites, respectively.

Many attempts to define the X–P–T stability of tourmaline are known to date, the majority of which converge to breakdown temperatures confined between 700 and 920 °C, depending on composition, at pressures up to

nearly 8 GPa (e.g., van Hinsberg et al. 2011). However, most data come from artificial systems, where tourmaline was added in excess to its ground host rock and the considered system was multiphase (e.g., Ota et al. 2008). At the same time, the high-temperature modifications of tourmaline alone were described in detail for Fe-dominant tourmalines and Fe–Mn-bearing elbaite (e.g., Fuchs et al. 1995, 2002; Pieczka and Kraczk 2004; Castañeda et al. 2006; Bačík et al. 2011; Bosi et al. 2019, and references therein). A common feature of the last experimental works is that they were principally focused on the Fe oxidation process. Besides, the thermal behavior of tourmaline needs to be fully described, and breakdown conditions, as well as post-breakdown products, need to be identified, similarly to what was recently reported for a Fe-rich fluor-elbaite in Celata et al. (2021).

The present work is focused on thermal behavior, breakdown temperature and products of a gem-quality natural sample of Mn-bearing elbaite from the Anjanabonoina pegmatite (Madagascar), with formula  $X(\text{Na}_{0.41}\square_{0.35}\text{Ca}_{0.24})_{\Sigma 1.00}Y(\text{Al}_{1.81}\text{Fe}^{3+}_{0.04}\text{Li}_{1.00}\text{Mn}^{3+}_{0.02}\text{Mn}^{2+}_{0.12}\text{Ti}_{0.01})_{\Sigma 3.00}Z\text{Al}_6[\text{T}(\text{Si}_{5.60}\text{B}_{0.40})_{\Sigma 6.00}\text{B}_{3.00}\text{O}_{27}V(\text{OH})_3]W[(\text{OH})_{0.50}\text{F}_{0.13}\text{O}_{0.37}]_{\Sigma 1.00}$ , structurally and chemically characterized by Bosi et al. (2021) at room conditions, and spectroscopi-

**Tab. 1** Single-crystal X-ray diffraction data details for samples of tourmaline from Madagascar heated in the air up to 750 °C and 850 °C, respectively

Sample	dhth750b	dhth850a
crystal size (mm)	0.28 × 0.25 × 0.20	0.40 × 0.20 × 0.04
<i>a</i> (Å)	15.7819(2)	15.7809(2)
<i>c</i> (Å)	7.08590(10)	7.09390(10)
<i>V</i> (Å <sup>3</sup> )	1528.42(4)	1529.96(4)
Data collection range, 2 $\theta$ (°)	6–75	6–75
<i>hkl</i> range	–26 ≤ <i>h</i> ≤ 26 –23 ≤ <i>k</i> ≤ 26 –11 ≤ <i>l</i> ≤ 9	–23 ≤ <i>h</i> ≤ 26 –26 ≤ <i>k</i> ≤ 26 –12 ≤ <i>l</i> ≤ 11
Number of reflections	11203	11409
Unique reflections, <i>R</i> <sub>int</sub> (%)	1770, 0.98	1872, 1.26
Flack parameter	0.05(6)	0.05(6)
<i>wR</i> <sub>2</sub> (%)	3.23	3.35
<i>R</i> <sub>1</sub> (%) all data	1.2	1.30
<i>R</i> <sub>1</sub> (%) for <i>I</i> > 2 $\sigma$ ( <i>I</i> )	1.2	1.27
GooF	1.120	1.097
Largest diff. peak and hole ( $\pm e^-/\text{\AA}^3$ )	–0.33 and 0.29	–0.32 and 0.31

*R*<sub>int</sub> – merging residual value; *R*<sub>1</sub> – discrepancy index, calculated from *F*-data; *wR*<sub>2</sub> – weighted discrepancy index, calculated from *F*<sup>2</sup> data; GooF – goodness of fit; Diff. Peaks – maximum and minimum residual electron density; Data collection temperature = 20 °C; Space-group *R3m*; *Z* = 3; MoK $\alpha$  radiation (0.71073 Å); Redundancy = 12; Absorption correction method – SADABS; Structural refinement program – SHELXL-2013.

cally characterized before and after thermal treatment at 750 °C. In order to complete the study of Bosi et al. (2021) with structural data from a treated sample, *in situ* structure behavior, and information on elbaite breakdown products, we applied a dual approach using both *in situ* and *ex situ* experiments, respectively, High-Temperature powder X-Ray diffraction (HT-pXRD) and single-crystal X-Ray diffraction (SC-XRD).

## 2. Experimental

### 2.1. Thermal treatment at 750 and 850 °C

Two crystal fragments of the Mn-bearing elbaite were heated in air at 750 °C (labeled as dhth750b) and 850 °C (labeled as dhth850a). Next, the samples were placed in a gold container and pushed into a pre-heated horizontal-tube furnace equipped with a quartz-glass tube. The heating experiments lasted for 90 and 6 hours, respectively, and the runs were ended by pushing the samples out to the cold zone of the quartz tube, leading to cooling down to 100 °C within 1 minute.

### 2.2. SC-XRD and SREF

The two tourmaline fragments heated in air at 750 and 850 °C were analyzed by the single-crystal X-Ray Diffraction on a Bruker KAPPA APEX-II single-crystal diffractometer (Sapienza University of Rome, Earth Scienc-

es Department), equipped with a charge-coupled device (CCD) area detector (6.2 × 6.2 cm active detection area, 512 × 512 pixels) and a graphite-crystal monochromator using MoK $\alpha$  radiation from a fine-focus sealed X-ray tube. The sample-to-detector distance was 4 cm. A total of 3577 exposures (step = 0.2°, time/step = 20 s) covering a full-sphere with an average redundancy of ~12 was collected. Final unit-cell parameters were refined using the Bruker AXS SAINT program on reflections with *I* > 10  $\sigma$ (*I*) in the range 6° < 2 $\theta$  < 75°. The intensity data were processed and corrected for Lorentz, polarization and background effects using the APEX2 software program of Bruker AXS. The data were corrected for absorption using

a multi-scan method (SADABS, Bruker AXS). The absorption correction led to an improvement in *R*<sub>int</sub> (from ~0.024 to ~0.017 for both samples). No violation of *R3m* symmetry was detected. Single crystal Structure REfinement (SREF) was done using the SHELXL-2013 program (Sheldrick 2015). Starting coordinates were taken from Bosi et al. (2021). Variable parameters were scale factor, extinction coefficient, atom coordinates, site-scattering values (for *X*, *Y* and *Z* sites) and atomic-displacement factors. Attempts to refine the extinction coefficient yielded values within its standard uncertainty, thus, it was not refined. Neutral scattering factors were used for the cations and oxygen atoms. The atomic model refinement is similar to that used for the untreated Mn-bearing elbaite (see Bosi et al. 2021, for details).

All the single-crystal diffraction data are listed in Tabs 1, 2 and 3; CIF files are available as electronic supplementary material.

### 2.3. HT-pXRD

A crystal fragment of Mn-bearing elbaite was ground in an agate mortar under ethanol. The powder was loaded in a 0.7 mm diameter SiO<sub>2</sub>-glass capillary that was kept open at one side. The capillary was fixed to a hollow corundum tube using Resbond® 989 and mounted and aligned on a standard goniometer head. A prototype of a heating chamber for capillaries, developed by MRI and Bruker AXS, was used for HT measurements. Details on the thermal calibration procedure of the chamber may

be found in Ballirano and Melis (2007).

*In situ* HT-pXRD data were collected on a Bruker AXS D8 Advance operating in  $\theta/\theta$  geometry in transmission mode. The investigated thermal range was 30–900 °C. The incident beam is focussed onto the capillary using a multilayer graded Göbel mirror. Soller slits are placed along with both the incident (2.3° opening angle) and diffracted (radial) beams. Data were measured with a position sensitive detector (PSD) VÅntec-1 set at an opening angle of 6° 2 $\theta$ . Details of the data collection are listed in Tab. 4. Each diffraction pattern required 5.5 h of counting time and the whole high-T experiment took ca. 8 days.

After reaching the maximum temperature of 900 °C, the powder was cooled back to ambient temperature (RT) within the chamber (estimated cooling rate of ca. 10 °C min<sup>-1</sup>). The capillary was opened at one side and the powder was removed, re-homogenized in an agate mortar and charged in a new borosilicate-glass capillary following the same procedure reported in Celata et al. (2021). It is worth mentioning that this procedure was adopted to avoid the probable occurrence of textured recrystallization at the walls of the capillary. However, re-homogenization included powder lying at the coldest extremity of the capillary where *T*, owing to thermal gradients, was considerably lower than that recorded by the thermocouple placed near the area bathed by the X-rays.

The diffraction data were evaluated by the Rietveld method using Topas V.6 (Bruker AXS 2016). The peak shape was modeled using the Fundamental Pa-

**Tab. 2** Fractional atom coordinates, equivalent isotropic and isotropic displacement parameters ( $\text{\AA}^2$ ) and site occupancies for the treated samples of tourmaline from Madagascar.

Sample/site	<i>x</i>	<i>y</i>	<i>z</i>	$U_{\text{eq}}$	Site occupancy
dhth750b					
X	0	0	0.2196(2)	0.0209(5)	Na <sub>0.37</sub> Ca <sub>0.29</sub>
Y	0.12172(3)	0.06086(2)	0.63800(9)	0.00761(14)	Li <sub>0.25</sub> Al <sub>0.69</sub> Mn <sub>0.06</sub>
Z	0.29674(2)	0.26008(2)	0.60744(6)	0.00609(6)	Al <sub>1.00</sub>
B	0.10913(5)	0.21826(9)	0.4516(2)	0.00597(19)	B <sub>1.00</sub>
T	0.19144(2)	0.18960(2)	0	0.00496(7)	Si <sub>0.92</sub> B <sub>0.08</sub>
O1	0	0	0.7730(3)	0.0193(4)	O <sub>0.87</sub> F <sub>0.13</sub>
O2	0.05999(4)	0.11999(7)	0.48839(17)	0.01290(19)	O <sub>1.00</sub>
O3	0.26096(9)	0.13048(4)	0.50727(15)	0.01177(17)	O <sub>1.00</sub>
O4	0.09388(4)	0.18775(8)	0.07465(16)	0.01060(16)	O <sub>1.00</sub>
O5	0.18572(8)	0.09286(4)	0.09511(15)	0.01096(16)	O <sub>1.00</sub>
O6	0.19395(5)	0.18384(5)	0.77404(11)	0.00745(11)	O <sub>1.00</sub>
O7	0.28650(5)	0.28590(4)	0.07599(10)	0.00719(11)	O <sub>1.00</sub>
O8	0.20942(5)	0.27002(5)	0.43693(11)	0.00728(11)	O <sub>1.00</sub>
H1	0	0	0.908(4)	0.023	H <sub>0.38</sub>
H3	0.2538(18)	0.1269(9)	0.378(3)	0.014	H <sub>1.00</sub>
dhth850a					
X	0	0	0.2185(2)	0.0209(5)	Na <sub>0.36</sub> Ca <sub>0.29</sub>
Y	0.12195(4)	0.06098(2)	0.63766(8)	0.00739(14)	Li <sub>0.21</sub> Al <sub>0.74</sub> Mn <sub>0.06</sub>
Z	0.29663(2)	0.25981(2)	0.60671(6)	0.00621(7)	Al <sub>1.00</sub>
B	0.10920(5)	0.21840(11)	0.4512(2)	0.0061(2)	B <sub>1.00</sub>
T	0.19142(2)	0.18965(2)	0	0.00499(7)	Si <sub>0.93</sub> B <sub>0.08</sub>
O1	0	0	0.7706(3)	0.0178(4)	O <sub>0.87</sub> F <sub>0.13</sub>
O2	0.06005(4)	0.12009(8)	0.48791(17)	0.0121(2)	O <sub>1.00</sub>
O3	0.26004(9)	0.13002(5)	0.50800(15)	0.01166(19)	O <sub>1.00</sub>
O4	0.09403(4)	0.18806(9)	0.07532(16)	0.01086(18)	O <sub>1.00</sub>
O5	0.18545(9)	0.09272(5)	0.09467(15)	0.01119(18)	O <sub>1.00</sub>
O6	0.19346(5)	0.18369(5)	0.77381(11)	0.00756(12)	O <sub>1.00</sub>
O7	0.28667(5)	0.28598(5)	0.07558(10)	0.00727(12)	O <sub>1.00</sub>
O8	0.20948(5)	0.27008(5)	0.43647(11)	0.00739(12)	O <sub>1.00</sub>
H1	0	0	0.906(4)	0.021	H <sub>0.38</sub>
H3	0.2506(19)	0.1253(9)	0.380(3)	0.014	H <sub>1.00</sub>

**Tab. 3** Selected bond lengths ( $\text{\AA}$ ) for the treated tourmaline samples.

Sample	dhth750b	dhth850a	Sample	dhth750b	dhth850a
X–O2 ( $\times 3$ )	2.5135(16)	2.5194(16)	Z – m. a. n.	13	13
X–O5 ( $\times 3$ )	2.6872(12)	2.6823(13)	B–O2	1.3682(16)	1.3686(18)
X–O4 ( $\times 3$ )	2.7640(12)	2.7635(13)	B–O8 ( $\times 2$ )	1.3750(9)	1.3747(10)
<X–O>	2.655	2.655	<B–O>	1.372	1.372
X – m. a. n.	9.788(10)	9.842(11)	B – m. a. n.	5	5
Y–O1	1.9190(12)	1.9150(12)	T–O6	1.6053(8)	1.6086(8)
Y–O2 ( $\times 2$ )	1.9629(8)	1.9659(8)	T–O7	1.6032(6)	1.6039(7)
Y–O6 ( $\times 2$ )	1.9450(8)	1.9420(8)	T–O4	1.6145(4)	1.6155(5)
Y–O3	2.1166(13)	2.0995(13)	T–O5	1.6296(5)	1.6295(5)
<Y–O>	1.986	1.981	<T–O>	1.613	1.614
Y – m. a. n.	11.230(4)	11.670(4)	T – m. a. n.	13.307(3)	13.325(3)
Z–O6	1.8765(7)	1.8823(8)			
Z–O7	1.8820(7)	1.8832(7)			
Z–O8	1.8821(7)	1.8831(7)			
Z–O8'	1.8972(7)	1.8973(8)			
Z–O7'	1.9380(7)	1.9409(7)			
Z–O3	1.9625(5)	1.9585(6)			
<Z–O>	1.906	1.908			

**Tab. 4** Miscellaneous data of the data collection and Rietveld refinements. Definition of the statistical indicators as indicated in Young (1993).

2 $\theta$ range (°)	7–145
2 $\theta$ step-size (°)	0.021798
Counting time (s)	3
T <sub>max</sub> (°C)	900
T steps (°C)	25
*R <sub>p</sub> (%)	1.889–2.198
*R <sub>wp</sub> (%)	2.375–2.772
*R <sub>Bragg</sub> (%)	0.732–1.162
*D <sub>wd</sub>	0.796–1.130
$\chi^2$	1.396–1.590

\* – Up to 825 °C, i.e., before starting the breakdown process.

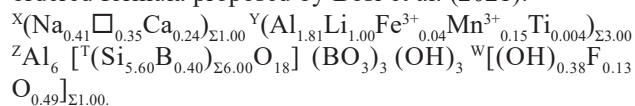
rameters Approach (Cheary and Coelho 1992). An absorption correction was applied using the equation of Sabine et al. (1998) for a cylindrical sample and the procedure described by Ballirano and Maras (2006) was followed for handling the correlation existing between displacement parameters and absorption. The isotropic displacement parameters were constrained as follow:  $B_Y = B_Z = B_B = B_T$ ;  $B_{O2} = B_{O3} = B_{O4} = B_{O5} = B_{O6} = B_{O7} = B_{O8}$ . The total site scattering at  $Y+Z$  sites was forced to be constant throughout the analyzed thermal range. Preferred orientation effects were corrected using spherical harmonics (8th-order, nine refinable parameters) following the procedure reported by Ballirano (2003) for selecting the appropriate number of terms. Starting structural data were those obtained from SREF (see below) and each refined structure at a given non-ambient  $T$  was used as input for the subsequent  $T$ .

### 3. Results and discussion

#### 3.1. SC-XRD and SREF

Compared to the untreated sample of Bosi et al. (2021), the sample heated up to 750 °C (dhth750b) shows a reduction of the unit-cell  $a$ -parameter from 15.7935(4) to 15.7819(2) Å. In contrast, the  $c$ -parameter remains constant concerning the untreated sample (about 7.086 Å). The observed decrease in  $a$  can be interpreted as the result of the Mn

oxidation from +2 to +3, which occurs approximately between 470 and 650 °C (Fig. 1). The oxidation of Mn is also supported by optical absorption data, which show a significant increase in the intensity of the  $Mn^{3+}$ -absorption band associated with the purplish-red color intensity of the treated sample reported in Bosi et al. (2021). Accordingly, a reduction in  $\langle Y-O \rangle$  is observed, from 1.979 Å in the untreated sample to 1.975 Å in the heated one. The  $\langle Z-O \rangle$  remains practically constant (1.906 Å), basically because the  $Z$  site is fully occupied by Al and therefore is not involved in the process. Therefore, the structural data for the sample dhth750b thermally treated at 750 °C confirm the ordered formula proposed by Bosi et al. (2021):

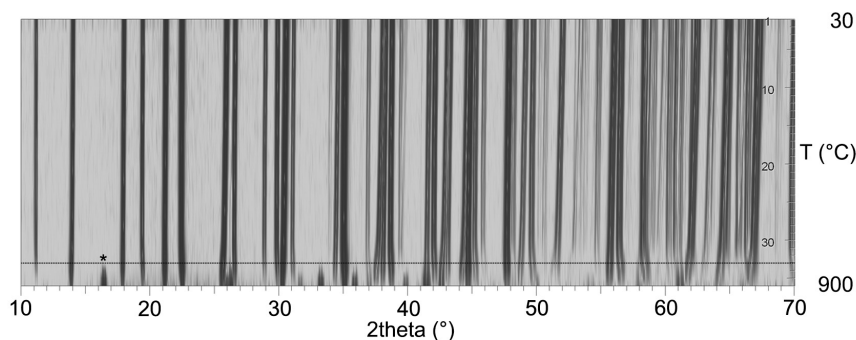


In this regard, the observed increase of the  $Mn^{3+}$  absorption bands strongly support the Mn oxidation.

The sample heated up to 850 °C (dhth850a) shows an additional decrease of the  $a$ -parameter down to 15.7809(2) Å, together with a shortening of  $\langle Y-O \rangle$  to 1.972 Å. As the oxidation process was ended, such behavior could be ascribed to the partial disorder generated by Al–Li substitution, with Li moving to the  $Z$  site and being substituted by Al (a smaller cation compared to Li) from the  $Z$  site, thus leading the  $YO_6$  polyhedron to shrink. Alongside, Li slightly bulked the  $ZO_6$  polyhedron up, leading to a  $\langle Z-O \rangle$  of 1.908 Å from the previous value of 1.906 Å and sizing up the  $c$ -parameter to 7.0939(1) Å. The partial Li–Al disorder over  $Y$  and  $Z$  is also consistent with the refined  $Y$ -site scattering (in terms of mean atomic number,  $m. a. n.$ ).  $Y$ - $m. a. n.$  of sample dhth850a is significantly larger than those of samples dhth750b and untreated: respectively, 11.68(5) > 11.23(5) and 11.13(4), which reflects the presence of cations heavier than Li at the  $Y$  site (as, for example, Al), corresponding to the possible site populations  ${}^Y(\text{Al}_{1.91}\text{Li}_{0.90}\text{Fe}^{3+}_{0.04}\text{Mn}^{3+}_{0.15}\text{Ti}_{0.004})_{\Sigma 3.00}$   ${}^Z(\text{Al}_{5.90}\text{Li}_{0.10})_{\Sigma 6.00}$ .

#### 3.2. HT-pXRD

##### 3.2.1. Breakdown products



Miscellaneous information regarding the refinements is listed in Tab. 4, a magnified view of the whole data set, in the form of a pseudo-Guinier plot, is shown in Fig. 1 and a representative example of Rietveld plots

**Fig. 1** Magnified view (10–70° 2 $\theta$ ) of the full data set of the heating cycle shown as a pseudo-Guinier plot.



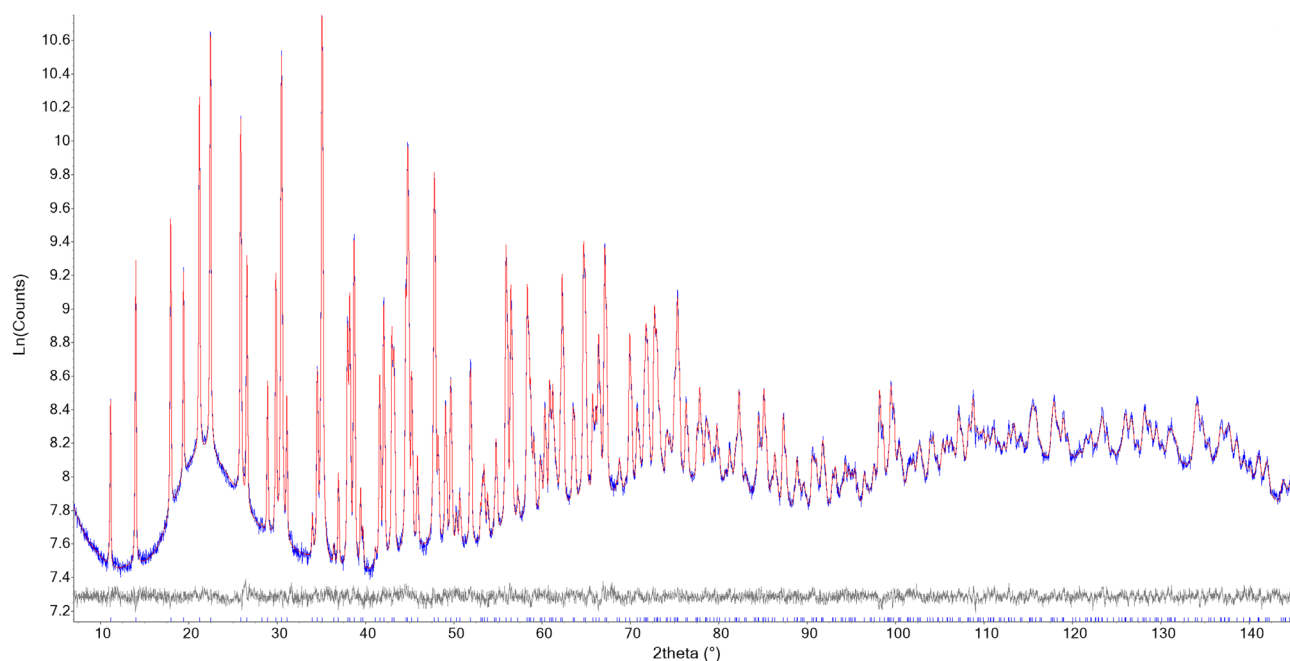


**Fig. 2** Representative example of the Rietveld plots of the diffraction pattern collected at 275 °C. Blue: experimental; red: calculated; grey: difference; vertical bars: position of calculated Bragg reflections of the tourmaline studied. Intensities on a logarithmic scale.

in Fig. 2. CIF files of the structures refined at the various  $T$  are given in ESM.

The first evidence of the structural breakdown of the Mn-bearing elbaite was detected at 850 °C because of the occurrence of very weak diffraction reflections attributed to a mullite-like phase (marked with a star in Fig. 1). This is approximately the same temperature as reported

for fluor-elbaite under similar experimental conditions (Celata et al. 2021). At higher  $T$ , the material consists prevalently of the mullite-like phase, and the diffraction patterns show a drastic reduction of tourmaline reflections intensities, preventing an accurate derivation of its structural parameters. Therefore, only cell parameters derived at 850 and 875 °C will be further discussed in

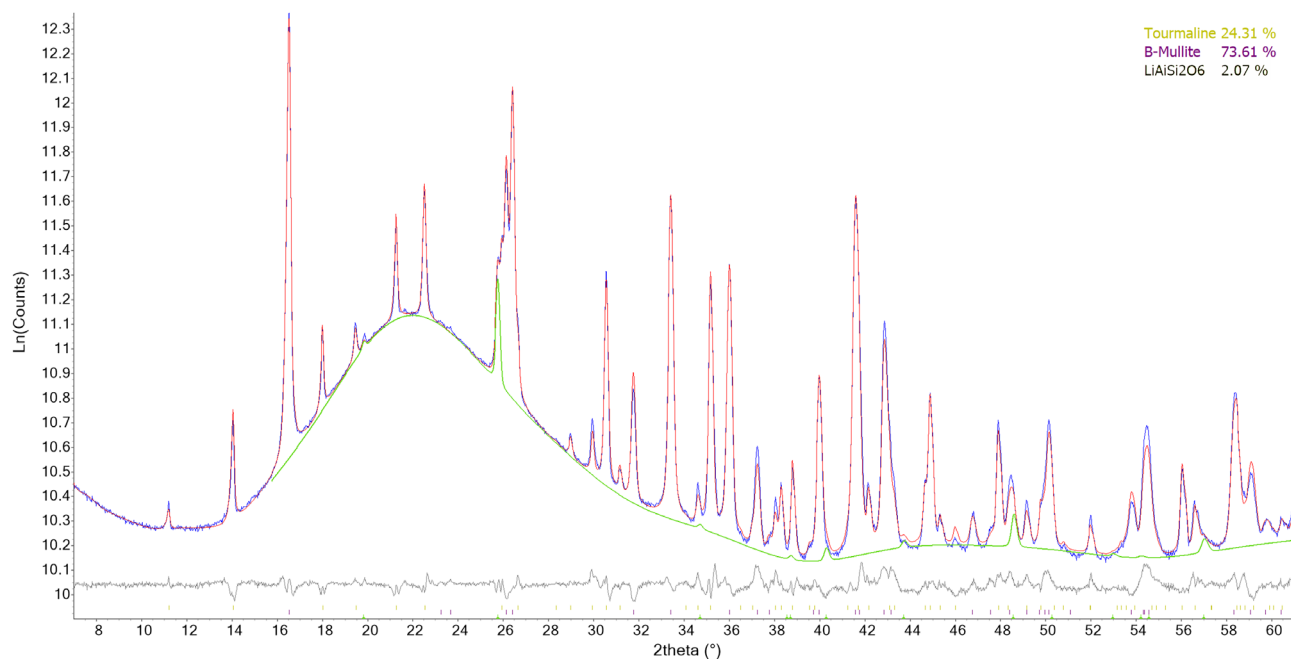


**Fig. 3** Magnified 10–60°  $2\theta$  view of the Rietveld plots of the products of the breakdown of the tourmaline studied. Blue: experimental; red: calculated; green: calculated contribution of  $\gamma$ -LiAlSi<sub>2</sub>O<sub>6</sub>; grey: difference; vertical bars: position of calculated Bragg reflections of (from above to below) tourmaline (unreacted), B-mullite, and  $\gamma$ -LiAlSi<sub>2</sub>O<sub>6</sub>. Intensities on a logarithmic scale.

**Tab. 5** Comparison of the unit-cell parameters of the tourmaline sample before and after thermal treatment.

	SCXRD		PXRD	
	Untreated	Treated	Untreated	Back ambient <i>T</i>
<i>a</i> (Å)	15.7935(4)	15.7819(2)	15.7928(1)	15.7752(3)
<i>c</i> (Å)	7.0860(2)	7.0859(1)	7.0842(1)	7.0917(2)
<i>V</i> (Å <sup>3</sup> )	1530.69(9)	1528.42(4)	1530.16(2)	1528.38(7)

the following without any reference to possible structural modification. The breakdown was completed at 900 °C. Analysis of the diffraction pattern of the sample cooled down to ambient temperature (Fig. 3) clearly shows the prevailing mullite-like phase, occurrence of subordinate relicts of unreacted tourmaline caused by the re-homogenization of the powder (Celata et al. 2021),

**Tab. 6** Refined unit-cell parameters and volume at the various *T*.

<i>T</i> (°C)	<i>a</i> (Å)	<i>c</i> (Å)	<i>V</i> (Å <sup>3</sup> )	wt. % mullite-like	wt. % γ-LiAlSi <sub>2</sub> O <sub>6</sub>
30	15.7928(1)	7.0842(1)	1530.16(2)	–	–
50	15.7933(1)	7.0852(1)	1530.47(2)	–	–
75	15.7960(1)	7.0872(1)	1531.43(2)	–	–
100	15.7973(1)	7.0888(1)	1532.04(2)	–	–
125	15.7983(1)	7.0902(1)	1532.52(2)	–	–
150	15.8002(1)	7.0919(1)	1533.27(2)	–	–
175	15.8020(1)	7.0937(1)	1534.01(2)	–	–
200	15.8039(1)	7.0957(1)	1534.80(2)	–	–
225	15.8055(1)	7.0974(1)	1535.49(2)	–	–
250	15.8075(1)	7.0993(1)	1536.29(2)	–	–
275	15.8095(1)	7.1013(1)	1537.11(2)	–	–
300	15.8115(1)	7.1031(1)	1537.90(2)	–	–
325	15.8143(1)	7.1055(1)	1538.95(2)	–	–
350	15.8170(1)	7.1078(1)	1539.98(2)	–	–
375	15.8191(1)	7.1100(1)	1540.86(2)	–	–
400	15.8219(1)	7.1124(1)	1541.94(2)	–	–
425	15.8232(1)	7.1143(1)	1542.60(2)	–	–
450	15.8253(1)	7.1166(1)	1543.49(2)	–	–
475	15.8271(1)	7.1187(1)	1544.31(2)	–	–
500	15.8277(1)	7.1207(1)	1544.87(2)	–	–
525	15.8295(1)	7.1231(1)	1545.73(2)	–	–
550	15.8301(1)	7.1253(1)	1546.32(2)	–	–
575	15.8307(1)	7.1275(1)	1546.92(2)	–	–
600	15.8306(1)	7.1299(1)	1547.42(2)	–	–
625	15.8309(1)	7.1322(1)	1547.98(2)	–	–
650	15.8320(1)	7.1350(1)	1548.80(2)	–	–
675	15.8329(1)	7.1374(1)	1549.49(2)	–	–
700	15.8342(1)	7.1402(1)	1550.36(2)	–	–
725	15.8353(1)	7.1434(1)	1551.28(2)	–	–
750	15.8363(1)	7.1475(1)	1552.35(2)	–	–
775	15.8341(1)	7.1532(1)	1553.17(3)	–	–
800	15.8217(2)	7.1624(1)	1552.73(4)	–	–
825	15.8039(2)	7.1751(1)	1551.98(4)	–	–
850*	15.7896(2)	7.1880(1)	1551.95(4)	5.7(5)	–
875*	15.7790(3)	7.1971(2)	1551.85(6)	36.0(4)	tr.
900	–	–	–	96.4(2)	3.6(2)

tr. stands for "traces".

and presence of some amorphous material, likely a cooling product of a silicate melt derived from the tourmaline breakdown.

With respect to the Fe-rich fluor-elbaite (Celata et al. 2021) and Fe-dominant tourmalines heated in the air (e.g., Bačík et

al. 2011), neither hematite nor spinel was detected here, along with B-mullite as breakdown products of tourmaline. Anyway, of particular interest is the occurrence of an additional relatively strong reflection at ca.  $2\theta = 25.75^\circ$  ( $d = 3.457$  Å). This reflection was not observed in the diffraction pattern of breakdown products of fluor-elbaite (Celata et al. 2021), and it can be assigned to the γ-polymorph of

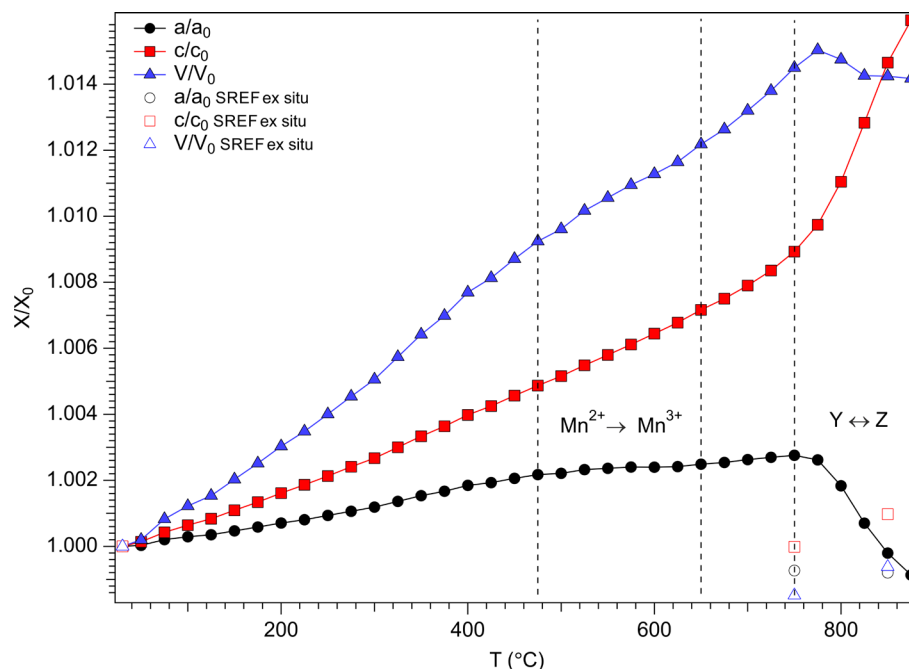
LiAlSi<sub>2</sub>O<sub>6</sub> (space group *P6<sub>2</sub>22*; Li 1968). Naturally occurring as virgilite (French et al. 1978), this phase represents a stuffed β-quartz structure. It is worth noting the existence of a solid-solution series between β-quartz (QZ) and γ-LiAlSi<sub>2</sub>O<sub>6</sub> (SP) and the observed material is expected to lay somewhere between the two end members. Reported unit-cell parameters for virgilite (SP<sub>61</sub>QZ<sub>39</sub>) are  $a = 5.132(1)$  Å,  $c = 5.454(1)$  Å (French et al. 1978) whereas those of synthetic γ-LiAlSi<sub>2</sub>O<sub>6</sub> are  $a = 5.217(1)$  Å,  $c = 5.464(1)$  Å (Li 1968). For comparison, the refined cell parameters of the present breakdown product were  $a = 5.166(1)$  Å,  $c = 5.440(2)$  Å, pointing out a composition significantly displaced toward the SP endmember.

Unit-cell parameters of the mullite-like phase, refined in the space group *Pbam*, were  $a = 7.5151(2)$  Å,  $b = 7.6431(2)$  Å,  $c = 2.8157(1)$  Å,  $V = 161.73(1)$  Å<sup>3</sup> and are consistent with those of B-mullites (Lührs et al. 2014). Several anhydrous ternary B<sub>2</sub>O<sub>3</sub>–Al<sub>2</sub>O<sub>3</sub>–SiO<sub>2</sub> (BAS) phases are known (see for example Werding and Schreyer 1992; Buick et al. 2008; Grew et al. 2008; Novák et al. 2015; Cempírek et al. 2016) whose unit-cell volumes are multiple

integers of the mullite one (ca.  $168 \text{ \AA}^3$ ) and an increased B content produces a progressive contraction. Unit cell parameters of the present B-mullite are smaller than those of the phase arising from the breakdown of fluor-elbaite ( $V = 164.22 \text{ \AA}^3$ ; Celata et al. 2021), suggesting a higher content of  $\text{B}_2\text{O}_3$ . An estimation of the B content done using the regression equations proposed by Lühns et al. (2014) indicates ca. 16–17 mol. %  $\text{B}_2\text{O}_3$ .

A comparison between the chemical composition of the present and the fluor-elbaite sample (Celata et al. 2021) outlines a few relevant characteristics valuable to justify the correspondingly different breakdown products. Despite the higher B content of the present sample [0.40 atoms per formula unit (*apfu*) B are also allocated at T site], the Al/B ratio is almost equal (2.32 vs. 2.30 respectively). Differently, the Si/B ratio is lower in the present sample (1.65 vs. 2). Moreover, Li is more abundant in the present sample than in fluor-elbaite (1 *apfu* vs. 0.86 *apfu*). Finally, Fe (and to a minor extent Mn, and Zn) is present as traces in the present sample, whereas it exceeds 1 *apfu* in fluor-elbaite. The higher B content of the present pristine sample positively correlates with the estimated higher mol. %  $\text{B}_2\text{O}_3$  of the B-mullite arising from its structural breakdown than that of the B-mullite produced from the fluor-elbaite breakdown. The occurrence of a Li-bearing crystalline material among the breakdown products of the present sample is reasonable due to its higher Li content compared to fluor-elbaite, where it was preferentially allocated into the glass phase. However, it is worth mentioning that high contents of Li have also been found in boromullite and vranaite (Novák et al. 2015; Cempírek et al. 2016), and, in principle, some Li could enter the structure of both B-mullite samples produced from tourmalines breakdown. The presence of different amounts of Li may potentially contribute to the observed differences in cell volume. The relevant transition elements content of fluor-elbaite is allocated, at the breakdown, in spinel and hematite. Such oxides are not observed in the breakdown products of the present sample owing to the minor content of Fe and Mn in the pristine material. Despite the Si/B ratio of the present recrystallized B-mullite being lower than that of pristine tourmaline (ca. 0.75–1 : 1 for an approximate  $\text{Al}_{8.5}\text{B}_{1.5}\text{Si}_2\text{O}_{19}$ – $\text{Al}_8\text{B}_2\text{Si}_2\text{O}_{19}$

**Fig. 4** Change of normalized unit-cell parameters with  $T$  for the tourmaline studied.



**Tab. 7** Refined unit-cell parameters and volume of the mullite-like phase at the various  $T$ .

$T$ (°C)	$a$ (Å)	$b$ (Å)	$c$ (Å)	$V$ (Å <sup>3</sup> )
850	7.555(1)	7.688(4)	2.8225(9)	163.9(1)
875	7.5504(3)	7.6911(3)	2.8244(1)	164.02(1)
900	7.5479(2)	7.6891(2)	2.8255(1)	163.98(1)

composition as compared to 1.65 : 1), we may hypothesize that the Si-rich amorphous component retrieved at the end of the breakdown process still contains significant B. Moreover, considering the chemical composition of the pristine material, we may infer that the silicate amorphous component should also contain Na, Ca, Mn, Fe and  $\text{H}_2\text{O}$ .

Interestingly, the unit-cell parameters of the relict tourmaline are reasonably close to those observed at ambient  $T$  for the sample heated at 850 °C and analyzed by SREF (Tab. 5). This suggests that this is the highest temperature in the coldest region of the capillary, located at ca. 4 cm from the center of the focussed X-ray beam, which has a width of ca. 12 mm.

### 3.2.2. Thermal expansion and HT structure modifications

The unit-cell parameters of the Mn-bearing elbaite at variable  $T$  are listed in Tab. 6, and the relative expansion of the same parameters for each  $T$  is shown in Fig. 4. Table 6 also reports the quantitative phase analysis (QPA) of the material in the 850–900 °C thermal range indicates a fast increase in the mullite-like phase content. Finally, Tab. 7 lists the unit-cell parameters of the mullite-like phase in the same 850–900 °C thermal range showing only marginal variations, as expected for refractory material.



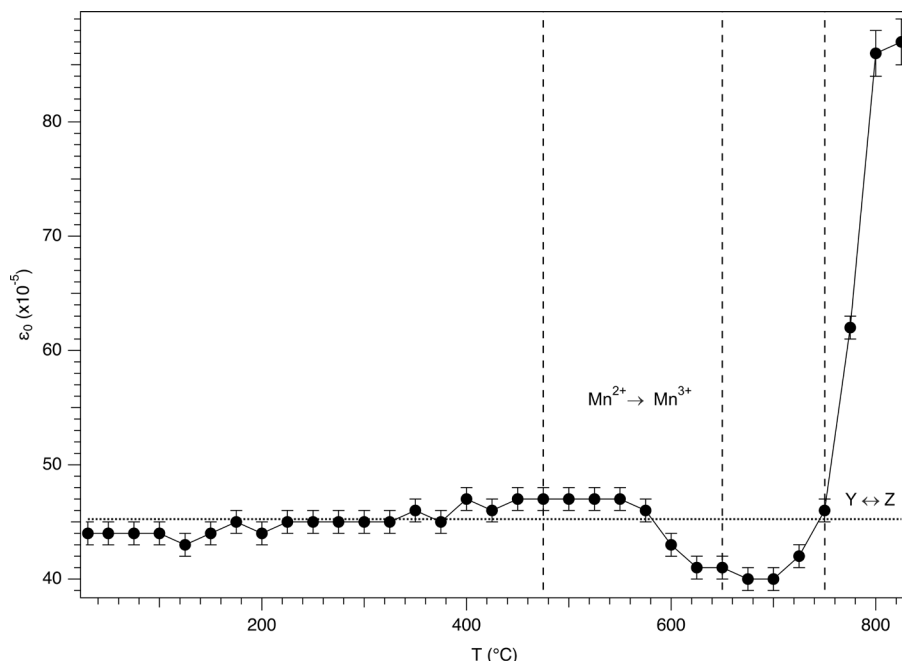


**Fig. 5** Variation of  $\epsilon_0$  microstrain with  $T$  for the tourmaline studied. The dotted horizontal line, corresponding to the  $\epsilon_0$  value at ambient  $T$ , is drawn as a guide for the eye.

The behavior of the tourmaline unit-cell parameters is quite complex, and several discontinuities were observed. The  $a$ -parameter deviates from its gradually increasing trend, for the first time, at 500°C and shows a reduced expansion up to 650°C, suddenly followed by a restored expansion up to 750°C; above this  $T$ , the  $a$ -parameter contracts significantly, a behavior not observed by Celata et al. (2021) in Fe-rich fluor-elbaite. The  $c$ -parameter has a more regular behavior; it shows a linear increase until 750°C; then it is followed by a faster (exponential) expansion rate.

In the case of Fe-rich fluor-elbaite, the deviation of the  $a$ -parameter from the increasing trend occurs ap-

proximately at the same  $T$ , but it is much more relevant in magnitude. This different behavior can be explained based on the interpretation that has been attributed to this contraction. In the case of Fe-rich fluor-elbaite, the relatively strong shortening of the  $a$ -parameter has been attributed to the onset of the  $\text{Fe}^{2+}$  oxidation to  $\text{Fe}^{3+}$ , counterbalanced by the deprotonation of  $(\text{OH})^-$  groups (Celata et al. 2021). Due to the large amount of  $\text{Fe}^{2+}$  in the pristine fluor-elbaite (0.94 *apfu*), such a process significantly affects the  $a$ -parameter. On the other hand, in the case of the present tourmaline sample, the relatively small deviation of the  $a$ -parameter from the increasing trend may be assigned to the onset of the  $\text{Mn}^{2+}$  oxidation to  $\text{Mn}^{3+}$ , counterbalanced by the deprotonation of  $(\text{OH})^-$  groups. However, the small amount of  $\text{Mn}^{2+}$  in the pristine tourmaline sample (0.12 *apfu*) produces only minor, albeit detectable, variation in the  $a$ -parameter.

Analysis of the variation with  $T$  of the  $\epsilon_0$  microstrain (lattice strain), which is defined as  $\beta_1 = 4\epsilon_0 \tan \theta$  ( $\beta_1 =$  integral breadth of the  $j^{\text{th}}$  reflection), optimized during the Rietveld refinements (Ballirano and Sadun 2009), reveals differences with respect to fluor-elbaite. Whereas in the

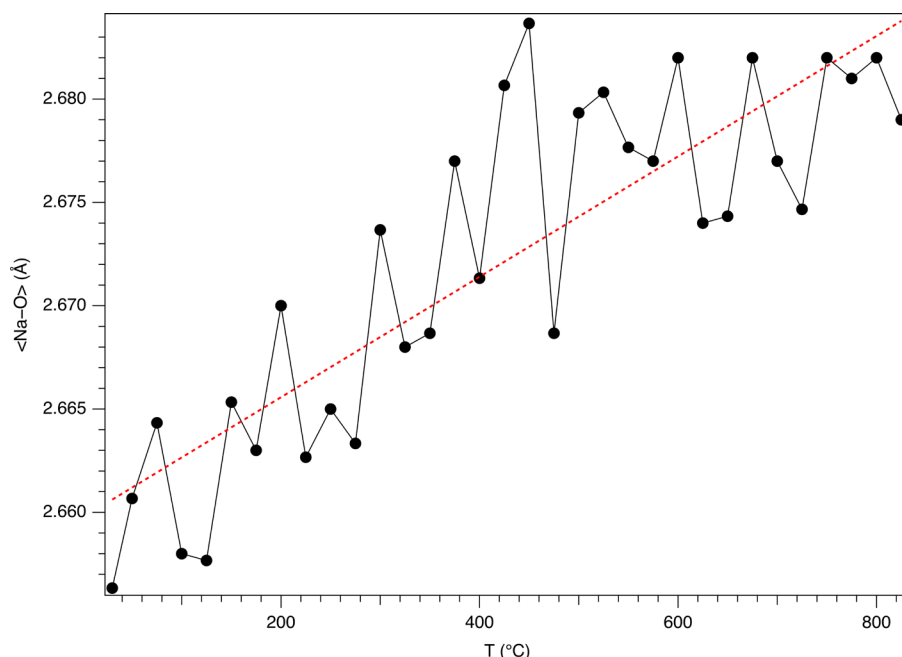


**Fig. 6** Variation of  $\langle X-O \rangle$  bond distances with  $T$  for the tourmaline studied.

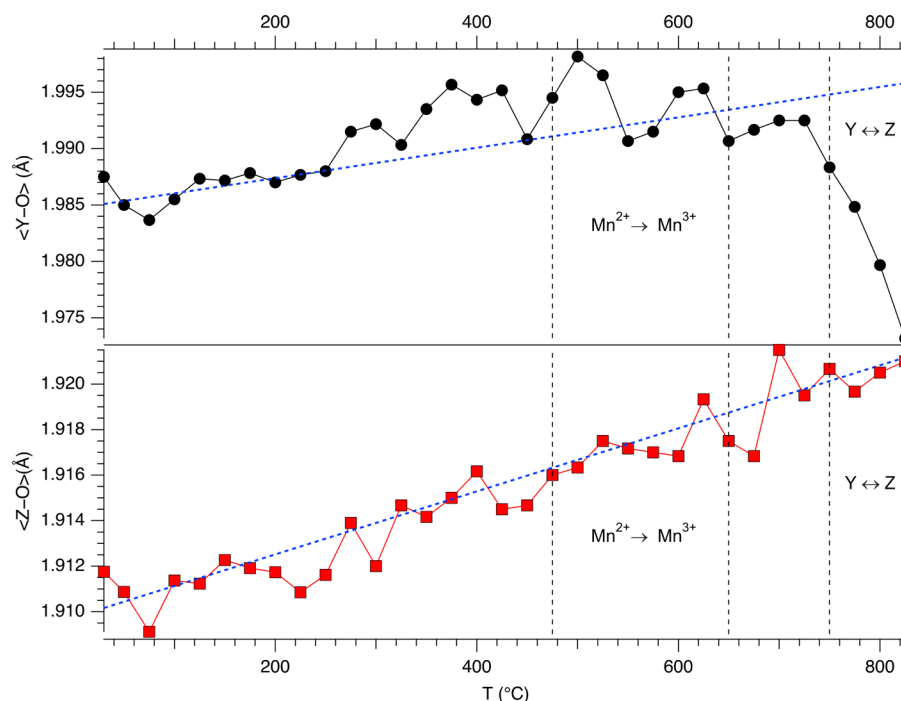


**Fig. 7** Dependence of  $\langle Y-O \rangle$  (upper panel) and  $\langle Z-O \rangle$  (lower panel) bond distances from  $T$  for the tourmaline studied.

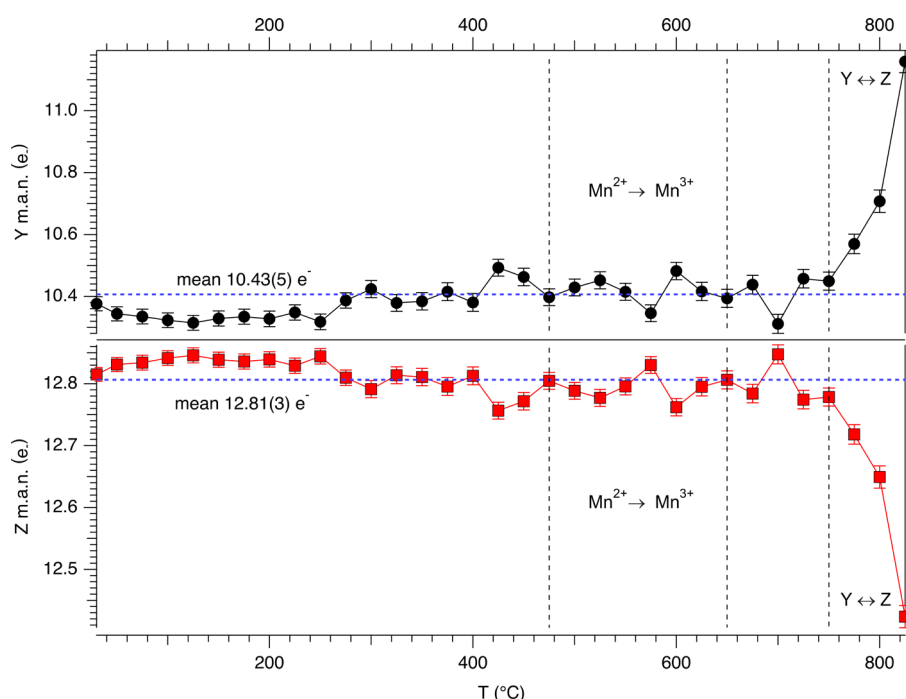
case of fluor-elbaite  $\epsilon_0$  shows a significant increase in the same thermal range where the unit-cell parameters deviate from the regular trends. The present tourmaline sample experiences a minor reduction at  $T$  slightly higher than those at which Mn oxidation occurs. Subsequently, in correspondence with the abrupt  $a$ -parameter contraction,  $\epsilon_0$  markedly increases (Fig. 5). Differences in the magnitude of the transient variations of  $\epsilon_0$  are related to the different amounts of oxidized transition elements (and corresponding deprotonation) in the two samples.

Analysis of the structural changes reveals that the  $\langle X-O \rangle$  mean bond distance shows a fairly regular increase with  $T$  (Fig. 6). The dependence of  $\langle Y-O \rangle$  and  $\langle Z-O \rangle$  bond distances on  $T$  highlights their different behavior (Fig. 7). In particular,  $\langle Z-O \rangle$  regularly increases up to the breakdown, whereas  $\langle Y-O \rangle$  marginally increases up to 750°C, and then contracts up to the breakdown  $T$ . The interpretation of the observed  $\langle Y-O \rangle$  contraction at the same  $T$  at which the  $a$ -parameter exhibits a significant contraction is not easy (this point is discussed below).

**Fig. 8** Evolution with  $T$  of the site scattering (in  $epfu$ ) at the  $Y$  (upper panel) and  $Z$  (lower panel) sites for the tourmaline studied.

### 3.2.3. Compression of the structure near the breakdown temperature: Al-Li disorder

Figure 8 shows the variation of the site scattering (s.s.) at the  $Y$  and  $Z$  sites with temperature. As can be seen and expected, s.s. are reasonably constant up to 750°C; their mean values are:  $Y = 31.29(15)$  electrons per formula unit ( $epfu$ ) and  $Z = 76.86(18)$   $epfu$ . Near breakdown temperature, the start of the migration of s.s. from  $Z$  to  $Y$  site indicates an onset of an intracrystalline cation ex-



change process. The unique process that we can invoke is that some amounts of Li migrate from the slightly larger  $YO_6$  polyhedron to the adjacent slightly smaller  $ZAlO_6$  polyhedron, which makes Al move to the *Y* site. Because the empirical ionic radii of  $^{6}Li$  and  $^{6}Al$  are 0.751(9) and 0.547(3) Å, respectively (Bosi 2018), the small contraction of  $\langle Y-O \rangle$  may be explained by the intracrystalline order-disorder reaction  $^YLi + ^ZAl \rightarrow ^ZLi + ^YAl$ , which has not been documented so far. The expected increased expansion of  $\langle Z-O \rangle$  might be possibly masked by thermal expansion effects and by the double multiplicity of the *Z* site with respect to *Y*. From refined s.s., ca. 0.09 Li pfu are expected to be exchanged at 825 °C. This value is in line with that inferred from SC-XRD (see above) and possibly extends to ca. 0.18 apfu at 870 °C, but this result should be accepted with caution owing to potential correlations caused by the occurrence in a mixture of both mullite-like phase and  $\gamma$ -LiAlSi<sub>2</sub>O<sub>6</sub>. It is worth noting that in the case of the present tourmaline sample, the difference between  $\langle Y-O \rangle$  and  $\langle Z-O \rangle$  in the whole explored thermal range (0.05–0.08 Å) is significantly smaller than that of Fe-rich fluor-elbaite (0.08–0.13 Å), perhaps facilitating the onset of the proposed order-disorder reaction.

Moreover, the different thermal behavior with respect to Fe-rich fluor-elbaite is also given in terms of different crystalline breakdown products, in particular  $\gamma$ -LiAlSi<sub>2</sub>O<sub>6</sub>.

#### 4. Conclusions

A purplish-red Mn-bearing elbaite was structurally investigated through both *in situ* and *ex situ* HT experiments with the results of which ended up being in a fairly reasonable agreement. At above 470 °C, a shrink of the unit-cell *a*-parameter was observed along with the downsizing of the  $YO_6$  polyhedron, owing to the thermally induced oxidation of Mn<sup>2+</sup> into Mn<sup>3+</sup>. A further contraction of the *a*-parameter and  $\langle Y-O \rangle$  above 752 °C was explained as a partial Li-Al disorder between the *Y* and *Z* sites.

The breakdown temperature of Mn-bearing elbaite was constrained at 825 °C with the detection of the first breakdown product represented by B-mullite. The breakdown products from the HT-pXRD experiments were collected and identified at ambient temperature via pXRD, being mostly represented by B-mullite and  $\gamma$ -LiAlSi<sub>2</sub>O<sub>6</sub>.

*Acknowledgments:* Sapienza University of Rome grant (Prog. Università 2020 to F. Bosi) is gratefully acknowledged.

*Electronic supplementary material.* The crystallographic information file (CIF) for both of described structures are available online at the Journal web site (<http://dx.doi.org/10.3190/jgeosci.347>).

#### References

- BAČÍK P, OZDÍN D, MIGLIERINI M, KARDOŠOVÁ P, PENTRÁK M, HALODA J (2011) Crystallochemical effects of heat treatment on Fe-dominant tourmalines from Dolní Bory (Czech Republic) and Vlachovo (Slovakia). *Phys Chem Miner* 38: 599–611
- BALLIRANO P (2003) Effects of the choice of different ionization level for scattering curves and correction for small preferred orientation in Rietveld refinement: the MgAl<sub>2</sub>O<sub>4</sub> test case. *J Appl Crystallogr* 36: 1056–1061
- BALLIRANO P, MARAS A (2006) In-situ X-ray transmission powder diffraction study of the kinetics of the light induced alteration of realgar ( $\alpha$ -As<sub>4</sub>S<sub>4</sub>). *Eur J Mineral* 18: 589–599
- BALLIRANO P, MELIS E (2007) Thermal behaviour of  $\beta$ -anhydrite CaSO<sub>4</sub> to 1,263K. *Phys Chem Miner* 34: 699–704
- BALLIRANO P, SADUN C (2009) Thermal behavior of trehalose dihydrate (T<sub>h</sub>) and  $\beta$ -anhydrous trehalose (T <sub>$\beta$</sub> ) by in-situ laboratory parallel-beam X-ray powder diffraction. *Struct Chem* 20: 815–823
- BOSI F (2018) Tourmaline crystal chemistry. *Amer Miner* 103: 298–306
- BOSI F, SKOGBY H, HÅLENIUS U (2019) Thermally induced cation redistribution in fluor-elbaite and Fe-bearing tourmalines. *Phys Chem Miner* 46: 371–383
- BOSI F, CELATA B, SKOGBY H, HÅLENIUS U, TEMPESTA G, CIRIOTTI ME, BITTARELLO E, MARENGO A (2021) Mn-bearing purplish-red tourmaline from the Anjanaboina pegmatite, Madagascar. *Mineral Mag* 85: 242–253
- BUICK I, GREW ES, ARMBRUSTER T, MEDENBACH O, YATES MG, BEBOUT, GE, CLARKE GL (2008) Boromullite, Al<sub>3</sub>B-Si<sub>2</sub>O<sub>19</sub>, a new mineral from granulite-facies metapelites, Mount Stafford, central Australia and a natural analogue of a synthetic “boron-mullite”. *Eur J Mineral* 20: 935–950
- BRUKER AXS (2016) Topas V6: General profile and structure analysis software for powder diffraction data. Bruker AXS, Karlsruhe, Germany.
- CASTAÑEDA C, EECKHOUT SG, DA COSTA GM, BOTELHO NF, DE GRAVE E (2006) Effect of heat treatment on tourmaline from Brazil. *Phys Chem Miner* 33: 207–216
- CELATA B, BALLIRANO P, ANDREOZZI GB, BOSI F (2021) In-situ high-temperature behaviour of fluor-elbaite: breakdown conditions and products. *Phys Chem Miner* 48: 24
- CEMPÍREK J, GREW ES, KAMPF AR, MA C, NOVÁK M, GADAS P, ŠKODA R, VAŠINOVÁ-GALIOVÁ M, PEZZOTTA F, GROAT LA, KRIVOVICEV SV (2016) Vránaite, ideally Al<sub>16</sub>B<sub>4</sub>Si<sub>4</sub>O<sub>38</sub>, a new mineral related to boralsilite, Al<sub>16</sub>B<sub>6</sub>Si<sub>2</sub>O<sub>37</sub>, from the Manjaka pegmatite, Sahatany Valley, Madagascar. *Amer Miner* 101: 2108–2117
- CHEARY RW, COELHO AA (1992) A Fundamental Parameters Approach of X-ray line-profile fitting. *J Appl Crystallogr* 25: 109–121

- DUTROW BL, HENRY D (2011) Tourmaline: A geologic DVD. *Elements* 7(5): 301–306
- FRENCH BM, JEZEK PA, APPLEMAN DE (1978) Virgilite: a new lithium aluminum silicate mineral from the Macusani glass, Peru. *Amer Miner* 63: 461–465
- FUCHS Y, LAGACHE M, LINARES J, MAURY R, VARRET F (1995) Mössbauer and optical spectrometry of selected schörl-dravite tourmalines. *Hyperfine Interact* 96: 245–258.
- FUCHS Y, LAGACHE M, LINARES J (2002) Oxydation expérimentale de Fe-tourmalines et corrélation avec une déprotonation des groupes hydroxyle. *C R Geosci* 334: 245–249
- GREW ES, GRAETSCH HA, PÖTER B, YATES MG, BUICK I, BERNHARDT H-J, SCHREYER W, WERDING G, CARSON CJ, CLARKE GL (2008) Boralsilite,  $Al_{16}B_6Si_2O_{37}$ , and "boron-mullite:" Compositional variations and associated phases in experiment and nature. *Amer Miner* 93: 283–299
- HENRY DJ, NOVÁK M, HAWTHORNE FC, ERTL A, DUTROW BL, UHER P, PEZZOTTA F (2011) Nomenclature of the tourmaline-supergroup minerals. *Amer Miner* 96: 895–913
- LI C-T (1968) The crystal structure of  $LiAlSi_2O_6$  III (high-quartz solid solution). *Z Kristallogr* 127: 327–348
- LÜHRS H, SOELLRADL S, KING SP, HANNA JV, KONZETT J, FISCHER RX (2014) Ambient and high-pressure synthesis, composition, and crystal structure of B-mullites. *Cryst Res Technol* 49: 21–31
- NOVÁK M, CEMPÍREK J, GADAS P, ŠKODA R, VAŠINOVÁ-GALIOVÁ M, PEZZOTTA F, GROAT LA (2015) Boralsilite and Li,Be-bearing "boron mullite"  $Al_8B_2Si_2O_{19}$ , breakdown products of spodumene from the Manjaka pegmatite, Sahatany Valley, Madagascar. *Canad Mineral* 53: 357–374
- OTA T, KOBAYASHI K, KUNIHITO T, NAKAMURA E (2008) Boron cycling by subducted lithosphere; insights from diamondiferous tourmaline from the Kokchetav ultra-high-pressure metamorphic belt. *Geochim Cosmochim Acta* 72: 3531–3541
- PIECZKA A, KRACZKA J (2004) Oxidized tourmalines – a combined chemical, XRD and Mössbauer study. *Eur J Mineral* 16: 309–321
- SABINE TM, HUNTER BA, SABINE WR, BALL CJ (1998) Analytical expressions for the transmission factor and peak shift in absorbing cylindrical specimens. *J Appl Crystallogr* 31: 47–51
- SHELDRIK GM (2015) Crystal structure refinement with SHELXL. *Acta Crystallogr C* 71: 3–8
- VAN HINSBERG V, HENRY DJ, MARSCHALL HR (2011) Tourmaline: an ideal indicator of its host environment. *Canad Mineral* 49: 1–16
- WERDING G, SCHREYER W (1992) Synthesis and stability of werdingite, a new phase in the system  $MgO-Al_2O_3-B_2O_3-SiO_2$  (MABS), and another new phase in the ABS-system. *Eur J Mineral* 4: 193–207
- YOUNG R (1993) Introduction to the Rietveld method. In: YOUNG RA (ed) *The Rietveld method*. Oxford University Press, pp 1–38

### 2.2.3 Uvite



# In situ high-temperature behaviour and breakdown conditions of uvite at room pressure

Paolo Ballirano<sup>1</sup> · Beatrice Celata<sup>1</sup> · Ferdinando Bosi<sup>1</sup>

Received: 23 June 2022 / Accepted: 15 September 2022 / Published online: 11 October 2022  
© The Author(s) 2022

## Abstract

The thermal behaviour of an uvite from San Piero in Campo (Elba Island, Italy) was investigated at room pressure through in situ high-temperature powder X-ray diffraction (PXRD), until the breakdown conditions were reached. The variation of uvite structural parameters (unit-cell parameters and mean bond distances) was monitored together with site occupancies and we observed the thermally induced Fe oxidation process counterbalanced by (OH)<sup>-</sup> deprotonation, which starts at 450 °C and is completed at 650 °C. The uvite breakdown reaction occurs between 800 and 900 °C. The breakdown products were identified at room temperature by PXRD and the breakdown reaction can be described as follows: tourmaline → indialite + yuanduliite + plagioclase + “boron-mullite” phase + hematite.

**Keywords** Uvite · HT-PXRD · Thermal expansion · Iron oxidation · Deprotonation · Intracrystalline cation exchange · Structural breakdown

## Introduction

Tourmalines are a mineral supergroup of complex borosilicates occurring in different geological settings, from diagenetic stages to ultra-high-pressure (UHP) environments (e.g., Henry and Dutrow 1996; Dutrow and Henry 2011; Lussier et al. 2016). Such an extensive stability field is due both to the capacity of tourmaline to adjust its composition depending upon the formation environment and to its crystal structure (discussed below).

The general chemical formula of tourmaline is:  $XY_3Z_6T_6O_{18}(BO_3)_3V_3W$ , where  $X = Na^+, K^+, Ca^{2+}, \square$  (=vacancy);  $Y = Al^{3+}, Fe^{3+}, Cr^{3+}, V^{3+}, Mg^{2+}, Fe^{2+}, Mn^{2+}, Li^+$ ;  $Z = Al^{3+}, Fe^{3+}, Cr^{3+}, V^{3+}, Mg^{2+}, Fe^{2+}$ ;  $T = Si^{4+}, Al^{3+}, B^{3+}$ ;  $B = B^{3+}$ ;  $V = (OH)^-, O^{2-}$ ;  $W = (OH)^-, F^-, O^{2-}$ . The non-italicized letters X, Y, Z, T and B represent groups of cations at the <sup>[9]</sup>X, <sup>[6]</sup>Y, <sup>[6]</sup>Z, <sup>[4]</sup>T and <sup>[3]</sup>B crystallographic sites (italicized letters), and the letters V and W represent groups of anions accommodated at the [3]-coordinated O3 and O1 crystallographic sites, respectively. Tourmaline-supergroup minerals are primarily classified into three

groups, vacant, alkali and calcic, based on the X-site occupancy (Henry et al. 2011). A further level of classification into subgroups is based on charge arrangements at the Y and Z sites. Tourmalines are also distinguished by the dominant anion at the W position of the general formula into hydroxy-, fluor- and oxy-species.

Tourmaline structure is inextricably built over the triangular planar (BO<sub>3</sub>) group, which is bonded to the trigonal antiprism XO<sub>9</sub> and to YO<sub>6</sub> octahedron. Each one of the XO<sub>9</sub> antiprisms is linked to a ring of six tetrahedra [T<sub>6</sub>O<sub>18</sub>]. All those structural elements of tourmaline constitute separate islands that extend along c crystallographic axis. Finally, the structural backbone of tourmaline is made by ZO<sub>6</sub> polyhedra that tie the islands together thus giving tourmaline the mechanical properties that makes it a very resistant mineral in clastic sediments and UHP environments (e.g., Bosi 2018). Also for this reason, tourmaline is able to give inferences about the chemical conditions of its formation (Dutrow and Henry 2011). Thus, tourmaline is stable in a variety of geological setting, including where crustal material is recycled through subduction zones down to the upper mantle (Henry and Dutrow 1996; Ota et al. 2008a,b; Shimizu and Ogasawara 2013). Tourmaline can also form in subduction environments in presence of B-bearing aqueous fluids, when the other phases in paragenesis with it reach their breakdown conditions and some elements are recycled in tourmaline's structure which is stable at those depths, so

✉ Beatrice Celata  
beatrice.celata@uniroma1.it

<sup>1</sup> Dipartimento di Scienze della Terra, Sapienza Università di Roma, Piazzale A. Moro 5, 00185 Rome, Italy



that it may form, or overgrow (if it was pre-existing in the recycled material) with a new composition, depending upon the elements available to be incorporated. At greater depths, tourmaline itself experiences breakdown, and aqueous fluids are released and may escape once again going metasomatize the surrounding rocks, reducing both their solidus temperature and the viscosity of possibly associated melt (Pichavant 1981; Dingwell et al. 1992).

If subducting serpentinites are strictly coupled with carbonaceous (meta)sediments, the release of Ca-rich metasomatic fluids along the slab is likely to occur as a consequence of dehydration reactions, going for example to form strongly Ca-enriched patches and layers of hybrid rocks (lawsonite-bearing) in metagabbro matrix (Tartarotti et al. 2019). Those Ca-rich metasomatic fluids may also lead to the formation of Ca-bearing tourmaline that acts as Ca-carrier at greater depths until the breakdown conditions are reached. In some cases, tourmaline can experience an extreme chemical evolution that ends up with a change in its nomenclature, for example from alkali to calcic, following the possible substitution scheme for Ca incorporation into tourmaline reported in Henry and Dutrow (1990).

The breakdown conditions of tourmaline are composition-dependent and a reference diagram of tourmaline stability field is reported in van Hinsberg et al. (2011), mainly regarding alkali tourmalines (schorl and dravite) and vacant ones (magnesian-foitite).

The occurrence of Ca-rich tourmalines in nature was experimentally demonstrated to be a function of pressure, temperature and metamorphic fluids composition (Berryman et al. 2016), but calcic tourmalines remain so far the less investigated in terms of thermal behaviour, dehydration and breakdown products, also because uvite, ideally  $\text{CaMg}_3(\text{Al}_5\text{Mg})(\text{Si}_6\text{O}_{18})(\text{BO}_3)_3(\text{OH})_3(\text{OH})$ , was only recently officially approved by the International Mineralogical Association's Commission on Nomenclature and Classification as a new mineral species of tourmaline supergroup (Bosi et al. 2022).

The present work aims at investigating the thermal behaviour and stability of the calcic tourmaline uvite, at room pressure (RP). The holotype of uvite from San Piero in Campo (Elba Island, Italy), described by Bosi et al. (2022) with formula  $^X(\text{Ca}_{0.61}\text{Na}_{0.35}\square_{0.04})_{\Sigma 1.00}^Y(\text{Mg}_{1.51}\text{Fe}^{2+}_{0.47}\text{Al}_{0.70}\text{Fe}^{3+}_{0.14}\text{Ti}_{0.18})_{\Sigma 3.00}^Z(\text{Al}_{4.54}\text{Fe}^{3+}_{0.18}\text{V}^{3+}_{0.02}\text{Mg}_{1.27})_{\Sigma 6.01}^T(\text{Si}_{5.90}\text{Al}_{0.10})_{\Sigma 6.00}(\text{BO}_3)_3^V(\text{OH})_3^W[(\text{OH})_{0.55}\text{F}_{0.05}\text{O}_{0.40}]_{\Sigma 1.00}$ , was studied by in situ high-temperature powder X-ray diffraction (HT-PXRD) up to the structural breakdown.

## Experimental

A fragment of an uvite crystal was gently ground in an agate mortar under ethanol. The resulting powder was loaded in a 0.7 mm-diameter  $\text{SiO}_2$ -glass capillary kept open at one

side. To avoid unwanted movements of the powder along the capillary, some kaolin wool-glass was used as a stopper at the open side. Finally, the capillary was fixed to a hollow corundum tube using an HT cement. In situ HT-PXRD experiments were performed using a heating chamber for capillaries, developed by MRI and Bruker AXS, placed along the beam path of the diffractometer. Relevant features and details of the thermal calibration procedure of the chamber may be found in Ballirano and Melis (2007).

Data were measured, using  $\text{CuK}\alpha$  radiation, on a Bruker AXS D8 Advance, operating in  $\theta/\theta$  geometry in transmission mode, fitted with focussing multilayer graded (Göbel) mirrors placed along the incident beam and Soller slits on both the incident ( $2.3^\circ$  opening angle) and diffracted (radial) beams. Intensities were collected by a position sensitive detector (PSD) VÅntec-1 set at an opening angle of  $6^\circ 2\theta$ .

At the end of the heating run, the capillary was cooled back at room temperature (RT) within the chamber with a  $10^\circ\text{C}/\text{min}$  rate. The powder was removed from the capillary, re-homogenized and loaded in a new borosilicate-glass capillary following the same procedure, aimed at reducing the possible effect of textured recrystallization at the walls of the capillary, adopted by Celata et al. (2021) and Ballirano et al. (2022). Data collection was performed keeping the sample outside the chamber using the same angular range, step-scan size, and counting time of the HT measurements (see Table 1).

Data were evaluated by the Rietveld method using Topas V.6 (Bruker AXS 2016) which implements the Fundamental Parameters Approach (FPA: Cheary and Coelho 1992) to describe the peak shape. Absorption correction for a cylindrical sample was performed using the equation of Sabine et al. (1998) and the procedure described by Ballirano and Maras (2006) was applied for handling the correlation existing between displacement parameters and absorption. The isotropic displacement parameters were constrained as follows:  $B_Y = B_Z = B_B = B_T$ ;

**Table 1** Miscellaneous data of the data collection and Rietveld refinements

$2\theta$ range ( $^\circ$ )	7–135
$2\theta$ step-size ( $^\circ$ )	0.021798
Counting time (s)	4
$T_{\text{max}}$ ( $^\circ\text{C}$ )	900
$T$ steps ( $^\circ\text{C}$ )	25
Heating rate ( $^\circ\text{C}/\text{min}$ )	0.5
RP (%)	0.960–1.255
$R_{\text{wp}}$ (%)	1.232–1.676
$R_{\text{Bragg}}$ (%)	0.649–0.851
DWd	1.190–1.526
$\chi^2$	1.046–1.346

Definition of the statistical indicators as indicated in Young (1993)

$B_{O1} = B_{O2} = B_{O3} = B_{O4} = B_{O5} = B_{O6} = B_{O7} = B_{O8}$ ;  $B_{H1} = B_{H3} = 1.2 * B_{O1}$ . Texture effects were corrected using spherical harmonics (8th-order, nine refinable parameters), selecting the number of appropriate terms by using the approach of Ballirano (2003). Starting structural data were taken from Bosi et al. (2022) and each refined structure at a given non-ambient  $T$  was used as input for the subsequent  $T$ . Experimental conditions and miscellaneous information regarding the refinements are listed in Table 1, a magnified 3D-plot of the full data set is shown in Fig. 1, and a representative example of Rietveld plots is shown in Fig. 2. CIFs of the uvite structure refined at the various  $T$  are given in online resource.

## Results and discussion

### Breakdown products of uvite

The first evidence of uvite structural breakdown was observed at 800 °C owing to the occurrence of weak diffraction reflections that were subsequently assigned with the help of the diffraction pattern collected on the material cooled to RT. The breakdown was completed at the  $T$  of 900 °C. The diffraction pattern of the sample cooled down at RT (Fig. 3) was refined by the Rietveld method keeping fixed all structural parameters to reference data except for unit-cell parameters. Therefore, the resulting quantitative phase analysis (QPA) must be considered as semi-quantitative. Data indicate the occurrence of prevailing indialite, ideally  $Mg_2Al_3[AlSi_5O_{18}]$  (Balassone et al. 2004), plus yuanfuliite,

ideally  $Mg(Fe^{3+},Al)O(BO_3)$  (Appel et al. 1999), plagioclase, a “boron-mullite” phase (labelled as  $Al_4B_2O_9$  in the graph; Fischer et al. 2008) and hematite as breakdown products of uvite. According to various determinative methods (Kroll 1983) and considering the relatively large standard uncertainty of the refined cell parameters, plagioclase composition could be restrained to the 75–90 An mol% range. All these phases were also identified in the HT diffraction patterns collected at  $T \geq 800$  °C, indicating that they were not produced during the cooling process. Furthermore, no intensity variation of the broad bump centred at  $\sim 22^\circ 2\theta$ , due to the capillary glass, was observed at the end of the thermal heating run testifying the absence of relevant amounts of amorphous material.

The observed assemblage of phases is significantly different with respect to that resulting from the thermal breakdown of both Fe-rich fluor-elbaite (Celata et al. 2021) and Mn-bearing fluor-elbaite (Ballirano et al. 2022). In particular, the mullite-like phase reported as the prevailing crystalline product of Fe-rich fluor-elbaite and Mn-bearing fluor-elbaite breakdown is replaced by indialite. This is due to the occurrence of significant Mg and lower Al content of the pristine uvite sample (5.24 atoms per formula unit, apfu) as compared to the fluor-elbaite ones (5.96 and 7.81 apfu, respectively).

Moreover, the absence of abundant B-rich amorphous material is justified by the occurrence, among the breakdown products of uvite, of two different phases (yuanfuliite and boromullite) where B may be accommodated.

Owing to the limited amount of “boron mullite” in mixture, it was not possible to derive reliable unit-cell

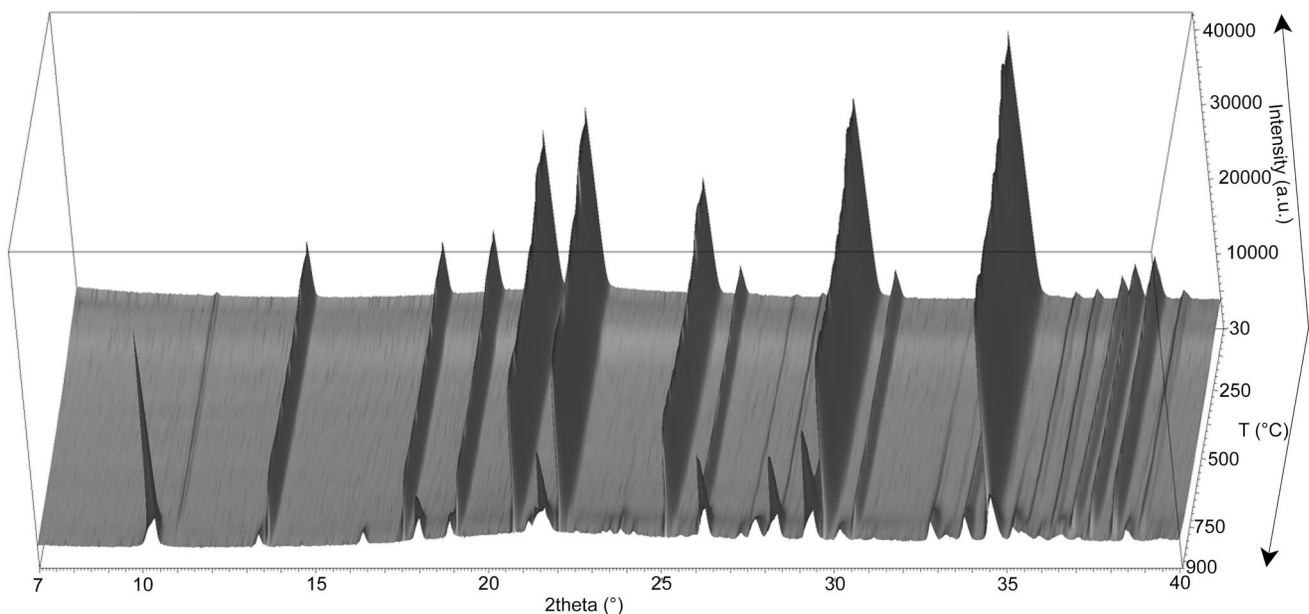


**Fig. 1** Magnified 7–40° 2 $\theta$  3D-view of the full data set collected in the 30–900 °C thermal range



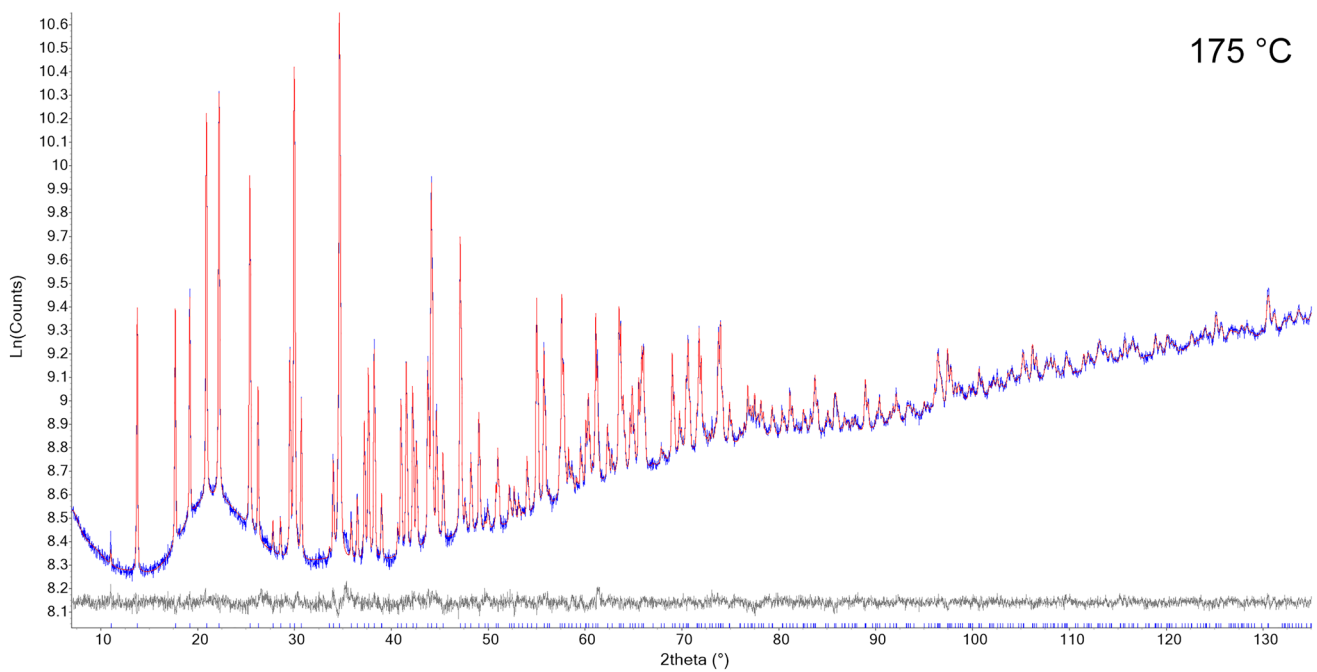


**Fig. 2** Representative example of the Rietveld plots of the diffraction pattern collected at 175 °C. Blue: experimental; red: calculated; grey: difference; vertical bars: position of calculated Bragg reflections of the uvite studied

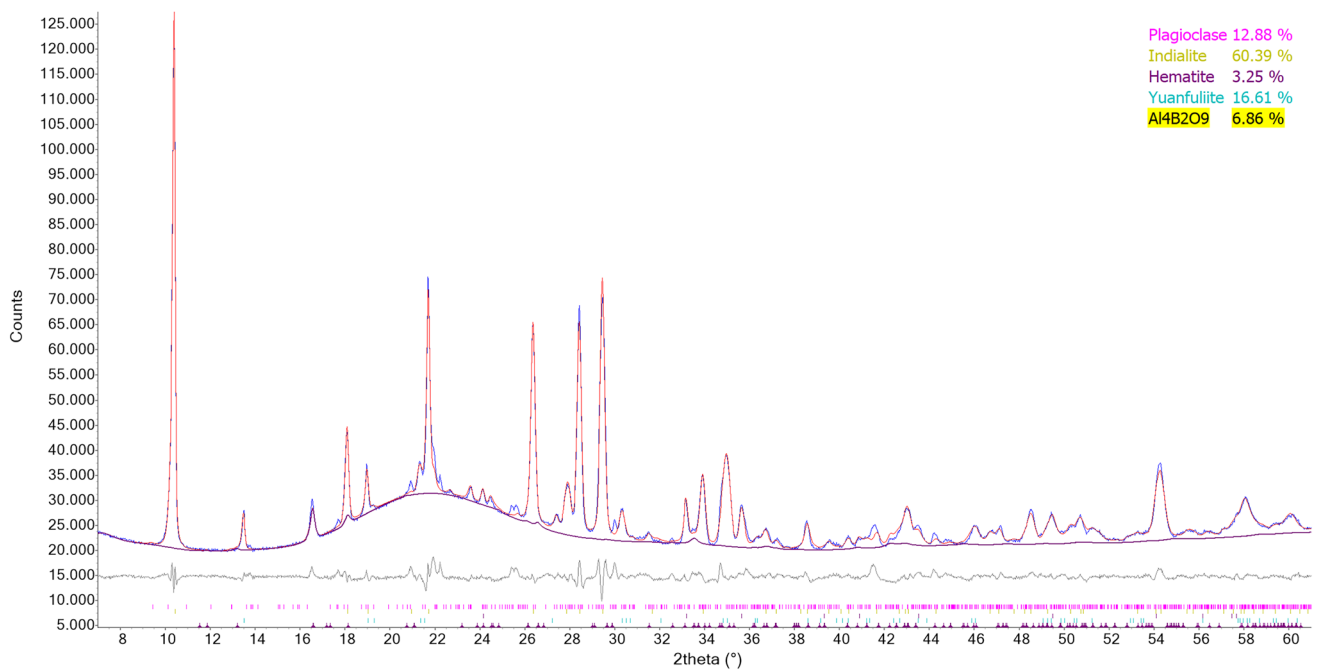


**Fig. 3** Magnified 7–60° 2θ view of the Rietveld plots of the products of breakdown of the uvite studied. Blue: experimental; red: calculated; grey: difference; vertical bars: position of calculated Bragg reflections of (from above to below) plagioclase, indialite, hematite,

yuanduliite and “boron mullite”. The contribution of “boron mullite” (labelled as  $\text{Al}_4\text{B}_2\text{O}_9$  in the legend) is indicated as a continuous magenta line

parameters to characterize in detail its chemistry as it was done for the  $\text{Al}_2\text{O}_3\text{-B}_2\text{O}_3\text{-SiO}_2$  (ABS) phases arising from the breakdown of fluor-elbaite samples (Celata et al. 2021; Ballirano et al. 2022).

Thus, after uvite breakdown, Ca is hosted in plagioclase (75–90% An) and allegedly in both indialite and yuanfuliite (< 0.10 apfu). No melt was observed, so, at these conditions, no B–Ca-bearing aqueous fluids are produced.

Our experimental results can be intended as a preliminary study of the lower limit of uvite's stability field, setting the stage for future HP–HT experiments aimed to mimic the conditions of a subducting slab to better understand the role and behaviour of Ca–tourmaline in dehydration processes and release of Ca-bearing metasomatic fluids.

### Thermal expansion and HT structure modifications

Variation of unit-cell parameter values at each  $T$  for the uvite sample is reported in Table 2, and shown in a graphical way in Fig. 4. The dependence of the unit-cell parameters from  $T$  was modelled using the Berman equation (Berman 1988). This approach indicated the occurrence of a discontinuity at 450 °C, and for this reason, the fitting was limited to a maximum  $T$  of 425 °C. The corresponding functions are shown as continuous red lines in Fig. 4. Table 3 lists the relevant parameters of the fitted functions that are compared to those of Fe-rich fluor-elbaite (Celata et al. 2021) and Mn-bearing fluor-elbaite (recalculated from the published data of Ballirano et al. 2022). Data indicate that the  $c$ -parameter is softer than the  $a$ -parameter against  $T$ . It is worth noting that uvite expands at a rate slightly greater than that of both Fe-rich fluor-elbaite and Mn-bearing fluor-elbaite.

The dependence of the normalized unit-cell parameters with  $T$  is reported in Fig. 5. The trend is very similar to that observed in both Fe-rich fluor-elbaite and Mn-bearing fluor-elbaite (Celata et al. 2021; Ballirano et al. 2022).

The first deviation from the regularly increasing trend of the  $a$ -parameter occurs at 450 °C and it ends at 625 °C; above this  $T$ , the  $a$ -parameter increases again with approximately the same rate observed below 450 °C. The  $c$ -parameter shows a discontinuity at the same  $T$  (450 °C) consisting in a very small inflexion before regaining the same expansion rate. The data measured at  $T=900$  °C, during the onset of the breakdown, apparently deviate from the trends, but they are affected by a high standard uncertainty value. It is worth noting that Mn-bearing fluor-elbaite shows a diverging behaviour for the  $a$ - and  $c$ -parameter at  $T$  exceeding 750 °C that may be related to the onset of the intracrystalline order–disorder reaction  ${}^Y\text{Li} + {}^Z\text{Al} \rightarrow {}^Z\text{Li} + {}^Y\text{Al}$  (Ballirano et al. 2022).

Based on reference data (Celata et al. 2021; Ballirano et al. 2022), the discontinuity of the unit-cell parameters' dependence from  $T$  observed in the 450–625 °C

**Table 2** Refined cell parameters of the studied uvite at the various temperatures

$T$ (°C)	$a$ (Å)	$c$ (Å)	Volume (Å <sup>3</sup> )
30	15.97430 (7)	7.22915 (4)	1597.574 (16)
50	15.97556 (7)	7.23068 (5)	1598.166 (18)
75	15.97774 (8)	7.23283 (5)	1599.076 (19)
100	15.97902 (8)	7.23433 (5)	1599.666 (19)
125	15.98156 (8)	7.23662 (5)	1600.682 (18)
150	15.98344 (8)	7.23857 (5)	1601.490 (18)
175	15.98529 (8)	7.24063 (5)	1602.315 (19)
200	15.98734 (8)	7.24250 (5)	1603.140 (19)
225	15.98915 (8)	7.24465 (5)	1603.980 (19)
250	15.99199 (8)	7.24716 (5)	1605.11 (2)
275	15.99436 (8)	7.24963 (5)	1606.13 (2)
300	15.99709 (8)	7.25208 (5)	1607.22 (2)
325	15.99985 (9)	7.25473 (5)	1608.36 (2)
350	16.00159 (9)	7.25682 (6)	1609.17 (2)
375	16.00454 (9)	7.25930 (5)	1610.32 (2)
400	16.00636 (9)	7.26132 (6)	1611.13 (2)
425	16.00847 (9)	7.26340 (6)	1612.02 (2)
450	16.00939 (10)	7.26504 (6)	1612.57 (2)
475	16.01013 (10)	7.26654 (6)	1613.05 (2)
500	16.01033 (10)	7.26831 (6)	1613.48 (2)
525	16.01014 (10)	7.27038 (6)	1613.91 (2)
550	16.00973 (10)	7.27229 (6)	1614.25 (2)
575	16.01016 (10)	7.27507 (6)	1614.95 (2)
600	16.01014 (10)	7.27735 (6)	1615.45 (2)
625	16.01128 (10)	7.27979 (6)	1616.22 (2)
650	16.01295 (10)	7.28216 (6)	1617.09 (2)
675	16.01465 (10)	7.28404 (6)	1617.85 (2)
700	16.01706 (10)	7.28628 (6)	1618.83 (2)
725	16.01871 (10)	7.28813 (6)	1619.58 (2)
750	16.02091 (10)	7.29026 (6)	1620.50 (2)
775	16.02372 (11)	7.29274 (6)	1621.62 (3)
800	16.02665 (11)	7.29551 (7)	1622.83 (3)
825	16.0290 (4)	7.2980 (2)	1623.86 (10)
850	16.031 (2)	7.2977 (12)	1624.2 (5)

thermal range is caused by the onset of the transition elements (TEs) oxidation process which is coupled to deprotonation at the H1 and/or H3 sites. In the case of uvite, the equation describing the process takes the form of  $(\text{Fe}^{2+}) + (\text{OH})^- \rightarrow (\text{Fe}^{3+}) + (\text{O}^{2-}) + 1/2\text{H}_2(\text{g})$ , (Bosi et al. 2019). In fact, such a discontinuity is similar to that observed in Fe-rich fluor-elbaite and Mn-bearing fluor-elbaite (Celata et al. 2021; Ballirano et al. 2022); the magnitude of the contraction of the cell parameters is consistent with the corresponding amounts of TEs (Fe-rich fluor-elbaite: 1.12 apfu  $\text{Fe}^{2+} + \text{Mn}^{2+}$ ; uvite, 0.47 apfu  $\text{Fe}^{2+}$ ; Mn-bearing fluor-elbaite, 0.12 apfu  $\text{Mn}^{2+}$ ).

**Fig. 4** Variation of unit-cell parameters with  $T$  for the studied uvite. The continuous red lines represent the fitted Berman functions for  $a$ ,  $c$  and vol. Parameters of the corresponding functions are listed in Table 3

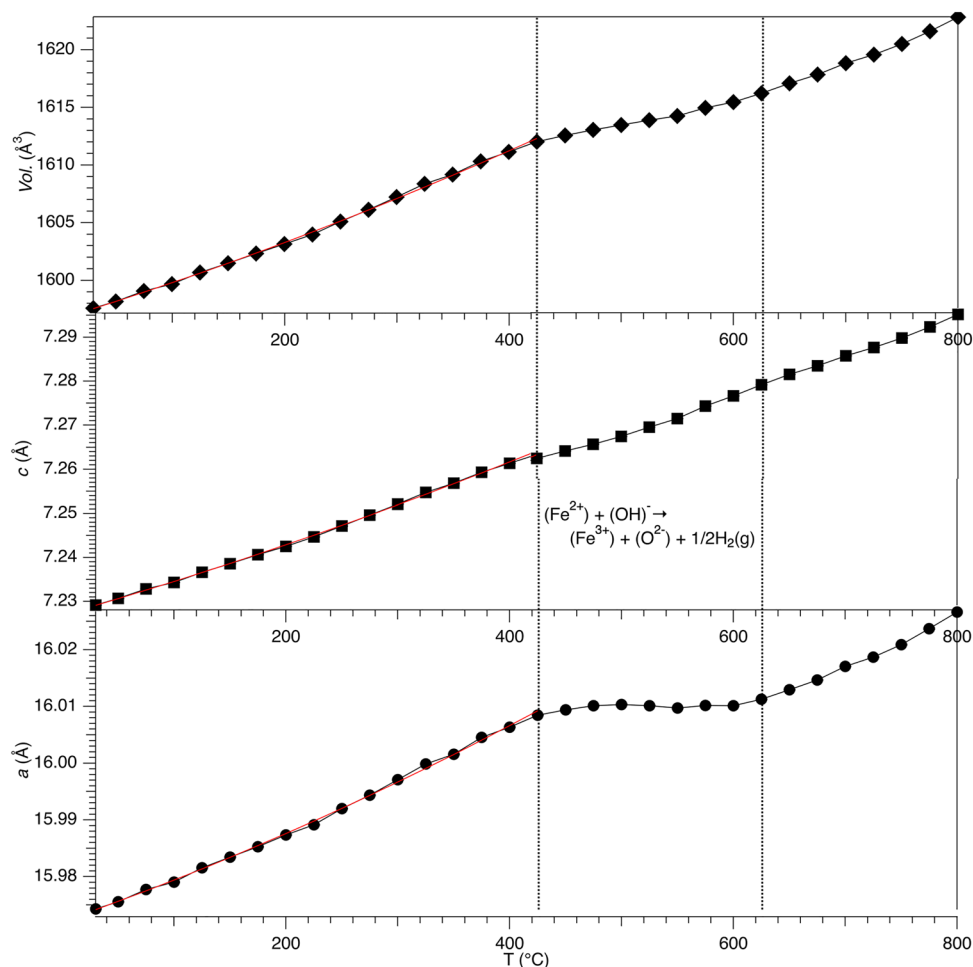
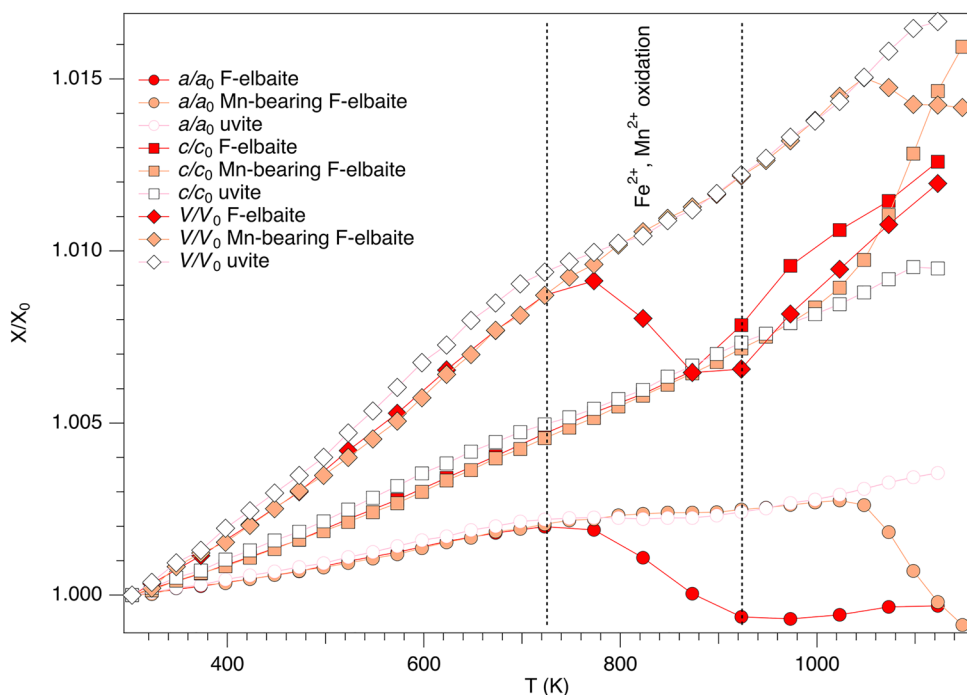


**Table 3** Relevant parameters of the fitting procedure by the Berman equation of the unit-cell parameters vs  $T$  data, up to oxidation, of different tourmaline samples

	$V_0, a_0, c_0$ ( $\text{\AA}^3, \text{\AA}, \text{\AA}$ )	$a_0$ ( $\times 10^{-5} \text{ K}^{-1}$ )	$a_1$ ( $\times 10^{-8} \text{ K}^{-2}$ )
$V$ ( $\text{\AA}^3$ )			
Uvite	1597.54 (8)	1.93 (6)	2.1 (3)
Fe-rich fluor-elbaite	1564.38 (6)	1.59 (5)	2.6 (3)
Mn-bearing fluor-elbaite	1530.15 (7)	1.56 (5)	2.6 (3)
$a$ ( $\text{\AA}$ )			
Uvite	15.97420 (23)	0.448 (18)	0.55 (9)
Fe-rich fluor-elbaite	15.91875 (19)	0.371 (17)	0.66 (10)
Mn-bearing fluor-elbaite	15.7927 (3)	0.36 (2)	0.69 (10)
$c$ ( $\text{\AA}$ )			
Uvite	7.22912 (17)	1.04 (3)	0.97 (15)
Fe-rich fluor-elbaite	7.12842 (8)	0.849 (16)	1.32 (9)
Mn-bearing fluor-elbaite	7.08421 (9)	0.841 (16)	1.23 (8)

Data for Fe-rich fluor-elbaite from Celata et al. (2021). Data for Mn-bearing fluor-elbaite recalculated from Ballirano et al. (2022). Please notice that in Celata et al. (2021), the values of  $a_1$  were erroneously listed as  $\times 10^{-9} \text{ K}^{-2}$  instead of  $10^{-8} \text{ K}^{-2}$ . Temperature of reference = 30 °C (303 K). Uvite  $T_{\text{max}}$  698 K, step 25 °C; Fe-rich fluor-elbaite  $T_{\text{max}}$  698 K, step 50 °C; Mn-bearing fluor-elbaite  $T_{\text{max}}$  723 K, step 25 °C

**Fig. 5** Dependence of the normalized unit-cell parameters from  $T$  for uvite. For comparison purpose, data from Fe-rich fluor-elbaite (Celata et al. 2021) and Mn-bearing fluor-elbaite (Ballirano et al. 2022) are also reported



As far as the structural modifications are referred to, the  $\langle X-O \rangle$  mean bond distance is characterized by a regular increase with  $T$  which is nicely fitted by a linear dependence (Fig. 6).

The dependences of  $\langle Y-O \rangle$  and  $\langle Z-O \rangle$  bond distances from  $T$  display contrasting behaviours (Figs. 7, 8). The  $\langle Y-O \rangle$  bond distance increases in a fairly regular way from 2.045 to 2.065 Å. Minor dispersion of the data

from the linear trend may be possibly related to the effect of the minor TEs' oxidation. Differently, this behaviour is evident in the case of Fe-rich fluor-elbaite, whose TEs' content is significantly higher than that of uvite. In fact, a contraction of the  $\langle Y-O \rangle$  bond distance, in the thermal range where the TEs' oxidation occurs (Celata et al. 2021), is observed and ascribed to the smaller ionic radius of  $Fe^{3+}$  than that of  $Fe^{2+}$ . Differently, the  $\langle Z-O \rangle$

**Fig. 6** Variation of  $\langle X-O \rangle$  bond distance with  $T$  for the studied uvite

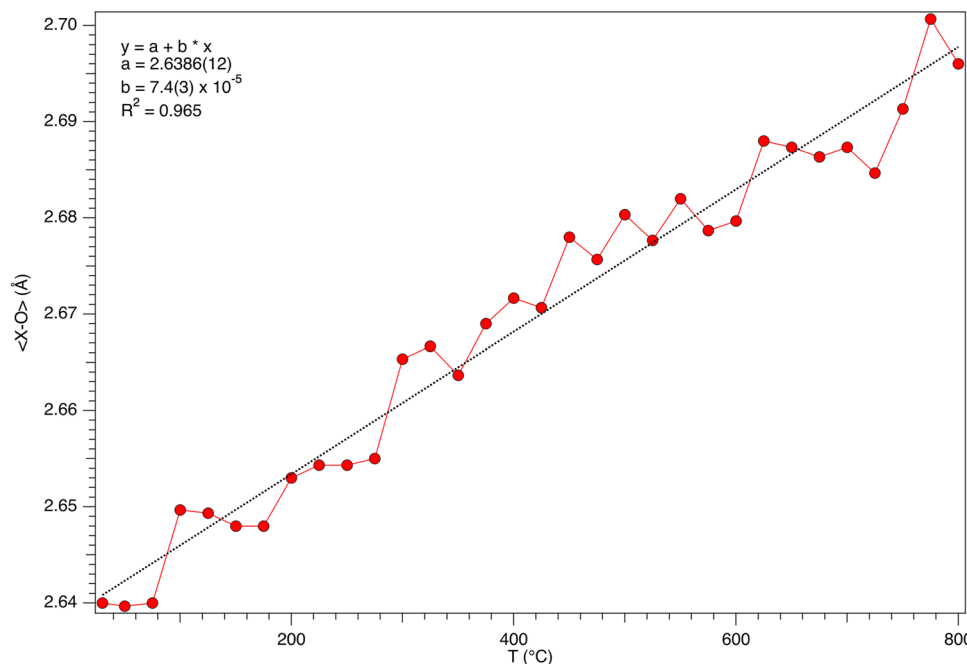


**Fig. 7** Dependence of  $\langle Y-O \rangle$  bond distances from  $T$  for the studied uvite

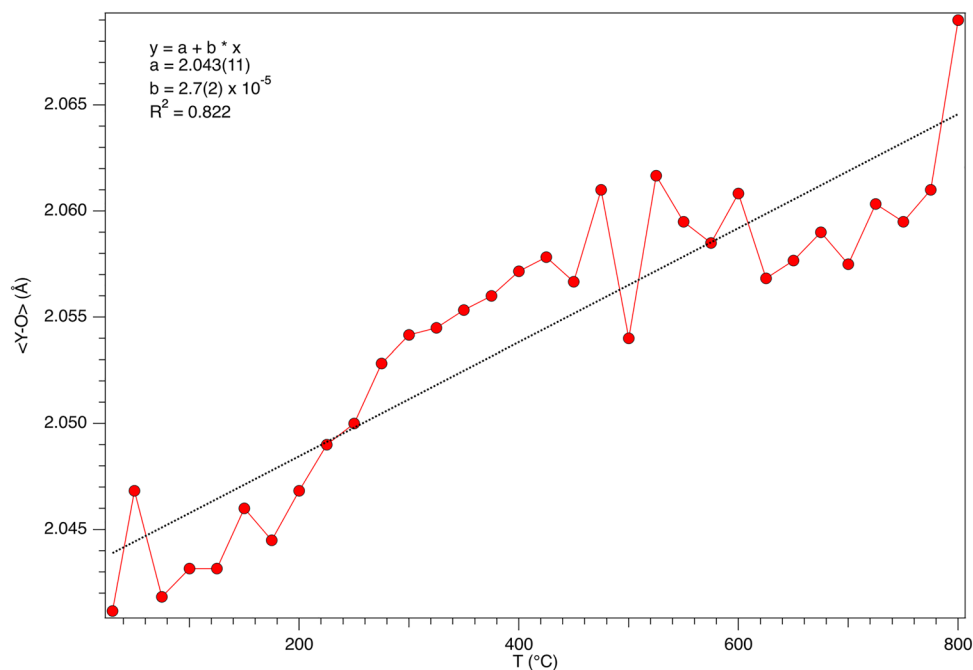
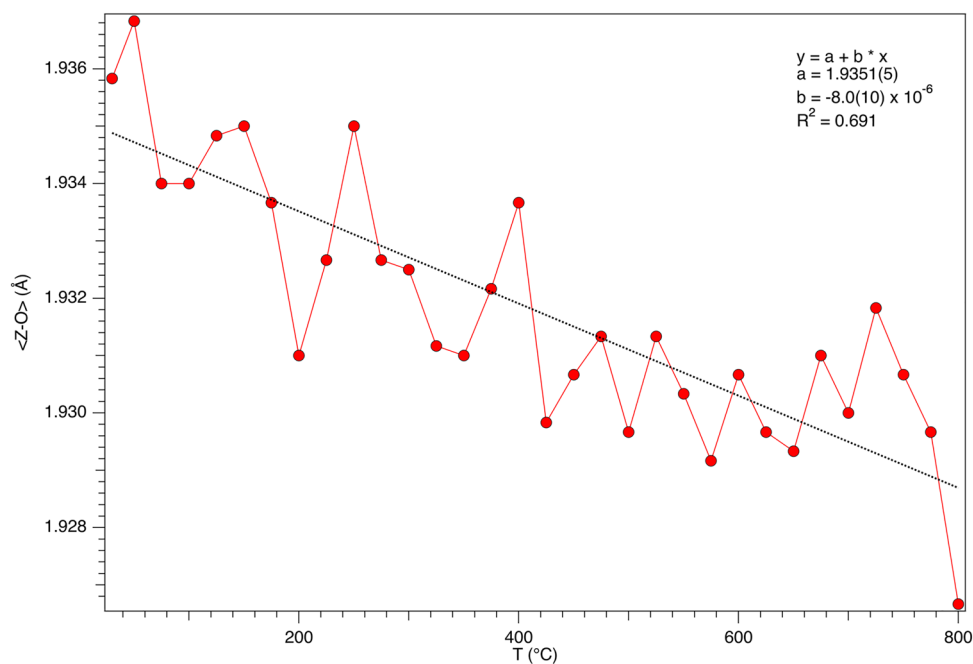


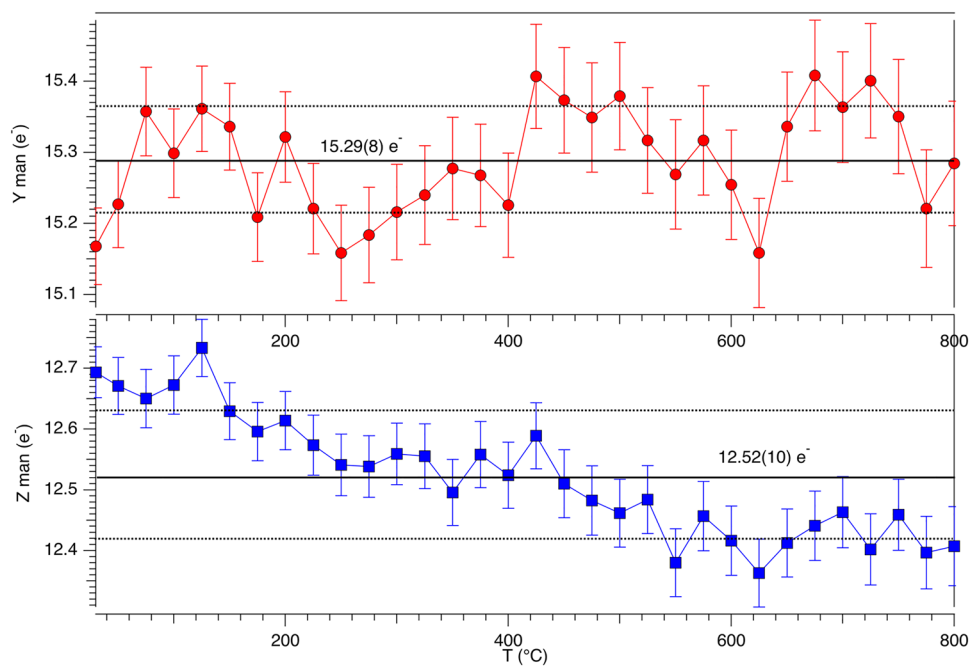
**Fig. 8** Dependence of  $\langle Z-O \rangle$  bond distances from  $T$  for the studied uvite



bond distance shows a very minor decrease, from 1.935 to 1.929 Å, as a function of  $T$ . It is unclear whether the decrease is significant or not as it is of a magnitude comparable to the standard uncertainty of individual  $Z-O$  bond distances. Such a variation could be possibly attributed to minor intracrystalline order–disorder reaction such as  ${}^Y\text{Fe} + {}^Z\text{Al} \rightarrow {}^Z\text{Fe} + {}^Y\text{Al}$  described by Ballirano et al. (2022) for Mn-bearing fluor-elbaite. However, analysis of

the mean atomic number ( $\text{man}$ ; Hawthorne et al. 1995) at both  $Y$  and  $Z$  sites (Fig. 9) shows that the small, constant reduction of  $\text{man}$  at  $Z$ , is not counterbalanced by a proportional increase at  $Y$ . This reduction may hence be related to the simplification adopted to constrain the displacement parameters of atoms at the  $Y$ ,  $Z$ ,  $B$  and  $T$  sites to be equal throughout the various refinements.

**Fig. 9** Evolution with  $T$  of mean atomic number ( $\mu_{\text{an}}$ ) at the  $Y$  (upper panel) and  $Z$  (lower panel) sites for the studied uvite. Thick black lines indicate the average values, whereas the dotted lines indicate the  $1\sigma$  level



## Conclusions

The thermal behaviour of uvite was investigated for the first time up to structural breakdown through in situ HT-PXRD.

Well before the breakdown, heating the uvite at 450 °C in air was enough to set the Fe oxidation out, counterbalanced by the deprotonation reaction:  $(\text{Fe}^{2+}) + (\text{OH})^{-} \rightarrow (\text{Fe}^{3+}) + (\text{O}^{2-}) + 1/2\text{H}_2(\text{g})$ .

Tourmaline breakdown products have been identified as indialite (prevalent) yuanduliite, plagioclase, a “boron-mullite” phase, and hematite. No melt was produced after uvite breakdown and Ca is stored in plagioclase (75–90% An).

**Acknowledgements** F.B acknowledges funding by Sapienza University of Rome grant (Prog. Università 2020) and the Ministero dell’Università e della Ricerca through the Project PRIN 2020 “HYDROX–HYDRous- vs OXo-components in minerals: adding new pieces to the Earth’s  $\text{H}_2\text{O}$  cycle puzzle”, prot. 2020WYL4NY. Comments and suggestions by Eleanor Berryman and the anonymous referee were much appreciated.

**Author contributions** PB and BC wrote the main manuscript text and PB prepared all figures and tables. All authors reviewed the manuscript.

**Funding** Open access funding provided by Università degli Studi di Roma La Sapienza within the CRUI-CARE Agreement.

## Declarations

**Competing interests** The authors declare no competing interests.

**Conflict of interest** The authors declare that there is no conflict of interest.

**Open Access** This article is licensed under a Creative Commons Attribution 4.0 International License, which permits use, sharing, adaptation, distribution and reproduction in any medium or format, as long as you give appropriate credit to the original author(s) and the source, provide a link to the Creative Commons licence, and indicate if changes were made. The images or other third party material in this article are included in the article's Creative Commons licence, unless indicated otherwise in a credit line to the material. If material is not included in the article's Creative Commons licence and your intended use is not permitted by statutory regulation or exceeds the permitted use, you will need to obtain permission directly from the copyright holder. To view a copy of this licence, visit <http://creativecommons.org/licenses/by/4.0/>.

## References

- Appel PWU, Bigi S, Brigatti MF (1999) Crystal structure of yuanduliite and its relationships with warwickite. *Eur J Mineral* 11:483–491
- Balassone G, Franco E, Mattia CA, Puliti R (2004) Indialite in xenolithic rocks from Somma-Vesuvius Volcano (southern Italy): crystal chemistry and petrogenetic features. *Am Mineral* 89:1–6
- Ballirano P (2003) Effects of the choice of different ionization level for scattering curves and correction for small preferred orientation in Rietveld refinement: the  $\text{MgAl}_2\text{O}_4$  test case. *J Appl Crystallogr* 36:1056–1061
- Ballirano P, Maras A (2006) In situ X-ray transmission powder diffraction study of the kinetics of the light induced alteration of realgar ( $\alpha\text{-As}_4\text{S}_4$ ). *Eur J Mineral* 18:589–599
- Ballirano P, Melis E (2007) Thermal behaviour of  $\beta$ -anhydrite  $\text{CaSO}_4$  to 1263 K. *Phys Chem Miner* 34:699–704

- Ballirano P, Celata B, Skogby H, Andreozzi GB, Bosi F (2022) HT breakdown of Mn-bearing elbaite from the Anjanabonoina pegmatite, Madagascar. *J Geosci*. <https://doi.org/10.3190/jgeosci.347>
- Berman RG (1988) Internally-consistent thermodynamic data for minerals in the system  $\text{Na}_2\text{O}-\text{K}_2\text{O}-\text{CaO}-\text{MgO}-\text{FeO}-\text{Fe}_2\text{O}_3-\text{Al}_2\text{O}_3-\text{SiO}_2-\text{TiO}_2-\text{H}_2\text{O}-\text{CO}_2$ . *J Petrol* 29:445–522
- Berryman EJ, Wunder B, Rhede D, Schettler G, Franz G, Heinrich W (2016) P-T-X-controls on Ca and Na distribution between Mg–Al tourmaline and fluid. *Contrib Mineral Petrol* 171:31
- Bosi F (2018) Tourmaline crystal chemistry. *Am Mineral* 103:298–306
- Bosi F, Biagioni C, Pezzotta F, Skogby H, Hålenius U, Cempírek J, Hawthorne FC, Lussier A, Abdu YA, Day MC, Fayek M, Clark CM, Grice JD, Henry DJ (2022) Uvite,  $\text{CaMg}_3(\text{Al}_5\text{Mg})(\text{Si}_6\text{O}_{18})(\text{BO}_3)_3(\text{OH})_3(\text{OH})$ , a new, but long anticipated mineral species of the tourmaline supergroup from San Piero in Campo (Elba Island, Italy). *Mineral Mag*. <https://doi.org/10.1180/mgm.2022.54>
- Bosi F, Skogby H, Hålenius U (2019) Thermally induced cation redistribution in fluor-elbaite and Fe-bearing tourmalines. *Phys Chem Miner* 46:371–383
- AXS Bruker (2016) Topas V6: general profile and structure analysis software for powder diffraction data. Bruker AXS, Germany
- Celata B, Ballirano P, Andreozzi G, Bosi F (2021) In situ high-temperature behaviour of fluor-elbaite: breakdown conditions and products. *Phys Chem Miner* 48:24
- Chery RW, Coelho AA (1992) A fundamental parameters approach of X-ray line-profile fitting. *J Appl Crystallogr* 25:109–121
- Dingwell DB, Knoche R, Webb SL, Pichavant M (1992) The effect of  $\text{B}_2\text{O}_3$  on the viscosity of haplogranitic liquids. *Am Mineral* 77:457–461
- Dutrow B, Henry D (2011) Tourmaline: a geologic DVD. *Elements* 7:301–306
- Fischer RX, Kahlenberg V, Voll D, MacKenzie KJD, Smith ME, Schnetger B, Brumsack H-J, Schneider H (2008) Crystal structure of synthetic  $\text{Al}_4\text{B}_2\text{O}_9$ : a member of the mullite family closely related to boralsilite. *Am Mineral* 93:918–927
- Hawthorne FC, Ungaretti L, Oberti R (1995) Site populations in minerals: terminology and presentation of results of crystal-structure refinement. *Can Mineral* 33:907–911
- Henry DJ, Dutrow BL (1990) Ca substitution in Li-poor aluminous tourmaline. *Can Mineral* 28:111–124
- Henry DJ, Dutrow BL (1996) Metamorphic tourmaline and its petrologic applications. In: Grew ES, Anovitz LM (eds), *Boron: mineralogy, petrology and geochemistry*. *Rev Mineral Geochem* 33:503–557
- Henry DJ, Novák M, Hawthorne FC, Ertl A, Dutrow BL, Uher P, Pezzotta F (2011) Nomenclature of the tourmaline supergroup minerals. *Am Mineral* 96:895–913
- Kroll H (1983) Lattice parameters and determinative methods for plagioclase and ternary feldspars. *Rev Mineral* 2,2nd ed: 101–120
- Lussier A, Ball NA, Hawthorne FC, Henry DJ, Shimizu R, Ogasawara Y, Ota T (2016) Maruyamaite,  $\text{K}(\text{MgAl}_2)(\text{Al}_5\text{Mg})\text{Si}_6\text{O}_{18}(\text{BO}_3)_3(\text{OH})_3\text{O}$ , a potassium-dominant tourmaline from the ultrahigh-pressure Kokchetav massif, northern Kazakhstan: description and crystal structure. *Am Mineral* 101:355–361
- Ota T, Kobayashi K, Katsura T, Nakamura E (2008a) Tourmaline breakdown in a pelitic system: implications for boron cycling through subduction zones. *Contrib Mineral Petrol* 155:19–32
- Ota T, Kobayashi K, Kunihiro T, Nakamura E (2008b) Boron cycling by subducted lithosphere; insights from diamondiferous tourmaline from Kokchetav ultrahigh-pressure metamorphic belt. *Geochim Cosmochim Acta* 72:3531–3541
- Pichavant M (1981) An experimental study of the effect of boron on a water saturated haplogranite at 1 Kbar vapour pressure. *Contrib Mineral Petrol* 76:430–439
- Sabine TM, Hunter BA, Sabine WR, Ball CJ (1998) Analytical expressions for the transmission factor and peak shift in absorbing cylindrical specimens. *J Appl Crystallogr* 31:47–51
- Shimizu R, Ogasawara Y (2013) Diversity of potassium-bearing tourmalines in diamondiferous Kokchetav UHP metamorphic rocks: a geochemical recorder from peak to retrograde metamorphic stages. *Asian J Earth Sci* 63:39–55
- Tartarotti P, Martin S, Meyzen CM, Benciolini L, Toffolo L (2019) Structural evolution and metasomatism of subducted metaophiolites in the Northwestern Alps. *Tectonics* 38:4185–4206
- van Hinsberg V, Henry DJ, Marschall HR (2011) Tourmaline: an ideal indicator of its host environment. *Can Mineral* 49:1–16
- Young RA (1993) Introduction to the Rietveld method. In: Young RA (ed) *The Rietveld method*. Oxford University Press, Oxford, pp 1–38

**Publisher's Note** Springer Nature remains neutral with regard to jurisdictional claims in published maps and institutional affiliations.



#### 2.2.4. Schorl



## Thermal behavior of schorl up to breakdown temperature at room pressure

Paolo Ballirano <sup>1</sup>, Beatrice Celata <sup>1,\*</sup>, Ferdinando Bosi <sup>1</sup>,  
Christopher E. Beckett-Brown <sup>2</sup>, Giovanni B. Andreozzi <sup>1</sup><sup>1</sup> Department of Earth Sciences, Sapienza University of Rome, Piazzale Aldo Moro, 5-I-00185  
Roma, Italy<sup>2</sup> Geological Survey of Canada, Ottawa, Ontario K1A 0E8, Canada

### ARTICLE INFO

Submitted: September 2022

Accepted: January 2023

Available on line: January 2023

\* Corresponding author:

beatrice.celata@uniroma1.it

Doi: 10.13133/2239-1002/17859

How to cite this article:

Ballirano P. et al. (2023)

Period. Mineral. 92, 23-32

### ABSTRACT

Schorl is one of the most widespread tourmaline compositions in the world, known from many different geological settings. Its role as boron and water carrier has been moderately investigated together with its stability field. In this study, the richest schorl in Fe<sup>2+</sup> content was investigated to constraint its breakdown temperature at room pressure through *in situ* powder X-Ray Diffraction (*in situ* pXRD), its breakdown products and the coupled thermally induced dehydrogenation-dehydrogenation process experienced approaching the breakdown conditions.

Schorl turned out to begin its breakdown at 850 °C with the first appearance of hematite, followed by a dominant B-mullite phase. The breakdown reaction of schorl can be expressed as follows: 2NaFe<sup>2+</sup><sub>3</sub>Al<sub>6</sub>(BO<sub>3</sub>)<sub>3</sub>Si<sub>6</sub>O<sub>18</sub>(OH)=3Fe<sub>2</sub>O<sub>3</sub>+4/3Al<sub>9</sub>Si<sub>2</sub>BO<sub>19</sub>+(Na- Si-B-rich) glass+4H<sub>2</sub>O.

The breakdown process is completed at 950 °C, when no trace of residual tourmaline is found. Annealing the schorl at 450 °C in air was enough to set the Fe oxidation out, counterbalanced by the deprotonation reaction: (Fe<sup>2+</sup>)+(OH)<sup>-</sup> → (Fe<sup>3+</sup>)+(O<sup>2-</sup>)+1/2H<sub>2</sub>(g).

Keywords: Schorl; HT-pXRD; thermal expansion; iron oxidation; deprotonation; intracrystalline cations exchange; structural breakdown.

### INTRODUCTION

Tourmalines are classified as a supergroup of complex borosilicates, being the dominant boron minerals commonly found as accessory phases in sedimentary, metamorphic, and igneous rocks.

Their ubiquity is given by different factors: the capacity to accommodate a variety of chemical elements in their crystal structure, so as to adapt to different geological environments, and the features of their crystal structure itself hence their mechanical resistance.

The general formula for tourmaline supergroup minerals is: XY<sub>3</sub>Z<sub>6</sub>T<sub>6</sub>O<sub>18</sub>(BO<sub>3</sub>)<sub>3</sub>V<sub>3</sub>W, where X=Na<sup>+</sup>, K<sup>+</sup>, Ca<sup>2+</sup>, □ (=vacancy); Y=Al<sup>3+</sup>, Fe<sup>3+</sup>, Cr<sup>3+</sup>, V<sup>3+</sup>, Mg<sup>2+</sup>, Fe<sup>2+</sup>, Mn<sup>2+</sup>, Li<sup>+</sup>;

Z = Al<sup>3+</sup>, Fe<sup>3+</sup>, Cr<sup>3+</sup>, V<sup>3+</sup>, Mg<sup>2+</sup>, Fe<sup>2+</sup>; T=Si<sup>4+</sup>, Al<sup>3+</sup>, B<sup>3+</sup>; B = B<sup>3+</sup>; V=(OH)<sup>-</sup>, O<sup>2-</sup>; W = (OH)<sup>-</sup>, F<sup>-</sup>, O<sup>2-</sup>. The unitalicized letters X, Y, Z, T and B represent groups of cations at the [9]X, [6]Y, [6]Z, [4]T and [3]B crystallographic sites (italicized letters), whereas the letters V and W represent groups of anions accommodated at the [3]-coordinated O3 and O1 crystallographic sites, respectively. Tourmaline-supergroup minerals are primarily classified into three groups, vacant, alkali and calcic, based on the X-site occupancy (Henry et al., 2011). A further level of classification into subgroups is based on charge arrangements at the Y and Z sites. Tourmalines are also distinguished by the dominant anion at the W position of the general formula into hydroxy-

fluor- and oxy-species. A more comprehensive discussion on tourmaline crystal-chemistry is given in Bosi (2018).

Depending on its composition, tourmaline appeared to be stable at different pressure and temperature conditions: a preliminary diagram of the extensive tourmaline's stability field was provided by van Hinsberg et al. (2011). Most of the experimental work done to investigate the boundaries of tourmaline's stability field was carried out on dravite or schorl (which are the most widespread compositions), considered in an artificial multi-phase system (Robbins and Yoder, 1962; Holtz and Johannes, 1991; Ota et al., 2008). Pure tourmaline systems with samples of dravitic and schorlitic composition were investigated at High Temperature (HT) and Room Pressure (RP) by Pieczka and Kraczk (2004), Bačík et al. (2011), Liu et al. (2019), Hovis et al. (2022). The present work aims at constraining the breakdown temperature of a natural schorl, ideally  $\text{NaFe}^{2+}_3\text{Al}_6(\text{Si}_6\text{O}_{18})(\text{BO}_3)_3(\text{OH})_3(\text{OH})$ , as reported by Andreozzi et al. (2020), in a mono-phase system through *in situ* High-Temperature powder X-Ray Diffraction (HT-pXRD) at room pressure, focusing on the thermally induced dehydrogenation-oxidation coupled mechanism and identifying the eventual breakdown products.

## EXPERIMENTAL

A representative black Seagull schorl single crystal was selected and a small fragment was separated and gently ground under ethanol in an agate mortar. The same material was analyzed in detail by Andreozzi et al. (2020) that reported an empirical formula  $X(\text{Na}_{0.74}\square_{0.24}\text{K}_{0.01}\text{Ca}_{0.01})_{\text{S}1.00} Y(\text{Fe}^{2+}_{2.05}\text{Al}_{0.92}\text{Ti}_{0.02}\text{Mn}_{0.01}\text{Zn}_{0.01})_{\text{S}3.00} Z(\text{Al}_{5.41}\text{Fe}^{2+}_{0.53}\text{Mg}_{0.06})_{\text{S}6.00} (\text{Si}_6\text{O}_{18}) (\text{BO}_3)_3 V(\text{OH})_3 W[(\text{OH})_{0.46}\text{F}_{0.41}\text{O}_{0.13}]$ . The resulting powder was loaded in the tip of a 0.5 mm diameter  $\text{SiO}_2$ -glass capillary. A wad of kaolin wool-glass was used as a stopper to avoid movements of the powder along the capillary. The portion of the capillary filled by the powder was of ca. 25 mm in length. Subsequently, the capillary was fixed to a hollow corundum tube using a HT cement and aligned onto a standard goniometer head.

*In situ* HT-pXRD data were collected using a heating chamber whose description, as well as details of its thermal calibration, can be found in Ballirano and Melis (2007).

Diffraction data were measured, using  $\text{CuK}\alpha$  radiation, with a Bruker AXS D8 Advance which operates in transmission mode. The instrument is fitted with focusing multilayer graded (Göbel) mirrors along the incident beam, Soller slits on both the incident ( $2.3^\circ$  opening angle) and diffracted (radial) beam, and with a position sensitive detector (PSD) VÅntec-1 set at an opening angle of  $6^\circ 2\theta$ .

According to the large transition elements (TE) content of the sample, both a high absorption (calculated  $\mu\text{R}=3.18$ , for an estimated packing efficiency of 60%) and a significant secondary fluorescence were expected.

Preliminary data collections confirmed the existence of the problem, possibly limiting the extraction of reliable structural parameters especially at HT. A diffraction pattern was measured at room temperature (RT) outside the chamber for a characterization of the sample owing to the possible chemical inhomogeneity of the crystal from which the fragment was extracted. The pattern indicated the occurrence in mixture of traces of quartz.

High-*T* data were measured in the 30-925 °C range. After reaching the maximum temperature, the capillary was cooled back at RT within the chamber with a 10 °C/min cooling rate. Following the procedure adopted by Celata et al. (2021) and Ballirano et al. (2022 a,b), to avoid the effect of textured recrystallization at the walls of the capillary, the powder was extracted, re-homogenized, and loaded in a new capillary for performing a data collection keeping the capillary outside the chamber.

Data were evaluated by the Rietveld method using Topas V.6 (Bruker AXS 2016). This program adopts the Fundamental Parameters Approach (FPA: Cheary and Coelho, 1992) to model the peak shape. The equation of Sabine et al. (1998) was used to correct for absorption effects of a cylindrical sample and the procedure described in Ballirano and Maras (2006) was followed to remove the correlation existing between displacement parameters and absorption. The isotropic displacement parameters were constrained as follow:  $B_Y=B_Z=B=B_T$ ;  $B_{O1}=B_{O3}$ ;  $B_{O2}=B_{O4}=B_{O5}=B_{O6}=B_{O7}=B_{O8}$ ;  $B_{H1}=B_{H3}=1.2 * B_{O1}$ . Owing to the impossibility to refine simultaneously the site occupancy fraction (*sof*) and the displacement parameter of the *X* site, the *sof* was kept fixed at the starting value. Preferred orientation effects were modelled using spherical harmonics (8<sup>th</sup>-order, nine refinable parameters: Ballirano, 2003). Starting structural data were taken from Andreozzi et al. (2020) and each refined structure at a given non-ambient *T* was used as input for the subsequent *T*. Miscellaneous data of the RT data collection and of the Rietveld refinement are listed in Table 1. Unit-cell parameters determined at RT are shown in Table 2, relevant bond distances, isotropic displacement parameters, and mean atomic number (*man*; Hawthorne et al., 1995) at RT are reported in Table 3. Miscellaneous data of the HT data collection and of the Rietveld refinements are given in Table 4. A magnified 3D-plot of the full data set is shown in Figure 1 and a representative example of Rietveld plots is shown in Figure 2. The CIF of the schorl structure refined at RT is given in Online Resource.

## RESULTS AND DISCUSSION

### RT structure of the schorl sample

The Rietveld refinement confirms the occurrence in mixture of 1.22(5) wt% of quartz (Figure S1).

The structure at RT is in close agreement, despite

Table 1. Miscellaneous data of the RT data collection and Rietveld refinement.

2 $\theta$ range (°)	7-145
2 $\theta$ step-size (°)	0.021798
Counting time (s)	8
R <sub>p</sub> (%)	0.521
R <sub>wp</sub> (%)	0.807
R <sub>Bragg</sub> (%)	0.429
DWd	1.296
$\chi^2$	1.751
Quartz (wt%)	1.22(5)

Definition of the statistical indicators as indicated in Young (1993).

Table 2. Unit-cell parameters at RT of the schorl sample. Data of Andreozzi et al. (2020) are reported for comparison.

	Andreozzi et al. (2020)	Present work
<i>a</i> (Å)	15.9957(3)	16.00573(11)
<i>c</i> (Å)	7.1863(2)	7.19134(6)
<i>V</i> (Å <sup>3</sup> )	1592.36(7)	1595.48(3)

the relatively large standard uncertainties (ss), with that refined from single-crystal X-ray diffraction measurements (Andreozzi et al., 2020). However, the present unit-cell parameters are slightly larger than those of reference data (Table 2), suggesting some chemical differences between the two fragments as already reported by Sinclair and Richardson (1992). Moreover, refined *man* (Table 3) indicates its increase at the *Y* site in the present sample [22.93(11) vs 22.06(4)], whereas that at *Z*, it is similar [13.93(9) vs 14.14(3)] to the data of Andreozzi et al. (2020).

Bond distances are consistent with the data of Andreozzi et al. (2020) showing only minor differences. Both <*Y-O*> and <*Z-O*> are slightly shorter in the present sample (2.034 Å vs 2.051 Å and 1.914 Å vs 1.924 Å) and they nicely plot within the structural-stability limits for tourmaline minerals (Bosi and Lucchesi, 2007; Bosi, 2018; Andreozzi et al., 2020). By contrast, the observed <*X-O*> is slightly longer (2.716 Å vs 2.700 Å) than that reported by Andreozzi et al. (2020). It is worth noting that the observed differences in mean bond-distances are of the order of 2-3s of the individual bond distances, thus

Table 3. Relevant bond distances (Å), group of isotropic displacement parameters (Å<sup>2</sup>: see text for explanation) and mean atomic number (*man*) of *Y* and *Z* sites. Data of Andreozzi et al. (2020) are reported for comparison.

	Andreozzi et al. (2020)	Present work
<i>X</i> B <sub>iso</sub>	1.785	1.1(2)
< <i>Y,Z,B,T</i> > B <sub>iso</sub>	0.541	0.79(3)
< <i>O</i> <sub>1,3</sub> > B <sub>iso</sub>	1.864	2.08(18)
< <i>O</i> <sub>2,4,8</sub> > B <sub>iso</sub>	0.766	0.65(6)
<i>man Y</i>	22.06(4)	22.93(11)
<i>man Z</i>	14.14(3)	13.93(9)
<i>B-O</i> (2)	1.366(2)	1.378(18)
<i>B-O</i> (8) x2	1.3807(13)	1.373(8)
< <i>B-O</i> >	1.376	1.375
<i>T-O</i> (6)	1.6063(9)	1.610(5)
<i>T-O</i> (7)	1.6093(8)	1.629(5)
<i>T-O</i> (4)	1.6267(5)	1.621(4)
<i>T-O</i> (5)	1.6397(5)	1.598(4)
< <i>T-O</i> >	1.621	1.615
<i>X-O</i> (2) x3	2.514(2)	2.565(10)
<i>X-O</i> (5) x3	2.7635(15)	2.782(9)
<i>X-O</i> (4) x3	2.8210(15)	2.801(9)
< <i>X-O</i> >	2.700	2.716
<i>Y-O</i> (2) x2	2.0020(8)	2.015(5)
<i>Y-O</i> (6) x2	2.0414(9)	2.024(6)
<i>Y-O</i> (1)	2.0640(15)	2.048(7)
<i>Y-O</i> (3)	2.1546(15)	2.075(9)
< <i>Y-O</i> >	2.051	2.034
<i>Z-O</i> (6)	1.8753(9)	1.871(5)
<i>Z-O</i> (7)	1.8901(8)	1.879(6)
<i>Z-O</i> (8)	1.8910(9)	1.897(6)
<i>Z-O</i> (8)	1.9326(9)	1.908(7)
<i>Z-O</i> (7)	1.9710(9)	1.965(6)
<i>Z-O</i> (3)	1.9819(6)	1.961(4)
< <i>Z-O</i> >	1.924	1.914

Table 4. Miscellaneous data of the HT data collection and Rietveld refinements.

2 $\theta$ range (°)	7-135
2 $\theta$ Step-size (°)	0.021798
Counting time (s)	4
T <sub>max</sub> (°C)	925
T steps (°C)	25
Heating rate (°C/min)	0.5
Rp (%)	0.878-1.014
Rwp (%)	1.172-1.243
R <sub>Bragg</sub> (%)	0.385-0.548
DWd	1.131-1.730
$\chi^2$	1.090-1.389

they may be considered as questionable. For this reason, we did not attempt to correlate variation of *man* and mean bond distances to discuss modifications of the present *Y* and *Z* site populations.

#### Breakdown products of schorl

The first evidence of schorl structural breakdown was observed at 850 °C owing to the occurrence of weak extra diffraction reflections (Figure 1). These reflections progressively increased in intensity at the expenses of those of schorl. The breakdown was completed at 925 °C as signaled by the complete disappearance of the schorl reflections. The diffraction pattern of the sample cooled down at RT (Figure 3) was used for identifying the schorl breakdown products and the pattern was refined by the Rietveld method constraining all structural parameters to reference data, except for the unit-cell parameters.

Consequently, the resulting quantitative phase analysis (QPA) must be considered as semi-quantitative. Data indicate the occurrence of prevailing B-mullite and hematite as schorl breakdown products plus some amorphous material (Table 5). The occurrence of relicts of unreacted schorl results from the re-homogenisation of the powder. In fact, this procedure admixed powders coming not only from the portion bathed by the X-rays but also from inner zones of the capillary affected by some thermal gradient.

All these crystalline phases were also identified in the HT diffraction patterns collected at *T* 800 °C, therefore, clearly indicating that they were not produced during the cooling process. The observed assemblage of phases is similar to that observed for both Fe-rich fluor-elbaite (Celata et al., 2021) and Mn-bearing fluor-elbaite (Ballirano et al., 2022a) but is significantly different with respect to that resulting from the thermal breakdown of uvite (Ballirano et al., 2022b). In fact, the B-mullite-like phase reported as the prevailing crystalline product of the breakdown of schorl, Fe-rich fluor-elbaite, and Mn-bearing fluor-elbaite, in uvite did not form and indialite was instead observed as the dominant breakdown product.

Evaluation of the unit-cell parameters of B-mullite (Table 5) provided interesting crystal-chemical and structural information. Unit-cell parameters of B-mullite are similar to those of the product of the thermal breakdown of Fe-rich fluor-elbaite (Celata et al., 2021), whereas they are larger than those of the equivalent phase arising from the breakdown of Mn-bearing fluor-elbaite (Ballirano et al., 2022a) (Table S1). In this regard, it is worth noting that Lührs et al. (2014) have shown the existence of relations linking unit-cell parameters and B<sub>2</sub>O<sub>3</sub> mol% content of B-mullites. Generally speaking, an increase of the B<sub>2</sub>O<sub>3</sub> mol% content produces a progressive contraction of the

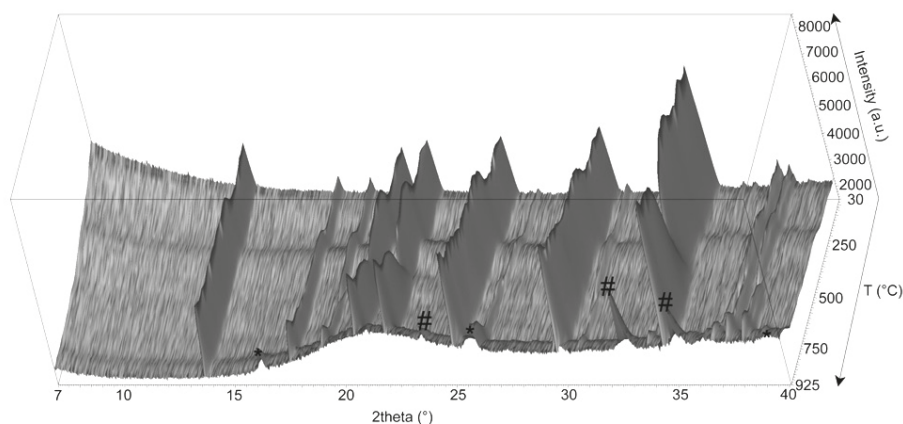


Figure 1. Magnified view (7-40° 2 $\theta$ ) of the full data set of the heating cycle of schorl.

\* relevant reflections of hematite;# relevant reflections of B-mullite.

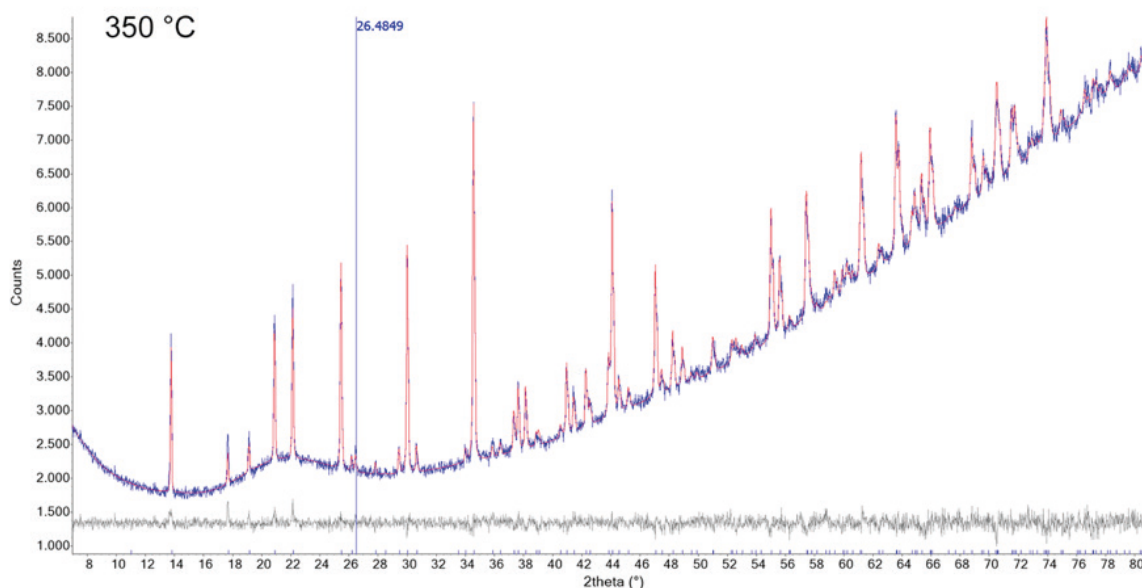


Figure 2. Magnified 7-80° 2θ view of a representative example of the Rietveld plots of the diffraction pattern collected at 350 °C. Blue: experimental; red: calculated; grey: difference; below: vertical bars indicate the position of calculated Bragg reflections of schorl. The vertical blue line identifies the position of the strongest reflection of quartz.

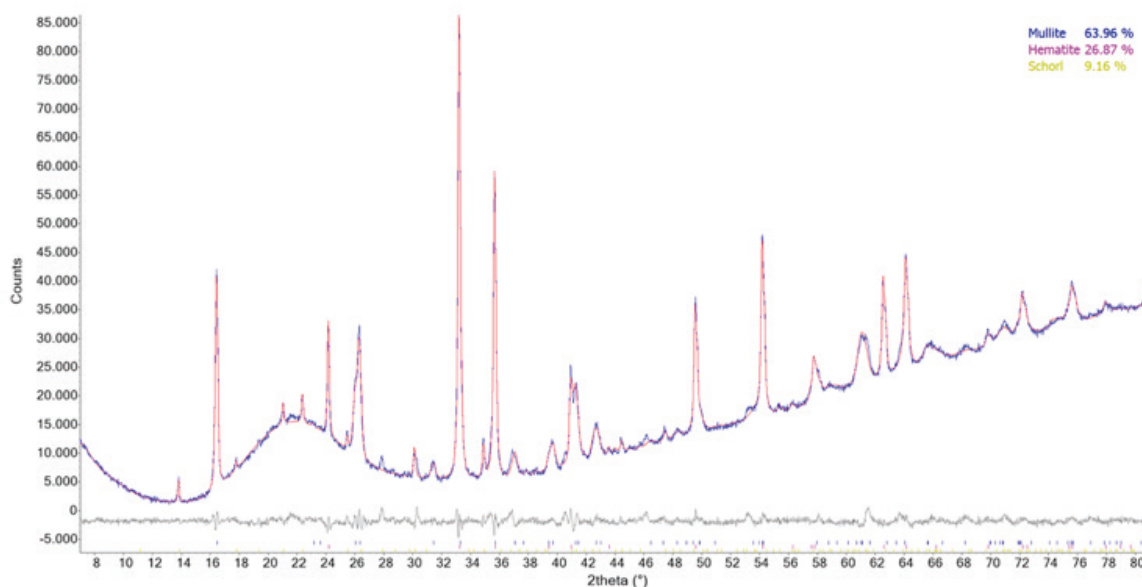


Figure 3. Magnified 7-80° 2θ view of the Rietveld plots of the products of breakdown of the schorl. Data collected at RT. Blue: experimental; red: calculated; grey: difference; vertical bars: position of calculated Bragg reflections of (from above to below) B-mullite, hematite, and schorl (unreacted). Intensities on logarithmic scale.

unit-cell values. Accordingly, in the case of the B-mullite arising from the thermal breakdown of both schorl and Fe-rich fluor-elbaite, the  $B_2O_3$  content may be estimated, by using the various regression equations of Lührs et al. (2014), to ca. 10 mol%, whereas it is significantly

higher for the B-mullite arising from the breakdown of Mn-bearing fluor-elbaite (16-17 mol%: Ballirano et al., 2022a). The different  $B_2O_3$  mol% of the B-mullites reflects the different  $B_2O_3$  content of the pristine tourmalines. In fact, Mn-bearing fluor-elbaite contains 0.40 additional B



Table 5. RT unit-cell parameters and quantitative phase analysis (QPA) of the thermal breakdown products of schorl.

Phase	Space group	<i>a</i> (Å)	<i>b</i> (Å)	<i>c</i> (Å)	<i>V</i> (Å <sup>3</sup> )	wt%
B-Mullite	<i>Pbam</i>	7.5307(5)	7.6703(6)	2.8427(2)	164.20(2)	64.0(6)
Hematite	<i>R-3c</i>	5.02610(9)	= <i>a</i>	13.7084(3)	299.904(13)	26.9(5)
Tourmaline after HT	<i>R3m</i>	15.8577(14)	= <i>a</i>	7.2115(9)	1570.5(3)	9.2(3)
Pristine schorl	<i>R3m</i>	16.0050(3)	= <i>a</i>	7.1910(2)	1595.26(7)	100

atoms per formula unit (*apfu*) at the *T* site (Ballirano et al., 2022a).

### Thermal expansion

The dependence of the studied schorl cell parameters from *T* is reported in Table 6, and their relative expansion as a function of *T* is shown in Figure 4.

The trend of the studied schorl is very similar to that observed in Fe-rich fluor-elbaite (Celata et al., 2021), Mn-bearing fluor-elbaite (Ballirano et al., 2022a) and uvite (Ballirano et al., 2022b) (Figure 5). The main event is evidenced by the significant contraction of the unit-cell parameters occurring, approximately, in the 450-675 °C thermal range. However, this contraction is more pronounced for schorl, consistently with the larger TE content as compared to that of the other tourmaline samples (schorl: 2.58 apfu Fe<sup>2+</sup>; Fe-rich fluor-elbaite: 0.94 apfu Fe<sup>2+</sup>+0.18 apfu Mn<sup>2+</sup>; uvite: 0.47 apfu Fe<sup>2+</sup>; Mn-bearing fluor-elbaite: 0.12 apfu Mn<sup>2+</sup>). Based on reference data, the contraction is produced by the onset of the TE oxidation process, coupled to deprotonation at H1 and/or H3 sites. In the case of schorl the general equation describing the process takes the form of (Fe<sup>2+</sup>)+(OH)<sup>-</sup> → (Fe<sup>3+</sup>)+(O<sup>2-</sup>)+1/2H<sub>2</sub>(g), (Bosi et al., 2019). The thermal range for the onset of the coupled dehydrogenation-oxidation process converges with those observed in literature (e.g. Hovis et al., 2022; Pieczka and Kraczka, 2004; Castañeda et al., 2006; McKeown, 2008; Bačik et al., 2011; Filip et al., 2012; Liu et al., 2019) and it was constrained at ca. 450 °C.

It is worth noting that, in the 550-625 °C thermal range, a significant peak broadening/splitting is observed. This phenomenon may be explained by the simultaneous strong contraction of the unit-cell parameters and the presence of some longitudinal thermal gradient (Table 6).

The variation of the unit-cell parameters with *T* was modelled up to 425 °C, i.e. before the onset of TE oxidation, using the Berman equation (Berman 1988). Table 7 reports the relevant parameters of the fitting procedure. Data indicate that the *a*-parameter is softer than the *c*-parameter against *T*, coherently with other analyzed tourmalines. Uvite is, among those analyzed, the tourmaline showing

the largest thermal expansion whereas elbaite minerals are characterized by smaller and very similar *a*<sub>0</sub> and *a*<sub>1</sub> parameters. Schorl has an intermediate behavior (Figure 5 and Table 7). Our findings agree with Hoang et al. (2013), where variation of cell parameters, experienced before the breakdown, is correlated to the amount of TE (Fe<sup>2+</sup> ions, and therefore to the oxidation of Fe<sup>2+</sup> to Fe<sup>3+</sup>).

The unit-cell parameters of the relict tourmaline recovered at RT after the heating run (Table 5) shows a significant contraction as compared to the pristine schorl, clearly indicating that the (Fe<sup>2+</sup>)+(OH)<sup>-</sup> → (Fe<sup>3+</sup>)+(O<sup>2-</sup>)+1/2H<sub>2</sub>(g) reaction has taken place and has been quenched to RT.

Unfortunately, the quality of the diffraction data prevents us from a detailed description of the structural modifications occurring during the heating run.

Unit-cell parameters of B-mullite and hematite during the thermal breakdown of schorl are reported in Table 8.

### Schorl stability field

Referring to the diagram reported in van Hinsberg et al. (2011), the results obtained by our experimental work prove that schorl is still stable with respect to literature data (Holt and Johannes, 1991) when temperature approaches 825 °C and that breakdown is experienced between 825 and 850 °C. Schorl breakdown temperature at 3 Kbar from literature data is considerably lower, 750-775 °C (Holt and Johannes, 1991), mainly because it was analyzed in a SiO<sub>2</sub> saturated system in order to mimic a natural gneiss even if doped with an excess of tourmaline, and also because a certain water content (0.6 to 6.0 wt% H<sub>2</sub>O) was added to the starting material.

### CONCLUSIONS

The thermal behavior of schorl was investigated up to structural breakdown through *in situ* HT-pXRD. Results show higher breakdown temperature (~850 °C) with respect to the literature. Annealing the schorl at 450 °C in air was enough to set the Fe oxidation out, counterbalanced by the deprotonation reaction: (Fe<sup>2+</sup>)+(OH)<sup>-</sup> → (Fe<sup>3+</sup>)+(O<sup>2-</sup>)+1/2H<sub>2</sub>(g).

Tourmaline breakdown products were identified



Table 6. Refined unit-cell parameters of the studied schorl at the various temperatures.

In italics: thermal range where peak broadening/splitting was observed due to strong contraction of the unit-cell parameters and the presence of some longitudinal thermal gradient. \* In mixture with B-mullite and hematite. Breakdown completed at 925 °C.

T (°C)	<i>a</i> (Å)	<i>c</i> (Å)	<i>V</i> (Å <sup>3</sup> )	wt% <i>B-mullite</i>	wt% <i>hematite</i>
30	16.0050(3)	7.19099(15)	1595.26(7)	-	-
50	16.0057(3)	7.19236(15)	1595.70(7)	-	-
75	16.0079(3)	7.19435(15)	1596.57(7)	-	-
100	16.0091(3)	7.19564(15)	1597.11(7)	-	-
125	16.0110(3)	7.19794(15)	1597.99(7)	-	-
150	16.0129(3)	7.19980(15)	1598.80(7)	-	-
175	16.0143(3)	7.20142(16)	1599.43(7)	-	-
200	16.0165(3)	7.20364(15)	1600.35(7)	-	-
225	16.0181(3)	7.20577(15)	1601.14(7)	-	-
250	16.0201(3)	7.20787(15)	1602.02(7)	-	-
275	16.0224(3)	7.21013(16)	1602.98(7)	-	-
300	16.0242(3)	7.21226(17)	1603.82(7)	-	-
325	16.0260(3)	7.21442(18)	1604.65(8)	-	-
350	16.0287(3)	7.21713(17)	1605.81(8)	-	-
375	16.0309(3)	7.21963(18)	1606.79(8)	-	-
400	16.0322(3)	7.22168(17)	1607.51(8)	-	-
425	16.0350(3)	7.22434(17)	1608.68(8)	-	-
450	16.0363(4)	7.22664(19)	1609.44(9)	-	-
475	16.0367(4)	7.2284(2)	1609.91(9)	-	-
500	16.0368(5)	7.2307(2)	1610.45(11)	-	-
525	16.0365(5)	7.2327(3)	1610.83(12)	-	-
550	<i>16.0306(7)</i>	<i>7.2332(3)</i>	<i>1609.75(15)</i>	-	-
575	<i>16.0142(11)</i>	<i>7.2339(5)</i>	<i>1606.6(3)</i>	-	-
600	<i>15.9737(13)</i>	<i>7.2391(7)</i>	<i>1599.7(3)</i>	-	-
625	<i>15.9327(8)</i>	<i>7.2454(4)</i>	<i>1592.8(2)</i>	-	-
650	15.9180(4)	7.2528(2)	1591.51(10)	-	-
675	15.9150(4)	7.2587(2)	1592.23(10)	-	-
700	15.9176(3)	7.26292(18)	1593.66(8)	-	-
725	15.9180(3)	7.26553(18)	1594.38(8)	-	-
750	15.9208(3)	7.26905(19)	1595.65(8)	-	-
775	15.9227(3)	7.2734(2)	1596.98(8)	-	-
800	15.9236(4)	7.27787(19)	1598.15(8)	-	-
825	15.9255(3)	7.28344(18)	1599.76(7)	-	-
850*	15.9285(4)	7.28836(19)	1601.43(8)	-	2.3(2)
875*	15.9328(5)	7.2926(3)	1603.23(12)	26.0(3)	7.9(5)
900*	15.9314(15)	7.2914(9)	1602.7(4)	56.0(5)	12.1(11)
925	-	-	-	83.3(9)	16.7(9)

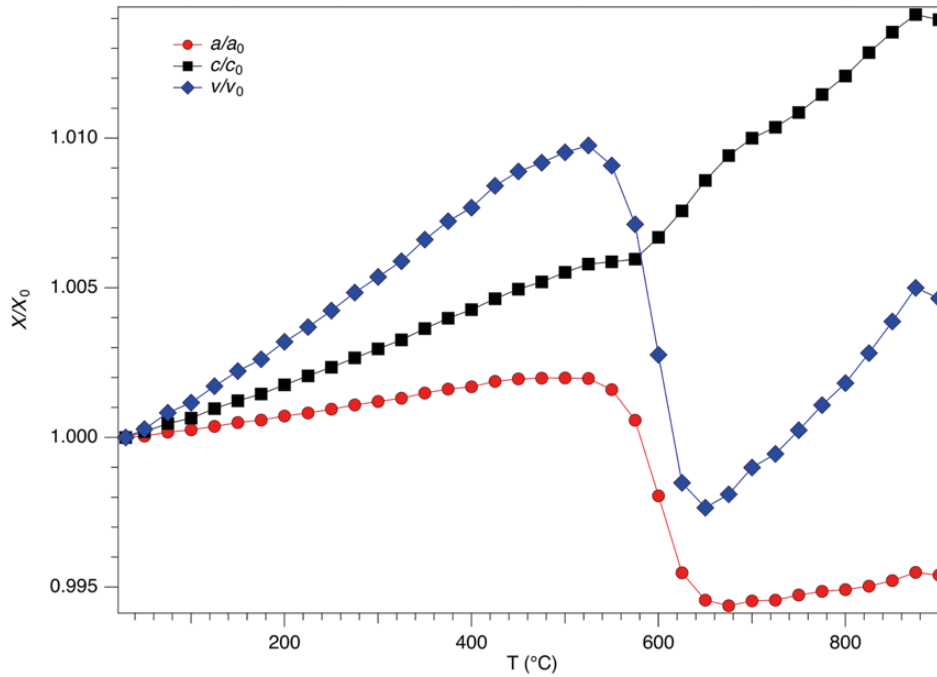


Figure 4. Variation of normalized unit-cell parameters with  $T$  for the schorl studied.

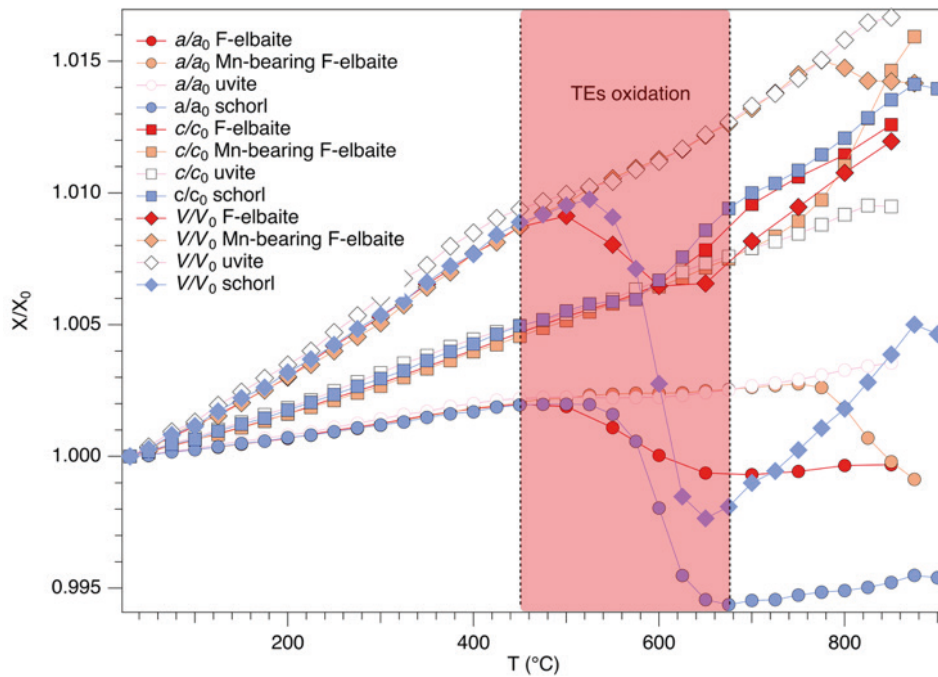


Figure 5. Comparison of the normalized unit-cell parameters from  $T$  for the various tourmaline species: schorl (present work), Fe-rich fluor-elbaite (Celata et al., 2021), Mn-bearing fluor-elbaite (Ballirano et al., 2022a), and uvite (Ballirano et al., 2022b). The pinkish area delimitates the common temperature range where transition elements oxidation occurs.

Table 7. Relevant parameters of the fitting procedure by the Berman equation of the unit-cell parameters vs  $T$  data, up to oxidation, for different tourmaline species. Data of Fe-rich fluor-elbaite, Mn-bearing fluor-elbaite and uvite from Celata et al. (2021) and Ballirano et al. (2022 a,b).

Temperature of reference = 30 °C (303 K).

Uvite  $T_{\max}$  425 °C, step 25 °C;

Schorl  $T_{\max}$  425 °C, step 25 °C;

Fe-rich fluor-elbaite  $T_{\max}$  425 °C, step 50 °C;

Mn-bearing fluor-elbaite  $T_{\max}$  450 °C, step 25 °C;

		$V_0, a_0, c_0$ (Å <sup>3</sup> , Å, Å)	$a_0$ (x 10 <sup>-5</sup> K <sup>-1</sup> )	$a_l$ (x 10 <sup>-8</sup> K <sup>-2</sup> )
$V$ (Å <sup>3</sup> )	Uvite	1597.54(8)	1.93(6)	2.1(3)
	Schorl	1595.22(5)	1.70(4)	2.19(19)
	Fe-rich fluor-elbaite	1564.38(6)	1.59(5)	2.6(3)
	Mn-bearing fluor-elbaite	1530.15(7)	1.56(5)	2.6(3)
$a$ (Å)	Uvite	15.97420(23)	0.448(18)	0.55(9)
	Schorl	16.00479(19)	0.386(14)	0.46(7)
	Fe-rich fluor-elbaite	15.91875(19)	0.371(17)	0.66(10)
	Mn-bearing fluor-elbaite	15.7927(3)	0.36(2)	0.69(10)
$c$ (Å)	Uvite	7.22912(17)	1.04(3)	0.97(15)
	Schorl	7.19103(10)	0.927(17)	1.28(8)
	Fe-rich fluor-elbaite	7.12842(8)	0.849(16)	1.32(9)
	Mn-bearing fluor-elbaite	7.08421(9)	0.841(16)	1.23(8)

Table 8. Unit-cell parameters of B-mullite and hematite during the thermal breakdown of schorl.

Phase	T (°C)	$a$ (Å)	$b$ (Å)	$c$ (Å)	volume (Å <sup>3</sup> )
	850	-	-	-	-
B-Mullite	875	7.579(4)	7.713(4)	2.8496(12)	166.56(14)
	900	7.571(2)	7.721(3)	2.8506(8)	166.62(9)
	925	7.5652(19)	7.730(2)	2.8504(7)	166.69(7)
	850	5.0740(12)	= $a$	13.819(5)	308.10(19)
Hematite	875	5.0801(3)	= $a$	13.8265(14)	309.02(5)
	900	5.0826(3)	= $a$	13.8349(11)	309.52(4)
	925	5.0827(3)	= $a$	13.8363(10)	309.56(5)

as a “boron-mullite” phase (dominant), and hematite plus some amorphous material and the breakdown reaction of schorl can be expressed as follows:  $2\text{NaFe}^{2+}_3\text{Al}_6(\text{BO}_3)_3\text{Si}_6\text{O}_{18}(\text{OH})=3\text{Fe}_2\text{O}_3+4/3\text{Al}_9\text{Si}_2\text{BO}_{19}+(\text{Na}-\text{Si}-\text{B-rich})\text{glass}+4\text{H}_2\text{O}$ .

#### ACKNOWLEDGEMENTS

We acknowledge W. David Sinclair (emeritus, Geological Survey of Canada) for collecting the sample material.

Funding by Sapienza University of Rome grant (Prog. Università 2020) is acknowledged together with Ministero dell’Università e della Ricerca through the project PRIN 2020



“HYDROX - HYDRous- vs OXo-components in minerals: adding new pieces to the Earth’s H<sub>2</sub>O cycle puzzle”, prot. 2020WYL4NY.

## REFERENCES

- Andreozzi G.B., Bosi F., Celata B., Capizzi L.S., Stagno V., Beckett-Brown C., 2020. Crystal-chemical behavior of Fe<sup>2+</sup> in tourmaline dictated by structural stability: insights from a schorl with formula Na<sup>Y</sup>(Fe<sup>2+</sup><sub>2</sub>Al)<sup>Z</sup>(Al<sub>5</sub>Fe<sup>2+</sup>)(Si<sub>6</sub>O<sub>18</sub>)(BO<sub>3</sub>)<sub>3</sub>(OH)<sub>3</sub>(OH,F) from Seagull batholith (Yukon Territory, Canada). *Physics and Chemistry of Minerals* 47, 3-9.
- Bačík P., Ozdín D., Miglierini M., Kardošová P., Pentrák M., Haloda J., 2011. Crystallochemical effects on heat treatment on Fe-dominant tourmalines from Dolní Bory (Czech Republic) and Vlachovo (Slovakia). *Physics and Chemistry of Minerals* 38, 599-611.
- Ballirano P., 2003. Effects of the choice of different ionization level for scattering curves and correction for small preferred orientation in Rietveld refinement: the MgAl<sub>2</sub>O<sub>4</sub> test case. *Journal of Applied Crystallography* 36, 1056-1061.
- Ballirano P., Celata B., Skogby H., Andreozzi G.B., Bosi F., 2022a. HT breakdown of Mn-bearing elbaite from the Anjanaboina pegmatite, Madagascar. *Journal of Geosciences* 67, 1-11. doi: 10.3190/jgeosci.347.
- Ballirano P., Celata B., Bosi F., 2022b. In-situ high-temperature behaviour and breakdown conditions of uvite at room pressure. *Physics and Chemistry of Minerals*, in press.
- Ballirano P. and Maras A., 2006. In-situ X-ray transmission powder diffraction study of the kinetics of the light induced alteration of realgar (α-As<sub>4</sub>S<sub>4</sub>). *European Journal of Mineralogy* 18, 589-599.
- Ballirano P. and Melis E., 2007. Thermal behaviour of β-anhydrite CaSO<sub>4</sub> to 1,263K. *Physics and Chemistry of Minerals* 34, 699-704.
- Berman R.G., 1988. Internally-consistent thermodynamic data for minerals in the system Na<sub>2</sub>O-K<sub>2</sub>O-CaO-MgO-FeO-Fe<sub>2</sub>O<sub>3</sub>-Al<sub>2</sub>O<sub>3</sub>-SiO<sub>2</sub>-TiO<sub>2</sub>-H<sub>2</sub>O-CO<sub>2</sub>. *Journal of Petrology* 29, 445-522.
- Bosi F., 2018. Tourmaline crystal chemistry. *American Mineralogy* 103, 298-306.
- Bosi F., Andreozzi G.B., Federico M., Graziani G., Lucchesi S., 2005. Crystal chemistry of the elbaite-schorl series. *American Mineralogy* 90, 1784-1792.
- Bosi F., Skogby H., Hälenius U., 2019. Thermally induced cation redistribution in fluor-elbaite and Fe-bearing tourmalines. *Physics and Chemistry of Minerals* 46, 371-383.
- Bruker AXS, 2016. Topas V6: General profile and structure analysis software for powder diffraction data. Bruker AXS, Karlsruhe, Germany.
- Castañeda C., Eeckhout S.G., da Costa G.M., Botelho N.F., De Grave E., 2006. Effect of heat treatment on tourmaline from Brazil. *Physics and Chemistry of Minerals* 33, 207-216.
- Celata B., Ballirano P., Andreozzi G., Bosi F., 2021. In-situ high-temperature behaviour of fluor-elbaite: breakdown conditions and products. *Physics and Chemistry of Minerals* 48, 24.
- Cheary R.W. and Coelho A.A., 1992. A Fundamental Parameters Approach of X-ray line-profile fitting. *Journal of Applied Crystallography* 25, 109-121.
- Dutrow B. and Henry D., 2011. Tourmaline: a geologic DVD. *Elements* 7, 301-306.
- Filip J., Bosi F., Novák M., Skogby H., Tuček J., Čuda J., Wildner M., 2012. Iron redox reactions in the tourmaline structure: High-temperature treatment of Fe<sup>3+</sup>-rich schorl. *Geochimica et Cosmochimica Acta* 86, 239-256.
- Hawthorne F.C., Ungaretti L., Oberti R., 1995. Site populations in minerals: terminology and presentation of results of crystal-structure refinement. *Canadian Mineralogist* 33, 907-911.
- Henry D.J., Novák M., Hawthorne F.C., Ertl A., Dutrow B.L., Uher P., Pezzotta F., 2011. Nomenclature of the tourmaline supergroup minerals. *American Mineralogist* 96, 895-913.
- Hoang L.H., Hien N.T.M., Chen X.-B., Yang I.S., 2013. Annealing effect in raman scattering of various types of tourmalines. *Journal of Applied Spectroscopy* 79, 881-887.
- Holtz F. and Johannes W., 1991. Effect of tourmaline on melt fraction and composition of first melts in quartzofeldspathic gneiss. *European Journal of Mineralogy* 3, 527-536.
- Liu X., Yu C., Yang W., Xie L., Liang S., 2019. Thermal decomposition kinetics of Fe-rich tourmaline. *European Journal of Mineralogy* 31, 919-928.
- Lührs H., Soellradl S., King S.P., Hanna J.V., Konzett J., Fischer R.X., 2014. Ambient and high-pressure synthesis, composition, and crystal structure of B-mullites. *Crystal Research Technology* 49, 21-31.
- McKeown D.A., 2008. Raman spectroscopy, vibrational analysis, and heating of buergerite tourmaline. *Physics and Chemistry of Mineralogy* 35, 259-270.
- Pieczka A. and Kraczka J., 2004. Oxidized tourmalines: a combined chemical, XRD and Mossbauer study. *European Journal of Mineralogy* 16, 309-321.
- Sabine T.M., Hunter B.A., Sabine W.R., Ball C.J., 1998. Analytical expressions for the transmission factor and peak shift in absorbing cylindrical specimens. *Journal of Applied Crystallography* 31, 47-51.
- Sinclair W.D. and Richardson J.M., 1992. Quartz-tourmaline orbicules in the Seagull Batholith, Yukon Territory. *Canadian Mineralogist* 30, 923-935.
- van Hinsberg V.J., Henry D.J., Marshall H.R., 2011. Tourmaline: An ideal indicator of its host environment. *Canadian Mineralogist* 49, 1-16.
- Young R.A., 1993. Introduction to the Rietveld method: In: Young R.A. (Ed.) “The Rietveld method”. Oxford University Press, 1-38.



This work is licensed under a Creative Commons Attribution 4.0 International License CC BY-NC-SA 4.0.

## 2.2.5. Axinite

### **In situ thermal behavior of axinite at room pressure and breakdown products**

Beatrice Celata<sup>1</sup>, Paolo Ballirano<sup>1</sup>, Giovanni B. Andreozzi<sup>1</sup>

<sup>1</sup> *Dipartimento di Scienze della Terra, Sapienza Università di Roma, Piazzale A. Moro 5, I-00185, Rome, Italy*

\* Corresponding author: [beatrice.celata@uniroma1.it](mailto:beatrice.celata@uniroma1.it)

Conflicts of interest: The authors declare no conflict of interest.

Beatrice Celata wrote the main manuscript text and Paolo Ballirano prepared all figures and tables and is responsible for the experimental work. Giovanni B. Andreozzi provided the experimental material. All Authors reviewed the manuscript.

**Running title: *In-situ* high-temperature behaviour of axinite**

#### **Abstract**

A natural sample of axinite from Luning, Nevada, with composition  $^{VI}[\text{Ca}_{3.94}\text{Mn}_{0.58}\text{Fe}^{2+}_{0.75}\text{Mg}_{0.77}\text{Zn}_{0.01}\text{Al}_{3.96}]^{IV}[\text{B}_{1.95}\text{Si}_{8.04}]\text{O}_{30.0}(\text{OH})_{2.0}$  was studied through in-situ High Temperature Powder X-Ray Diffraction (HT-pXRD) up to breakdown at room pressure.

The breakdown reaction occurs at 850 °C and the breakdown products were identified at room temperature by X-Ray Powder Diffraction (XRPD). The breakdown reaction can be described as follows: axinite  $\rightarrow$  anorthite + clinopyroxene + SiO<sub>2</sub> (Qtz) + (possible) amorphous material.

The uncertainties related to the refinement of diffraction data from a triclinic structure at high temperature were too large to obtain reliable information on dehydrogenation and iron oxidation of the studied sample.

**KEYWORDS:** axinite, HT-XRPD, thermal expansion, iron oxidation, deprotonation, structural breakdown.

## Introduction

Minerals of the axinite groups are little-known borosilicates occurring as accessory phases, commonly found in metamorphic environments, characterized by an ax morphology given by their acute edges. Seldom used as gemstones, axinites are colorful minerals ranging from blue to pinkish orange.

Axinite minerals crystallize in  $P\bar{1}$  space group in the triclinic crystal system. Their crystal-chemical formula is expressed as follows:  $[X1 X2 Y Z1 Z2]_2[T1 T2 T3 T4 T5]_2O_{30}(O_wOH_{1-w})_2$  (Andreozzi et al., 2004). The sites X1, X2, Y, Z1 and Z2 are octahedrally coordinated and sites T1, T2, T3, T4 and T5 are tetrahedrally coordinated. The X1 site accommodates Ca (and very minor Na), X2 is occupied by Ca (for tinzenite, X2 = Mn), Z1 = Al and Fe<sup>3+</sup>; Z2 = Al; T1, T2, and T3 = Si; T4 = Si (and presumably very minor B); T5 = B and minor Si, and four end-member terms are defined depending on the Y site population: axinite-(Mn) if Y = Mn (also true for tinzenite), axinite-(Fe) if Y = Fe<sup>2+</sup> or axinite-(Mg) if Y = Mg, with minor Al and Fe<sup>3+</sup> (Figure 1).

Most of the axinites described in literature range from axinite-(Fe) to (minor) axinite-(Mn) with very few samples falling in the axinite-(Mg) portion, see Fig. 1. Axinites composition is observed to vary depending on the metamorphic grade: more ferroan at low metamorphic grade and more manganoan with increasing metamorphic grade (Pringle and Kawachi, 1980).

The reason why we have an apparent lack of a complete Mn-Mg solid solution is allegedly to infer to the unusual enrichment in both Mn and Mg of formation fluids rather than a structural constraint.

Axinites are sorosilicates, therefore their fundamental unit is made of Si<sub>2</sub>O<sub>7</sub> groups. Two Si<sub>2</sub>O<sub>7</sub> groups are bonded by BO<sub>4</sub> tetrahedra in order to make a six-membered tetrahedral ring. For this reason, axinites can be also ascribed to the cyclosilicates class. Each tetrahedral ring is then stacked over a layer of X1-X2-Y-Z1-Z2 octahedra.

Axinites are boron carrier minerals in the crust, considered as an alternative phase to tourmaline in metamorphic environments (Andreozzi et al., 2000). Their crystal-chemistry has been extensively studied (e.g. Grew, 1996; Andreozzi et al., 2000; Andreozzi et al., 2004) but their stability field has not been investigated systematically. The only constraints related to axinites stability are given by extrapolation from natural samples and insights from their host rocks (Pringle and Kawachi 1980; Dubé and Guha 1993; Novák and Filip 2002; Filip et al., 2008) or experimental work performed on a Mn-Fe axinite by Waclawska et al. (1998) and an axinite-(Mn) by Krzhizhanovskaya et al. (2020).

In this work, the thermal behavior of a natural sample of (Mn,Fe,Mg)-bearing axinite from Luning, Nevada, was studied through in-situ High Temperature Powder X-Ray Diffraction (HT-pXRD) up to breakdown at room pressure.

## Experimental

The sample of axinite from Luning, Nevada, has composition  ${}^{\text{VI}}[\text{Ca}_{3.94}\text{Mn}_{0.58}\text{Fe}^{2+}_{0.75}\text{Mg}_{0.77}\text{Zn}_{0.01}\text{Al}_{3.96}]^{\text{IV}}[\text{B}_{1.95}\text{Si}_{8.04}]\text{O}_{30.0}(\text{OH})_{2.0}$  and was fully characterized by Andreozzi et al. (2000). A homogeneous fragment of this sample was grinded in an agate mortar under ethanol. The resulting powder was loaded in a 0.7 mm diameter  $\text{SiO}_2$ -glass capillary kept open at one side. To avoid unwanted movements of the powder along the capillary, some kaolin wool-glass was used as a stopper at the open side. Finally, the capillary was fixed to a hollow corundum tube using a HT cement. Data were measured, using  $\text{CuK}\alpha$  radiation, on a Bruker AXS D8 Advance, operating in  $\theta/\theta$  geometry in transmission mode, fitted with focussing multilayer graded (Göbel) mirrors placed along the incident beam and Soller slits on both the incident ( $2.3^\circ$  opening angle) and diffracted (radial) beams. Intensities were collected by a position sensitive detector (PSD) VÅntec-1 set at an opening angle of  $6^\circ 2\theta$ .

*In situ* HT-PXRD experiments were performed using a heating chamber for capillaries, developed by MRI and Bruker AXS, placed along the beam path of the diffractometer. Relevant features and details of the thermal calibration procedure of the chamber may be found in Ballirano and Melis (2007).

At the end of the heating run the capillary was cooled back at room temperature (RT) within the chamber with a cooling rate of  $10^\circ\text{C}/\text{min}$ . The powder was removed from the capillary, re-homogenized and loaded in a new borosilicate-glass capillary following the same procedure, aimed at reducing the possible effect of textured recrystallization at the walls of the capillary, developed by Celata et al. (2021) and Ballirano et al. (2022a; 2022b). Data collection was performed keeping the sample outside the chamber using the same angular range, step-scan size, and counting time of the HT measurements (see Table 1).

Data were evaluated by the Rietveld method using Topas V.6 (Bruker AXS 2016) which implements the Fundamental Parameters Approach (FPA: Cheary and Coelho 1992) to describe the peak shape. Absorption correction for a cylindrical sample was performed using the equation of Sabine et al. (1998) and the procedure described by Ballirano and Maras (2006) was applied for handling the correlation existing between displacement parameters and absorption. The isotropic displacement parameters were constrained as follow:  $B_Y = B_Z = B_B = B_T$ ;  $B_{O1} = B_{O2} = B_{O3} = B_{O4} = B_{O5} = B_{O6} = B_{O7}$



=  $B_{08}$ ;  $B_{H1} = B_{H3} = 1.2 * B_{01}$ . Texture effects were corrected using spherical harmonics (8th-order, nine refinable parameters), selecting the number of appropriate terms by using the approach of Ballirano (2003).

## Results and discussion

Breakdown of axinite at room pressure is constrained at  $T = 850\text{ }^{\circ}\text{C}$ , when no characteristic diffraction peaks could be detected any more (Figure 2, Table 2), consistent with literature data, where breakdown temperatures of  $897\text{ }^{\circ}\text{C}$  (Wacławska et al., 1998),  $890\text{ }^{\circ}\text{C}$  (Hemingway et al., 1996) and  $900\text{ }^{\circ}\text{C}$  (Krzhizhanovskaya et al., 2020) are reported. In the thermal range between  $775$  and  $850\text{ }^{\circ}\text{C}$  a splitting of the diffraction peaks was observed, due to the onset of a thermal gradient in the capillary. The breakdown products were identified as anorthite (64 %), a clinopyroxene-like phase  $\text{Ca}(\text{Mg}, \text{Fe}^{3+}, \text{Mn}^{3+})(\text{Al}, \text{Si})_2\text{O}_6$  (27 %) and quartz (8 %), as shown in Figure 3. Some amorphous material was also detected in this study in a very limited amount. A minor occurrence of tridimite was detected around  $900\text{ }^{\circ}\text{C}$ , but it was likely formed in correspondence of the hottest portion of the capillary due to the polymorphic transformation of some quartz, but during the re-homogenization of the powder at room temperature it was not observed anymore.

The breakdown products are consistent with literature data, which provide evidence of an incongruent melting of axinite resulting into anorthite and clinopyroxene (bustamite in Krzhizhanovskaya et al., 2020) or rankinite in Wacławska et al (1998) and some possible amorphous material.

The thermal behavior of axinite up to  $575\text{ }^{\circ}\text{C}$  is quite linear for all the unit cell parameters, with a sudden increase up to  $677\text{ }^{\circ}\text{C}$  followed again by a linear trend, as reported in Figure 4. The dependence of the unit-cell parameters from  $T$  up to a max  $T$  of  $575\text{ }^{\circ}\text{C}$  was modelled using the Berman equation (Berman 1988) and the relevant parameters of the fitting procedure are listed in Table 3. The major thermal expansion is ascribed to the  $b$  parameter.

The deviation from linearity above  $575\text{ }^{\circ}\text{C}$  is possibly explained with the oxidations of the transition elements (Fe and  $\text{Mn}^{2+}$ ) as commonly observed for other borosilicate minerals (e.g. for tourmaline: Bosi et al. 2019; Celata et al. 2021; Ballirano et al. 2022a; Ballirano et al. 2022b) and as was similarly observed by Hemingway et al. (1996) and Krzhizhanovskaya et al. (2020) for axinite, but differently from tourmaline (where a contraction of the  $\text{YO}_6$  polyhedra is observed) here we have an enhanced expansion, the origin of which is not clear. Some polymorphic transformation was claimed by Krzhizhanovskaya et al. (2020) to explain the bulk expansion of axinite structure above  $600\text{ }^{\circ}\text{C}$ , not completely substantiated by the oxidation-dehydrogenation only, but no evidence from diffraction

data was observed by these authors and in this work. Therefore, other explanations are required to justify the sharp thermal expansion showed by the sample at above 600 °C.

## References

- Andreozzi GB, Ottolini L, Lucchesi S, Graziani G, Russo U (2000) Crystal chemistry of the axinite-group minerals: A multi-analytical approach. *American Mineralogist* 85:698–706.
- Andreozzi GB, Lucchesi S, Graziani G, Russo U (2004) Site distribution of Fe<sup>2+</sup> and Fe<sup>3+</sup> in the axinite mineral group: New crystal-chemical formula. *American Mineralogist* 89: 1763–1771.
- Ballirano P (2003) Effects of the choice of different ionization level for scattering curves and correction for small preferred orientation in Rietveld refinement: the MgAl<sub>2</sub>O<sub>4</sub> test case. *Journal of Applied Crystallography* 36:1056-1061
- Ballirano P, Maras A (2006) In-situ X-ray transmission powder diffraction study of the kinetics of the light induced alteration of realgar ( $\alpha$ -As<sub>4</sub>S<sub>4</sub>). *European Journal of Mineralogy* 18:589-599
- Ballirano P, Melis E (2007) Thermal behaviour of  $\beta$ -anhydrite CaSO<sub>4</sub> to 1,263K. *Physics and Chemistry of Minerals* 34:699-704
- Ballirano P, Celata B, Skogby H, Andreozzi GB, Bosi F (2022a) HT breakdown of Mn-bearing elbaite from the Anjanabonoina pegmatite, Madagascar. *Journal of Geosciences* 67: 151–161.
- Ballirano P, Celata B, Bosi F (2022b) In situ high-temperature behaviour and breakdown conditions of uvite at room pressure. *Physics and Chemistry of Minerals* 49: 40.
- Berman RG (1988) Internally-consistent thermodynamic data for minerals in the system Na<sub>2</sub>O-K<sub>2</sub>O-CaO-MgO-FeO-Fe<sub>2</sub>O<sub>3</sub>-Al<sub>2</sub>O<sub>3</sub>-SiO<sub>2</sub>-TiO<sub>2</sub>-H<sub>2</sub>O-CO<sub>2</sub>. *Journal of Petrology* 29:4 45–522.
- Bosi F, Skogby H, Hålenius U (2019) Thermally induced cation redistribution in fluor-elbaite and Fe-bearing tourmalines. *Physics and Chemistry of Minerals* 46:371–383.
- Celata B, Ballirano P, Andreozzi G, Bosi F (2021) In-situ high-temperature behaviour of fluor-elbaite: breakdown conditions and products. *Physics and Chemistry of Minerals* 48:24.
- Cheary RW, Coelho AA (1992) A Fundamental Parameters Approach of X-ray line-profile fitting. *Journal of Applied Crystallography* 25:109-121
- Dubé B, Guha J (1993) Factors controlling the occurrence of ferro-axinite within Archean gold copper-rich quartz veins—Cooke mine, Chibougamau area, Abitibi greenstone-belt. *The Canadian Mineralogist*, 31, 905–916.

- Filip J, Kolitsch U, Novak M, Schneeweiss O (2006) The crystal structure of near-end-member ferroaxinite from an iron-contaminated pegmatite at Malešov, Czech Republic. *The Canadian Mineralogist* 44:1159-1170.
- Filip J, Dachs E, Tuček J, Novák M, Bezdička P (2008) Low-temperature calorimetric and magnetic data for natural end-members of the axinite group. *American Mineralogist* 93:548-557.
- Grew ES (1996) Borosilicates (exclusive of tourmaline) and boron in rock-forming minerals in metamorphic environments. In L.M. Anovitz and E.S. Grew, Eds., *Boron: Mineralogy, Petrology, and Geochemistry*, 33, 387–502. *Reviews in Mineralogy*, Mineralogical Society of America, Washington, D.C.
- Hemingway B, Evans HT Jr, Mazdab FK, Anovitz LM (1996) Thermal expansion of some borate and borosilicate minerals (fluorborite, danburite, sinhalite, datolite, elbaite, dravite, kornerupine, dumortierite, ferro-axinite, and manganaxinite) between 25 and about 1200°C. U.S. Geological Survey, 15 pp.
- Krzhizhanovskaya MG, Firsova VA, Bubnova RS, Britvin SN, Bubnova OG, Pekov IV (2020) The High-Temperature Behavior of Axinite-(Mn), Kornerupine, and Leucosphenite. *Geology of Ore Deposits* 62: 819–826.
- Novák, M. and Filip, J. (2002) Ferroan magnesioaxinite from hydrothermal veins at Lazany, Brno Batholith, Czech Republic. *Neues Jahrbuch Fur Mineralogie Monatshefte*, 9, 385–399.
- Pringle IJ, Kawachi Y (1980) Axinite mineral group in low-grade regionally metamorphosed rocks in southern New Zealand. *American Mineralogist*, 65:1119–1129.
- Sabine TM, Hunter BA, Sabine WR, Ball CJ (1998) Analytical expressions for the transmission factor and peak shift in absorbing cylindrical specimens. *Journal of Applied Crystallography* 31:47-51
- Vigier M, Fritsch E (2020) Pink axinite from Merelani, Tanzania: a natural luminescent mineral irradiated in the Neoproterozoic Mozambique Metamorphic Belt. *The Journal of Gemmology* 37(2):192-205
- Wacławska I, Pieczka A, Olkiewicz St, Zabinski W (1998) Thermal decomposition of axinite. *Journal of Thermal Analysis* 52:413–423.
- Young RA (1993) Introduction to the Rietveld method. Pp. 1-38 in: *The Rietveld method* (R.A. Young, editor). Oxford University Press

**Table 1** Miscellaneous data of the data collection and Rietveld refinements

$2\theta$ range ( $^{\circ}$ )	7-145
$2\theta$ step-size ( $^{\circ}$ )	0.021798
Counting time (s)	4
$T_{\max}$ (K)	1173
T steps (K)	25
Rp (%)	1.170-1.506
Rwp (%)	1.493-2.092
$R_{\text{Bragg}}$ (%)	0.268-0.505
DWd	1.033-1.750
$\chi^2$	1.057-1.430

Definition of the statistical indicators as indicated in Young (1993)

**Table 2** Refined cell parameters of the studied axinite at the various temperatures.

$T$ ( $^{\circ}\text{C}$ )	$a$ ( $\text{\AA}$ )	$b$ ( $\text{\AA}$ )	$c$ ( $\text{\AA}$ )	$V$ ( $\text{\AA}^3$ )
30	7.14759(9)	9.18426(13)	8.95243(13)	567.689(14)
50	7.14876(9)	9.18567(13)	8.95349(13)	567.929(13)
75	7.14968(9)	9.18731(13)	8.95388(13)	568.128(14)
100	7.15099(9)	9.18890(13)	8.95476(12)	568.373(14)
125	7.15209(9)	9.19057(12)	8.95606(12)	568.648(13)
150	7.15338(9)	9.19217(13)	8.95691(12)	568.888(13)
175	7.15474(10)	9.19418(13)	8.95798(13)	569.187(14)
200	7.15581(10)	9.19575(13)	8.95884(13)	569.416(14)
225	7.15720(10)	9.19750(13)	8.95996(13)	569.701(14)
250	7.15868(10)	9.19975(14)	8.96119(13)	570.031(15)
275	7.16032(10)	9.20193(14)	8.96240(14)	570.363(15)
300	7.16179(10)	9.20388(14)	8.96367(14)	570.674(15)
325	7.16361(10)	9.20605(14)	8.96524(14)	571.046(15)
350	7.16516(11)	9.20836(14)	8.96648(14)	571.386(16)
375	7.16687(10)	9.21057(14)	8.96799(14)	571.745(16)
400	7.16867(11)	9.21323(15)	8.96949(14)	572.140(16)

425	7.17000(11)	9.21500(15)	8.97071(14)	572.422(16)
450	7.17182(11)	9.21769(15)	8.97247(14)	572.844(16)
475	7.17331(11)	9.21954(14)	8.97389(14)	573.165(16)
500	7.17502(11)	9.22209(15)	8.97537(14)	573.550(16)
525	7.17659(11)	9.22376(15)	8.97625(15)	573.818(16)
550	7.17881(11)	9.22599(15)	8.97834(15)	574.271(16)
575	7.18146(13)	9.22743(17)	8.98019(16)	574.680(18)
600	7.18635(17)	9.22930(21)	8.98377(21)	575.420(24)
625	7.19351(23)	9.23041(28)	8.98854(28)	576.359(32)
650	7.20252(24)	9.23378(29)	8.99391(28)	577.630(32)
675	7.20883(21)	9.23524(26)	8.99702(25)	578.429(29)
700	7.21247(21)	9.23697(26)	8.99931(26)	578.966(29)
725	7.21732(23)	9.23883(28)	9.00278(27)	579.665(31)
750	7.22142(26)	9.24047(31)	9.00660(31)	580.324(36)
775	7.22552(38)	9.24048(42)	9.01001(44)	580.880(50)
800	7.23454(76)	9.23692(78)	9.01596(81)	581.796(126)
825	7.29046(64)	9.24500(76)	9.05987(76)	589.377(88)
850	7.29108(40)	9.24032(49)	9.06369(47)	589.433(56)

**Table 3** Relevant parameters of the fitting procedure by the Berman equation of the unit-cell parameters vs  $T$  up to the discontinuity with respect to the linear behavior

$V_0, a_0, b_0, c_0$ ( $\text{\AA}^3, \text{\AA}, \text{\AA}, \text{\AA}$ )	$\alpha_0$ ( $\times 10^{-5} \text{ K}^{-1}$ )	$\alpha_l$ ( $\times 10^{-8} \text{ K}^{-2}$ )
$V$	1.65(4)	2.22(14)
$a$	0.59(2)	0.98(16)
$b$	0.73(2)	0.59(8)
$c$	0.37(1)	0.72(4)

Temperature of reference = 298 K (25 °C) and  $T_{\text{max}}$  850 K (575 °C)

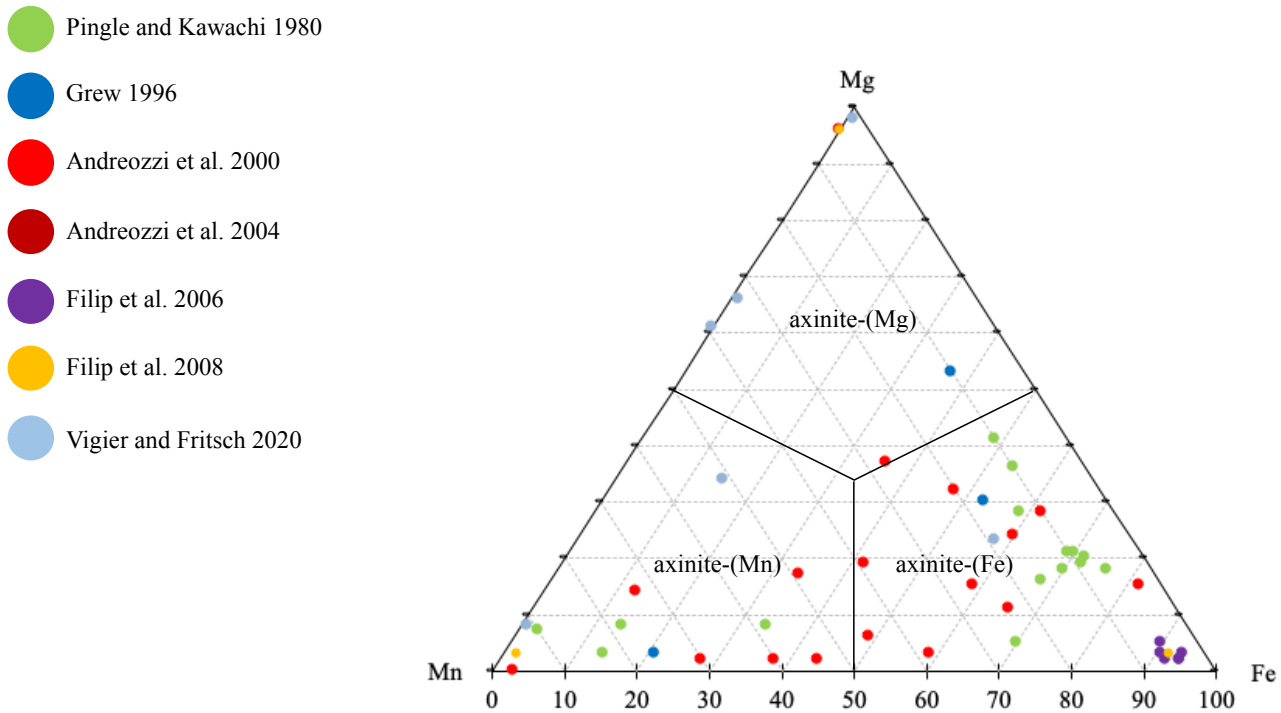


**Figure 1** Ternary plot for the axinites classification based on the dominant occupancy of the Y site. Coloured dots are compositions of axinites reported in literature from Grew (1996), Pringle and Kawachi (1980), Andreozzi et al. (2000) and (2004), Filip et al. (2006), Filip et al. (2008), Vigier and Fritsch (2020), and the red triangle represents axinite 46 from Luning (Nevada) that is considered in this study and characterized by Andreozzi et al. (2000).

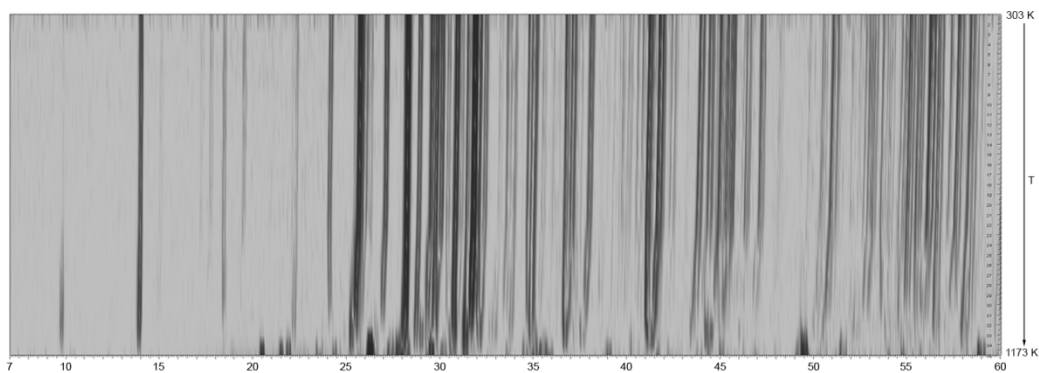


**Figure 2** 3D-view of the full data set collected in the 30-900 °C thermal range.

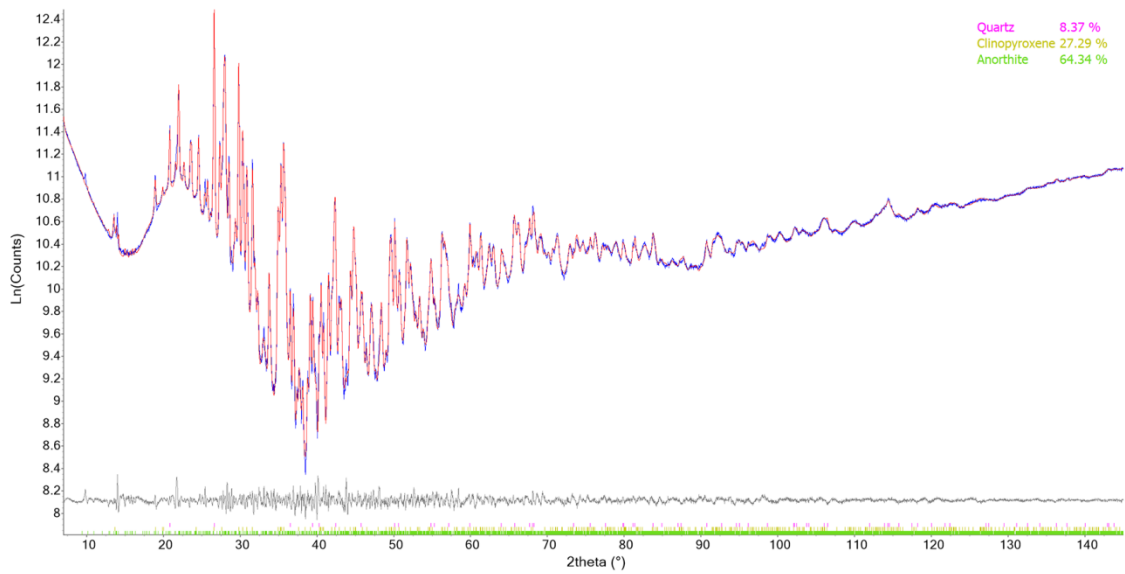


**Figure 3** Rietveld plots of the products of breakdown of the axinite sample. Blue: experimental; red: calculated; grey: difference; vertical bars: position of calculated Bragg reflections of (from above to below) quartz and clinopyroxene. The contribution of anorthite is indicated as a continuous green line.

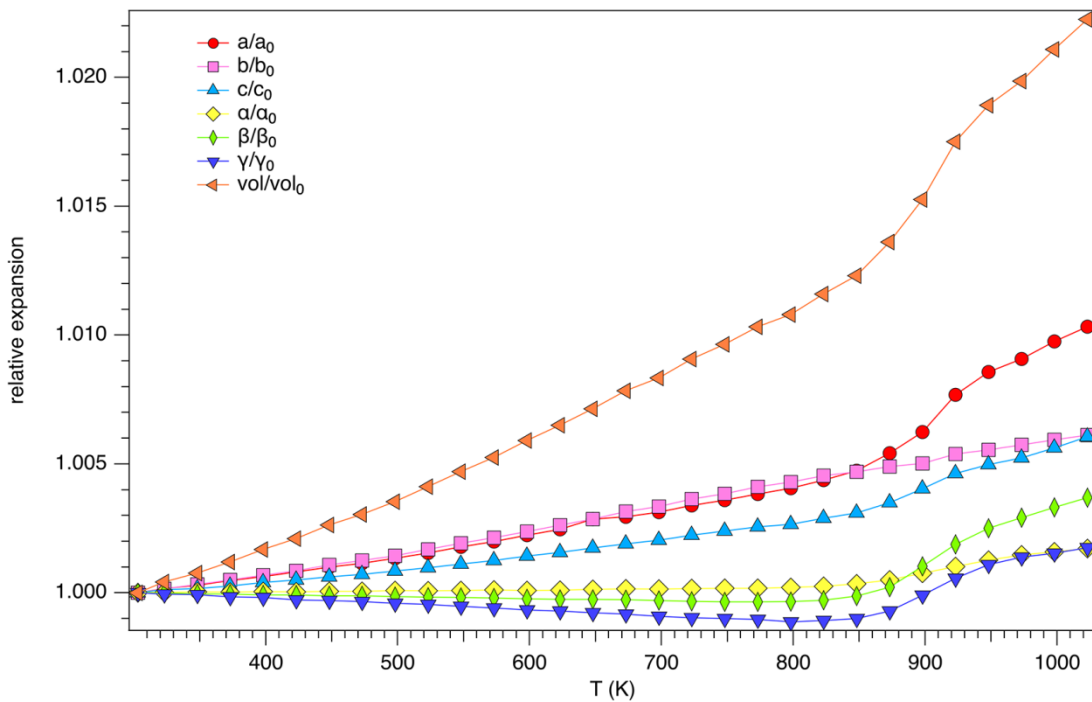
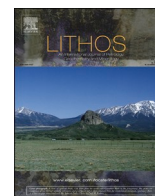


**Figure 4** Dependence of the normalized unit-cell parameters from  $T$  for the axinite sample.



## 2.3. High-Pressure High-Temperature experiments

### 2.3.1. Schorl



## Schorl breakdown at upper mantle conditions: Insights from an experimental study at 3.5 GPa

Beatrice Celata<sup>a, \*\*</sup>, Vincenzo Stagno<sup>a, b</sup>, Luca S. Capizzi<sup>a</sup>, Ferdinando Bosi<sup>a, c</sup>, Paolo Ballirano<sup>a</sup>, Annalisa D'Arco<sup>d</sup>, Veronica Stopponi<sup>a, e</sup>, Stefano Lupi<sup>d</sup>, Piergiorgio Scarlato<sup>b</sup>, Henrik Skogby<sup>f</sup>, Giovanni B. Andreozzi<sup>a, c, \*</sup>

<sup>a</sup> Department of Earth Sciences, Sapienza University of Rome, Italy

<sup>b</sup> National Institute of Geophysics and Volcanology, Rome, Italy

<sup>c</sup> CNR-IGAG c/o Department of Earth Sciences, Sapienza University of Rome, Italy

<sup>d</sup> INFN National Institute of Nuclear Physics, Rome, Italy

<sup>e</sup> CNR-IOM, c/o Area Science Park Basovizza, S.S. 14 - Km. 163,5, Trieste 34149, Italy

<sup>f</sup> Department of Geosciences, Swedish Museum of Natural History, Stockholm SE-10405, Sweden

### ARTICLE INFO

#### Keywords:

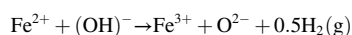
Tourmaline  
Schorl  
Structural breakdown  
HP-HT conditions  
Redox conditions  
Metasomatic fluids

### ABSTRACT

Hydrogen and B input throughout the Earth's mantle is continuously fed through a sequence of dehydration and breakdown reactions of hydrous and B-bearing mineral phases stable at different conditions along the subducting slabs. Therefore, the stability of minerals hosting these elements plays a fundamental role. Tourmaline hosts very large amounts of B (up to 14 wt% of B<sub>2</sub>O<sub>3</sub>) along with hydroxyl groups (up to 4 wt% of H<sub>2</sub>O), thus representing a crucial mineral to investigate the fate of B and H in diverse geological settings. The recent finding of tourmaline minerals in ultra-high pressure metamorphic rocks has raised important questions about the actual tourmaline stability field, paying special attention to the high pressure and temperature stability limits of the various tourmaline species.

A single-phase system made of natural schorl with the highest Fe<sup>2+</sup> concentration known so far (about 18 wt% of FeO) was studied at a fixed pressure (3.5 GPa) and several temperatures (500, 700, 750, 800, 850 and 950 °C) to preliminarily constrain its stability conditions, breakdown mechanisms and breakdown products. Experiments at high pressure-high temperature conditions were performed using a multi anvil apparatus under buffered oxygen fugacity through a Re/ReO<sub>2</sub> solid mixture. The experimental products were characterized through a multi-analytical approach consisting in Scanning Electron Microscopy imaging and Energy Dispersive System spectra acquisition, Electron MicroProbe analysis, powder X-Ray Diffraction, <sup>57</sup>Fe Mössbauer spectroscopy and reflectance Fourier Transform infrared spectroscopy.

At 3.5 GPa and T ranging from 500 up to 700 °C, the schorl experienced a partial Fe oxidation coupled with dehydrogenation:



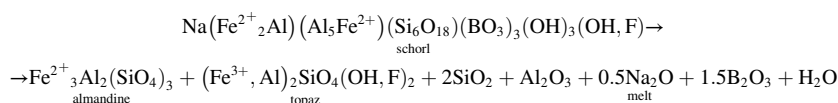
The observed Fe oxidation was limited to 30% (significantly lower than the full oxidation observed in experiments performed in air at room pressure), suggesting that oxidation-dehydrogenation is indeed a thermally activated process, but both environmental pressure and oxygen fugacity are important governing factors.

In the pure schorl system at 3.5 GPa, the structural breakdown started at  $T = 700$  °C and ended at 850 °C, resulting in the formation of almandine garnet as the first breakdown product together with topaz and a B-rich liquid phase:

\* Corresponding author at: Department of Earth Sciences, Sapienza University of Rome, Italy.

\*\* Corresponding author.

E-mail addresses: [beatrice.celata@uniroma1.it](mailto:beatrice.celata@uniroma1.it) (B. Celata), [gianni.andreozzi@uniroma1.it](mailto:gianni.andreozzi@uniroma1.it) (G.B. Andreozzi).



At 3.5 GPa and  $T \geq 850$  °C, tourmaline, garnet and topaz were not observed anymore and kyanite, prismatic and boromullite-like phases and corundum became stable. Both prismatic-like and boromullite-like phases identified by stoichiometry can incorporate B from the B-rich hydrous melt formed after schorl breakdown and may carry it to lower depths.

From our work it follows that the schorl-bearing granitoid rocks (or sediments) have the potential to form hydrous B-bearing metasomatic melts at 3.5 GPa and  $T \geq 700$  °C. In cold subduction environments, between the 700–800 °C isotherms, the schorl is expected to be stable up to ~100 km depth along the subducting slab, although an excess  $\text{SiO}_2$  might be responsible for a reduction in tourmaline stability. The role of tourmaline companion minerals on its breakdown conditions and products is left as future issue when a multi-phase system will be considered.

## 1. Introduction

Understanding the rheology of geological systems is crucial to explain the complex phenomena occurring at inaccessible parts of the Earth such as subduction zones, where crustal material experiences a recycling process and new phases are formed at different temperatures and pressures along the slab. Water is a key factor in affecting the rheology of any geological system, and hydrogen ions are naturally stored in the crystal structure of hydrous minerals; when they approach their breakdown conditions, some dehydrogenation occurs (i.e., the loss of  $\text{H}^+$  from the crystal structure), and water is progressively released into the system. Once the breakdown conditions of a specific mineral are reached, its crystal structure collapses and the hosted chemical elements, together with the remaining water, are thus ready to reorganize themselves in new structures which are stable at the new temperatures and pressures. In a dynamical view, the newly formed mineral phases become carriers of both the recycled elements and water at higher depths down the slab, until their breakdown conditions are reached, and their chemical elements are released once again. Notably, some of the released elements are strongly partitioned into the fluid phase (as holds true especially for B) and are therefore able to migrate and act as metasomatic fluids that can contaminate the surrounding rocks and promote their partial melting. Consequently, mapping out the water path through this sort of “relay race” along the slab down the mantle is important to get a more detailed picture of the rheological behavior of subduction systems. In fact, clusters of intermediate-depth earthquakes (~70–300 km, depth range of subducting slabs) have been observed as a common feature of many subduction zones [e.g., Tonga (Kawakatsu, 1985); Alaska (Ratchkovsky et al., 1997), northeast Taiwan (Kao and Rau, 1999), Cape Mendocino (Smith et al., 1993), northern Chile (Comte et al., 1999), eastern Aleutians (Hudnut and Taber, 1987)] due to “dehydration embrittlement”, that is the transition from ductile to brittle behavior of a rock due to dehydration reactions along the slab that release a certain amount of water, increasing the pore fluid pressure and overcoming the confining pressure of the rock (Seno and Yamasaki, 2003).

It was experimentally determined that accessory minerals in the subducting slab play a crucial role in water and light elements transport and release at least down to 300 km in depth (e.g., Ono, 1998; Schmidt and Poli, 1998). A suite of accessory minerals made of lawsonite, phengite and dravitic tourmaline was identified as a possible sequence of getters and carriers for light elements and water (Moriguti et al., 2004). Among such mineral phases, tourmaline is the most powerful to describe its hosting rock metamorphic history, as its composition is dependent from the environmental conditions of growth and it is preserved nearly forever due to tourmaline’s extremely slow intracrystalline diffusion rates (Hawthorne and Dirlam, 2011; Henry and

Dutrow, 1996). Tourmaline is the dominant carrier of boron in crustal, metamorphic and igneous rocks (e.g., Tag et al., 1999). From metamorphic assemblages, tourmaline can contain up to ~14 wt% of  $\text{B}_2\text{O}_3$  (i.e., >80 wt% of the whole-rock B content and much more than the ppm amounts incorporated into lawsonite and phengite) and ~4 wt% of  $\text{H}_2\text{O}$ , representing the most important carrier of these volatile elements within the continental upper crust (Grew et al., 2016; Henry and Dutrow, 1996). Its relevance in drawing up a track of the overall framework of water deep circulation stands in the solid constraint of its stability field boundaries. The  $P$ - $T$  stability field of just very few tourmaline compositions has been studied so far, considering both experimental works and constraints from natural samples all in multi-phase systems (e.g., Bebout and Nakamura, 2003; Marschall et al., 2008; Nakano and Nakamura, 2001; Ota et al., 2008a).

The general formula of tourmaline is  $\text{XY}_3\text{Z}_6\text{T}_6\text{O}_{18}(\text{BO}_3)_3\text{V}_3\text{W}$ , where the letters X, Y, Z and B represent groups of cations accommodated at the  $^{[9]}\text{X}$ ,  $^{[6]}\text{Y}$ ,  $^{[6]}\text{Z}$ ,  $^{[4]}\text{T}$  and  $^{[3]}\text{B}$  crystallographic sites (with superscript numbers indicating the coordination number); the letters V and W represent groups of anions accommodated at the O(3) and O(1) crystallographic sites, respectively. In detail, X =  $\text{Na}^+$ ,  $\text{K}^+$ ,  $\text{Ca}^{2+}$ , (= vacancy); Y =  $\text{Al}^{3+}$ ,  $\text{Fe}^{3+}$ ,  $\text{Cr}^{3+}$ ,  $\text{V}^{3+}$ ,  $\text{Mg}^{2+}$ ,  $\text{Fe}^{2+}$ ,  $\text{Mn}^{2+}$ ,  $\text{Zn}$ ,  $\text{Li}^+$ ,  $\text{Ti}^{4+}$ ; Z =  $\text{Al}^{3+}$ ,  $\text{Fe}^{3+}$ ,  $\text{Cr}^{3+}$ ,  $\text{V}^{3+}$ ,  $\text{Mg}^{2+}$ ,  $\text{Fe}^{2+}$ ; T =  $\text{Si}^{4+}$ ,  $\text{Al}^{3+}$ ,  $\text{B}^{3+}$ ; B =  $\text{B}^{3+}$ ; V =  $(\text{OH})^-$ ,  $\text{O}^{2-}$ ; W =  $(\text{OH})^-$ ,  $\text{F}^-$ ,  $\text{O}^{2-}$ .

Tourmaline has often been considered a crust mineral, but its occurrence in ultra-high-pressure metamorphic rocks (e.g., Ertl et al., 2010; Marschall et al., 2009) has raised important questions on its stability at pressure ( $P$ ) and temperature ( $T$ ) conditions of the Earth’s interior, even at depths where coesite and diamond occur. Further evidence of the stability of tourmaline at high  $P$  and  $T$  are represented by the occurrence of K-rich tourmaline, namely maruyamaite (Ota et al., 2008b; Shimizu and Ogasawara, 2013), as well as Na- and Ca-rich tourmaline (Korsakov et al., 2019) along with microdiamonds in paragneiss from the Kokchetav Massif (Kazakhstan).

The stability field of tourmaline was tentatively defined in van Hinsberg et al. (2011) by reviewing experimental results from literature, obtained using dravite (Krosse, 1995; Ota et al., 2008a; Robbins and Yoder, 1962), magnesio-foitite (Verdogen and Schreyer, 1984), Na-free and Na-bearing Mg-tourmalines (von Goerne et al., 1999), Fe-rich dravite (Kawakami, 2004), dravite-schorl (Spicer et al., 2004), and schorl (only represented by a single experiment at 0.3 GPa and about 760 °C, Holtz and Johannes, 1991). A significant contribution was given by Ota et al. (2008a) investigating tourmaline breakdown conditions in a metapelite-like system with a HP-HT multi-anvil apparatus in order to assess B release in subduction zones. These authors studied a natural dravite from Kokchetav Massif (Kazakhstan) mixed with quartz-bearing natural metapelite and reported a decomposition reaction through a metastable tourmaline between 800 and 900 °C at 4 GPa, and between

700 and 900 °C at 4.5 GPa, to form an assemblage consisting of garnet, clinopyroxene, phengite, coesite, kyanite and rutile plus B-rich fluids. However, the coexistence of B- and H-bearing minerals in the starting metapelite mixture did not allow them to constrain the *P-T* conditions for pure tourmaline stability. Besides, the small amount of Fe contained in the starting dravite (~4 wt% of FeO) precluded the possibility to use their experiments to address the role of Fe on tourmaline stability. The behavior of Fe-bearing tourmalines at room *P* and HT was later addressed by Bačík et al. (2011), Filip et al. (2012) and Bosi et al. (2016, 2018, 2019), who studied the speciation of Fe at the *Y* and *Z* sites of the tourmaline structure as a function of *T* and oxygen fugacity (*f*O<sub>2</sub>). In particular, Filip et al. (2012) performed heating experiments at room *P* on an Fe<sup>3+</sup>-rich schorl under both reduced and oxidized conditions; they observed that before the breakdown the Fe<sup>3+</sup>/Fe<sub>tot</sub> ratio increases or decreases as a function of *f*O<sub>2</sub> being balanced by H. Moreover, they concluded that schorl undergoes decomposition above 800 °C in air to form phases like mullite, hercynite, iron oxide plus an amorphous B-bearing phase.

To further explore the behavior of Fe-tourmalines at upper mantle depth, we investigated the HP-HT breakdown of a Fe-rich single-phase system, a natural schorl from the Yukon Territory (Canada), by performing experiments at a fixed *P* of 3.5 GPa and *T* ranging from 500 to 950 °C, and then studying the recovered run products.

## 2. Materials and methods

### 2.1. Starting material

The schorl sample here used for HP-HT breakdown experiments comes from a quartz-tourmaline orbicule found in the leucogranites of the Seagull batholith in the Yukon Territory, Canada (Sinclair and Richardson, 1992) and is acknowledged to be the Fe<sup>2+</sup>-richest schorl known so far, with about 18 wt% of FeO and the empirical formula  $X(\text{Na}_{0.74}\square_{0.24}\text{K}_{0.01}\text{Ca}_{0.01})_{\Sigma 1.00}Y(\text{Fe}_{2.05}^{2+}\text{Al}_{0.92}\text{Ti}_{0.02}\text{Mn}_{0.01}\text{Zn}_{0.01})_{\Sigma 3.00}Z(\text{Al}_{5.41}\text{Fe}_{0.53}^{2+}\text{Mg}_{0.06})_{\Sigma 6.00}T(\text{Si}_6\text{O}_{18})^B(\text{BO}_3)_3^V(\text{OH})_3^W[(\text{OH})_{0.46}\text{F}_{0.41}\text{O}_{0.13}]_{\Sigma 1.00}$  (Andreozzi et al., 2020).

### 2.2. Experimental conditions

The schorl crystal fragments were first selected under the optical microscope to minimize contamination from coexisting minerals (e.g., quartz and feldspars) and then grinded for 30 min to a fine powder. Due to the composition of the starting material, our experiments can be considered as performed in the Na<sub>2</sub>O-Al<sub>2</sub>O<sub>3</sub>-SiO<sub>2</sub>-FeO (NASF) plus B<sub>2</sub>O<sub>3</sub> plus H<sub>2</sub>O system. The powder was dried and doped with 20 wt% of a mixture of rhenium (99.9% purity) and rhenium (IV) oxide dihydrate (ReO<sub>2</sub>·2H<sub>2</sub>O) in 1:1 mol ratio so that the *f*O<sub>2</sub> could be nominally buffered during the experiments by the Re/ReO<sub>2</sub> system (RRO). The use of ReO<sub>2</sub>·2H<sub>2</sub>O was here preferred to ReO<sub>2</sub> to fasten the attainment of equilibrium *f*O<sub>2</sub> between the solid buffer mixture and the tourmaline starting material through the expected redox reaction:



with H<sub>2</sub> acting as a redox transfer. At the same time, the use of ReO<sub>2</sub>·2H<sub>2</sub>O implies the addition of <1 wt% free H<sub>2</sub>O to the whole starting material.

#### 2.2.1. HP-HT experiments

Experiments at HP were performed using the 840-ton Walker-type multi anvil press available at National Institute of Geophysics and Volcanology (INGV) in Rome (Italy). Cell assemblies made of MgO doped with 5 wt% of Cr<sub>2</sub>O<sub>3</sub> with 18-mm octahedra edge length (OEL) were used in combination with tungsten carbide second-stage anvils (F-grade) of 11-mm truncation edge length (TEL). A detailed sketch of the cell assembly is shown in Fig. S1 of Supplementary material. The experiments were performed using graphite capsules with a diameter of 2

mm, filled by a mixture of schorl + RRO as starting material and then wrapped by Re foil. The capsules were placed inside MgO sleeves of 3.5-mm diameter to act as a pressure medium. A cylindrical ZrO<sub>2</sub> sleeve surrounding the graphite heater (sleeve of 0.5 mm thick) was used as a thermal insulator. Pyrophyllite gaskets glued around the WC TEL were used as pressure transmitted-medium. A tiny amount of amorphous SiO<sub>2</sub> fine powder was placed between the capsule and the MgO sleeve and plugs as a pressure marker based on the quartz-coesite phase transition (Bose and Ganguly, 1995). The temperature during the experiments was monitored using a W-5%Re/W-26%Re thermocouple (C-type; diameter of 0.010 in.) inserted through a 4-hole alumina rod of 1.8 mm diameter and placed in contact with the top of the capsule. The experiments were conducted by increasing the pressure up to the target value at 1 GPa/h compression rate and then heated at 100 °C/min by supplying power to the furnace. The temperature was manually controlled within ±5 °C over the entire duration of the experiment by adjusting the output power. The experiments were finally quenched by shutting down the electrical power. A total of 6 runs were carried out at a pressure of 3.5 GPa and temperatures of 500, 700, 750, 800, 850 and 950 °C with a dwell time ranging from 2 to 10 h (see Table 1).

### 2.3. Analytical techniques

After recovering the run products from the cell assemblies, half of the capsule was embedded in epoxy resin and then polished under ethanol, while the other half was stored for further analyses. Textural analyses were performed on the polished samples using the JEOL JSM-6500F field emission scanning electron microscope (FE-SEM) equipped with an energy dispersive spectrometer (EDS) available at INGV (Rome) and using the FEI Quanta 400 scanning electron microscope (SEM) available at the Department of Earth Sciences (Sapienza University of Rome). Accurate quantitative data were acquired by electron microprobe (EMP) with the JEOL JXA-8200 Superprobe equipped with five wavelength-dispersive spectrometers also available at INGV (Rome) and with the CAMECA SX50 available at the Istituto di Geologia Ambientale e Geoingegneria (IGAG-CNR, Rome, Italy). Chemical analyses of the run products were performed employing an accelerating voltage of 15 kV and beam current of 7.5 and 20 nA (calibration for JEOL JXA-8200), and 15 kV and beam current of 15 nA (calibration for Cameca SX50), with a beam size of 1 to 10 μm of diameter. As for the JEOL instrument, the ZAF correction method was applied, and the following standards were used for quantitative measurements: olivine for Si, Mg and Fe; orthoclase for Al and K; albite for Na; apatite for Ca and F; rutile for Ti. As for the Cameca SX50 instrument, the PAP correction method was applied, and the following standards were used: wollastonite for Si and Ca; magnetite for Fe; rutile for Ti; corundum for Al; fluorophlogopite for F; periclase for

**Table 1**

Experimental conditions and recovered experimental products.

Run	<i>P</i> (GPa)	<i>T</i> (°C)	Time (h)	Buffer	log <i>f</i> O <sub>2</sub> (ΔFMQ)*	Experimental products
M108	3.5	500	6	n.d.	1.94	Tur
M99	3.5	700	4	n.d.	1.60	Tur, Grt
M98	3.5	750	6	Re, ReO <sub>2</sub> #	1.54	Tur, Grt, Tpz, Qtz, Ky
M100	3.5	800	3	Re, ReO <sub>2</sub> #	1.49	Tur, Grt, Tpz, glass
M104	3.5	850	2	Re#	1.44	Glass, Ky, Prm- like, Tur, Grt
M101	3.5	950	10	n.d.	1.35	Glass, Ky, Prm- like, Bmull-like, Crn

Mineral abbreviations: Tur = tourmaline; Grt = garnet; Tpz = topaz, Ky = kyanite; Prm = prismatic; Bmull = boromullite; Crn = corundum.

\* Relative to the fayalite-magnetite-quartz buffer.

# Re and ReO<sub>2</sub> observed by EBS image and/or p-XRD; n.d. = not distinguishable.

**Table 2**  
Representative EMP analyses of the recovered run products after HP-HT experiments at 3.5 GPa.

T (°C)/Run	Phase	SiO <sub>2</sub>	TiO <sub>2</sub>	Al <sub>2</sub> O <sub>3</sub>	FeO	MgO	CaO	Na <sub>2</sub> O	K <sub>2</sub> O	F	Tot
Room T	Tur	34.79	0.13	31.18	17.91	0.23	0.04	2.22	0.04	0.75	87.29
500/M108	Tur	34.32	0.40	29.66	17.76	0.27	0.06	2.57	0.06	1.09	86.20
700/M99	Tur	34.44	0.43	31.16	17.50	0.42	0.05	2.58	0.02	0.98	87.58
	Grt	36.06	0.14	21.10	39.44	0.15	0.57	0.11	0.00	0.43	98.01
750/M98	Tur	34.42	0.26	33.20	15.34	0.36	0.05	2.32	0.09	2.22	88.25
	Grt	35.30	0.36	19.55	40.87	0.84	0.16	0.12	0.01	0.30	97.50
800/M100	Tur	34.64	0.42	29.57	18.22	0.37	0.05	2.66	0.10	1.18	87.19
	Grt	34.38	0.20	19.55	40.71	0.22	0.22	0.17	0.00	0.36	95.81
	Tpz	32.74	0.12	54.10	0.85	0.00	0.04	0.04	0.01	10.52	98.40
	Fe-Tpz	33.20	0.19	42.59	8.49	0.14	0.01	1.12	0.07	5.95	91.80
	Glass	30.42	0.21	25.22	18.18	0.23	0.08	2.14	0.07	0.68	77.22
	Glass	33.91	0.49	14.00	21.51	0.70	0.13	3.62	0.22	1.64	76.20
850/M104	Ky	36.11	0.07	62.01	2.03	0.13	0.02	0.04	0.03	0.00	100.44
	Prm-like	35.16	0.32	39.46	10.95	0.33	0.07	1.62	0.11	0.99	88.99
	Tur	35.48	0.27	33.19	14.62	0.40	0.09	2.34	0.16	1.45	88.00
950/M101	Glass	40.20	0.63	17.53	17.98	3.43	0.66	2.37	1.15	1.07	85.02
	Ky	36.57	0.01	62.62	0.91	0.15	0.05	0.03	0.04	0.00	100.37
	Prm-like	25.80	0.43	45.85	11.64	2.00	0.43	1.46	0.77	0.54	88.97
	Bmul-like	13.86	0.24	74.75	6.13	0.84	0.18	0.76	0.43	0.16	97.34
	Crn	0.09	0.02	99.61	0.82	0.03	0.00	0.01	0.00	0.12	100.70

Note: Fe is reported as FeO. Mineral abbreviations: Srl = schorl starting material; Tur = tourmaline; Grt = garnet; Tpz = topaz; Fe-Tpz = Fe-bearing topaz; Ky = kyanite; Fe-Ky = Fe-bearing kyanite; Crn = corundum; Prm = prismatine; Bmul = boromullite.

Mg; jadeite for Na and orthoclase for K. Counting time was 10 s for peak and 5 s for background.

Part of the experimental material from run M98, M100 and M104 was used for powder X-ray Diffraction (p-XRD) for phases identification and quantitative phase analysis (QPA) using the Bruker AXS D8 Advance diffractometer with incident beam optics multilayer X-ray mirror Göbel and PSD VÅntec-1 detector, at the Department of Earth Sciences (Sapienza University of Rome). The instrument operates in transmission mode on capillary samples. Diffraction data were collected within the 5–145° 2 $\theta$  angular range, step size of 0.022°, and 10 s of counting time. Data were evaluated by the Rietveld method using Topas V.6 (Bruker, AXS, 2016). The sample M98 (from 750 °C) was also investigated by Mössbauer spectroscopy, using a conventional spectrometer system operated in constant-acceleration mode, available at the Department of Geosciences, Swedish Museum of Natural History. Due to the limited amounts of heat-treated material, a <sup>57</sup>Co rhodium matrix point-source with a nominal activity of 10 mCi was used. The absorber was prepared by grinding sample material together with thermoplastic resin, which was then shaped to a ca. 1-mm sized cylinder under mild heating (ca. 100 °C). The absorber was attached on strip tape and positioned closely in front of the point source by aid of an XYZ-stage. The spectrum was collected at room-temperature over the velocity range – 4.2 to +4.2 mm/s distributed over 1024 channels and was calibrated against an  $\alpha$ -Fe foil before folding and spectral fitting using the software MossA (Prescher et al., 2012).

Infrared spectroscopic measurements were conducted on both schorl starting material and recovered run products (M98, M99, M100 and M108). Tiny fragments of a schorl single crystal used as starting material for HP-HT experiments were studied in the mid-infrared region (600–4800 cm<sup>-1</sup>) by micro-reflectance Fourier-transform infrared spectroscopy (FTIR) spectroscopy using a Vertex 70v interferometer coupled with a Hyperion3000 microscope (Bruker Optics), a liquid nitrogen cooled MCT (HgCdTe) detector and a KBr beam splitter at the Material Science branch of SISSI beamline of Elettra Synchrotron Trieste (Italy). Measurements were carried out using a conventional Globar source with a resolution of 1 cm<sup>-1</sup> and an aperture of 60  $\mu$ m by collecting three acquisitions per area with an accumulation of 128 scans. Reflectance was calculated with respect to a gold mirror measured using the same pinhole aperture.

The polished run products were measured in reflection mode (normalized to an Au mirror) in the spectral region between 600 and 6000 cm<sup>-1</sup> at room T using a Bruker Vertex 70v vacuum spectrometer

equipped with IR Hyperion 1000 microscope available at the Department of Physics (Sapienza University, Rome). The field-of-view of each analyzed sample was adjusted by closing variable rectangular apertures, placed between the objective (15 $\times$ ) and the liquid nitrogen cooled MCT (Mercury Cadmium Telluride) detector, along the optical path. Three spectra for sample were collected by using 128 scans for each run with a spectral resolution set to 2 cm<sup>-1</sup>. To check potential influence of the aperture diameter on the spectra and the homogeneity of the samples, we varied the effective aperture diameter (only for samples M108). Each fixed aperture was used to collect both sample and the background spectra. No difference was noted in the reflectance spectra. The acquired reflectance spectra were normalized at maximum in the spectral range 600–6000 cm<sup>-1</sup>.

### 3. Results and discussion

#### 3.1. Chemical composition of the recovered experimental products

For each experiment, the recovered experimental products are listed in Table 1, their EMP analyses are reported in Table 2, and the quenched phases are shown in Fig. 1 a-h. In these experiments, both chemical homogeneity and lack of reaction rims or zoning were considered as the evidence of the achieved equilibrium of the run products, bearing in mind that the decomposition of the schorl used as starting material is expected to be driven by the fast diffusion of volatile elements like B and H. On the other hand, the kinetics of decomposition of tourmaline at HP-T remains to be accurately investigated at present.

This is the case of the run performed at 3.5 GPa and 500 °C (M108) that showed only subhedral Fe-rich tourmaline crystals with size from few to tens of microns, textural features consistent with products partially equilibrate and a composition very similar to the starting material (Fig. 1a and Table 2). Despite the need of time series experiments, currently missing in literature, the evidence that neither B<sub>2</sub>O<sub>3</sub> nor H<sub>2</sub>O were released can be taken as a first indication of the stability of the schorl at 500 °C. However, as we cannot totally exclude the quenched schorl being metastable, we are confident that this run set the starting point for future similar experiments.

At 3.5 GPa and 700 °C (M99), tourmaline is the dominant phase with a composition that is fairly well comparable with the starting material. An additional minor phase was identified via EMP (Table 2) as garnet with composition approaching pure almandine [Fe<sub>3</sub>Al<sub>2</sub>(SiO<sub>4</sub>)<sub>3</sub>]. The latter represents a product of the schorl breakdown.



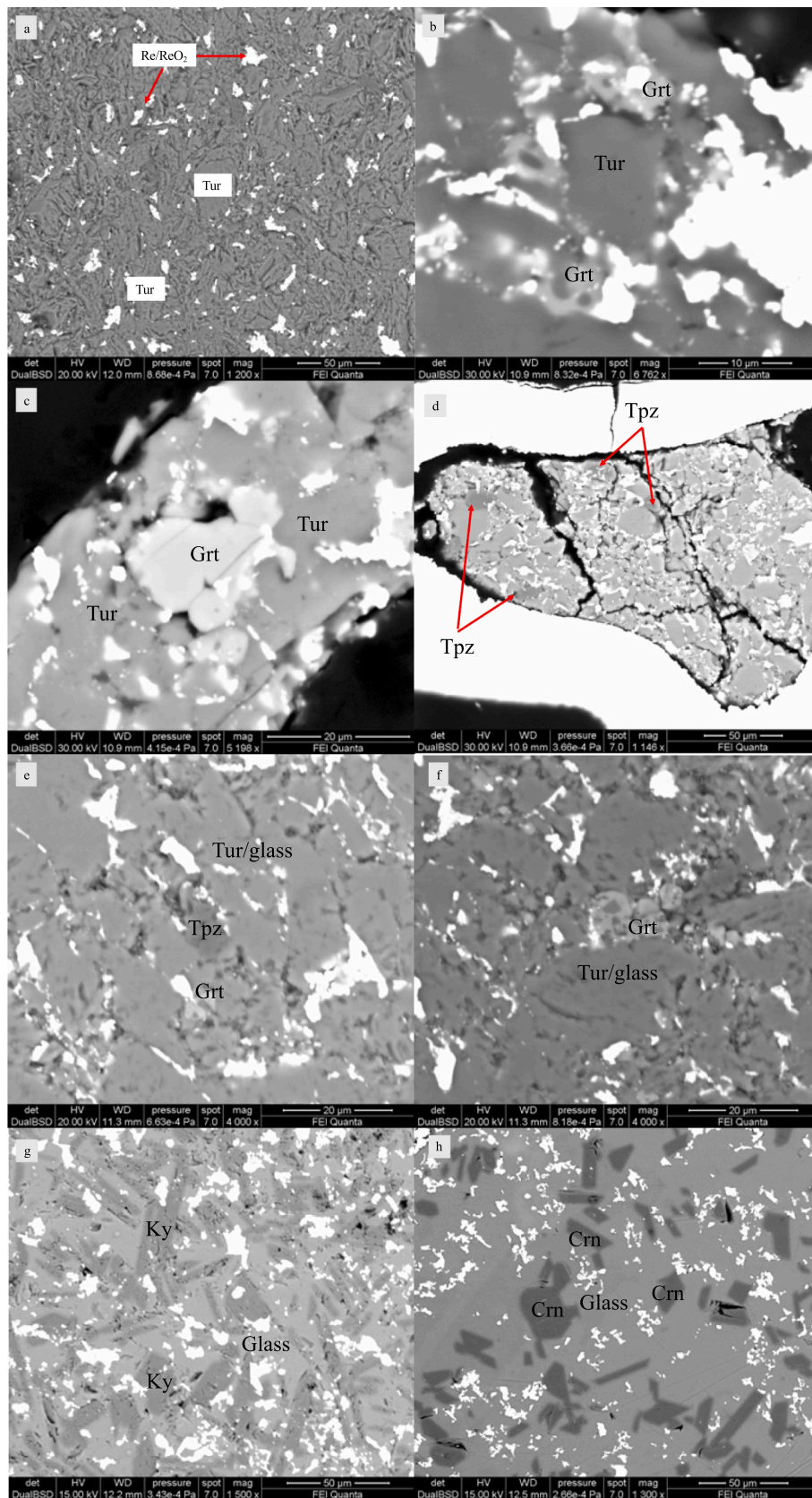


**Fig. 1.** Back-scattered electron images of the recovered experimental products at 3.5 GPa. Pictures (a) represents run M108 (500 °C), (b)-(c)-(d) are for M98 (750 °C), (e)-(f) are for M100 (800 °C), (g) is for M104 (850 °C), (h) is for M101 (950 °C). Mineral abbreviations: Tur = tourmaline, Grt = garnet, Tpz = topaz, Ky = kyanite, Crn = corundum.

In the experimental products recovered from the run performed at 750 °C (M98), both schorl and almandine are clearly observed (Fig. 1b). Textural analysis shows a well sintered quenched product, mostly consisting of schorl with irregular shape and subhedral almandine crystals up to ~20 µm (Fig. 1c). In addition to EMP, almandine was also identified by EDS, p-XRD (Fig. S2a in Supplementary material). Moreover, small rounded single crystals of topaz were spotted through SEM images and EDS spectra (Fig. 1d), representing another schorl breakdown product, the formation of which is due to the presence of F in the starting schorl (see Table 2).

At 800 °C (M100), topaz and Fe-rich topaz were identified by EMP (Fig. 1e and Table 2). A further step of the schorl breakdown is represented by the formation of an interstitial glassy phase coexisting with schorl and almandine, which locally embeds shreds of residual tourmaline (Fig. 1f). The glass is composed of SiO<sub>2</sub> ca. 30 wt%, Al<sub>2</sub>O<sub>3</sub> 25 wt%, FeO 18 wt%, Na<sub>2</sub>O 2 wt%, and volatiles/light elements ca. 25%. The occurrence of interstitial glass is also supported by p-XRD analysis, which show an increase of the intensity of the bump located in the 15–30° range of 2θ, in addition to the contribution of the capillary glass.

The run at 850 °C (M104) is dominated by glass (Fig. 1g and Fig. S2b of Supplementary material) and the occurrence of euhedral crystals of kyanite along with a prismatic-like phase is confirmed by EMP analysis. The glass is still volatile-rich (~24 wt%), with relatively higher SiO<sub>2</sub> (33.91 wt%) and lower Al<sub>2</sub>O<sub>3</sub> (14.00 wt%) contents (Table 2). The Si-depleted Al-rich phases kyanite and prismatic are the breakdown products of almandine and topaz, which are indeed rare or absent. Sparse remnants of Fe-depleted tourmaline are occasionally detected, indicating the refractory behavior of this mineral promoted by the P-T-X-time conditions of these experiments.

The run products at 950 °C (M101) show a dominant glassy phase (roughly twice the extent of M104) containing randomly dispersed euhedral crystals with prismatic and elongated morphology (Fig. 1h). With respect to the run M104, the glass composition is poorer in volatiles (~15 wt%), but higher in SiO<sub>2</sub> (40.20 wt%) as most silicatic minerals continued to experience breakdown. Several Si-depleted phases, such as a boromullite-like phase and corundum (the most abundant crystalline phase) were identified by EMP (Table 2). Compared to the previous runs, both M104 and M101 are characterized by the occurrence of new crystalline phases (prismatic-like and boromullite-like) that incorporate B from the B-rich aqueous fluid formed after the schorl breakdown. However, some B partitioning in the coexisting ultrabasic glass cannot be ruled out.

### 3.2. Iron oxidation state and crystal chemistry of the recovered tourmaline

As above-mentioned, during the HP-HT experiments the *f*O<sub>2</sub> was nominally buffered by the Re/ReO<sub>2</sub> solid mixture. Due to the low *T* of the experiments, the use of ReO<sub>2</sub>·2H<sub>2</sub>O was preferred to the common ReO<sub>2</sub> with the attempt to ensure redox reaction to the whole capsule via H<sub>2</sub> production (see reaction 1) rather than only limited to the mutual contact between RRO buffer and the near crystal. The complete absence of metallic Re in the experimental products would imply that no Fe oxidation had occurred, while the absence of ReO<sub>2</sub> would have implied consumption of O<sub>2</sub> from Eq. (1) likely due to the oxidation of Fe, according to the equilibrium:



being both Fe<sup>2+</sup> and Fe<sup>3+</sup> species easily accommodated in the tourmaline structure (e.g., Filip et al., 2012).

The presence of both Re and ReO<sub>2</sub> solid buffer in the run products with multiple phases occurring was, however, difficult to be confirmed by either SEM (differences in both brightness and EDS spectra are difficult to assess) or p-XRD analysis (Fig. S2 of Supplementary material) due to the limited amount of powder analyzed. The nominal *f*O<sub>2</sub> value of

RRO buffer was, however, calculated through the experimental calibration at ambient pressure by Pownceby and O'Neill (1994). The *f*O<sub>2</sub> value normalized to the FMQ (O'Neill St, 1987) is calculated to vary between 1.94 log units at 500 °C (M108) and 1.35 log units at 950 °C (M101) at 3.5 GPa (Table 1) consistently with what is proposed in shallow regions of the subducted slab (Cannaò and Malaspina, 2018; Stagno and Fei, 2020). Again, because of the difficulty in discriminating Re by ReO<sub>2</sub> in the run products, the calculated *f*O<sub>2</sub> shown in Table 1 must be considered as nominal *f*O<sub>2</sub> buffered during the experiments. Importantly, only for runs M98 and M100 the p-XRD shows undoubtedly the coexistence of Re and ReO<sub>2</sub> solid buffer. This finding led to the choice perform Mössbauer measurements on M98 to further investigate the possible redox mechanism summarized by reaction (2).

The Mössbauer absorption spectrum of the experimental sample containing schorl and almandine recovered from the run M98 is dominated by a combination of absorption doublets (Fig. 2). They are centered (δ) around 1 mm/s and display high quadrupole splitting (Δ*E*<sub>Q</sub>) between -1 and 3 mm/s. These hyperfine parameters are typical of Fe<sup>2+</sup>, but the evidence of a marked asymmetry in the central region between zero and 1 mm/s indicates that some Fe<sup>3+</sup> is also present. The spectrum was fitted by using four doublets, three assigned to Fe<sup>2+</sup> (δ = 1.10–1.31 mm/s) and one assigned to Fe<sup>3+</sup> (δ = 0.46 mm/s). Assuming similar recoil-free fractions for both Fe species, an Fe<sup>3+</sup>/Σ*F*e ratio of 0.23 was obtained (Table 3).

As schorl and almandine are the unique Fe-bearing phases identified in the run M98 (by p-XRD and EMP analysis), the doublet centered at 1.31 mm/s with the largest quadrupole splitting (3.49 mm/s) was assigned to Fe<sup>2+</sup> occurring at the dodecahedrally-coordinated X-site of the garnet structure (31% of the total spectrum), and the two remaining doublets were assigned to Fe<sup>2+</sup> mainly occurring at the octahedrally-coordinated Y site of the tourmaline structure (Amthauer et al., 1976; Andreozzi et al., 2008, 2020; Mikhailenko et al., 2020; Woodland and Ross, 1994). The assignment of the Fe<sup>3+</sup> doublet (23% of the total spectrum) is less straightforward. Usually, Fe<sup>3+</sup> in almandine-rich garnets is not abundant; as for example, the Fe<sup>3+</sup>/Fe<sub>tot</sub> ratios recently measured in the almandine-pyrope-grossular series were ranging between 0.02 and 0.10 (Mikhailenko et al., 2020). In the present sample, even adopting the maximum oxidation ratio previously observed, the garnet contribution to the Fe<sup>3+</sup> absorption doublet may be estimated at no >3% of the total spectrum, whereas the remaining 20% of the absorption should be assigned to the Fe<sup>3+</sup> of tourmaline. On these bases,

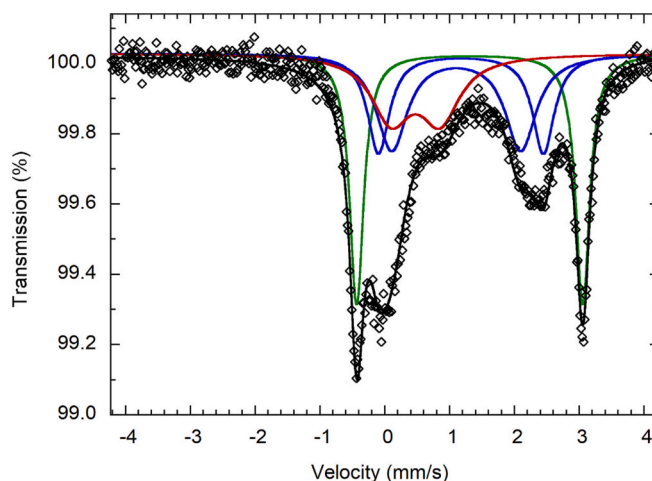


Fig. 2. Room temperature Mössbauer spectrum of sample M98 (3.5 GPa, 750 °C). The fitted absorption doublet assigned to Fe<sup>3+</sup> is drawn in red, those assigned to Fe<sup>2+</sup> in tourmaline in blue and the one to Fe<sup>2+</sup> in garnet in green. Diamonds denote measured spectrum, and black curve represents summed fitted spectra. (For interpretation of the references to colour in this figure legend, the reader is referred to the web version of this article.)



**Table 3**

Mössbauer parameters of tourmaline (Tur) and garnet (Grt) from the recovered run products M98 (3.5 GPa, 750 °C).

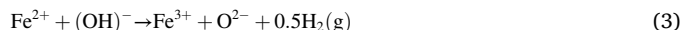
Sample	$\delta$	$\Delta E_Q$	$\Gamma$	% Area	Assignment
M98	1.31	3.49	0.26	31	Fe <sup>2+</sup> (Grt)
	1.17	2.55	0.41	20	Fe <sup>2+</sup> (Tur)
	1.10	1.99	0.56	26	Fe <sup>2+</sup> (Tur)
	0.46	0.76	0.75	23	Fe <sup>3+</sup> (Tur + Grt)

Notes: Data collected at room temperature;  $\delta$  = centroid shift (mm/s) with respect to  $\alpha$ -iron;  $\Delta E_Q$  = quadrupole splitting (mm/s);  $\Gamma$  = full width at half maximum (mm/s). Errors are estimated at about 0.02 mm/s for  $\delta$ ,  $\Delta E_Q$  and  $\Gamma$ , and no less than  $\pm 3\%$  for doublet areas.

for the run M98 the tourmaline Fe<sup>2+</sup> and Fe<sup>3+</sup> proportions were recalculated and resulted in the ratio 70:30. This ratio implies that, during the HP-HT treatment, the Fe<sup>2+</sup> in the schorl starting material partly oxidized just before breakdown (Fe<sup>3+</sup>/Fe<sub>tot</sub> varied from 0% to 30%), as

also indicated by the reduction of the  $a$  cell parameter of tourmaline observed in both M98 and M100 runs compared to the pristine material (Table S1 of Supplementary material). Note that the  $a$ -parameter contraction is consistent with the onset of Fe oxidation, as demonstrated by Celata et al. (2021) for a Fe<sup>2+</sup>-rich elbaite heated in air, in which the start of Fe<sup>2+</sup> oxidation occurred at 500 °C.

The thermally induced Fe oxidation process is balanced by a coupled dehydrogenation process, as summarized by the reaction:



The thermal Fe oxidation was already observed for schorl (Filip et al., 2012; Liu et al., 2019), schorl-dravitic tourmalines (Pieczka and Kraczka, 2004), Fe-dominant tourmalines (Bačik et al., 2011) and Fe-bearing tourmalines (Bosi et al., 2019; Celata et al., 2021). Namely, Bačik et al. (2011) and Bosi et al. (2016, 2018, 2019) documented the oxidation of Fe<sup>2+</sup> and the proportional loss of H<sup>+</sup> by recording the increase of the Fe<sup>3+</sup> signal in the Mössbauer spectra and the simultaneous

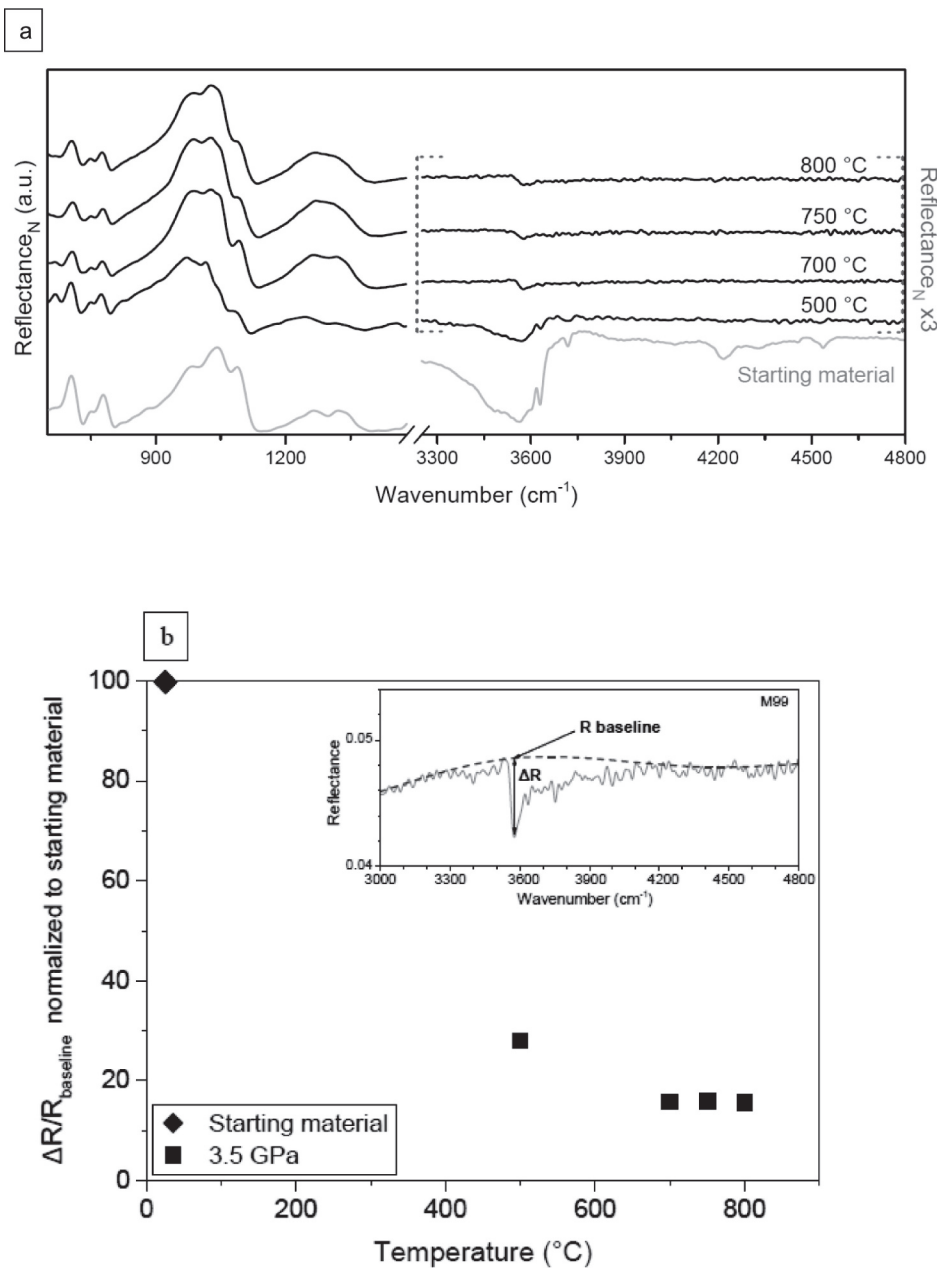


**Fig. 3.** Normalized reflectance FTIR spectra of quenched experimental runs conducted at 3.5 GPa and temperatures from 500 to 800 °C (black) compared with the natural starting material (grey). a) T-O (600–1100 cm<sup>-1</sup>), B–O (1200–1400 cm<sup>-1</sup>) and hydroxyl (3500–4500 cm<sup>-1</sup>) vibrational regions. As indicated, the normalized reflectance of experimental products is shown multiplied by a factor of 3 in the high frequency region to facilitate the visualization. b) Variation of  $\Delta R/R_{\text{baseline}}$  normalized to the starting material as a function of temperature. The inset illustrates an example of the procedure adopted for  $\Delta R/R_{\text{baseline}}$  relative to sample M99.

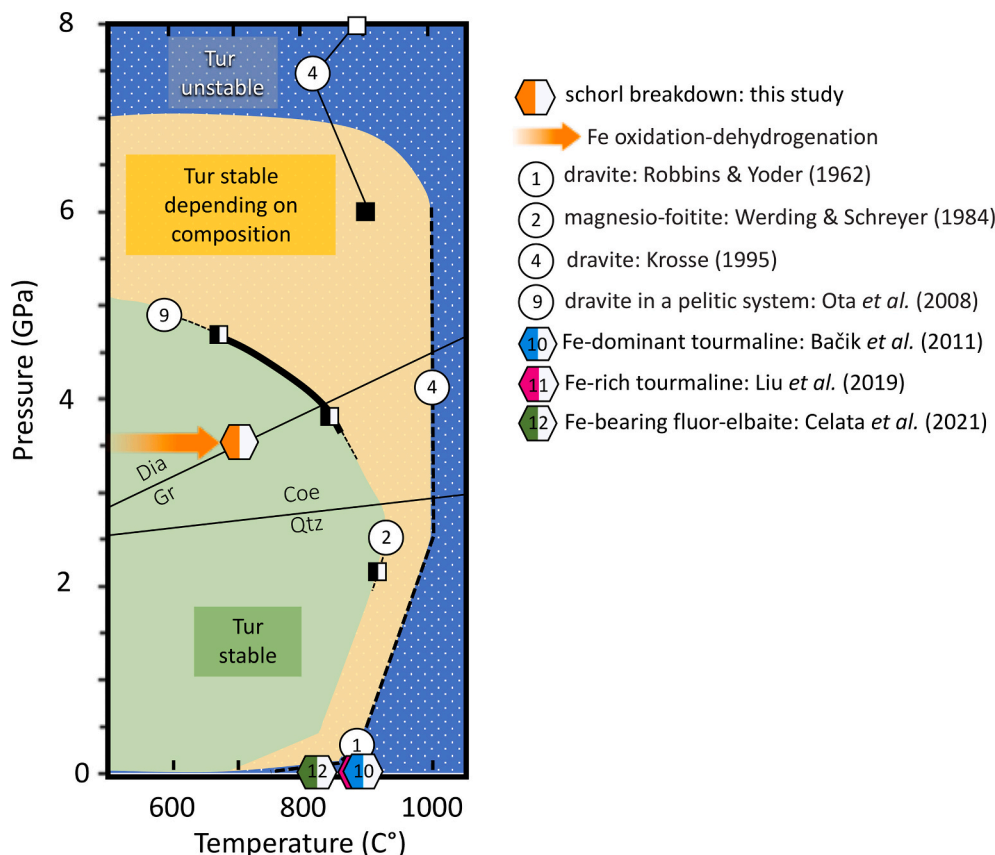


Fig. 4. *P-T* stability diagram for tourmaline of various compositions (after van Hinsberg et al., 2011). As in the original diagram, circles and squares represent constraints from natural samples and experimental data, dashed and thick lines are the extrapolations proposed by the same Authors; in this new version of the diagram, half-full hexagons stand for the present results and those of recent experimental works performed on natural samples.

decrease of the OH group signals in the IR spectra. In the present sample, when an oxidation rate of Fe corresponding to 30% is applied to the tourmaline retrieved from HP-HT experiments, Fe<sup>3+</sup> contents of about 0.80 atoms per formula unit (apfu) are obtained, balanced by H<sup>+</sup> loss of about 0.80 apfu [see reaction (3)].

Remarkably, the extent of the oxidation-dehydrogenation reaction observed for the present schorl (after the buffered HP-HT experiments) is considerably less pronounced (30%) than that (about 100%) observed in schorl and Fe-dominant tourmalines heated in air and at room pressure (Bačik et al., 2011; Filip et al., 2012). In previous studies, increased amounts of Fe<sup>3+</sup> were also observed to some extent even after heating the tourmaline under hydrogen atmosphere (Bosi et al., 2018, 2019; Filip et al., 2012). Present results compared with few earlier studies suggest that the oxidation-dehydrogenation is indeed a thermally activated process in which both pressure and environmental oxygen fugacity might represent important governing factors. Specifically, high temperature and high oxygen fugacity boost Fe oxidation while low-pressure conditions trigger the H<sup>+</sup> loss that can be only charge-balanced by a corresponding change in the Fe oxidation state according to reaction (3) (cf. Bosi et al., 2018, 2019). The same process is hindered by high pressure conditions that prevent H<sup>+</sup> loss and stabilize structural OH<sup>-</sup>.

All the studies regarding the effects of heat treatment on tourmaline agree that the Fe oxidation is triggered by  $T \geq 500$  °C at room pressure in air (Bačik et al., 2011; Castañeda et al., 2006; Celata et al., 2021; Liu et al., 2019; Pieczka and Kraczkza, 2004). Moreover, around 650 °C the Fe ions start to migrate from the Y to the Z sites, according to the intracrystalline order–disorder reaction  ${}^Y\text{Fe} + {}^Z\text{Al} \rightarrow {}^Z\text{Fe} + {}^Y\text{Al}$  (e.g., Bosi et al., 2019; Celata et al., 2021; Filip et al., 2012). Therefore, it can be assumed that in the present buffered HP-HT conditions, the oxidation-

dehydrogenation process of schorl started at temperatures above 500 °C, hampered by the low oxygen fugacity and the high pressure, and continued until the schorl breakdown, possibly coupled with intracrystalline cation order–disorder above 650 °C.

### 3.3. Schorl dehydration observed by micro-reflectance FTIR

Micro-reflectance spectra were acquired on tourmaline samples from runs M108, M99, M98 and M100 with the aim to investigate the loss of H at 3.5 GPa as a function of temperature in the interval 500–800 °C. The collected spectra were compared with the schorl starting material (see Fig. S3 of Supplementary material). The fingerprint region is characterized by spectral features assigned to stretching and bending vibrations between 600 and 1400 cm<sup>-1</sup> in rings of six TO<sub>4</sub> tetrahedra and (BO<sub>3</sub>) groups (Bosi et al., 2021; Shen et al., 2011). As shown in detail in Fig. S4 of Supplementary material for the high P runs at 500 and 800 °C, a combination of T-O-T bending and stretching, B-O bending and (Y,Z)-O stretching vibrations are visible in the runs in the frequency range between 600 and 800 cm<sup>-1</sup> along with the B-O stretching vibrations between 1200 and 1400 cm<sup>-1</sup> (Bosi et al., 2021; Reddy et al., 2007; Shen et al., 2011; Zhao et al., 2012); all of them can be referred to the schorl. The T-O vibrations located at 900–1150 cm<sup>-1</sup> are also consistent with the schorl starting material although an evident broadening/shoulder at about 900 cm<sup>-1</sup> is visible, likely raising from either the presence of Re/ReO<sub>2</sub> or the epoxy resin in which the sample was embedded.

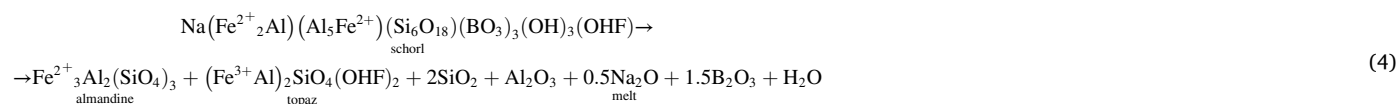
The sequence of spectra showed in Fig. 3a clearly reveals the gradual decrease of intensity in the OH region from 3300 to 4700 cm<sup>-1</sup> according to reaction (3). A first change is represented by the strong decrease of the peak around 3617 cm<sup>-1</sup> and the disappearance of the peaks at 4217, 4330 and 4536 cm<sup>-1</sup> (Fig. S5 of Supplementary material)

that can be taken as spectroscopic evidence that schorl at 500 °C reached the equilibrium. The main hydroxyl contribution is represented by the absorption at 3540 cm<sup>-1</sup> that is retained in the temperature interval of investigation (Fig. S5 of Supplementary material). The diagram in Fig. 3b is drawn by calculating  $\Delta R/R_{\text{baseline}}$  ratio, where  $\Delta R$  is the difference between R minimum value in the OH region, which occurs at about 3570 cm<sup>-1</sup>, and R value of the relative baseline ( $R_{\text{baseline}}$ , spline curve as shown in the inset of Fig. 3b), similarly to Yasuda (2014), divided by R baseline. The decrease of  $\Delta R/R_{\text{baseline}}$  up to 700 °C shown in Fig. 3b can be interpreted as the direct evidence of the partial dehydrogenation that schorl undergoes according to the reaction (3).

### 3.4. Tourmaline stability at upper mantle depth

Our experimental results provide first evidence that the start of schorl breakdown at 3.5 GPa occurs at 700 °C, a temperature markedly lower than that documented by previous studies performed either low or room pressure (i.e., about 760 °C in Holtz and Johannes, 1991; about 850–900 °C in Bačik et al., 2011; Filip et al., 2012; Liu et al., 2019; see Fig. 4). In absence of more time-dependent runs, the observed difference from this study can be attributed to the influence of both the environmental pressure and oxygen fugacity conditions. In addition, reaction (1) provides an excess H<sub>2</sub>O in the capsule environment (<1 wt%) that is expected to extend (or buffer) the stability of schorl by counterbalancing the effect of dehydrogenation caused by the *T* increase. This is a quite realistic scenario that can be ascribed to a hydrous subducting slab (Schmidt and Poli, 2003) and recently confirmed by the finding of hydrous minerals and fluids included in fibrous diamonds with a subduction-related origin (Weiss et al., 2015).

In our work, after the schorl breakdown, the presence of quenched glass in the run products at *T* ≥ 800 °C revealed the formation of a hydrous liquid enriched in Si, Al, Na and B, according to the following reaction:



On basis of reaction (4), the first liquid phase produced by the structural breakdown of schorl into almandine and topaz should contain ~32 wt% SiO<sub>2</sub>, 27 wt% Al<sub>2</sub>O<sub>3</sub>, 8 wt% Na<sub>2</sub>O, 28 wt% B<sub>2</sub>O<sub>3</sub> and 5 wt% H<sub>2</sub>O. This liquid phase will only change its composition at higher temperatures when almandine and topaz start to decompose, and Fe-free, Al-richer phases are stabilized. A reaction like (4) was proposed by Ota et al. (2008a) based on HP-HT experiments conducted on a multi-phase system mimicking a pelitic system doped with dravite. Analogously to our runs, both garnet and, later, kyanite occurred as breakdown products, suggesting their common formation despite the distinct chemical composition of the employed tourmaline. In addition, at 5.0 GPa and 700 °C Ota et al. (2008a) proposed the formation of a B-poor and H<sub>2</sub>O-rich fluid phase coexisting with garnet, clinopyroxene, boromuscovite (in phengite) and kyanite. The glass we observed (Table 2) has an Fe-rich ultrabasic nature because is in equilibrium with Fe-rich garnet, and its composition resembles, except for the volatile content likely consisting in B and H<sub>2</sub>O (±CO<sub>2</sub> from the oxidation of the capsule material), that obtained by Dasgupta et al. (2006) by melting experiments on a carbonated silica-deficient eclogite, with SiO<sub>2</sub> contents ranging from 30 to 40 wt%, FeO between 14 and 26 wt% and Na<sub>2</sub>O between 1.75 and 5.1 wt%. Indeed, the glass quenched by Dasgupta et al. (2006) is, to date, a valuable candidate for metasomatic liquids

that would form during subduction of a carbonated oceanic crust and would undergo Si-depletion by fluids removal.

To effectively model the genesis of tourmaline-driven metasomatic fluids, the HP-HT behavior of Mg-rich tourmalines such as dravite or maruyamaite should be studied as they would better mimic the fate of B-bearing pelitic sediments down to the Earth's mantle (with implications for redox processes as C-precipitation and partial melting), but experimental results on the redox sensitivity of dravite and maruyamaite are missing to date. In contrast, the Fe-rich and reduced nature of the studied schorl (with all Fe as Fe<sup>2+</sup>) allowed shedding light on the mechanism of Fe oxidation in tourmaline at HP-HT, and our results represent a valid guide to refer to in terms of Fe-rich tourmalines *P-T* stability, dehydrogenation, breakdown, and redox-driven fluid formation at upper mantle depth for pure tourmaline systems.

The breakdown products observed for the studied schorl are well comparable to those reported for dravite at *P* > 1 GPa and *T* ≥ 900 °C by Werding and Schreyer (1996) based on the experiments of Krosse (1995), namely an assemblage of garnet and topaz followed by glass, kyanite, corundum, prismatic-like and boromullite-like phases. Moreover, a boromullite-like phase was recently described as a breakdown product of the Fe<sup>2+</sup>-bearing fluor-elbaite studied by Celata et al. (2021). The occurrence of both prismatic- and boromullite-like phases is especially relevant because they may act as B-carriers towards higher depths, having a relatively extended stability field (e.g., Buick et al., 2008; Schreyer and Werding, 1997; Werding and Schreyer, 1996).

Finally, in case of schorl-rich granitoid rocks involved in a subduction process (e.g., Xiong et al., 2022), our experiments suggest that the crustal contribution to the subducting slab has the potential to form hydrous B-bearing metasomatic melts at *P* of 3.5 GPa and *T* ≥ 700 °C due to schorl breakdown. Referring to the global range of thermal models for subduction zones proposed by Syracuse et al. (2010) and assuming a geobarometric gradient of 0.3 kbar/km, we can expect that pure schorl is stable up to ~100 km depth along the subducting slab, that is in be-

tween the 700–800 °C isotherms. This model is also coherent with *P-T* curves estimated for subduction-zone terrains by Zimmermann et al. (1994) and Marschall et al. (2009). However, in a SiO<sub>2</sub>-saturated system, as a natural granitoid tourmaline-bearing rock, the breakdown temperature of tourmaline can be lower, as suggested by the experimental work of Ota et al. (2008a). Therefore, multi-phase experiments in a SiO<sub>2</sub>-saturated system are left as a future issue to investigate schorl breakdown in complex systems.

## 4. Summary and conclusions

At 3.5 GPa and *T* ≥ 700 °C, in a pure schorl system the schorl structure is not stable anymore. The HP-HT breakdown temperature we obtained for schorl is considerably lower than the breakdown temperatures recorded for other tourmalines reported in literature so far, as higher temperatures had been obtained for both schorl at low or room pressure and Al- and Mg-rich tourmaline pure systems. Besides, within the continental (sialic) crust, the schorl stability field is expected to be further reduced by the excess of SiO<sub>2</sub>.

At 3.5 GPa and above 500 °C, the schorl experienced a partial H<sup>+</sup> loss paralleled by Fe<sup>2+</sup> oxidation. The extent of this reaction, which is thermally activated, is controlled by both environmental pressure and oxygen fugacity (as confirmed in a run where both Re and ReO<sub>2</sub> coexist).

Indeed, the release of H by schorl is a two-step process, the first described as the dehydrogenation starting above 500 °C (reaction 3), the second consisting in the structural breakdown above 700 °C (reaction 4). The first step only releases a fraction of H of the schorl, quantified as 0.80 apfu with respect to its stoichiometry (and corresponding to H<sub>2</sub>O about 0.90 wt%); the second step releases the rest of H, namely 2.66 apfu (corresponding to H<sub>2</sub>O about 2.10 wt%). In addition, the second step also releases all the B content of the schorl, that is 3.00 apfu (corresponding to B<sub>2</sub>O<sub>3</sub> about 10 wt%).

After the schorl breakdown, the reaction products are represented by almandine garnet, topaz, Fe-rich topaz, and a B-rich aqueous melt. This could be particularly relevant in subduction environments, as the release of both H<sub>2</sub>O and B would act as a flux, lowering surrounding rock's melting point.

At 3.5 GPa and temperatures  $\geq$  850 °C, almandine and topaz were not observed anymore, while corundum, kyanite, prismatic-like and boromullite-like phases became stable. Remarkably, the last two phases can incorporate B from the B-rich hydrous melt formed after the schorl breakdown and may carry it to lower depths, in a sort of *relay race* from crust to upper mantle.

Supplementary data to this article can be found online at <https://doi.org/10.1016/j.lithos.2022.106999>.

## Declaration of Competing Interest

The authors declare that they have no known competing financial interests or personal relationships that could have appeared to influence the work reported in this paper.

## Acknowledgements

This work was supported by Sapienza University of Rome through “Fondi di Ateneo 2017 and 2018” to V.S. and F.B. Marcello Serracino (CNR, IGAG-Rome), Marco Albano (CNR, IGAG-Rome) and Manuela Nazzari (INGV, Rome1) are acknowledged for their support during the SEM and EMP analysis.

## References

- Amthauer, G., Annersten, H., Hafner, S.S., 1976. The Mössbauer spectrum of <sup>57</sup>Fe in silicate garnets. *Z. Krist.* 143, 14–55.
- Andreozzi, G.B., Bosi, F., Longo, M., 2008. Linking Mössbauer and structural parameters in elbaite-schorl-dravite tourmalines. *Am. Mineral.* 93, 658–666.
- Andreozzi, G.B., Bosi, F., Celata, B., Capizzi, L.S., Stagno, V., Beckett-Brown, C., 2020. Crystal-chemical behavior of Fe<sup>2+</sup> in tourmaline dictated by structural stability: insights from a schorl with formula Na<sup>V</sup>(Fe<sup>2+</sup>Al)<sup>Z</sup>(Al<sub>3</sub>Fe<sup>2+</sup>)(Si<sub>6</sub>O<sub>18</sub>)(BO<sub>3</sub>)<sub>3</sub>(OH)<sub>3</sub>(OH, F) from Seagull batholith (Yukon Territory, Canada). *Phys. Chem. Miner.* 47 (25), 3–9.
- Bačik, P., Ozdín, D., Miglierini, M., Kardošová, P., Pentrák, M., Haloda, J., 2011. Crystallochemical effects on heat treatment on Fe-dominant tourmalines from Dolní Bory (Czech Republic) and Vlachovo (Slovakia). *Phys. Chem. Miner.* 38, 599–611.
- Bebout, G.E., Nakamura, E., 2003. Record in metamorphic tourmalines of subduction-zone devolatilization and boron cycling. *Geology* 31 (5), 407–410.
- Bose, K., Ganguly, J., 1995. Quartz-coesite transition revisited: Reversed experimental determination at 500–1200 °C and retrieved thermochemical properties. *Am. Mineral.* 80, 231–238.
- Bosi, F., Skogby, H., Hälenius, U., 2016. Thermally induced cation redistribution in Fe-bearing oxy-dravite and potential geothermometric implications. *Contrib. Mineral. Petrol.* 171 (5), 1–14.
- Bosi, F., Skogby, H., Hälenius, U., Ciriotti, M.E., 2018. Experimental cation redistribution in the tourmaline lucchesiite, CaFe<sub>3</sub><sup>2+</sup>Al<sub>6</sub>(Si<sub>6</sub>O<sub>18</sub>)(BO<sub>3</sub>)<sub>3</sub>(OH)<sub>3</sub>O. *Phys. Chem. Miner.* 45, 621–632.
- Bosi, F., Skogby, H., Hälenius, U., 2019. Thermally induced cation redistribution in fluor-elbaite and Fe-bearing tourmalines. *Phys. Chem. Miner.* 46, 371–383.
- Bosi, F., Celata, B., Skogby, H., Hälenius, U., Tempesta, G., Ciriotti, M.E., Bittarello, E., Marengo, A., 2021. Mn-bearing purplish-red tourmaline from the Anjanabonoina pegmatite, Madagascar. *Mineral. Mag.* 85, 242–253.
- Bruker, AXS, 2016. Topas V6: general profile and structure analysis software for powder diffraction data. Bruker AXS, Karlsruhe.
- Buick, I.S., Grew, E.S., Armbruster, T., Medenbach, O., Yates, M.G., Bebout, G.E., Clarke, G.L., 2008. Boromullite, Al<sub>9</sub>BSi<sub>2</sub>O<sub>19</sub>, a new mineral from granulite-facies metapelites, Mount Stafford, Central Australia: a natural analogue of a synthetic “boron-mullite”. *Eur. J. Mineral.* 20 (5), 935–950.

- Cannaò, E., Malaspina, N., 2018. From oceanic to continental subduction: Implications for the geochemical and redox evolution of the supra-subduction mantle. *Geosphere* 14 (6), 2311–2336. <https://doi.org/10.1130/GES01597.1>.
- Castañeda, C., Eeckhout, S.G., da Costa, G.M., Botelho, N.F., De Grave, E., 2006. Effect of heat treatment on tourmaline from Brazil. *Phys. Chem. Miner.* 33, 207–216.
- Celata, B., Ballirano, P., Andreozzi, G.B., Bosi, F., 2021. In-situ high-temperature behaviour and breakdown conditions of fluor-elbaite. *Phys. Chem. Miner.* 48, 24.
- Comte, D., Dorbath, L., Pardo, M., Monfret, T., Haessler, H., Rivera, L., Frogneux, M., Glass, B., Meneses, C., 1999. A double-layered seismic zone in Arica, northern Chile. *Geophys. Res. Lett.* 26, 1965–1968.
- Dasgupta, R., Hirschmann, M.M., Stalker, K., 2006. Immiscible transition from Carbonate-rich to Silicate-rich Melts in the 3 GPa Melting Interval of Eclogite + CO<sub>2</sub> and Genesis of Silica-undersaturated Ocean Island Lavas. *J. Petrol.* 47, 647–671.
- Ertl, A., Marshall, H.R., Giester, G., Henry, D.J., Schertl, H.P., Ntafos, T., Luvizotto, G.L., Nasdala, L., Tillmanns, E., 2010. Metamorphic ultrahigh-pressure tourmaline: Structure, chemistry and correlations to P-T conditions. *Am. Mineral.* 95, 1–10.
- Filip, J., Bosi, F., Novák, M., Skogby, H., Tuček, J., Čuda, J., Wildner, M., 2012. Iron redox reactions in the tourmaline structure: High-temperature treatment of Fe<sup>3+</sup>-rich schorl. *Geochim. Cosmochim. Acta* 86, 239–256.
- Grew, E.S., Krivovichev, S.V., Hazen, R.M., Hystad, G., 2016. Evolution of structural complexity in boron minerals. *Can. Mineral.* 54, 125–143.
- Hawthorne, F.C., Dirlam, D.M., 2011. Tourmaline the indicator mineral: from atomic arrangement to Viking navigation. *Elements* 7 (5), 307–312.
- Henry, D.J., Dutrow, B.L., 1996. Metamorphic tourmaline and its petrologic applications. In: Grew, E.S., Anovitz, L.M. (Eds.), *Boron Mineralogy, Petrology and Geochemistry - Reviews in Mineralogy and Geochemistry*, 33, pp. 503–557.
- Holtz, F., Johannes, W., 1991. Effect of tourmaline on melt fraction and composition of first melts in quartzofeldspathic gneiss. *Eur. J. Mineral.* 3, 527–536.
- Hudnut, K.W., Taber, J.J., 1987. Transition from double to single Wadati-Benioff seismic zone in the Shumagin islands, Alaska. *Geophys. Res. Lett.* 14, 143–146.
- Kao, H., Rau, R.J., 1999. Detailed structures of the subducted Philippine Sea plate beneath Northeast Taiwan: a new type of double seismic zone. *J. Geophys. Res.* 104, 1015–1033.
- Kawakami, T., 2004. Tourmaline and boron as indicators of the presence, segregation and extraction of melt in pelitic migmatites: examples from the Ryoke metamorphic belt, SW Japan. *Trans. R. Soc. Edinb. Earth Sci.* 95, 111–123.
- Kawakatsu, H., 1985. Double seismic zone in Tonga. *Lett. Nature* 316, 53–55.
- Korsakov, A., Musiyachenko, K., Rezvukhina, O., Mikhailenko, D., Rezvukhin, D., Mikhno, A., 2019. Diamond Inclusions in Schörl-Uvite Tourmaline from the Kumdyl-Kol Garnet-Clinopyroxene Rocks (Kokchetav Massif). *Goldschmidt. Abstracts* 2019, 1743.
- Krosse, S., 1995. Hochdrucksynthese, Stabilität und Eigenschaften der Borsilikate Dravit und Kornerupin, sowie Darstellung und Stabilitätsverhalten eines Neuen Mg-Al-borates. Ruhr-Universität Bochum, Thesis.
- Liu, X., Yu, C., Yang, W., Xie, L., Liang, S., 2019. Thermal decomposition kinetics of Fe-rich tourmaline. *Eur. J. Mineral.* 31, 919–928.
- Marschall, H.R., Altherr, R., Kalt, A., Ludwig, T., 2008. Detrital, metamorphic and metasomatic tourmaline in high-pressure metasediments from Syros (Greece): intra-grain boron isotope patterns determined by secondary-ion mass spectrometry. *Contrib. Mineral. Petrol.* 155, 703–717.
- Marschall, H.R., Korsakov, A.V., Luvizotto, G.L., Nasdala, L., Ludwig, T., 2009. On the occurrence and boron isotopic composition of tourmaline in (ultra)high-pressure metamorphic rocks. *J. Geol. Soc.* 166, 811–823.
- Mercurio, M., Rossi, M., Izzo, F., Cappelletti, P., Germinario, C., Grifa, C., Pretelli, M., Vergara, A., Langella, A., 2018. The characterization of natural gemstones using non-invasive FT-IR spectroscopy: new data on tourmalines. *Talanta* 178, 147–159.
- Mikhailenko, D.S., Stagno, V., Korsakov, A.V., Andreozzi, G.B., Marras, G., Cerantola, V., Malygina, E.V., 2020. Redox state determination of eclogite xenoliths from Udachnaya kimberlite pipe (Siberian craton), with some implications for the graphite/diamond formation. *Contrib. Mineral. Petrol.* 175 (11), 1–17.
- Moriguti, T., Shibata, T., Nakamura, E., 2004. Lithium, boron and lead isotope and trace element systematics of Quaternary basaltic volcanic rocks in northeastern Japan: mineralogical controls on slab-derived fluid composition. *Chem. Geol.* 212 (1–2), 81–100.
- Nakano, T., Nakamura, E., 2001. Boron isotope geochemistry of metasedimentary rocks and tourmalines in a subduction zone metamorphic suite. *Phys. Earth Planet. Inter.* 127 (1–4), 233–252.
- O'Neill, H.C., 1987. Quartz-fayalite-iron and quartz-fayalite-magnetite equilibria and the free energy of formation of fayalite (Fe<sub>2</sub>SiO<sub>4</sub>) and magnetite (Fe<sub>3</sub>O<sub>4</sub>). *Am. Mineral.* 72, 67–75.
- Ono, S., 1998. Stability limits of hydrous minerals in sediment and mid-ocean ridge basalt compositions: implications for water transport in subduction zones. *J. Geophys. Res.* 103 <https://doi.org/10.1029/98JB01351>. issn: 0148-0227.
- Ota, T., Kobayashi, K., Katsura, T., Nakamura, E., 2008a. Tourmaline breakdown in a pelitic system: implications for boron cycling through subduction zones. *Contrib. Mineral. Petrol.* 155, 19–32.
- Ota, T., Kobayashi, K., Kunihiro, T., Nakamura, E., 2008b. Boron cycling by subducted lithosphere: insights from diamondiferous tourmaline from Kokchetav ultrahigh-pressure metamorphic belt. *Geochim. Cosmochim. Acta* 72, 3531–3541.
- Pieczka, A., Kraczka, J., 2004. Oxidized tourmalines: a combined chemical, XRD and Mossbauer study. *Eur. J. Mineral.* 16, 309–321.
- Pownceby, M.I., O'Neill, H.S.C., 1994. Thermodynamic data from redox reactions at high temperatures. IV. Calibration of the Re-ReO<sub>2</sub> oxygen buffer from EMF and NiO + Ni-Pd redox sensor measurements. *Contrib. Mineral. Petrol.* 118, 130–137.



- Prescher, C., McCammon, C., Dubrovinsky, L., 2012. MossA: a program for analyzing energy-domain Mössbauer spectra from conventional and synchrotron sources. *J. Appl. Crystallogr.* 45, 329–331.
- Ratchkovsky, N.A., Pujol, J., Biswas, N.N., 1997. Relocation of earthquakes in the Cook Inlet area, south Central Alaska, using the joint hypocenter determination method. *Bull. Seismol. Soc. Am.* 87, 620–636.
- Reddy, B.J., Frost, R.L., Martens, W.N., Wain, D.L., Kloprogge, J.T., 2007. Spectroscopic characterization of Mn-rich tourmalines. *Vib. Spectrosc.* 44, 42–49.
- Robbins, C.R., Yoder, H.S., 1962. Stability relations of Dravite, a Tourmaline. In: *Carnegie Institute of Washington Yearbook*, 61, pp. 106–108.
- Schmidt, M.W., Poli, S., 1998. Experimentally based water budgets for dehydrating slabs and consequences for arc magma generation. *Earth Planet. Sci. Lett.* 163, 361–379.
- Schmidt, M.W., Poli, S., 2003. Generation of mobile components during subduction of oceanic crust. In: *Treatise on Geochemistry*, 3, pp. 567–591.
- Schreyer, W., Werding, G., 1997. High-pressure behaviour of selected boron minerals and the question of boron distribution between fluids and rocks. *Lithos* 251–266.
- Seno, T., Yamasaki, T., 2003. Low-frequency tremors, intraslab and interplate earthquakes in Southwest Japan—from a viewpoint of slab dehydration. *Geophys. Res. Lett.* 30.
- Shen, L., Hu, J., Zhu, X.Q., Zhang, W.J., 2011. Identification of natural tourmaline and similar gems by diffuse reflection fourier transform middle infrared Spectrum. *Adv. Mater. Res.* 177, 610–612.
- Shimizu, R., Ogasawara, Y., 2013. Diversity of potassium-bearing tourmalines in diamondiferous Kokchetav UHP metamorphic rocks: a geochemical recorder from peak to retrograde metamorphic stages. *J. Asian Earth Sci.* 63, 39–55.
- Sinclair, D.W., Richardson, J.M., 1992. Quartz-tourmaline orbicules in the Seagull Batholith, Yukon Territory. *Can. Mineral.* 30, 923–935.
- Smith, S.W., Knapp, J.S., McPherson, R.C., 1993. Seismicity of the Gorda plate, structure of continental margin, and an eastward jump of the Mendocino triple junction. *J. Geophys. Res.* 98, 8153–8171.
- Spicer, E.M., Stevens, G., Buick, I.S., 2004. The low-pressure partial-melting behaviour of natural boron-bearing metapelites from the Mt. Stafford area, Central Australia. *Contrib. Mineral. Petrol.* 148, 160–179.
- Stagno, V., Fei, Y., 2020. The redox boundaries of Earth's interior. *Elements: Int. Magaz. Mineral., Geochem., Petrol.* 16 (3), 167–172.
- Syracuse, E.M., van Kelen, P.E., Abers, G.A., 2010. The global range of subduction zone thermal models. *Phys. Earth Planet. Inter.* 183, 73–90.
- Tag, S.L., Cho, H., Dyar, D.M., Grew, E.S., 1999. *Am. Mineral.* 84, 1451–1455.
- van Hinsberg, V.J., Henry, D.J., Marshall, H.R., 2011. Tourmaline: an ideal indicator of its host environment. *Can. Mineral.* 49, 1–16.
- von Goerne, G., Franz, G., Robert, J.L., 1999. Upper thermal stability of tourmaline + quartz in the system MgO-Al<sub>2</sub>O<sub>3</sub>-SiO<sub>2</sub>-B<sub>2</sub>O<sub>3</sub>-H<sub>2</sub>O and Na<sub>2</sub>O-MgO-Al<sub>2</sub>O<sub>3</sub>-SiO<sub>2</sub>-B<sub>2</sub>O<sub>3</sub>-H<sub>2</sub>O-HCl. *Can. Mineral.* 37, 1025–1039.
- Weiss, Y., McNeill, J., Pearson, D., et al., 2015. Highly saline fluids from a subducting slab as the source for fluid-rich diamonds. *Nature* 524, 339–342.
- Werdning, G., Schreyer, W., 1984. Alkali-free tourmaline in the system MgO-Al<sub>2</sub>O<sub>3</sub>-B<sub>2</sub>O<sub>3</sub>-SiO<sub>2</sub>-H<sub>2</sub>O. *Geochimica. Cosmochimica. Acta* 48 (6), 1331–1344.
- Werdning, G., Schreyer, W., 1996. Experimental studies on borosilicates and selected borates. In: Grew, E.S., Anovitz, L.M. (Eds.), *Boron: Mineralogy, Petrology and Geochemistry in the earth's Crust. Reviews in Mineralogy and Geochemistry*, 33, pp. 117–163.
- Woodland, A.B., Ross, C.R., 1994. A crystallographic and Mössbauer spectroscopy study of Fe<sup>2+</sup>Al<sub>2</sub>Si<sub>3</sub>O<sub>12</sub> - Fe<sup>2+</sup>Fe<sup>3+</sup>Si<sub>3</sub>O<sub>12</sub> (almandine-“skiagite”) and Ca<sub>3</sub>Fe<sup>3+</sup>Si<sub>3</sub>O<sub>12</sub> - Fe<sup>2+</sup>Fe<sup>3+</sup>Si<sub>3</sub>O<sub>12</sub> (andradite-“skiagite”) garnet solid solutions. *Phys. Chem. Miner.* 21 (3), 117–132.
- Xiong, J.-W., Chen, Y.X., Ma, H.Z., Schertl, H.P., Zheng, Y.F., Zhao, K.D., 2022. Tourmaline boron isotopes trace metasomatism by serpentinite-derived fluid in continental subduction zone. *Geochim. Cosmochim. Acta* 320, 122–142.
- Yasuda, A., 2014. A new technique using FT-IR micro-reflectance spectroscopy for measurement of water concentrations in melt inclusions. *Earth, Planets and Space* 66, 34.
- Zhao, C., Liao, L., Xia, Z., Sun, X., 2012. Temperature-dependent Raman and infrared Spectroscopy study on iron-magnesium tourmalines with different Fe content. *Vib. Spectrosc.* 62, 28–34.
- Zimmermann, R., Hammerschmidt, K., Franz, G., 1994. Eocene high pressure metamorphism in the Penninic units of the Tauern Window (Eastern Alps): evidence from 40Ar-39Ar dating and petrological investigations. *Contrib. Mineral. Petrol.* 117, 175–186.

### 3. Discussion and conclusions

According to the focus of this research project, which was the experimental determination of thermal behavior, breakdown conditions and products of a wide compositional suite of borosilicate minerals (specifically tourmaline and axinite), it was possible to firstly investigate the thermal behavior of the studied samples (Table 2) through the *in situ* HT PXRD at RP, which allowed to better understand the mechanisms leading up to breakdown.

For all the tourmaline and axinite compositions investigated, a similar thermal behavior was observed. First, a linear thermal expansion of the unit cell parameters was observed up to ~ 450 °C and 575 °C for tourmalines and axinite, respectively. The data were fitted using the Berman equation (Berman 1988) and it turned out that for tourmaline the *c*-parameter is *softer* with respect to the *a*-parameter against *T* (the *softness* is here meant as the extent to which a material expands upon heating).

For axinite, the measured thermal expansion coefficients showed that the *b*-parameter is the *softest* against *T*. Above the mentioned temperatures, tourmalines and axinite started to behave differently.

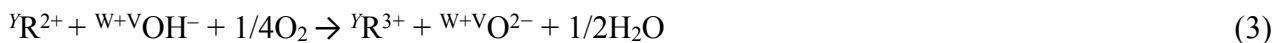
For tourmaline, a slight decrease of the thermal expansion was measured, specifically borne by volume and *a* parameter. Such a variation is due to the onset of a thermally induced coupled oxidation-dehydrogenation process as proposed first by Addison and Sharp (1962a) for amphiboles:



and adapted to tourmaline (schorl, Fe<sup>2+</sup>-bearing olenite and fluor-schorl) by Filip et al. (2012):



The validity of this model was experimentally demonstrated for all the tourmaline compositions investigated in this research project and also observed for Mn. Therefore, a more general reaction can be written as:



where R is the transition element hosted in the crystal structure of tourmaline at the *Y* site.

Therefore, during tourmaline progressive heating, partial water loss (intended as H<sup>+</sup> ions release) from the crystal structure is possible even before structural breakdown, and it is associated to the thermally-induced coupled oxidation-dehydrogenation.

As the oxidized transition element is smaller in terms of ionic radius with respect to the corresponding not oxidized atom, a downsizing of the YO<sub>6</sub> polyhedron (hosting the transition element) was also observed, leading to a decrease of both volume and *a* parameter.

The most the amount of transition elements accommodated in tourmaline's crystal structure, the most the extent of oxidation-dehydrogenation process experienced by structural parameters. In fact, schorl,

which contains the highest concentration of transition elements with respect to the other compositions here studied (schorl:  $\text{Fe}^{2+} = 2.05$  apfu; fluor-elbaite:  $(\text{Fe}^{2+} + \text{Mn}^{2+}) = 1.12$  apfu; uvite:  $\text{Fe}^{2+} = 0.47$  apfu; Mn-bearing fluor-elbaite:  $\text{Mn}^{2+} = 0.12$  apfu), is the most sensitive in terms of structural response to the oxidation-dehydrogenation phenomenon.

However, according to Addison and Sharp (1962b) the coupled mechanism of oxidation-dehydrogenation is actually more complex with respect to the simple reaction above mentioned (even if it was observed in amphiboles and phyllosilicates and it has not yet been investigated in tourmalines). It was described as a multi-stage process consisting in the main reaction (1) and two side reactions:



where reaction (4) occurs when there are no OH groups available on the mineral surface, and reaction (5) occurring at very high temperatures even in minerals that are not oxidizable.

For the side reaction (4) a charge transport mechanism is suggested, due to electron hopping across the structure from the inner not oxidized  $\text{Fe}^{2+}$  cations to the superficial oxidized  $\text{Fe}^{3+}$  cations and it would not involve any deprotonation. So,  $\text{Fe}^{2+}$  oxidizes to  $\text{Fe}^{3+}$ , transferring one of its electrons to gaseous  $\text{O}_2$  of the air that is accommodated on the surface of the crystal as  $\text{O}^{2-}$ .

The migration of electrons is supposed to require less energy than the ionic transport, hence the electron transfer from  $\text{Fe}^{2+}$  to an adjacent  $\text{Fe}^{3+}$  is thought to ensure the presence of the reactant  $\text{Fe}^{2+}$  at the surface.

Addison et al. (1962a, b) also proposed that the electron transfer can be stopped by ions that cannot accept electrons such as  $\text{Mg}^{2+}$ , consequently the higher the  $\text{Fe}^{2+}$  and the lower the content of  $\text{Mg}^{2+}$  the more easily  $\text{Fe}^{2+}$  can be accessible for oxidation.

For the electrons to move throughout the structure, a moderate conductivity is required. Tourmaline is known to be pyroelectric when heated and its pyroelectric coefficient at varying temperature is mainly originated from the intrinsic electric dipole moment changes of the  $\text{XO}_9$ ,  $\text{YO}_6$ ,  $\text{ZO}_6$ ,  $\text{TO}_4$ ,  $\text{BO}_3$  polyhedra along the  $c$ -axis. Each coordination polyhedron of tourmaline is equivalent to an electric dipole. When temperature changes, the positive and negative charge centers of ionic groups generate relative displacements, resulting in the change of intrinsic electric dipole moment of tourmaline. Specifically, Zhou et al. (2018) found that the deformations of the  $\text{SiO}_4$  tetrahedra and  $\text{BO}_3$  polyhedra the  $c$ -axis direction are the major responsible to the origins of the pyroelectricity of tourmaline at varying temperature.

There are different factors affecting the distortion of  $\text{SiO}_4$  polyhedra; for example the size of cations at the  $X$  site, where small cations as Ca are responsible for the shortening of  $X\text{-O}(4)$  and  $X\text{-O}(5)$  bond



lengths, leading to a larger distortion of the tetrahedral ring in terms of *ditrigonality* and *crimping* [when the bases of the tetrahedra are not parallel to (001) but are alternately tilted up and down by a small amount (Foit, 1989; Barton, 1969; Gorskaya et al., 1982)]. The *puckering* of the tetrahedral ring [i.e. the inwardly rotation of tetrahedra along the O(4)–O(5) axis] is instead affected by the chemical substitution occurring at the *Y* site where smaller cations lead to a larger distortion of the ring, as the substitution of Fe<sup>2+</sup> with a smaller and highly charged cation as Al<sup>3+</sup> leads to a compression of the *Y* octahedron, with a displacement of O(6) toward the threefold axis, thus affecting also the geometry of the tetrahedral ring (Foit, 1989).

Accordingly, Zhao et al. (2013) observed that structure, temperature, Fe content and valence affect polyhedron distortion parameters. Their results show that the bond-length and bond-angle distortion of the SiO<sub>4</sub> polyhedra in tourmaline decrease with increasing the Fe content, and the bond-length and bond-angle distortion of the SiO<sub>4</sub> polyhedra increases with increasing the heat treatment time, indicating that the temperature, iron content and valence are important factors affecting the geometry of the SiO<sub>4</sub> tetrahedral ring in tourmaline and, consequently, its pyroelectric properties.

Contemporarily, the OH<sup>-</sup> group are also re-generated at the surface by protons hopping from one oxygen on the adjacent oxygens from the interior of the crystal (Addison and Sharp, 1962a; Addison et al., 1962a, b), according to the following reaction:

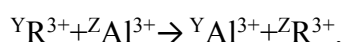


In tourmaline structure, diffusion of H<sup>+</sup> has been experimentally investigated and the diffusion coefficient was reported as 10<sup>-16</sup> (m<sup>2</sup>s<sup>-1</sup>) by Desbois and Ingrin (2007). Notably, the rate of diffusion is two to three times faster along the *c* direction and the configuration of tetrahedral rings pointing in the same direction makes a preferential way for H to diffuse along the structure.

In amphiboles, there is only one structural site, O(4), potentially able to accept a transient H in amphiboles due to its underbonding (Addison and Sharp, 1962a). However, in tourmaline structure there are no underbonded oxygens.

Oxidation as a function of time was not investigated in this work but Susta (2016) observed that in amphiboles the process is not time-dependent.

Further annealing of tourmaline produced a partial intracrystalline cation-exchange between the *Y* and *Z* site, with aluminum coming from the *Z* site going to substitute the oxidized transition element R<sup>3+</sup> at the *Y* site (exception made for Mn-bearing fluor-elbaite where Li was unexpectedly observed to migrate from *Y* to *Z* site instead of Mn):



Since the ionic radius of aluminum is fairly smaller with respect to that of the oxidized transition elements ( $\text{Fe}^{3+}$  and  $\text{Mn}^{3+}$ ), a shrinking of the  $\text{YO}_6$  polyhedron, due to the increased occupancy of aluminum in substitution of the oxidized transition element, was observed.

Accordingly, both volume and  $a$  parameter dropped sharply. The  $c$  parameter increased to compensate.

For axinite, the model above discussed does not apply, as the deviation from linearity of its thermal expansion at above  $575\text{ }^\circ\text{C}$  outlines an expansion of the unit-cell parameters, not clearly explained by the oxidation-dehydrogenation model predicted for tourmaline, that should have reasonably led to a contraction of the structure along the columns of  $\text{AlO}_6$  and  $(\text{Mg,Fe})\text{O}_6$  octahedra.

Further investigation on axinite structure is needed to figure out such a structural behavior during annealing.

Moving forward into the next objectives of this work, breakdown conditions of the samples here considered were reached through high-temperature  $HT$  and high-temperature high-pressure  $HT$ - $HP$  experiments. The breakdown of each phase was fixed in correspondence of the appearance of its first breakdown product.

With reference to the tourmaline here studied *in situ* at  $RP$ , despite their different composition in terms of  $X$  and  $Y$  site occupancy (see Table 2), all of them experienced breakdown at temperatures falling within a very narrow range: from  $803$  to  $850\text{ }^\circ\text{C}$ . This means that the different occupancy of sites  $X$  and  $Y$  does not substantially affect the stability of tourmaline.

Accordingly to what reported by Bosi (2018), the entire tourmaline structure can be interpreted as a continuous 3D framework of  $\text{AlO}_6$  polyhedra ( $Z$  sites) enclosing the structural "islands" made up of  $X$ - $Y$ - $T$ - $B$  polyhedra (Figure 4). Therefore, what actually matters for tourmaline to behave differently in terms of thermal behavior and stability is the  $Z$  site composition. In fact, all the tourmalines here investigated share the same  $Z$  site occupancy, which is dominated by  $\text{Al}$ .

When cations as  $\text{Fe}^{3+}$ ,  $\text{Cr}^{3+}$  and  $\text{V}^{3+}$  substitute  $\text{Al}$  at the  $Z$  site, the structure should be highly affected in its thermal behavior, as they are different in terms of chemical *hardness*. *Hard* cations as  $\text{Al}^{3+}$  are small in ionic radius, have high charge and behave as hard spheres, meaning that they do not deform in different ways to match the local environment. *Soft* cations commonly have a small ionic radius, low charge and are strongly polarizable. With respect to  $\text{Al}^{3+}$ , the above mentioned  $\text{Fe}^{3+}$ ,  $\text{Cr}^{3+}$  and  $\text{V}^{3+}$  are *softer*. Consequently, it is reasonable to expect a different thermal behavior and breakdown temperature at  $RP$  of  $(\text{Fe}^{3+}, \text{Cr}^{3+}, \text{V}^{3+})$ -rich tourmaline compositions (namely, povondraite, oxy chromium-dravite and oxy vanadium-dravite). Unfortunately, no data about the breakdown temperature of such phases are available to date.

The schorl was the only tourmaline composition investigated at *HP*, and the first appearance of garnet at 700 °C and 3.5 GPa was chosen as the criterion to fix its breakdown temperature. Comparing this breakdown temperature with those observed at *RP* for schorl and other tourmaline compositions, and also considering the data reported in van Hinsberg et al. (2011), it can be stated that the high pressure is largely responsible of lowering the stability of tourmaline.

In natural environments as cold subduction systems (see Syracuse et al., 2010), the borosilicates here studied are therefore stable in the inner colder core of the downgoing slab, even if the eventual saturation in SiO<sub>2</sub> might lower even further the breakdown temperature, as suggested by the experimental work of Ota et al. (2008).

With reference to axinite, annealing at *RP* led to the structural collapse at 850 °C, consistently with literature data regarding axinites of similar composition. No obvious correlation between composition and breakdown temperature was to date observed.

The structural breakdown (the conditions of which were above-mentioned) of the tourmalines and axinites here considered, resulted in the formation of different products with or without the production of a melt. When a melt was produced as a result of breakdown, the obtained data show that it was usually enriched in B<sub>2</sub>O<sub>3</sub>, SiO<sub>2</sub> and H<sub>2</sub>O.

The crystalline phases that occur after tourmaline breakdown are mostly represented by aluminosilicates as mullite-like phases (dominant at *RP*) and garnet (at *HP*). Boron-bearing mullite-type compounds were identified as new B carriers in a hypothetical scenario of a post-tourmaline paragenesis.

As regards axinite, after breakdown it melts incongruently at 850 °C, giving products as anorthite and clinopyroxene and quartz, plus a very minor amount of amorphous material where boron and water are supposed to be stored.

## Implications

Tourmaline at high-temperature and high-pressure conditions (comparable to those occurring in the shallower portion of a slab down to 120 Km) can release structural water as both H<sup>+</sup> ions, during the thermally-induced coupled oxidation-dehydrogenation process, and OH<sup>-</sup> groups, during the breakdown reaction. The amount of water released during the oxidation-dehydrogenation process in this work was only evaluated for schorl composition through <sup>57</sup>Fe Mössbauer spectroscopy, being equal to 0.80 apfu with respect to tourmaline stoichiometry (corresponding to H<sub>2</sub>O about 0.90 wt.%).

The remaining water amount released during breakdown is equal to 2.66 apfu (corresponding to H<sub>2</sub>O about 2.1 wt.%).

Water content (intended as structural water represented by both H<sup>+</sup> and OH<sup>-</sup>) is one of the most influential factors on melting behavior of silicate rocks, plastic deformation of subducting material and electrical conductivity at high-temperature and high-pressure conditions. Consequently, determining the distribution of water in the Earth's mantle is a substantial issue in solid Earth geophysics and geochemistry. Hydrogen in nominally anhydrous minerals can enhance the electrical conductivity of the upper mantle and transition zone. High conductivity anomalies are in fact widely observed both in the continental mid-crust as well as backarc and forearc regions of subduction zones, characterized by conductivity values of 0.01–1 S/m (Hu et al. 2017) and are assigned to the occurrence of fluids released by dehydration of hydrous minerals (commonly represented by amphiboles, chlorite, zoisite and talc) along the subducting slab. Therefore, it is crucial to investigate how water is carried down the slab and define the processes through which it is released.

#### Open questions

The mineral phases investigated in this research project were only considered in a mono-phase system, thus neglecting the role of other phases that naturally occur as companion minerals in the hosting rocks. The breakdown conditions of the examined borosilicates might likely be considerably affected by the presence of other minerals, therefore, further research on borosilicates breakdown considered in their natural assemblages should be pursued.

Moreover, an oxidation-dehydrogenation process was observed before breakdown during the annealing of the tourmaline samples with both *in situ* and *ex situ* analytical techniques, but it was not always possible to obtain quantitative data about the amount of H<sup>+</sup> lost during the process. Consequently, specific experiments could be designed to address this issue, for example thermogravimetric analysis (TGA) or, if only Fe is present as transition element, Mössbauer spectroscopy to be performed on the annealed powder.

As regards the axinite, it is still unclear why the oxidation-dehydrogenation process was not observed after the annealing, as the bond valence sum clearly showed that hydrogen is still bonded to the structure. Even the sharp thermal expansion showed by the sample at above 600 °C remains unexplained, as it is not likely that a polymorph transformation occurred, as instead is reported in literature as a possible interpretation.

## Acknowledgments

I am deeply grateful to Prof. Giovanni B. Andreozzi for his dedication and trust in this project. His critical review and vision actually raised the bar of this research.

Prof. Ferdinando Bosi and Prof. Paolo Ballirano are acknowledged for the valuable assistance during the experimental work and data treatment. The meaningful dialogue we established helped me pursuing the goal of my research project.

## References

- Addison WE, Sharp JH (1962a) Amphiboles. Part III. The reduction of crocidolite. *Journal of Chemical Society* 3693–3698.
- Addison WE, Sharp JH (1962b) A mechanism for the oxidation of ferrous iron in hydroxylated silicates. Meeting of the Clay Minerals Group of the Mineralogical Society, Leeds, 73–79.
- Addison CC, Addison WE, Neal GH, Sharp JH (1962a) Amphiboles. Part I. The oxidation of crocidolite. *Journal of Chemical Society*, 1468–1471.
- Addison WE, Neal GH, Sharp JH (1962b). Amphiboles. Part II. The kinetics of oxidation of crocidolite. *Journal of Chemical Society*, 1472–1475.
- Barton R Jr (1969) Refinement of the crystal structure of buergerite and the absolute orientation of tourmalines. *Acta Crystallographica B*25: 1524–1533.
- Berman RG (1988) Internally-consistent thermodynamic data for minerals in the system Na<sub>2</sub>O–K<sub>2</sub>O–CaO–MgO–FeO–Fe<sub>2</sub>O<sub>3</sub>–Al<sub>2</sub>O<sub>3</sub>–SiO<sub>2</sub>–TiO<sub>2</sub>–H<sub>2</sub>O–CO<sub>2</sub>. *Journal of Petrology* 29:445–522.
- Bosi F (2018) Tourmaline crystal chemistry. *American Mineralogist* 103: 298–306.
- Desbois G, Ingrin J (2007) Anisotropy of hydrogen diffusion in tourmaline. *Geochimica et Cosmochimica Acta* 71(21): 5233–5243.
- Filip J, Bosi F, Novák M, Skogby H, Tuček J, Čuda J, Wildner M (2012) Iron redox reactions in the tourmaline structure: high-temperature treatment of Fe<sup>3+</sup>-rich schorl. *Geochimica et Cosmochimica Acta* 86:239–256.
- Foit FF Jr (1989) Crystal chemistry of alkali-deficient and tourmaline structural relationships. *American Mineralogist*, 74: 422–431.
- Gorskaya MG, Frank-Kamenetskaya OV, Rozhdestvenskaya IV (1982) Refinement of the structure of Al-rich elbaite and some aspects of the crystal chemistry of tourmalines. *Soviet Physics Crystallography* 27(1): 63–66.

- Hu H, Dai L, Li H, Hui K, Sun W (2017) Influence of dehydration on the electrical conductivity of epidote and implications for high-conductivity anomalies in subduction zones. *Journal of Geophysical Research: Solid Earth* 122:2751–2762
- Ota T, Kobayashi K, Katsura T, Nakamura E (2008) Tourmaline breakdown in a pelitic system: implications for boron cycling through subduction zones. *Contributions to Mineralogy and Petrology* 155: 19-32
- Susta U (2016) Dehydration and deprotonation processes in minerals: development of new spectroscopic techniques. Doctoral thesis
- Syracuse EM, van Kelen PE, Abers GA (2010). The global range of subduction zone thermal models. *Physics of the Earth and Planetary Interiors* 183:73–90.
- van Hinsberg V, Henry DJ, Marschall HR (2011) Tourmaline: an ideal indicator of its host environment. *The Canadian Mineralogist* 49:1–16
- Zhao C, Liao L, Yao Cheng JY (2013) Influence of temperature, the content and valence of Fe in tourmaline on their polyhedron distortion. *Journal of the Chinese Ceramic Society* 41(1): 103–109.
- Zhou G, Liu H, Chen K, Gai X, Zhao C, Liao L, Shen K, Fan Z, Shan Y (2018) The origin of pyroelectricity in tourmaline at varying temperature. *Journal of Alloys and Compounds* 744: 328–336.